Photophysical Properties of Protonated Aromatic Hydrocarbons

Thesis by

Vadym A. Kapinus

In Partial Fulfillment of the Requirements

for the Degree of

Doctor of Philosophy

California Institute of Technology

Pasadena, California

2005

(Defended December 14, 2004)

Acknowledgements

I have greatly enjoyed the years I have spent at Caltech and it will be hard to express my thanks to the many people to whom I am indebted to for such unforgettable experiences.

First, I was fortunate to have Professor Geoffrey Blake as my research advisor. I appreciate the energy, enthusiasm and support that Geoff provided during my graduate career. The door of his office was always open for students, he always welcomed new ideas, and would have a few suggestions when the experiment did not work. Most of all, I value the freedom that Geoff gave me in conducting research. I would also like to thank Professors Jack Beauchamp and Mitchio Okumura for some of the discussions I had with them.

When I joined the Blake group, I was working closely on the experiments with Sheng Wu and Zulfikar Morbi. I learned many things about non-linear optical devices from Sheng, and later I had a long collaboration with him on a number of tunable solid state light sources. Zulf and I worked on the carbon chain project, and from him I learned many useful things about lab management and experimental techniques. He was also the one who started me on programming the remote control of digital oscilloscopes, which later became the main part of my data collection software. Susanna Widicus-Weaver helped me in my attempt to record the microwave spectrum of protonated benzene. Michael Morton was the beta tester for the BGSpecT software.

The Blake group was an interesting place to work and I would like to thank some of its former and current members for providing a friendly working environment, and for lending a hand or a good word when I needed them: Susanna, Mike, Zulf, Sheng, Hui Zhang, Zifu Wang, François Jeanneret, Rogier Braakman and Daniel Holland.

Administrative assistants, Janis Haskell and Leticia Calderon from GPS division were very helpful with placing orders and solving some organizational questions. I would also like to acknowledge the help of the people from the Chemistry machine shop for their quality work on the parts for my experiment: Mike Roy, Guy Duremburg, Ray Garcia and Steven Olson. Tom Dunn from the Chemistry electronics shop was helpful with circuit designs and was generous with borrowing his high voltage probe. Tony Solyom from the Biology Division fixed a few chillers and vacuum pumps for me. I also enjoyed our long conversations on various topics. My thanks go to the Thaddeus group from Harvard for sharing their designs of the discharge source and the electronic circuitry for it.

With Andrei Deev, a longtime friend and roommate since my undergraduate years, I had many discussions about science and life in general. Ironically, we both ended up at Caltech, in the same department, and conducting research in related areas – even having our thesis defense scheduled on the same day!

Many other people at Caltech contributed to the quality of my non-academic life, and became my friends. Julia Lyubovitsky taught me quite a few subtle things about american culture, first when doing homework together and later, during our long lunch chats. Leo Eisner used my weakness for good food to introduce me to the sport of orienteering. Together, we had many unforgettable moments, especially at Mt. Piños, Redwoods, Lake Tahoe and the Sierras.

Ulyana Dyudina, Andrei Khodakovsky, Andrey Bereznyak and Dmitry Novikov were my buddies on hiking trips – from going up to the local mountains, to going down to the Grand

Canyon. They, and some other members of russian-speaking community (Andy Greenberg and Galina Lokshina, George Shapovalov and Kira Kostenko, Alexander Putilin, Vadim Borokhov, Alexei Dvoretskii, Ivan Mokhnal and Dmitry Kossakovski) did not allow me to lose the cultural connection with my homeland.

I would like to thank my soccer teammates from the Red Square and Kicking Buck teams, especially Jim Kempf, Lou Madsen and Gabriel Brandt.

I became a fan and a participant of another sport at Caltech: dancesport. Derrick Bass, the legendary guru of the Caltech Ballroom Dance Club, taught me my first steps. His thorough teaching style (what else can you expect from a theoretical physicist?) sparked my competitive spirit and interest in good technique. Our activities were not only limited to the dance floor with many other members of the 'old' team, including my first partner Meina Xu, Andreea Boca, Kok Win Goh, Joseph Chen, Christina Lam, Andrej Zlatos, Tammy Lam, Helen Claudio, Ania Kashina, Ulyana, Galka, Sasha. I also enjoyed working closely with the members of the CBDC organizing committee, especially Michael Fleming, Megan Ferguson and Keith Brown.

My dancing hobby profoundly changed my life by leading me to cross paths with my wife, Vanessa, who from just being a friend and dance partner became my best friend and partner in life. Her friendly words and warm smile gave me a lot of energy during the past two years. I express my great appreciation for her love, encouragement, patience and faith in me.

Finally, I would like to thank my family, especially my parents, Alexander and Nelya. They always provided me with freedom of choice and supported my interest in science, even when that interest led me to distant shores.

Abstract

Diffuse interstellar bands (DIBs) were first observed in the visible region of the electromagnetic spectrum in the 1920s, with over a hundred features now discovered out to near-IR wavelengths. Since their initial discovery, many attempts have been made to identify the species that are responsible for the DIBs. Polycyclic aromatic hydrocarbons (PAHs) and their derivatives are among the likely candidates for DIB carriers, as demonstrated by the intense unidentified IR emission bands from 3.3 – 11.3 μm that strongly point to their presence of aromatic species in the interstellar medium (ISM). The $S_1 \leftarrow S_0$ electronic transitions for small PAHs lie in the near-UV, however, so only large neutral PAHs with 30+ carbon atoms can absorb at the visible wavelengths characteristic of the DIBs. In diffuse clouds and dense cloud envelopes that are exposed to the harsh interstellar radiation field, molecules are expected to be ionized. Positively charged PAHs are predicted to acquire a hydrogen atom to form thermodynamically stable protonated PAHs in diffuse clouds. These are closed-shell molecular ions with electronic transitions that are red-shifted compared to neutral PAHs, so even small protonated PAHs can, in principle, produce absorption bands in the visible.

Little is known about the photophysical properties of these compounds, however, so this thesis presents an experimental and theoretical analysis of two-, three-, and four-ring protonated PAHs. Theoretically, density functional theory calculations using the B3LYP

functional were used to study protonated PAHs in their ground electronic state. In particular, the energetics of the various potential protonated PAH isomers were calculated along with the proton tunneling or hopping barriers between them. The relative energies of the lowest lying photodissociation pathways were also calculated. It was found that the different isomers of protonated PAHs likely exist in thermodynamic equilibrium under interstellar conditions, thanks to the moderate (∼15 – 20 kcal/mol) barriers to proton migration. Photochemically, the loss of an H atom or H_2 molecule from a protonation site were identified as the most favorable dissociation channels for protonated PAHs. The H and H_2 loss channels were found to be within a few kcal/mol of each other in energy, and about 45 – 60 kcal/mol above the ground state, depending on the parent molecule and isomer.

Following the ground state geometry optimizations and energy calculations, the Configuration Interaction Singles (CIS) method was used to estimate the positions of the electronic transitions for protonated PAHs. Depending on the PAH and isomer, red shifts up to 150 nm were predicted even for small systems, i.e., protonated naphthalene, anthracene, phenanthrene and pyrene. This places the $S_1 \leftarrow S_0$ transitions of essentially all protonated PAHs well into the DIB wavelength region.

In order to investigate these predictions experimentally, a robust hydrogen discharge source was designed to produce protonated PAHs. Laser photodissociation of protonated PAHs was first studied with an excimer laser/reflectron time-of-flight mass spectrometer under ultrahigh vacuum conditions that mimic those in the ISM. Small protonated PAHs were found to be very photostable. Indeed, it was determined that nanosecond pulse length photodissociation is multiphoton even at short wavelengths (193 nm). For protonated anthracene, the dissociation limit was estimated to be 13 – 15 eV, which is much higher than the predicted thermodynamic threshold of 2.5 – 3.0 eV. This was attributed to the onset of rapid intramolecular vibrational relaxation (IVR) upon electronic excitation.

Thanks to the excellent photostability of protonated PAHs, a cluster photodissociation approach was used to locate the electronic transitions of protonated anthracene between 420 and 540 nm. Clusters with water molecules were produced in a two-valve mixing discharge source. Visible photodissociation spectrum of these clusters was recorded using a novel optical parametric oscillator (OPO) with low beam divergence. The OPO utilizes a hybrid matching scheme involving BBO type I and II crystals in a rotated prism cavity. The observed protonated anthracene absorption bands are very wide (20 nm FWHM) – too wide to account for the DIBs. Again, this spectral broadening most likely results from rapid IVR induced by the high density of states in protonated PAHs. Such strong, wide bands may be important contributors to the overall visual extinction in the diffuse ISM and should efficiently produce infrared emission such as that seen in the Unidentified Infrared emission features, or UIRs.

Contents

List of Figures

List of Tables

Chapter 1

Protonated Polycyclic Aromatic Hydrocarbons and the Interstellar Medium

1.1 Interstellar Molecules

Although hydrogen is the most abundant element in the universe, it is other elements that determine the complexity of interstellar chemistry. Besides hydrogen and helium which account for 98% of the mass of a gas of 'solar composition,' the next most abundant elements are oxygen, carbon, and nitrogen (Table 1.1). Together with hydrogen, these elements form the main building blocks for molecules detected in the interstellar medium, or ISM.

Table 1.1: Abundance of the more common chemical elements in the solar system [4].

Element		Abundance Atoms / 10^6 Si
H	Hydrogen	$2.72{\cdot}10^{10}$
He	Helium	$2.15{\cdot}10^{9}$
O	Oxygen	$2.01{\cdot}10^{7}$
C	Carbon	$1.21{\cdot}10^{7}$
Ne	Neon	$3.76{\cdot}10^{6}$
N	Nitrogen	$2.48{\cdot}10^{6}$
Mg	Magnesium	$1.08{\cdot}10^{6}$
Si	Silicon	$1.00{\cdot}10^{6}$
Fe	Iron	$9.00{\cdot}10^{5}$
S	Sulfur	$5.15{\cdot}10^{5}$

Table 1.2: Identified interstellar and circumstellar molecules and molecular ions (as of Dec. 2004).

Number of atoms								
2	3	4	5	6	7	8	9	10+
H_2	H_2O	NH_3	CH_4	CH_3OH	$HCCCH_3$	CH_3COOH	$(CH_3)_2O$	$(CH_3)_2CO$
CO	H_2S	H_2CO	SiH_4	CH_3SH	$HC(O)CH_3$	$HC(O)OCH_3$	C_2H_5OH	$(CH_2OH)_2$
CSi	HCN	H_2CS	CH_2NH	C_2H_4	CH_3NH_2	H_3C_3-CN	C_2H_5CN	
CP	HNC	C_2H_2	NH_2CN	HC_4H	$CH_2CH(CN)$	$HOCH_2C(O)H$	CH_3C_4H	HC_8CN
CS	CO_2	HNCO	CH_2CO	CH_3CN	HC_4-CN	C_6H_2	HC_6CN	
NO	SO_2	HNCS	HCOOH	CH_3NC	C_6H	C_6H_2	C_8H	C_6H_6
NS	MgCN	H_3O^+	HCC-CN	$HC(O)NH_2$	c-C_2H_4O	C_2H_6		$OC(CH_2OH)_2$
SO	MgNC	$HOCO^+$	HCC-NC	HCCC(O)H	$CH_2CH(OH)$	C_7H		
HCl	NaCN	C_3S	c-C_3H_2	C_5H		$H_2CCHC(O)H$		$HC_{11}N$
NaCl	N_2O	H_2CN	l-C_3H_2	HC_3NH^+				
KCl	NH_2	c-C_3H	CH_2CN	C_5O				
AlCl	OCS	l-C_3H	C_4H	C_5N				
AlF	HCO	HCCN	C_4Si					
PN	C_3	H_2CO^+	C_5					
SiN	C_2H	C_2CN	HNCCC					
SiO	HCO^+	C_3O	H_2COH^+					
SiS	HOC^+	$HCNH^+$						
NH	N_2H^+	CH_2D^+						
OH	HNO	CH_3						
C_2	HCS^+	SiC_3						
CN	H_3^+	ND_3						
HF	C_2O							
CO^+	C_2S							
SO^+	SiC_2							
CH	AlNC							
CH^+	CH_2							
SH	SiCN							
LiH								
FeO								

Nearly 150 molecules and molecular ions have been detected in interstellar and circumstellar environments to date [5,6] (Table 1.2). Most of them are small, 2 – 4 atom molecules. Many of the larger molecules are linear or highly symmetric and have large dipole moments which facilitate their detection. There must be many more less abundant or not as strongly absorbing/emitting molecules in the ISM that have not yet been detected or positively identified. One such suite of molecules involves polycyclic aromatic hydrocarbons (PAHs) and their derivatives. While PAHs are believed to be present in the ISM in large quantities, benzene is the only aromatic molecule for which a possible detection has been reported using high resolution spectroscopy such as that used to assemble Table 1.2 [7].

1.2 PAHs and the Unidentified IR Emission Bands

In 1973, an Unidentified Infrared Emission band (UIR) was observed at 11.3 μm from a planetary nebulae [8]. A few other observations of a variety of objects added 3.3, 6.2, 7.7, 8.6, 12.7, 14.2, and 16.2 μm bands to the UIR list [9–13]. The strongest emission was observed from dusty regions bathed in the intense UV radiation from nearby young stars. The emitting species could not be identified exactly, although some conclusions were made about their nature.

Associated with these UIR bands is a pseudo-continuum component whose color temperature is independent of the distance from the exciting star [14]. Thus, both the continuum and bands must be produced by the 'heating' associated with the absorption of a single photon [15,16]. This requires the species responsible for the emission to be intermediate in size, between small molecules and macroscopic dust grains ($\sim$20 – 50 atoms). It has been noted that some of the vibrations of aromatic hydrocarbons are close in wavelength to many of the UIR features [17]. Based on intensity ratios and the correlation observed among different

UIRs, it has been suggested that the PAHs which generate these IR bands are peripherally hydrogenated, should have pericondensed structures, and may be ionized [16, 18].

Numerous laboratory experiments have been conducted to measure the IR and visible spectra of neutral and ionic PAHs, and the results have been compared to astronomical observations [19–21]. From laboratory measurements, it was established that both neutral and cationic PAHs may be UIR carriers [22], but that ionized PAHs provide a better match to the general characteristics observed in the interstellar spectra. Density functional calculations added protonated PAHs to that list [23]. Although no single PAH species can account for the full suite of UIR features alone, it is possible to approximate the observed astronomical spectra by a mixture of many different PAHs [24].

PAHs are believed to be ubiquitous in the ISM, for the UIR features are observed throughout the galaxy. As a class, they may be the most abundant organic species in the ISM, and may account for up to 20% of total interstellar carbon [25]. They may also be responsible for other astronomical features, such as the Diffuse Interstellar Bands, discussed next.

1.3 The Diffuse Interstellar Bands

The Diffuse Interstellar Bands, or DIBs, present the longest-standing puzzle in astronomical spectroscopy [26]. The DIBs are $1 - 200$ cm^{-1} wide features in seen visible and near infrared spectra of reddened stars, produced by the absorption of star light by species in diffuse or translucent interstellar clouds. They were originally discovered in 1922 [27], but their interstellar nature was only established some twelve years later [28, 29]. By 1975, 39 DIBs had been discovered [30]. Thanks to ongoing improvements in astronomical spectrographs and especially in CCD arrays, a large number of weaker DIBs have now been discovered. Based on more recent surveys [31–33], for example, there are more than 150 known DIBs that span the wavelength interval from 380 to 950 nm (Figure 1.1).

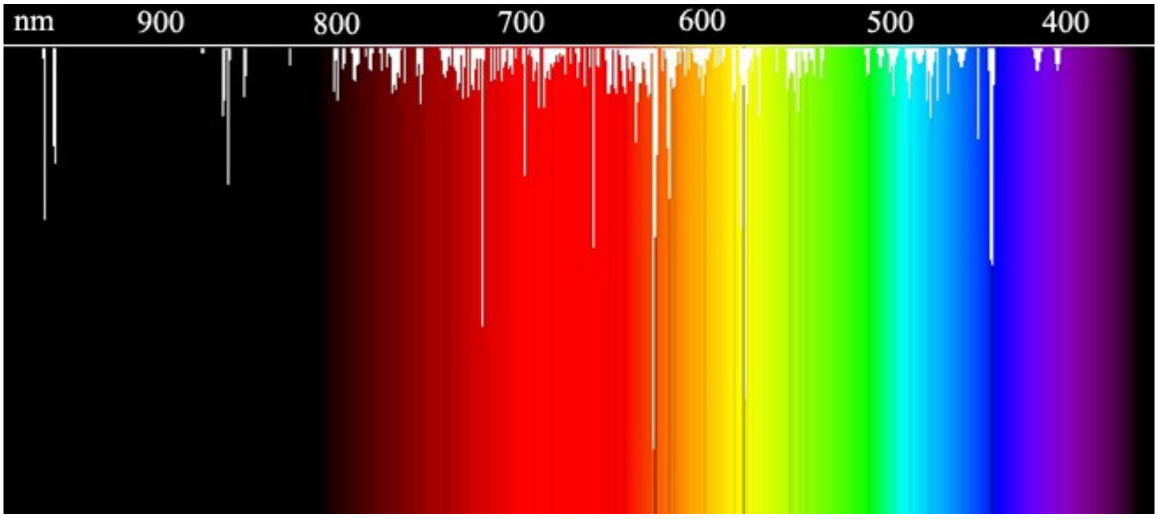

Figure 1.1: A synthetic spectrum of the diffuse interstellar bands, based on the DIB compilation in [1]. The image is from [2].

Many different theories have been proposed to account for the DIBs. The wide range of DIB widths and the fact that a few of the DIBs are seen in emission toward unusual objects points to the molecular nature of the species responsible. Carriers cannot reside on or within dust particles or grains because particle size, shape and composition influence the peak positions and profiles, which have not been observed astronomically. Since a wide variety of carbon-containing species are found in space and since the overall strength of the DIBs is well correlated with the [C]/[H] ratio, carbonaceous molecules or radicals are the most attractive candidates. Among them are [34, 35]:

1. Highly unsaturated hydrocarbons (carbon chains)
2. Polycyclic aromatic hydrocarbons (PAHs)
3. Fullerenes and their derivatives

4. Porphyrins
5. Other unspecified organics

The first two classes have been studied extensively in the laboratory setting, and therefore, will be reviewed here.

1.3.1 Carbon Chains and the DIBs

Carbon chains have been cited as promising candidates for DIB carriers for many years [36, 37]. Their conjugated systems of electrons produce intense $\pi - \pi^*$ transitions at visible and UV wavelengths. Both the electronic oscillator strengths and dipole moments of (apolar) carbon chains increase with chain length, a fact that has enabled the detection of quite long chains – up to $HC_{11}N$ and C_8H – in dark molecular clouds by radio astronomy methods [38,39]. Laboratory spectra of carbon chains have been measured in microwave [40–42], visible, and UV [43–47] wavelength ranges. Such studies culminated in measurements of the electronic absorption spectra of carbon chain anions C_6^-, C_7^-, C_8^- and C_9^-, whose π – π^* transitions were found to be very close to a number of DIBs [48, 49]. More detailed astronomical spectroscopy failed to yield a definite assignment of any DIBs to carbon chain anions [50–52], but even so, it is not possible to completely rule out carbon chains as potential DIB carriers – especially large chains where very strong excited state (S_n, $n \geq 2$) bands move into the visible [53].

1.3.2 PAHs and the DIBs

PAHs are good candidates for DIB carriers. They are thought to be present in a large number of environments in the ISM from the widespread detection of the UIRs. While the UIRs provide important constraints on the *type* of material responsible for the emission, they are sufficiently broad and entangled that the identification of specific molecular species is not possible. These bands are believed to be emitted by large, internally excited molecules, and the only way to efficiently generate such excitation is through the absorption of visible or UV photons. The first electronic transitions of small, multi-ring neutral PAHs lie in the near-UV. For example, the $S_1 \leftarrow S_0$ transition for anthracene occurs at 361.17 nm, and that for pyrene at 367.43 nm. A PAH molecule needs to have at least 25 – 30 carbon atoms to absorb strongly in the visible range, and the number of carbon atoms must be significantly larger in order to achieve absorption in the red and near IR parts of the spectrum where many DIBs are located.

On the other hand, even small PAH cations absorb visible and near-IR photons. For example, the $D_2 \leftarrow D_0$ transitions of the naphthalene and phenanthrene cations lie at 670.65 nm and 891.90 nm, respectively; the $D_3 \leftarrow D_0$ transition of the naphthalene cation has been measured to be 454.85 nm. The ionization energies of PAHs are below 9.3 eV, and for PAHs with more than two aromatic rings they are less than 7.9 eV. Neutral PAHs should therefore be ionized rapidly in the regions of the ISM exposed to UV radiation, i.e., close to stars or in diffuse interstellar clouds.

A few attempts have been made to compare PAH electronic spectra with the DIBs [54–56], but while there are some close coincidences, no DIBs have been found to have an exact match with the measured electronic transitions of neutral PAHs or their cations. In general, if PAHs are indeed DIB carriers, one might expect them to be responsible for the wider DIB features due to their large sizes as compared to the molecules detected by high resolution spectroscopy.

In the past, the lack of laboratory data for PAHs led to a suite of extensive studies in matrices [56–59], helium droplets [60, 61] and the gas phase (both isolated [61–69] and in clusters [69–74]). There are, however, several experimental challenges that make it difficult to obtain the spectra of cold, isolated, multi-ring PAHs which could be directly compared with the DIBs.

In the gas phase, it is hard to achieve high PAH concentrations due to the low vapor pressure of the solid. For example, most PAH samples have to be heated to high temperatures, sometimes in excess of 300 – 500 °C, in order to carry out direct absorption studies or to efficiently seed them into molecular beams. The heated vapor is vibrationally hot, which in turn, leads to significant spectral broadening. Furthermore, PAH cations are usually created in some form of a discharge which leads to even broader spectra, thanks to the high electron temperature in such sources.

To alleviate some of these concerns, the spectra of clusters of small PAHs with argon atoms have been recorded [69–74]. Cluster dissociation has been especially useful in obtaining the spectra of cold PAH cations with rare gases [71–74]. Here, neutral PAH clusters were threshold photoionized to yield the PAH^+-Rg species. In principle, both vibrational and electronic spectra of PAH cations can be obtained in this fashion, but the spectra acquired are shifted from that of bare chromophore, sometimes by 100 – 200 cm^{-1} – thus, precluding a direct comparison to the DIBs or the UIR features.

Similar studies of PAHs in argon and neon matrices conducted at cryogenic temperatures suffer from similar limitations. The PAH concentration can be varied as they are deposited into a matrix and as a result, very good signal-to-noise ratios can be obtained with a relatively simple apparatus. The main problems with PAH spectra in matrices are the spectral shift and the broadening due to interactions with matrix atoms, but such data sets form an excellent overview from which to select candidate molecules for more detailed study.

1.4 Protonated PAHs

1.4.1 Protonated PAHs in ISM

Neutral PAHs in the ISM may be ionized by UV radiation. The PAH cations created may react with highly abundant hydrogen to form protonated PAHs. In order to pursue quantitative chemical modeling, the reaction rates between hydrogen and PAH cations, dehydrogenated cations, and protonated PAHs were measured in flowing afterglow-selected ion flow tube experiments for benzene, naphthalene and pyrene [75]. No significant reactions were observed between PAH cations or protonated PAHs with H_2 molecules, but PAH cations reacted with atomic hydrogen at nearly the Langevin rate ($\sim 10^{-10}$ cm^3/s) to form protonated PAHs. Dehydrogenated PAH cations associated with H atoms at almost the same rate. On the other hand, the association of protonated PAHs with atomic hydrogen was found to be ≥ 100 times slower. This led authors to conclude that protonated PAHs would be a dominant form of PAHs in ISM regions with a high ionization rate and hydrogen atom abundance such as diffuse or translucent clouds.

Based on these experiments, the interstellar chemistry involving benzene/naphthalene cations and hydrogen atoms have been considered [76]. It was concluded that even at low densities, the radiative association with H is very efficient, and that the H_2 molecule loss dissociation channel for protonated species is not likely to be important in these reactions.

Another source of protonated PAHs in the denser regions of the ISM may be the proton transfer from known protonated species such as H_3^+, HCO^+, H_3O^+ [77–81], to neutral PAHs. Reaction rate studies of proton transfer to a range of organic compounds in a recent flowing afterglow-selected ion flow tube experiment [82] found that the proton transfer to alkanes, alkenes and alkynes was dissociative, non-dissociative or both, depending on whether the proton donor was H_3^+, H_3O^+ or N_2H^+, respectively. Aromatic hydrocarbons, on the other hand, underwent only non-dissociative proton transfer, forming protonated PAHs.

To extend such laboratory results on a few selected species to the more general population of potential DIB and UIR carriers in the ISM, a statistical theory has been developed to consider the hydrogenation and charge states of PAHs in diffuse interstellar clouds [83, 84]. The main result was that small PAHs, specifically those with less than 20 carbon atoms, would be destroyed by the interstellar UV radiation field; intermediate size PAHs with 20 – 30 carbon atoms would be highly dehydrogenated but stable; and large PAHs would be nearly fully hydrogenated, and even protonated. In terms of the overall charge balance, large PAHs were predicted to be essentially 100% ionized, with 60 – 80% of intermediate size PAHs estimated to be in their cationic or protonated forms.

Both of the experiments outlined above indicate that protonated PAHs should exist in the ISM, especially for large, multi-ring PAHs. Smaller PAHs should exist in a wide range of hydrogenation and charge states that depend sensitively on the H/H_2 ratio and the UV radiation flux. In particular, the photostability of each type of PAH will play an important role in the overall chemical speciation of the important suite of compounds.

1.4.2 Protonated PAHs and the DIBs

Protonated PAHs are closed-shell ions. Their electronic structure is closely related to that of neutral PAHs in that protonated PAHs retain a system of conjugated electrons which is responsible for the lowest energy $\pi - \pi^*$ electronic transitions. As described in Chapter 3, such transitions are expected to be red-shifted with respect to the same transition in the corresponding neutral PAH. The amount of this shift is not known, but from simple energetic considerations, it is expected to be on the order of a few tens of nanometers. Thus, even small PAHs with only 3 – 4 aromatic rings may absorb in the DIB wavelength range.

1.4.3 Other Applications of Protonated Aromatics

Aromatic electrophilic substitution reactions are an important class of reactions in organic chemistry. Such substitution reactions occur in two steps:

$$AH + E^+ \rightleftharpoons AHE^+ \rightarrow AE + H^+$$

where AH is a neutral aromatic molecule and E is an electrophilic reagent (Cl, Br, NO_3, SO_3H, etc.). Protonated aromatic molecules are believed to be intermediates in these aromatic electrophilic substitution reactions [85].

In living organisms, many molecules form hydrogen bonds. UV radiation may break some of these bonds and lead to the formation of protonated aromatic species. The study of protonated aromatics may help lead to a better understanding of the radiation damage processes that occur in biological cells.

1.4.4 Previous Studies of Protonated Aromatics

UV spectra of protonated aromatic compounds (carbonium ions) were studied in anhydrous solution with HF and BF_3 [86]. These spectra consisted of broad absorption bands and were located at visible wavelengths. To re-examine these results, solution spectra for the complexes of aromatic compounds with Al_2Br_6 and Al_2Cl_6 have been recorded [87]. When the $C_6H_6{\cdot}Al_2Br_6$ complex was stabilized with HBr, protonated benzene was created. The UV spectrum of this solution displayed a broad structureless band with a maximum near 330 – 340 nm and another broad absorption feature at wavelengths shorter than 275 nm. A systematic study of UV, IR and NMR spectra of protonated aromatic compounds performed in similar solutions [88] found UV absorption band maxima at 332 nm for protonated benzene, 390 nm for protonated naphthalene, 408 nm for protonated anthracene, 510 nm for protonated phenanthrene, and 476 nm for protonated pyrene.

More directly relevant to the results presented in this thesis are the gas phase photodissociation spectra of organic compounds obtained in an ion cyclotron resonance mass spectrometer [89, 90]. Among the experiments carried out was the UV photodissociation of protonated benzene. The recorded spectrum had two broad featureless absorption bands with maxima at 330 and 240 nm. These bands corresponded to the $S_1 \leftarrow S_0$ and $S_2 \leftarrow S_0$ electronic transitions of protonated benzene. The protonation led to relatively large red-shifts: ∼80 nm for the S_1 electronic state and ∼40 – 50 nm for the S_2 state; the widths of the bands measured were ∼25 – 35 nm FWHM. The spectrum was recorded with 10 nm resolution and most likely, the dissociation was multiphoton [91].

The structure of protonated benzene has been the subject of a number of theoretical studies [92–95]. Originally, σ- and π-complexes were considered as two possible structures. The proton binds to a carbon atom in the σ-complex forming a CH_2 site, while in the π-complex, the proton binds to the system of aromatic electrons. Later, the bridged structure in which the proton binds to the C–C bond was added for consideration. These studies have established that the σ-complex is a stable isomer of protonated benzene, the bridged structure is a first order transition state, and the π-complex is a second order transition state.

For larger systems, the structures and vibrational frequencies of protonated naphthalene, protonated pyrene, protonated coronene and protonated circumcoronene have been calculated using density functional theory [23]. All stable isomers were found to have σ-complex structures. Reactions of H atoms with PAH cations to form the protonated σ-complexes were found to be exothermic by 55 – 62 kcal/mol. The energies for both isomers and the barrier height for 1–2 isomerization of protonated naphthalene have been calculated as well. The main goal of this study was to investigate vibrational spectra of protonated PAHs and, possibly, compare them with the UIRs.

Symmetric and asymmetric C–H stretching vibrations of the CH_2 site of protonated PAHs are characteristic of the σ-complex structure. The spectrum of these vibrations has been measured in gas phase IR dissociation experiments with clusters of protonated benzene with Ar, N_2, CH_4 and H_2O [3,96], an experiment that provided solid experimental proof that the σ-complex is the stable, lowest energy isomer of protonated benzene. The cluster experiment was promptly followed by the IR multiphoton dissociation spectroscopy of protonated benzene using free electron laser in the 6.2 – 9.3 μm wavelength region [97].

1.5 Research Goals

The goal of this thesis is to study the gas phase properties of protonated PAHs and their interaction with visible and UV radiation. The purpose is to assess whether small protonated PAHs are an important component of ‘molecular grains’ in the ISM, and to investigate the relationship between protonated PAHs and the DIBs. Another outcome of the study would be a better understanding of intrinsic properties of protonated PAHs. There are two main questions addressed by the research presented here:

1. Do protonated PAHs exist in the interstellar medium?
2. Are protonated PAHs the carriers of the diffuse interstellar bands?

To date, only the low resolution spectrum of protonated benzene has been recorded in the gas phase. Electronic spectra of protonated polycyclic aromatic molecules with a few aromatic rings need to be recorded, and data obtained should be compared with the observed DIBs. Photodissociation has been chosen as the method to record the spectra of protonated PAHs in this thesis, whose structure is described below.

Density functional theory calculations are performed in Chapter 2 in order to analyze the possible dissociation channels of protonated PAHs. In addition, the fate of protonated PAHs upon their recombination with electrons is investigated. Chapter 3 concentrates on the electronic structure of protonated PAHs and on predictions for the $S_1 \leftarrow S_0$ electronic transition wavelengths. A full compendium of the results from Chapters 2 and 3 is presented in Appendix A. The photostability of protonated PAHs is investigated in Chapter 5 via their photodissociation by visible and UV nanosecond lasers. The visible photodissociation spectrum of clusters of protonated anthracene with water is discussed in Chapter 6. The results are summarized in Chapter 7. Chapter 4 contains a detailed description of the experimental setup and some of its most important components. Draft drawings of the discharge parts and critical electric circuit diagrams are located in Appendix B. Appendix C contains the documentation for the data acquisition software developed in this thesis.

Chapter 2

Ground State Calculations for Protonated PAHs

2.1 Introduction

Ab initio ground electronic state calculations can be used to determine geometries and energies of all possible protonated PAH isomers and thereby examine whether there are common properties and general trends among this class of compounds. In addition, the stability and allowed dissociation channels need to be investigated to guide the interpretation of the spectroscopic data presented later in this thesis, while the geometries serve as the starting point for calculation of the energies of excited electronic states.

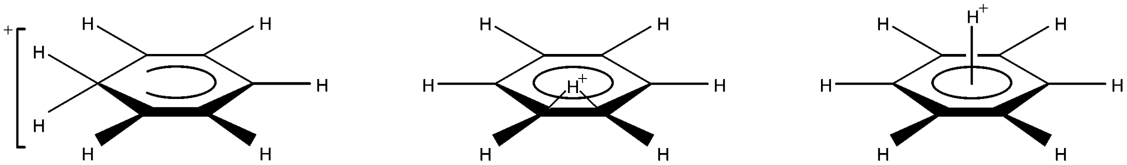

1 **2** **3**

Figure 2.1: Structures for protonated benzene PES stationary points. Adapted from [3].

There have been a number of quantum chemical calculations performed on the structures of protonated benzene [92–95]. Three stationary points on its potential energy surface were identified (Figure 2.1). They are the σ complex structure (1), the H^+ bridged structure (2), and a π complex of benzene and H^+ (3). Structure (1) is the global minimum (the most stable form) and the other two are first and second order transition states, respectively. Their relative energies were calculated to be 0, 6.4 and 49.3 kcal/mol [3].

Fairly low level results on the structures of stable isomers for selected protonated PAHs (naphthalene, pyrene, coronene, circumcoronene) and their vibrational spectra have also been calculated [23]. An extensive suite of quantum chemical calculations for benzene, naphthalene, anthracene, phenanthrene and pyrene is presented in this chapter. Although benzene is technically not a PAH molecule, it was considered here as a well-studied aromatic test system. Before turning to the results themselves, the nomenclature of protonated PAHs and the computational approach will be covered first.

2.2 Methodology

2.2.1 Naming Conventions

The naming of different isomers of protonated PAHs is based on the IUPAC nomenclature of neutral PAHs. Figure 2.2 outlines the conventional numbering of carbon atoms in neutral PAHs. The numbers in **bold** depict the stable isomers of protonated PAHs. Fusion carbon atoms at the juncture of two aromatic rings are usually not numbered, but they are referenced in certain calculations, especially for protonated naphthalene and anthracene. These atoms are therefore labeled with numbers in *italics*.

For protonated PAHs, the naming system is illustrated by the following example: when H^+ is attached to C atom number 1 of naphthalene or C atom number 9 of anthracene, for example, the 1–hydronaphthalene and 9–hydroanthracene cations are formed, respectively.

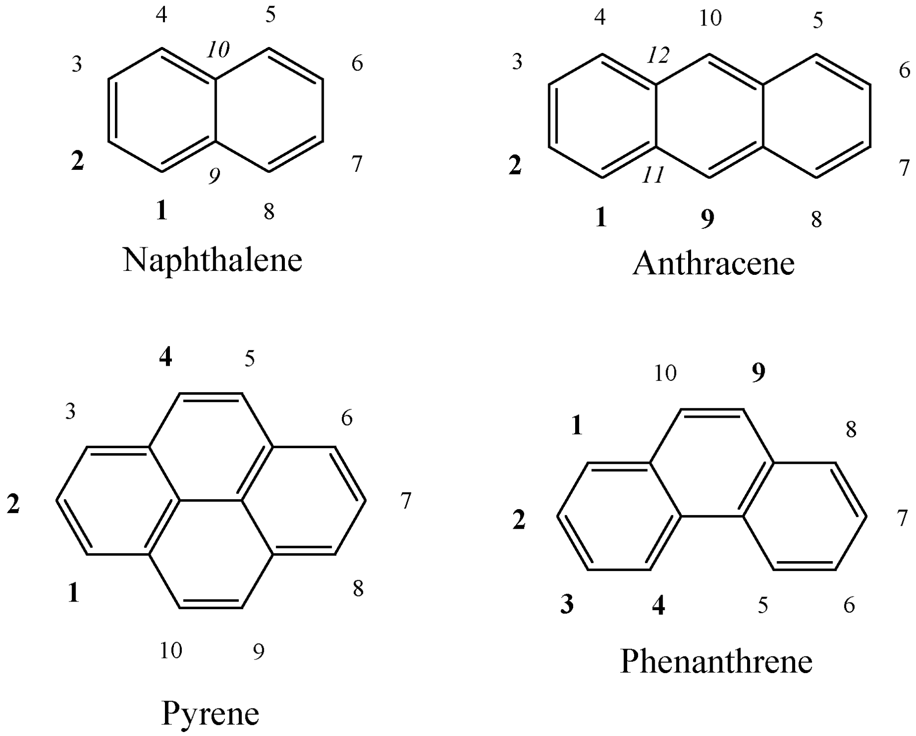

Figure 2.2: Carbon atom numbering conventions for neutral PAHs.

For simplicity, in this thesis the notation isomer 1 of protonated naphthalene and isomer 9 of protonated anthracene, or 1–$C_{10}H_9^+$ and 9–$C_{14}H_{11}^+$ will be used. The notation 1–2 $C_{10}H_9^+$ thus designates a transition state between 1–$C_{10}H_9^+$ and 2–$C_{10}H_9^+$, while 6→1 $C_{10}H_8^+$ describes 1–$C_{10}H_9^+$ with a hydrogen atom removed from carbon number 6 of naphthalene. This is an isomer of naphthalene cation, where a hydrogen atom has been moved from carbon atom 6 to carbon atom 1. Similarly, 1–$C_{10}H_7^+$ designates the naphthalene cation with a hydrogen atom removed from the carbon 1 position.

2.2.2 Software

Contemporary desktop personal computer (PC) systems are now sufficiently powerful to perform *ab initio* calculations on moderately complex systems in reasonable times. Although they are not as powerful as mainframe systems, they are very attractive from the price and availability perspective. GAUSSIAN 98, Revision A.9 [98] (the most widely used version) for Microsoft Windows was used to carry out all calculations mentioned below.

2.2.3 Choice of the Computer System

Most central processing units (CPUs) on the PC market are manufactured by Intel and Advanced Microdevices (AMD). Software performance depends strongly on the computer hardware, the most important of which is the CPU (specifically its architecture and clock speed). A few tests were therefore performed to determine the best performing PC for GAUSSIAN calculations and consisted of two different calculations (italics below correspond to commands within GAUSSIAN 98):

The first test was to optimize the geometry of isomer 1 of protonated anthracene:

 # Opt=(CalcAll,Tight,GDIIS) rB3LYP/6–311++G(d,p) Guess=Mix

This calculation is performed mostly in memory and takes about 24 hours.

The second calculation was to optimize the geometry of protonated benzene:

 # Opt rMP2/6–311+G(d,p) Guess=Mix

This calculation takes only about 1.5 hours, but carries out substantial read/write operations with the hard drive.

The following PC systems, differing mostly by CPU type, were tested:

P4–3.6 – CPU Intel Pentium 4, 3.4 GHz running at 3.67 GHz (8% overclock), RAM 1 Gb Dual DDR 433 (2×433 MHz), Hard drive ATA–5 (133Mb/s), Windows XP SP1.

P4–2.7 – CPU Intel Pentium 4, 2.66 GHz running at 2.72 GHz (2.26% overclock), RAM 1 Gb RDRAM (1066 MHz), Hard drive ATA–5 (133 Mb/s), Windows XP SP1.

A–XP – CPU AMD Athlon XP, 2800+ running at 2.11 GHz (0% overclock), RAM 1 Gb

Dual DDR 333 (2×333 MHz), Hard drive SATA (150 Mb/s), Windows 2000 SP4.

A–64 – CPU AMD Athlon 64, 3000+ running at 2.10 GHz (5% overclock), RAM 1 Gb DDR 433 (433 MHz), Hard drive ATA–5 (133 Mb/s), Windows XP SP1.

Results for each system are presented in Table 2.1 from which it is clear that at present, PCs with Intel Pentium 4 CPUs run GAUSSIAN 98 calculations faster than AMD Athlon CPUs, rated for approximately the same equivalent clock speed. Almost all calculations described in this thesis were performed on the P4–2.7 and P4–3.6 systems.

Table 2.1: PC performance tests with GAUSSIAN 98.

PC System	P4–3.6	P4–2.7	A–XP	A–64
CPU Clock, MHz	3638	2720	2112	2100
Equivalent CPU Clock Rating, MHz	3638	2720	2800	3150
In-memory job, s	63900	86286	106568	–
High disk swap job, s	4536	5484	7102	5665

2.2.4 Theory Level and Basis Set

Density functional theory (DFT) [99, 100] has proven to be a good alternative to Linear Combination of Atomic Orbitals-Molecular Orbital (LCAO-MO) *ab initio* methods, especially for aromatic hydrocarbons. The advantages of DFT calculations are in their speed and smaller computer resource requirements. One such method denoted B3LYP (Becke three-parameter functional [101] with Lee-Yang-Parr correlation functional [102]) was used in previous calculations of protonated PAH structures [23] and has been selected here to optimize the geometries and calculate vibrational frequencies of several systems.

The basis set was constrained to be the same for all molecules studied, with a calculation limit of no more than 1 week chosen to define the basis set size. For the largest molecule studied – protonated pyrene – the biggest basis set is 6–311++G** (McLean-Chandler 6–311G basis set [103, 104] with polarization functions (d,p) [105] and diffuse functions

++ [106]).

In addition to being faster, DFT performs most integral calculations in memory and requires little swap space on the computer hard drive. For comparison, the Møller-Plesset MP2 6–311++G(d,p) method on protonated benzene uses about 10 Gb of the swap space. For protonated naphthalene at the same theory level and basis set, the required amount of the swap space would exceed 16 Gb which is the maximum allowed by 32-bit versions of GAUSSIAN 98.

Geometry optimization was performed in a few steps, where the basis set size was slowly increased to speed convergence. At the largest basis set, the vibrational frequencies were calculated as a part of the optimization process. The total calculational procedure was as follows:

1. A model of the molecule was built in the GAUSSIAN 98 visualization package GaussView, version 2.1 [107].
2. The geometry was optimized with the 6–31G basis set.
3. The geometry was optimized with the 6–31+G(d) basis set.
4. The geometry was optimized with the 6–311G(d,p) basis set.
5. The geometry was optimized with the 6–311++G(d,p) basis set.

In step 5, the specific calculation call was:

```
# Opt=(CalcAll,Tight,GDIIS) B3LYP/6–311++G(d,p) NoSymm Guess=Mix
```

Options *CalcAll*, *Tight* and *GDIIS* were used to assure better convergence, while *CalcAll* was used to predict the frequencies and intensities of IR-active vibrational modes. The *NoSymm* switch proved important in stabilizing the convergence criteria for molecules with rotational symmetry, especially neutral PAHs and their cations.

2.3 Geometries

2.3.1 Protonated Benzene, Naphthalene, Anthracene and Pyrene

Appendix A (Tables A.2 – A.20) contains GAUSSIAN Z-matrices for the optimized geometries of neutral benzene, naphthalene, anthracene and pyrene, as well as stable isomers of their protonated forms. The calculated dipole moments, A, B and C rotational constants, and derived molecular symmetry groups are also listed there (Table A.1).

Protonated benzene $C_6H_7^+$ has only one isomer, while the transition state for isomerization (1–2 $C_6H_7^+$) is that of the bridged structure (2) from Figure 2.1. Molecular models of these structures are shown in Figure 2.3.

Protonated naphthalene has two principal isomers: 1– and 2–$C_{10}H_9^+$ (Figure 2.4). An additional isomer 9–$C_{10}H_9^+$ is much higher in energy and has a very low barrier for isomerization into 1–$C_{10}H_9^+$. Thanks to the increasing number of isomers, there are now several isomerization transition states: 1–2, 2–3 (not shown), 1–9 and 9–10.

Protonated anthracene has three main principal isomers: 1–, 2– and 9–$C_{14}H_{11}^+$. Again, the 11–$C_{14}H_{11}^+$ isomer is much higher in energy and has a very low barrier for isomerization into 9–$C_{14}H_{11}^+$. Figure 2.5 presents a number of molecular models of these isomers and the 1–2, 2–3 (not shown), 1–11 (not shown), 9–11 and 11-12(not shown) transition states accessed by proton tunneling or hopping.

Protonated phenanthrene has five stable isomers: 1–, 2–, 3–, 4– and 9–$C_{14}H_{11}^+$ (Figure 2.6). Thanks to the much more complex potential energy surface, higher energy isomers and transition states are not considered here.

Protonated pyrene has three main isomers: 1–, 2– and 4–$C_{16}H_{11}^+$ (Figure 2.7). Less stable isomers and transition states are not considered here.

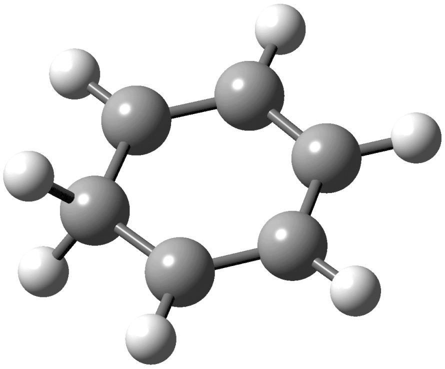

$C_6H_7^+$

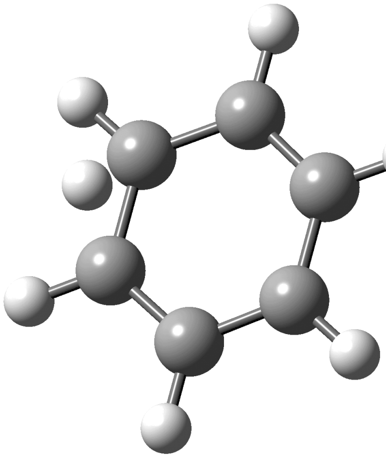

1-2 $C_6H_7^+$

Figure 2.3: Structures of protonated benzene $C_6H_7^+$ and its isomerization transition state 1–2 $C_6H_7^+$.

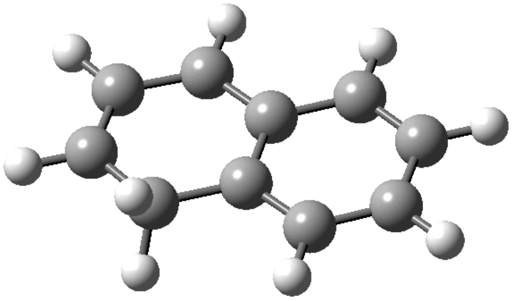

$1-C_{10}H_9^+$

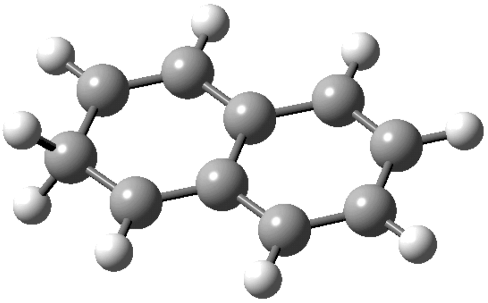

$2-C_{10}H_9^+$

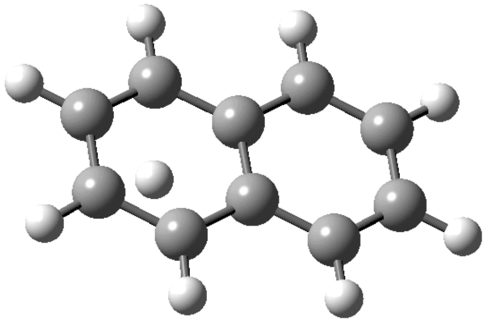

1-2 $C_{10}H_9^+$

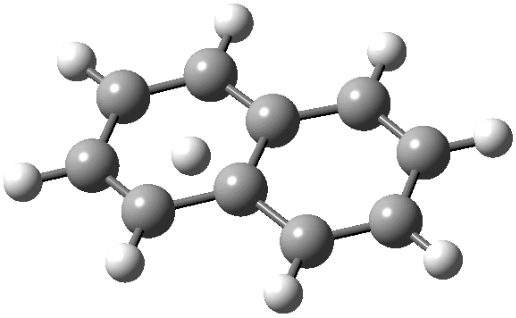

1-9 $C_{10}H_9^+$

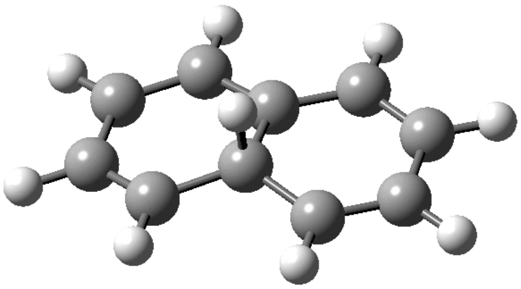

$9-C_{10}H_9^+$

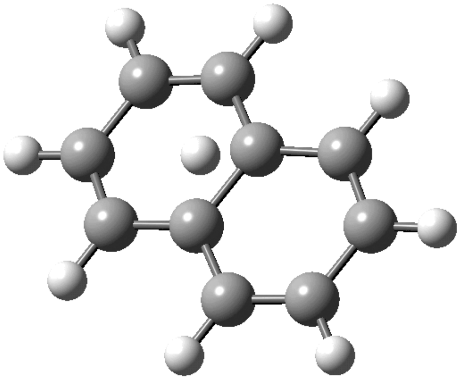

9-10 $C_{10}H_9^+$

Figure 2.4: Structures of the protonated naphthalene $C_{10}H_9^+$ isomers 1,2 and 9, along with three of the isomerization transition states that connect them.

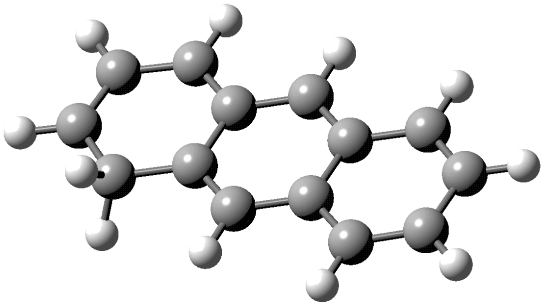

$1\text{-}C_{14}H_{11}^{+}$

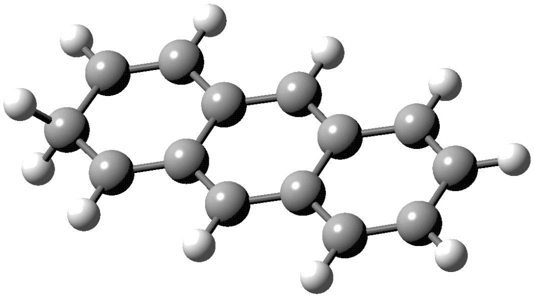

$2\text{-}C_{14}H_{11}^{+}$

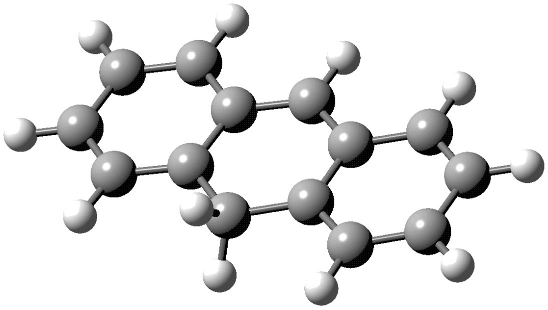

$9\text{-}C_{14}H_{11}^{+}$

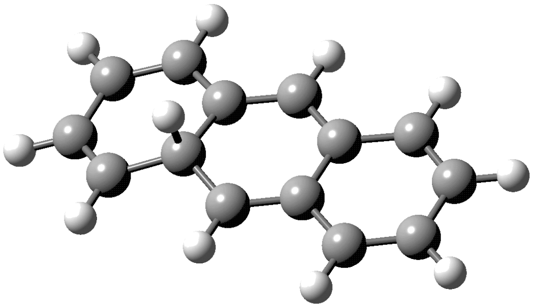

$11\text{-}C_{14}H_{11}^{+}$

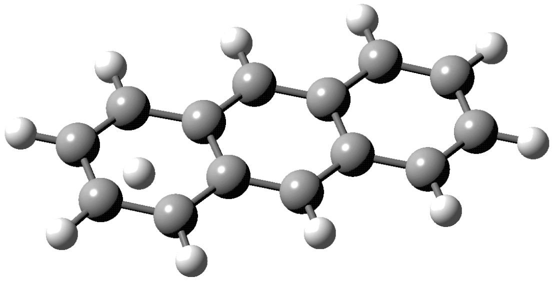

$1\text{-}2\ C_{14}H_{11}^{+}$

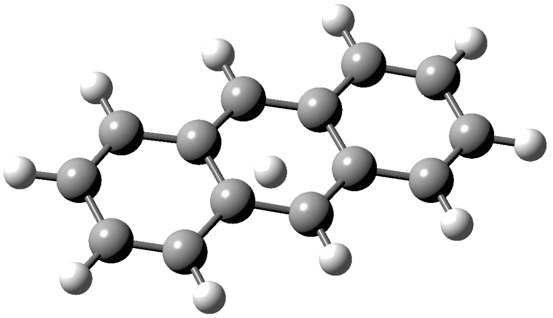

$9\text{-}11\ C_{14}H_{11}^{+}$

Figure 2.5: Structures of the protonated anthracene $C_{14}H_{11}^{+}$ isomers 1, 2, 9 and 11, along with two of the lowest barrier isomerization transition states.

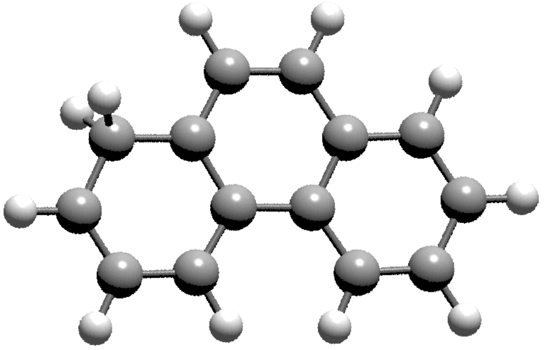

$1-C_{14}H_{11}^{+}$

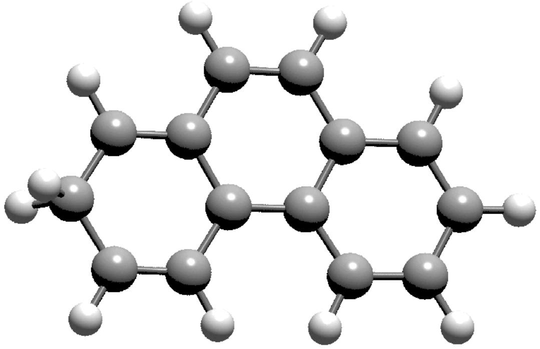

$2-C_{14}H_{11}^{+}$

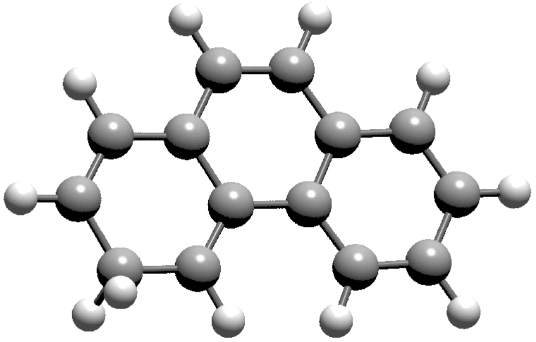

$3-C_{14}H_{11}^{+}$

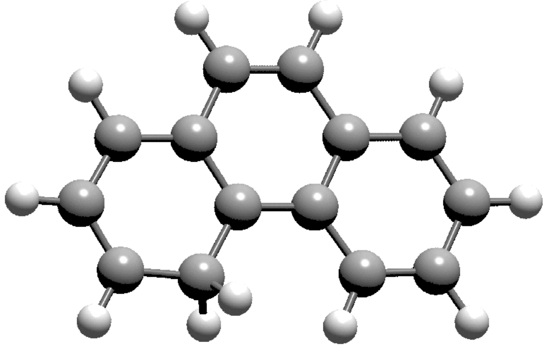

$4-C_{14}H_{11}^{+}$

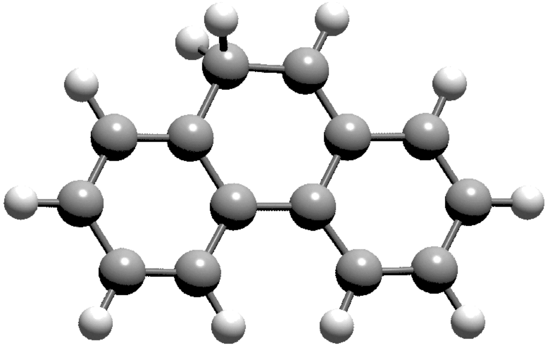

$9-C_{14}H_{11}^{+}$

Figure 2.6: Structures of the protonated phenanthrene $C_{14}H_{11}^{+}$ isomers 1, 2, 3, 4 and 9.

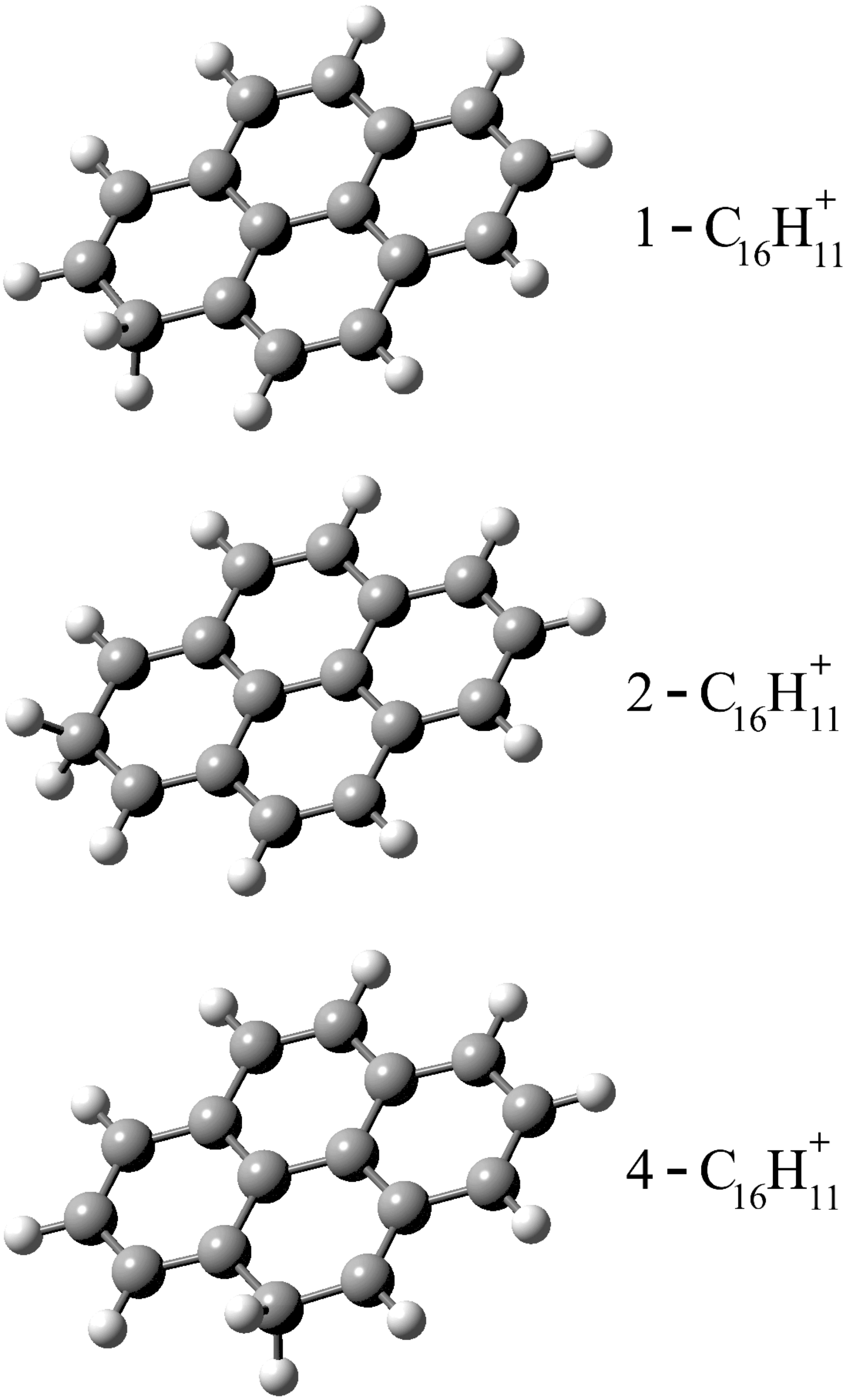

Figure 2.7: Structures of the protonated pyrene $C_{16}H_{11}^{+}$ isomers 1, 2 and 4.

2.3.2 Typical Geometry Changes Upon Protonation

Small but noticeable geometrical changes occur upon the protonation of aromatic hydrocarbons. In stable isomers, the proton binds to the carbon atom, forming a σ complex and changing the hybridization from sp^2 to sp^3. C–C bonds for the sp^3 carbon elongate due to electron density redistribution by 0.07 – 0.12 Å, while C–C bonds for an adjacent sp^2 carbon atom shorten by 0.02 – 0.06 Å (Figure 2.8 – 1). For CH_2 sites, the lengths of the C–H bonds are predicted to be 1.10 Å– somewhat longer than the 1.085 Å predicted for the CH sites. The H–C–H angle values for CH_2 sites are in the range 100 – 104 degrees.

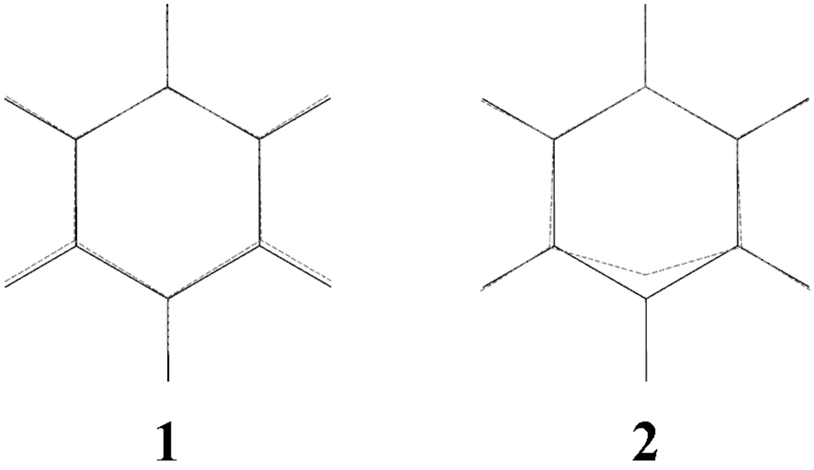

Figure 2.8: Benzene geometry changes (dashed line). 1 – during protonation, 2 – during cation dehydrogenation.

The carbon backbone of the protonated molecule is predicted to remain planar. A few ‘flatness’ tests were performed with protonated naphthalene and anthracene, where the initial geometries of ions were set to resemble cyclohexane. Geometry optimization was then performed with the MP2 and B3LYP methods using different size basis sets. The convergence to a true minimum, not a saddle point on the potential energy surface, was verified by making sure that all vibrational eigenfrequencies were real. In each of these tests, all carbon atoms settled into a plane. Thus, the protonated PAHs are predicted to have either C_s or C_{2v} symmetry, depending on the isomer (Appendix A, Table A.1).

The less stable isomers, where the proton binds to a ring fusion carbon, are no longer planar thanks to changes in the hybridization at the protonation site. In the transition states, the carbon backbone bends out-of-plane by a small amount. For transition states that do not involve fusion carbons, the change in the dihedral angle is only 1 degree. For transition states with fusion carbon, the bending distortion is closer to 5 degrees.

2.3.3 Geometries of Dehydrogenated PAH Cations

As described below, the properties of various forms of dehydrogenated PAHs may be important in catalytic cycles that can form molecular hydrogen in the diffuse interstellar medium. Here, only the geometries of benzene, naphthalene and anthracene dehydrogenated cations were calculated as a first step in the consideration of such cycles. Theoretically, the dehydrogenated carbon atom is being pulled closer to the middle of the ring. This leads to an increase of the C–C–C angle at the dehydrogenation site from 120° to 143 – 149°, and a decrease in the adjacent C–C–C angles to 102 – 108° (Figure 2.8 – 2). $C_6H_5^+$ and 1–$C_{10}H_7^+$ remained flat, while the other dehydrogenated cations considered were found to distort from the planar symmetries of the protonated PAHs.

2.3.4 Geometries of Hydrogenated and Dehydrogenated PAHs

Due to their low ionization energies, atomic carbon and many carbonaceous species are expected to be ionized in diffuse interstellar clouds. The amount of free electrons in these objects is then approximately the same as the amount of carbon, and electron recombination may be one of the major ways of removal for protonated PAHs. Geometries for singly hydrogenated and dehydrogenated benzene, naphthalene, and anthracene are calculated as a part of the recombination process investigation.

From all of the considered hydrogenated PAHs which essentially are neutralized protonated PAHs, the carbon backbone was not planar only in 9–$C_{14}H_{11}$. C–C bonds of the hydrogenation site were longer by ∼0.01 Å and the H–C–H angle was ∼1° larger than in protonated PAHs. The rest of the geometry was similar to protonated PAHs.

All considered dehydrogenated PAHs had planar geometries. Dehydrogenation would typically result in the radical site carbon atom retraction into the ring, which led to C–C bond shortening by ∼0.02 – 0.03 Å.

2.4 Calculated Values

2.4.1 Vibrational Frequencies

As was mentioned above, the vibrational frequencies and IR intensities of the protonated PAH isomers were calculated here as a part of the geometry optimization. The effect of the level of theory and basis set size on the calculated vibrational frequencies of organic molecules has been studied previously [108–110]. Typically, the calculated vibrational frequencies are larger than the experimental values due to the harmonic nature of the *ab initio* estimate. Thus, the predicted vibrational frequencies must be scaled down by modest amounts to agree with the experiment. The actual scaling factor depends on the level of theory employed, the basis set, and the type of vibration.

To derive the scaling factors for the B3LYP 6–311++G(d,p) calculations presented here, the vibrational frequencies were calculated for neutral benzene and anthracene and compared to the experimental gas phase frequencies [111, 112]. A detailed comparison of the results are presented in Appendix A (Tables A.21, A.22), which shows that the scaling factors are ∼0.962 for C–H stretching vibrations (frequencies above 2000 cm^{-1}) and ∼0.982 for the rest. These scaling factors were then used to determine vibrational frequencies of protonated PAHs, neutral PAHs and their cations and to thereby calculate the zero point vibrational energy (ZPE) content of all molecules and ions. The ZPE values were then used to correct the relative energies of isomers and reaction channels (2.5). The full list of the scaled vibrational frequencies for neutral and protonated PAHs is listed in Appendix A (Tables A.23 – A.27) along with the IR vibrational spectra in stick form (Figures A.1 – A.19). In the latter figures, the height of the vertical lines in each spectrum depicts the IR intensities. As a comparison, similar spectra for protonated naphthalene and pyrene convoluted with 20 cm^{-1} linewidth to simulate interstellar spectra were reported in [23].

2.4.2 Proton Affinities

As a part of the ground state energy calculations, the proton affinities for the neutral PAHs were estimated. The resulting values were a good measure of the precision of the calculations. Here, the proton affinities were calculated as an energy difference between the neutral PAH (equivalently, a geometry for PAH–H^+ where the proton is far from the molecule) and the isomers of the protonated PAHs (where the proton is bound to the molecule). These values were then compared with the available experimental values [113, 114]. It should be noted that for molecules with more than one protonation site, it is theoretically possible to calculate the properties for individual isomers, while the experimental data necessarily average over the isomers present in the laboratory. For anthracene and pyrene, the predicted variation in proton affinity is large, with the experimental value nicely bracketed by theory. As one can see from Table 2.2, the match is ∼2 – 3 kcal/mol, or approximately a

1.5% difference. Hence, the relative values of the energy levels may be trusted to roughly this level.

Table 2.2: Experimental and calculated proton affinities of neutral aromatics.

Molecule	Experimental (kcal/mol)	Calculated (kcal/mol)	H^+ site
Benzene	179.3	182.19	1
Naphthalene	191.9	196.20	1
		193.30	2
Anthracene	209.7	203.84	1
		200.80	2
		212.50	9
Phenanthrene	197.3	199.80	1
		197.80	2
		199.25	3
		198.73	4
		199.60	9
Pyrene	207.7	211.24	1
		197.02	2
		200.98	4

2.4.3 Ionization Energies

Ionization energies are calculated as the energy difference between the cation and neutral molecule, and were corrected by the ZPE values. The results are compared with the experimental ionization energies [113] for benzene [65,66], naphthalene [68,70], anthracene [69], phenanthrene and pyrene [115] in Table 2.3. The calculated values are consistently lower than experiment by ~0.3 eV (6.9 kcal/mol), but the differences predicted here are not as

Table 2.3: Experimental and calculated ionization energies of neutral aromatics.

Molecule	Experimental (eV)	Calculated (eV)
Benzene	9.24378	9.0562
Naphthalene	8.1442	7.8655
Anthracene	7.4233	7.1002
Phenanthrene	7.891	7.5845
Pyrene	7.426	7.1427

large as for those calculated previously with the B3LYP 4–31G method [116].

Ionization energies were also calculated for hydrogenated and dehydrogenated benzene, naphthalene, and anthracene (Appendix A, Table A.36). The typical values for hydrogenated PAHs were in the range of 6.2 – 6.4 eV, which is lower than for neutral PAHs. For deprotonated PAHs, the values were higher (in the 7.7 – 8.0 eV range). If any of these species are present in diffuse interstellar clouds, they should be promptly ionized, yielding protonated PAHs and dehydrogenated PAH cations respectively.

For isomer 2 of protonated naphthalene, the ionization energy needed to yield a doubly charged ion was calculated in order get an idea of the likely range of values for protonated PAHs. The calculated value is 12.9147 eV, 297.81 kcal/mol. Photons below the ionization threshold of 13.6 eV for hydrogen atoms are widely present in the diffuse interstellar medium. This calculation suggests that doubly charged PAH species will need to be considered in models of the charge states of PAHs in the galaxy.

2.5 Energy Landscapes

The energy landscape diagrams for protonated PAHs were investigated thoroughly in order to compare the energetics of different isomers and possible dissociation channels. These calculations serve two main goals. First, it is essential to find the difference in the stability of different isomers in their ground state for the same protonated PAH molecule, including the heights of the isomerization barriers. This information, together with the excited states calculations presented in Chapter 3, are essential to the interpretation of the experimental data on the photophysical and electronic state properties of protonated PAHs (Chapters 5 and 6). Second, since photodissociation was chosen as a method for recording the spectra of protonated PAHs, it is important to know which dissociation channels are feasible, their energetics, and their Franck-Condon overlap with the ground state(s).

In all energy landscape diagrams below, the energy of the lowest dissociation channel was set as the energy zero. Hence, in this energy scale, the stable isomers have negative energies.

2.5.1 Protonated Benzene

Isomerization and dissociation calculations on protonated benzene have been performed numerous times [92–95]. At the level of theory employed here, the only isomer of protonated

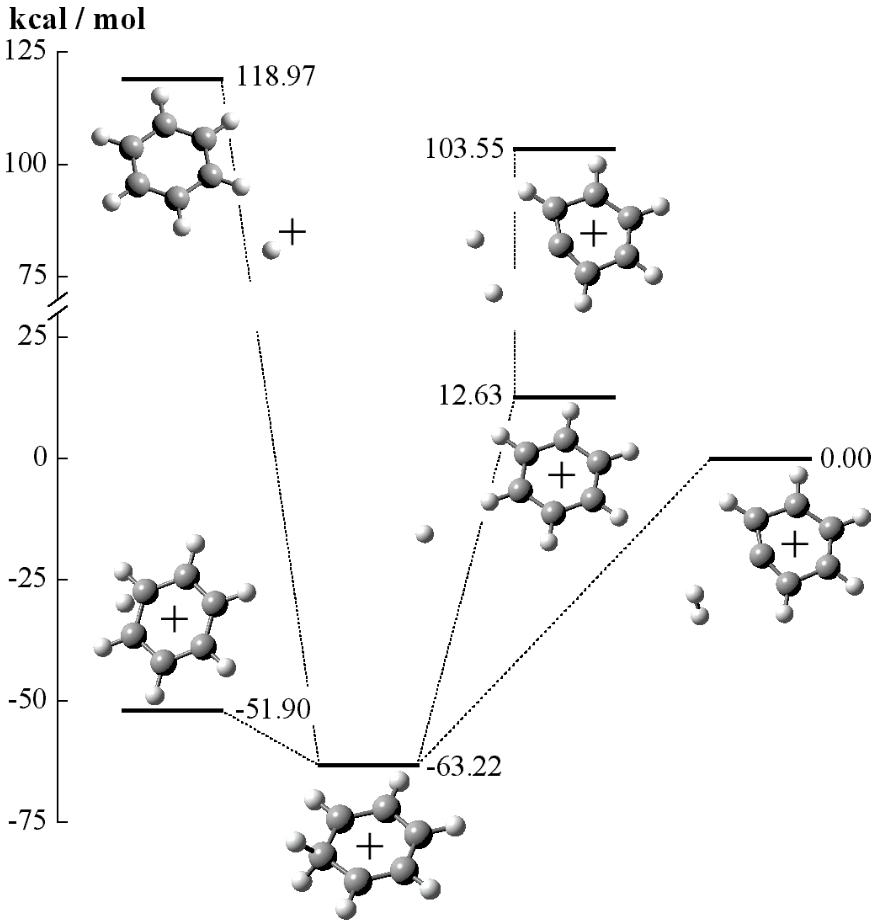

Figure 2.9: The energy landscape for protonated benzene.

benzene is stable with respect to dissociation by 63.22 kcal/mol (Figure 2.9, Table A.28 in Appendix A). The only possible 1–2 isomerization results in the identical isomer and has a barrier height of 11.32 kcal/mol.

The lowest dissociation channels are predicted to occur through the loss of an H_2 molecule (0.00 kcal/mol) or a hydrogen atom (12.63 kcal/mol) from the protonation site. The loss of H_2 most likely has a barrier, but the barrier height was not calculated here due to the difficulty of locating the transition state geometry. The H atom loss channel does not appear to have a barrier. A sequential loss of two hydrogen atoms is much higher in energy than the loss of H_2 molecule. Finally, the loss of an H atom from CH sites and the cleavage of C–C bonds are not considered here as they lie much higher in energy. In addition, the loss of the proton from the CH_2 site lies 118.97 kcal/mol above the lowest dissociation channel – a very large number! Thus, the protonation of neutral benzene in the gas phase cannot occur by simply attaching a proton to it. Thus, the more favorable protonation mechanism in the interstellar medium occurs via proton transfer from H_3^+ in dense clouds or through the radiative association reaction of PAH radical cations with atomic hydrogen in the diffuse clouds. A sequential loss of two H atoms, with the first H atom arising from the CH_2 site, followed by C–H bond cleavage, is 103.55 kcal/mol above the lowest dissociation channel. Such a dissociation pathway would only be possible for very highly vibrationally excited species.

2.5.2 Protonated Naphthalene

The energetics of the reaction between the naphthalene cation ($C_{10}H_8^+$) and an H atom, and the energies for isomers 1 and 2 of protonated naphthalene and the isomerization barrier between them, have been calculated previously at the B3LYP 4–31G level [23, 117]. The

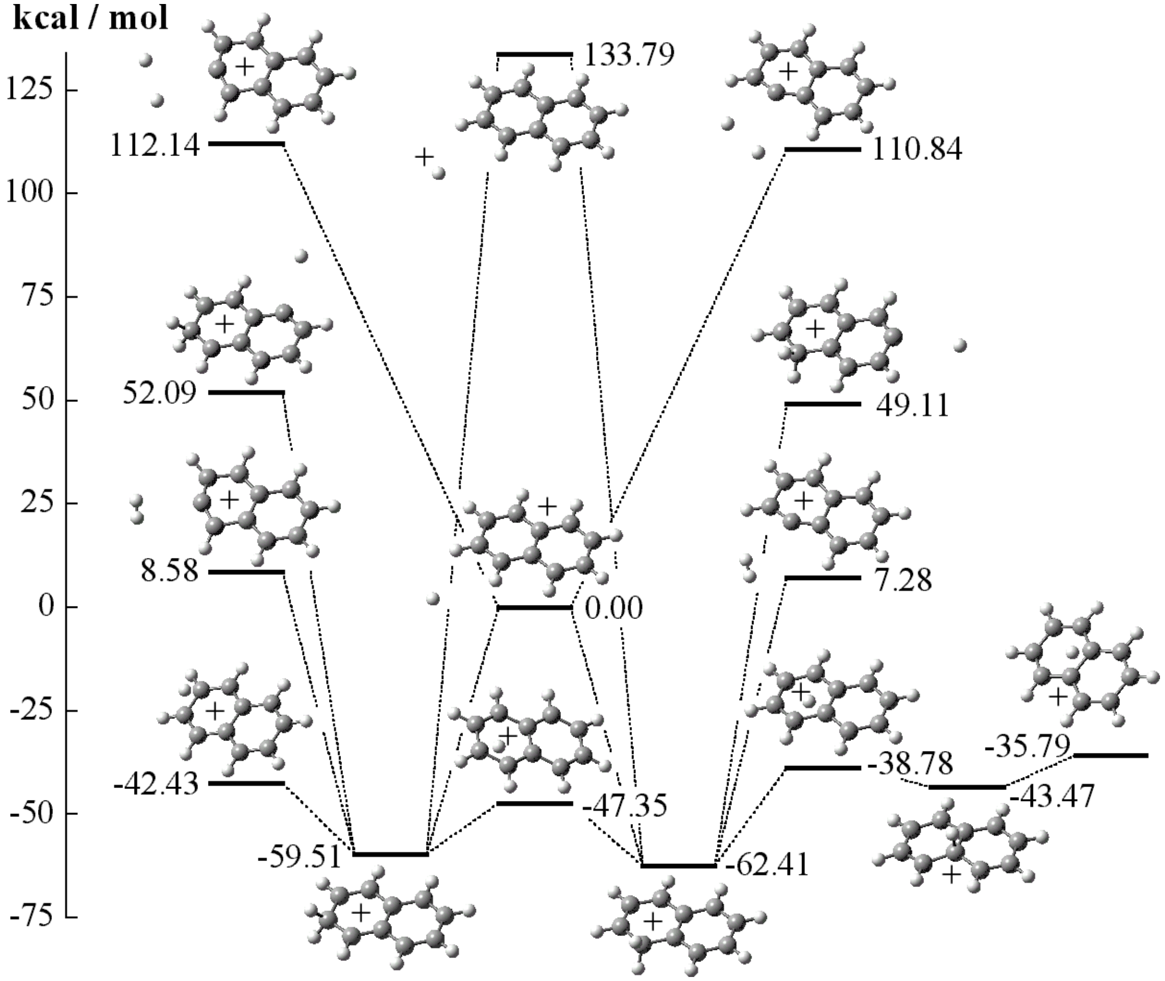

Figure 2.10: The energy landscape of protonated naphthalene.

two isomers of protonated naphthalene are stable with respect to dissociation by 62.41 kcal/mol (1–$C_{10}H_9^+$) and 59.51 kcal/mol (2–$C_{10}H_9^+$), respectively (Figure 2.10, Table A.29 in Appendix A). Isomer 2 can undergo 2–3 isomerization into an identical isomer (through a barrier of 17.08 kcal/mol) and 2–1 isomerization into the more stable 1–$C_{10}H_9^+$ isomer (barrier height 12.06 kcal/mol). Given sufficient energy, proton hopping can convert isomer 1 into isomer 2 (barrier height 15.06 kcal/mol) and isomer 9 (barrier height 23.63 kcal/mol) in which the proton is bound to a ring fusion carbon. Energetically, isomer 9 is less stable than isomer 1 by 18.94 kcal/mol and has a low barrier for 9–1 or 9–8 isomerization (barrier height 4.69 kcal/mol). It can also undergo 9–10 isomerization across the ring fusion into an identical isomer (barrier height 7.68 kcal/mol). Thus, it is unlikely that isomer 9 would be important under interstellar conditions.

The lowest dissociation channel for protonated naphthalene is the loss of an H atom from the protonation site (0.00 kcal/mol). The next – not so distant in energy – occurs via the loss of H_2 from the protonation site (7.28 kcal/mol for isomer 1 and 8.58 kcal/mol for isomer 2). The energies for the loss of H atom from C–H sites (not the protonation sites) were calculated as well. As for protonated benzene, they are substantially higher in energy: 49.11 ± 1.36 kcal/mol for isomer 1 (for a full listing see Table A.29 in Appendix A) and 52.09 ± 1.39 kcal/mol for isomer 2 (c.f. the bottom part of Table A.29 in Appendix A). The CH site dissociation channels of protonated naphthalene are therefore unlikely to be important in the interstellar medium. The loss of a proton from the CH_2 site is 133.79 kcal/mol above the lowest dissociation channel. Finally, the sequential loss of two H atoms, first from the CH_2 site and then another H atom, has energies of 110.84 kcal/mol (for isomer 1) and 112.14 kcal/mol (for isomer 2) above the lowest dissociation channel.

2.5.3 Protonated Anthracene

Protonated anthracene has three isomers that are stable with respect to dissociation by 52.41 kcal/mol (1–$C_{14}H_{11}^+$), 49.36 kcal/mol (2–$C_{14}H_{11}^+$) and 61.06 kcal/mol (9–$C_{14}H_{11}^+$) (Figure 2.11, Table A.30 in Appendix A), respectively. Isomer 2 can undergo 2–3 isomerization into an identical isomer (barrier height 21.20 kcal/mol) and 2–1 isomerization (barrier height 14.49 kcal/mol). The reverse 2–1 isomerization has a barrier height of 17.54 kcal/mol, while the 1-11 isomerization must surmount a barrier height of 27.84 kcal/mol in order to place the proton at a ring fusion carbon. Energetically, isomer 11 is less stable

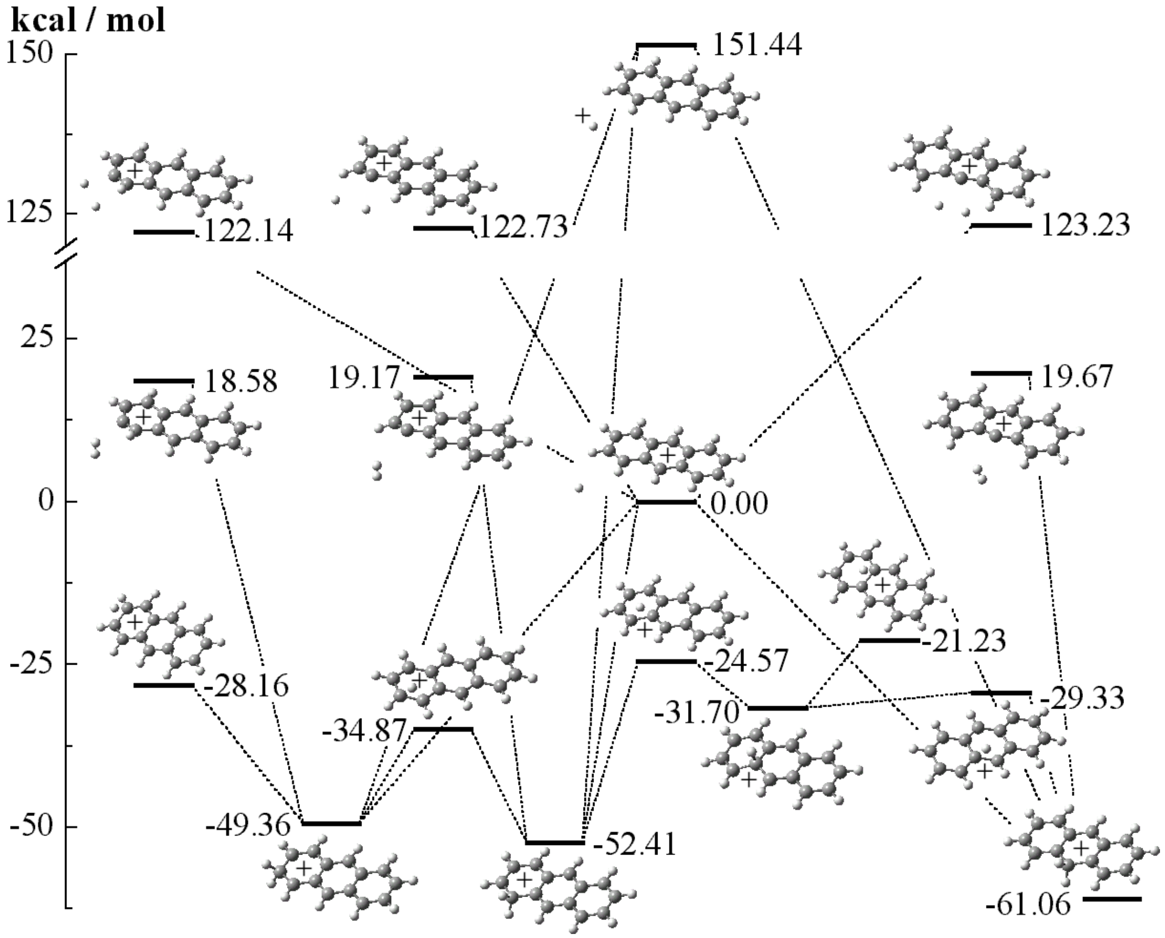

Figure 2.11: Protonated anthracene energy landscape.

than isomer 1 by 20.70 kcal/mol and has a very low barrier for 11–9 isomerization into the most stable isomer 9 (barrier height 2.37 kcal/mol). As with protonated naphthalene, it is therefore unlikely that the ring fusion isomer would be an important DIB carrier. Isomer 11 can also undergo 11–12 isomerization across the ring fusion into an identical isomer (barrier height 10.47 kcal/mol). Isomer 9 can undergo only 9–11 isomerization (barrier height 31.73 kcal/mol).

The lowest dissociation channel for protonated anthracene is the loss of an H atom from the protonation site (0.00 kcal/mol). The loss of an H_2 molecule from the protonation site is nearly isoenergetic for all three isomers (19.17 kcal/mol for isomer 1, 18.58 kcal/mol for isomer 2 and 19.67 kcal/mol for isomer 9). The loss of a proton from the CH_2 site is again quite unfavorable at an energy of 151.44 kcal/mol above the lowest dissociation channel. A sequential loss of two H atoms, first from the CH_2 site and then another H atom, have energies 122.73 kcal/mol (for the isomer 1), 122.14 kcal/mol (for isomer 2) and 123.23 kcal/mol (for isomer 9) above the lowest dissociation channel.

2.5.4 Protonated Phenanthrene

Protonated phenanthrene provides an interesting and more complex counterpart to protonated anthracene in that it has five stable isomers, each of which can potentially contribute DIB features. Because of its complex potential energy surface, no tunneling and fewer dissociation pathways are calculated here (Figure 2.12, Table A.31 in Appendix A). Unlike the other protonated aromatic molecules discussed in this chapter, the protonated phenanthrene isomers are almost isoenergetic and are stable with respect to dissociation by 59.53 kcal/mol ($1\text{–}C_{14}H_{11}^{+}$), 57.53 kcal/mol ($2\text{–}C_{14}H_{11}^{+}$), 58.98 kcal/mol ($3\text{–}C_{14}H_{11}^{+}$), 58.46 kcal/mol ($4\text{–}C_{14}H_{11}^{+}$) and 59.33 kcal/mol ($9\text{–}C_{14}H_{11}^{+}$), respectively.

By analogy with protonated naphthalene and anthracene, the lowest dissociation channel for protonated phenanthrene is the loss of an H atom from the protonation site (0.00 kcal/mol). The loss of a proton from the CH_2 site lies 140.27 kcal/mol above the lowest dissociation channel and will not be considered further.

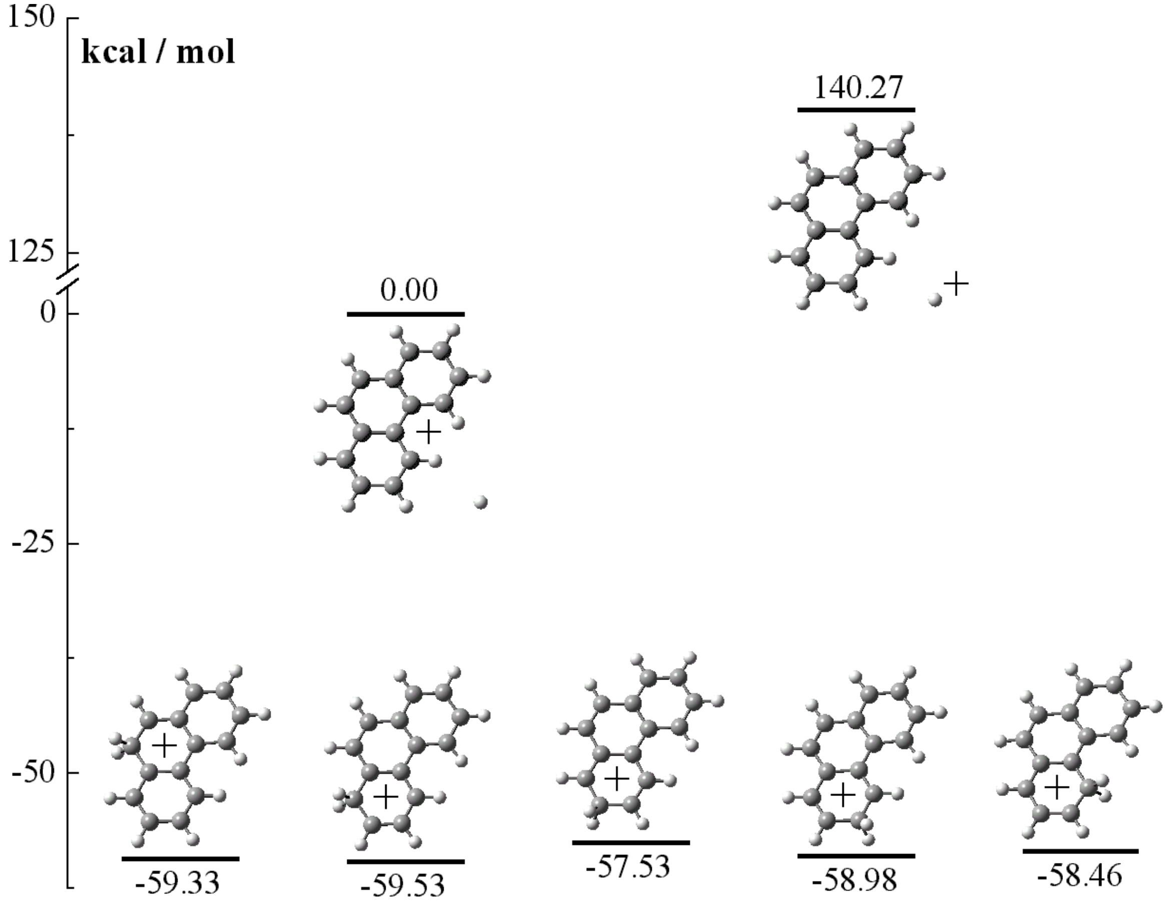

Figure 2.12: A simplified version of the protonated phenanthrene energy landscape.

2.5.5 Protonated Pyrene

Protonated pyrene has three isomers that are stable with respect to dissociation by 60.28 kcal/mol (1–$C_{16}H_{11}^{+}$), 46.57 kcal/mol (2–$C_{16}H_{11}^{+}$) and 50.52 kcal/mol (4–$C_{16}H_{11}^{+}$) (Figure 2.13, Table A.32 in Appendix A). As with the smaller protonated PAHs, the lowest dissociation channel for protonated pyrene is calculated to occur via the loss of an H atom from the protonation site (0.00 kcal/mol). The loss of a proton from the CH_2 site is 150.46 kcal/mol above the H atom loss channel.

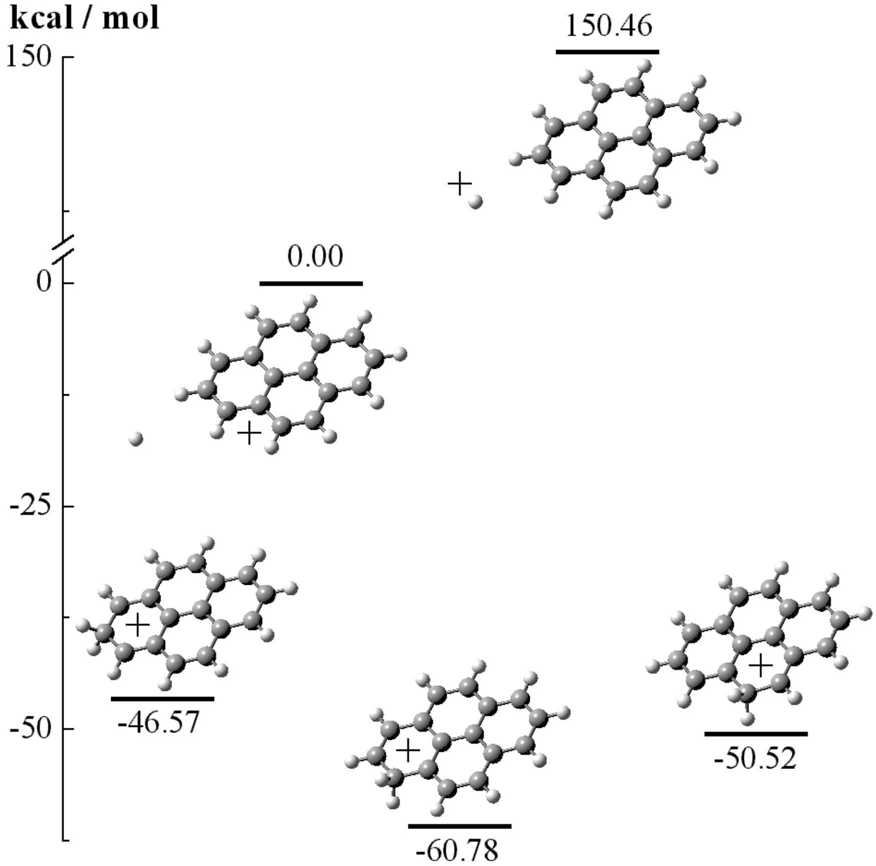

Figure 2.13: The energy landscape of protonated pyrene (not complete).

2.5.6 Hydrogenated PAHs

The main goal of this suite of calculations was to investigate the fate of protonated PAHs during electron recombination. Only the energies of hydrogenated PAH stable isomers and hydrogen loss channels were calculated, and only hydrogenated benzene, naphthalene, and anthracene were considered. The results are presented in Figures 2.14 – 2.16 and Tables A.33 – A.35 (Appendix A).

The lowest energy dissociation channel is the loss of a hydrogen atom from the CH_2 site, and as in the case for protonated PAHs, its energy was set to 0.00 kcal/mol. The next channel is the loss of an H_2 molecule from the hydrogenation site, and lies only 5.5 – 6.0

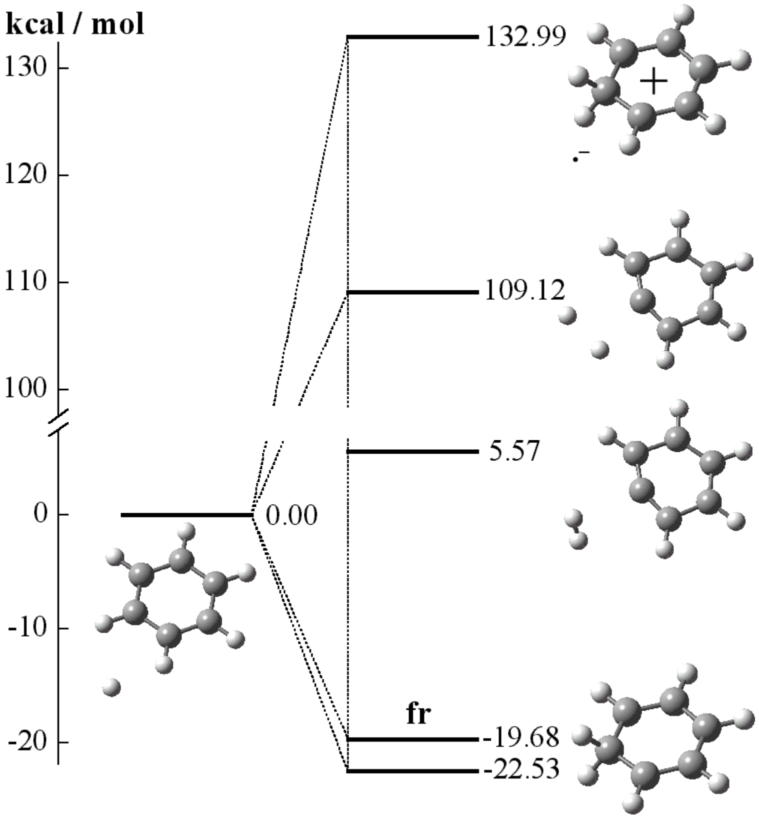

Figure 2.14: Hydrogenated benzene energy landscape.

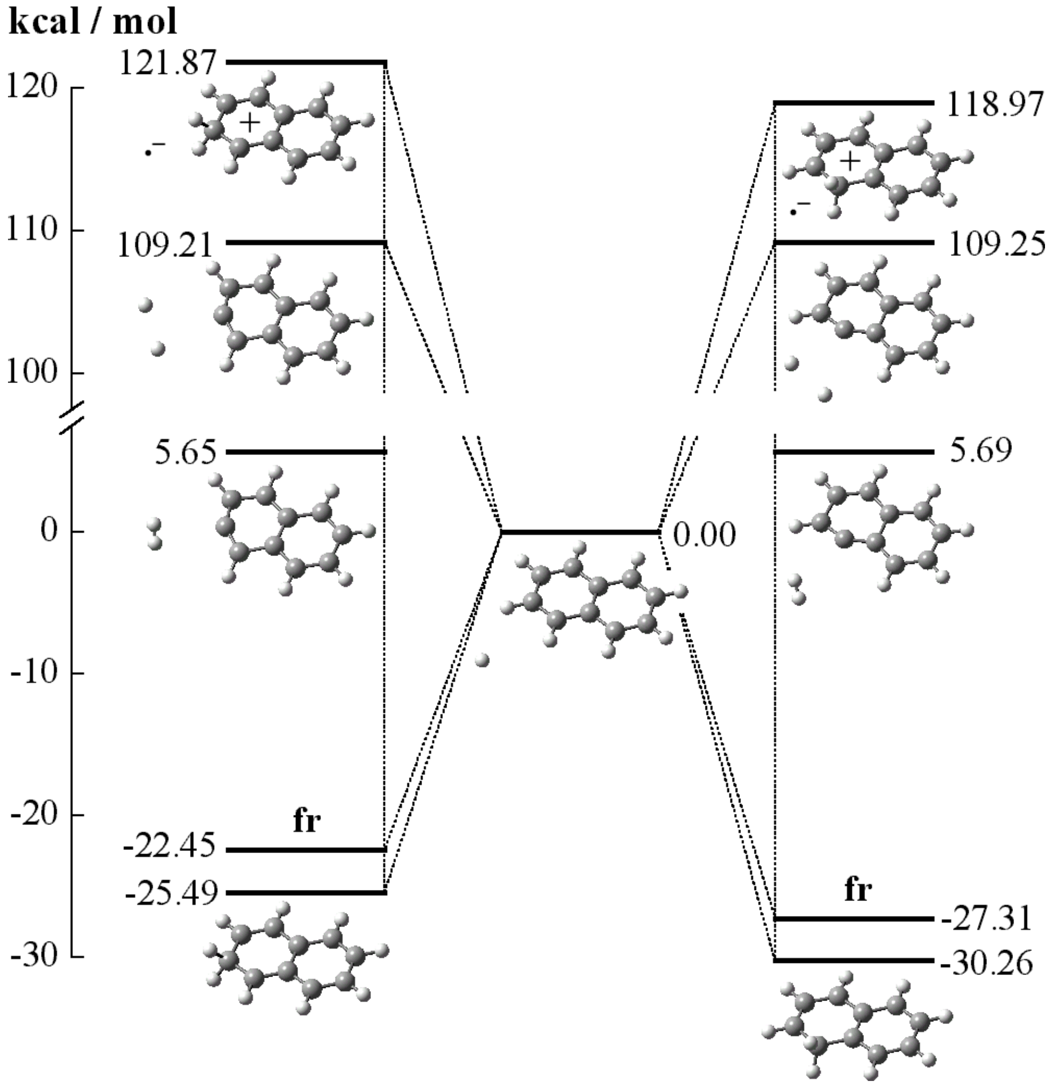

Figure 2.15: Hydrogenated naphthalene energy landscape.

kcal/mol higher in energy. A sequential loss of two hydrogen atoms, one of which is from the hydrogenation site – is almost 110 kcal/mol above the lowest energy channel.

Species labeled as **fr** (frozen) designate hydrogenated PAHs with geometries fixed to that of the protonated PAHs and energies that were corrected by ZPEs of protonated PAHs. Such geometries are not those appropriate for equilibrium, but rather, represent initial structures that are formed immediately after recombination. The energies of these structures are ∼3 kcal/mol above those of the equilibrium structures.

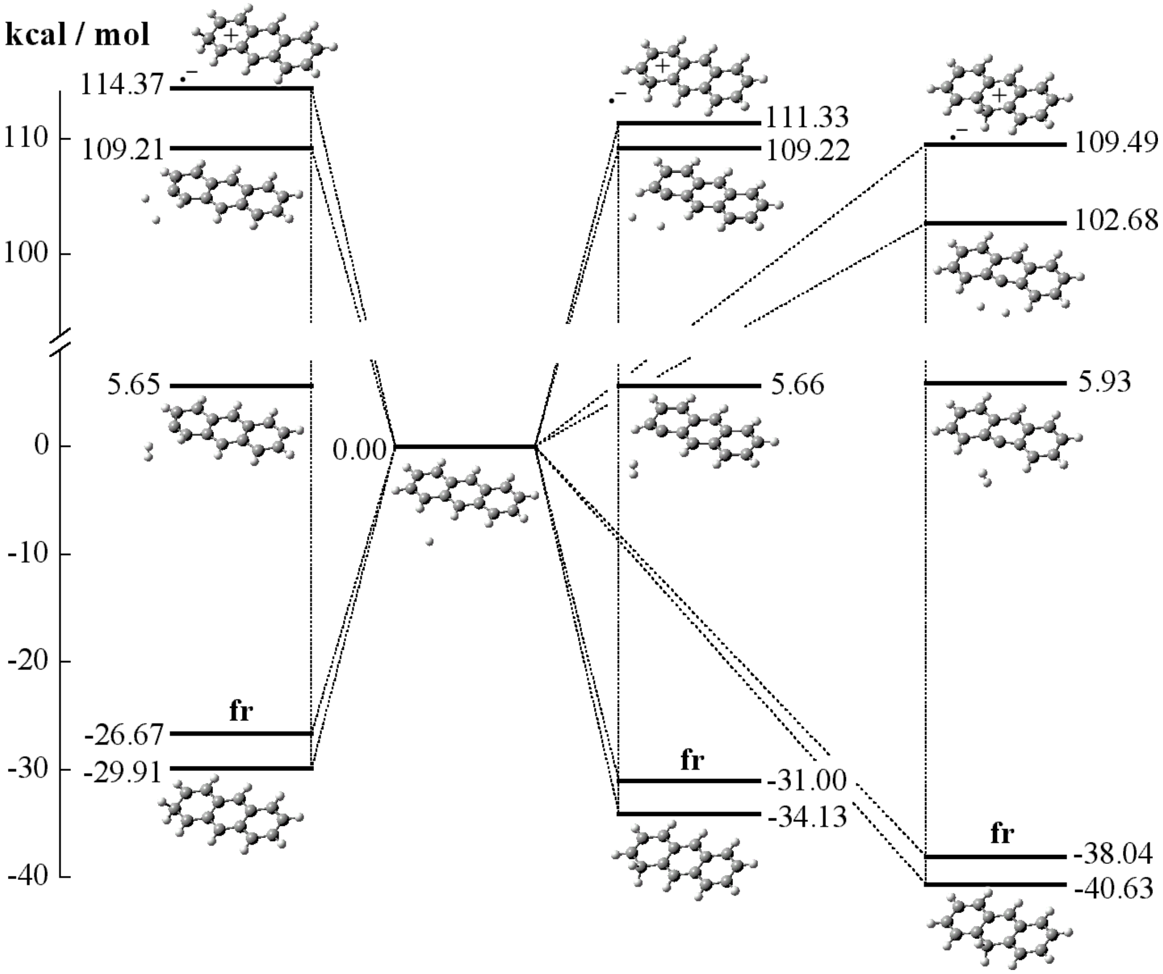

Figure 2.16: Hydrogenated anthracene energy landscape.

As a general trend, hydrogenated species become more stable with respect to dissociation as the size of the molecule grows. While hydrogenated benzene is stable by only 22.53 kcal/mol, isomers 1, 2 and 9 of hydrogenated anthracene are stable by 34.13, 29.91 and 40.63 kcal/mol, respectively. Since protonated PAHs have similar ionization energies, the amount of excess energy decreases with PAH size. For larger PAHs, the dissociation yield should drop substantially because the extra energy can be vibrationally distributed over the full molecule via IVR processes. In all cases, hydrogenated PAHs are less stable than protonated PAHs since they are not closed shell species.

2.6 Discussion

In regions of the interstellar medium exposed to ultraviolet photons (translucent clouds, H II regions, the diffuse medium), PAHs will exist in a variety of charge states. Anions typically have rapid photodetachment rates, and so cationic species are the most likely ionized form of interstellar PAHs. Neutral PAH precursors, for example, can acquire a positive charge either via ionization (UV or cosmic rays) or through the reactions with charged particles. In dense regions of the ISM such as molecular clouds, neutral PAH molecules can be protonated in collisions with H_3^+ or HCO^+, thanks to their high proton affinities. Being closed-shell species, protonated PAHs are not as reactive as PAH cations – often referred as cation radicals – and would therefore be expected to be rather stable in the interstellar medium. This is reflected in the energetics of the cationic PAH species, with the above calculations demonstrating that protonated PAHs are more stable than their radical cation cousins. In addition, the observed laboratory reaction rates between H atoms and protonated benzene, naphthalene, pyrene, their cations, and dehydrogenated cations [75] all suggest that protonated PAHs can be created efficiently from radical cation precursors. Hence, if PAHs exist in the interstellar medium and can survive UV radiation, an extremely important component of the charge balance is likely to be carried by PAHs in their protonated form.

During protonation of aromatic molecules, the molecular symmetry decreases. This has important spectroscopic implications for the protonated PAHs as DIB and UIR carriers. For example, the IR spectrum of protonated PAHs should be more dense since more vibrational modes would be IR active. While there are no microwave spectra of neutral aromatic hydrocarbons and their cations (unless they heterocyclic forms are examined) due to their lack of a permanent dipole moment (Appendix A, Table A.1), their protonated analogs do have significant dipole moments (at the protonation site) and should in principle be observable in the microwave with sufficient sensitivity. For example, 1–0 transition in protonated benzene should lie near ∼8209 MHz and could thus be searched for with standard FTMW techniques in the laboratory, as was successfully carried out for the phenyl radical C_6H_5 [118].

2.6.1 Changes in the Vibrational Spectrum

IR vibrational spectra of PAHs change significantly upon protonation (Appendix A, Figures A.1 – A.19), most likely due to the reduction in the molecular symmetry [23] (Appendix A, Table A.1) and the concomitant increase in the number of allowed IR vibrational transitions. The biggest change is in the 1100 – 1600 cm^{-1} range, where the neutral PAHs have only few, typically weak vibrations. The protonated PAHs, on the other hand, have their strongest lines in this region and the density of bands is high. Furthermore, the protonated PAH vibrational bands are located very close to 6.2 – 6.3 μm and 8.6 μm features in the interstellar UIR spectrum [23].

Another change is the dramatic decrease in the intensities of C–H stretch vibrations in 3000 – 3100 cm^{-1} range and the appearance of new CH_2 stretching vibrations that are not present at all in the neutral and cation spectra. The CH_2 vibrations (symmetric and asymmetric stretches) are separated by 1 – 20 cm^{-1} and located from 2830 – 2910 cm^{-1}. Experimentally, it is these vibrations that were recorded in the cluster dissociation spectrum of protonated benzene–Ar [3, 96]. The CH_2 vibrations are red-shifted from the aromatic C–H stretching modes and are located at wavelengths that can contribute to the red wing of 3.29 μm (3040 cm^{-1}) UIR feature. Since the exact frequencies depend on the

PAH molecule and the isomer, the CH_2 vibrational doublet from protonated PAHs will be difficult to observe astronomically, but these vibrations may well explain a part of, but not all, of the 3.29 μm red wing [23, 96].

2.6.2 Proton Mobility

When a protonated PAH molecule is excited vibrationally but without sufficient energy to dissociate, it can isomerize by intramolecular proton transfer from one carbon atom to another. This behavior is uniquely inherent to protonated PAHs. Neutral PAHs and their radical cations do not possess this dynamical possibility, which may have important ramifications under interstellar conditions. Depending on the level of excitation, the proton migration may occur only between two adjacent isomers, within one carbon ring, or over the entire carbon framework. The proton can even migrate from one ring to another via a ring fusion carbon, though this can only occur at rather higher levels of internal excitation since the isomer protonated at the ring fusion is rather unstable. Proton tunneling across the ring fusion is possible only in protonated catacondensed PAHs (naphthalene, anthracene, phenanthrene, tetracene, etc.) In protonated pericondensed PAHs (pyrene, coronene, ovalene, etc.), the migration can only occur on the outside of the molecule via 2-ring fusion carbon isomers since the protonation at the inner, 3-ring fusion sites is energetically prohibitive.

The ratio of the protonated PAH isomers in the ISM during formation is most likely to be statistical. For naphthalene it would be 1 : 1 (isomer 1 : isomer 2); for anthracene – 2 : 2 : 1 (isomer 1 : isomer 2 : isomer 9); for phenanthrene – 2 : 2 : 2 : 2 : 1 (isomer 1 : isomer 2 : isomer 3 : isomer 4 : isomer 9); and for pyrene – 2 : 1 : 2 (isomer 1 : isomer 2 : isomer 4). If the protonated PAH ion is later excited vibrationally (collisionally or by radiation), it may isomerize. In a large ensemble, this will scramble the initial isomer distribution and is most likely to change it closer to a thermodynamic equilibrium of isomers. On the other hand, the true thermodynamic equilibrium may be not attainable if the UV excitation rate is too high. The actual rate for reaching the equilibrium may be calculated only as a part of a model where isomerization rate dependence on the excitation energy is calculated for each isomer and then compared to the IR fluorescence lifetime. In general, the isomerization probability is the highest shortly after initial excitation, and then is reduced with every emitted IR photon.

Even in cold environments, the isomer distribution will not settle to the most stable isomer only. For example, in the case of interstellar methyl isocyanide, the amount of the metastable isomer CH_3NCH^+ is predicted to be $\sim 10-25\%$ of the amount for the stable isomer CH_3CNH^+, in spite of the isomer energy difference of 10 kcal/mol and the barrier of 65 kcal/mol [119].

Proton mobility also dramatically increases the density of the vibrational states once the internal energy rises above the isomerization barriers. Since these barriers correspond to ~visible wavelength photons, the proton mobility in protonated PAHs may well lead to significant broadening of their electronic spectra, a topic discussed at greater length in Chapter 6. The photostability should also be greatly enhanced, which would lead to improved survivability of protonated PAHs under interstellar conditions.

2.6.3 Dissociation Channels

For protonated benzene, the lowest energy dissociation channel is the loss of the hydrogen molecule H_2 from the protonation site, with an H atom loss not much higher in energy. The loss of 2 a.m.u. (either H_2 or 2H) was observed in protonated benzene UV photodissociation experiments [90].

According to the B3LYP calculations for polycyclic molecules, the lowest energy dissociation channel is the loss of a single hydrogen atom (H) from the protonation site, with the loss of a hydrogen molecule (H_2) higher in energy by only 10 – 20 kcal/mol. Interestingly, only the loss of H_2 molecules (or two H atoms) has been observed in the UV multiphoton dissociation of protonated anthracene and pyrene (Chapter 5). The sequential loss of two hydrogens was also observed in the CW visible photodissociation of coronene cations [120]. Both of these experiments illustrate the higher stability of the closed-shell protonated species compared to the open-shell cations. This stability also seems to be strongly influenced by the composition of the photodissociation products.

Other dissociation channels (H loss from non-protonation site, C–C bond cleavage or H^+) loss are much higher in energy and are therefore very unlikely to be important processes in interstellar photodissociation.

Typical dissociation energies for the two lowest channels are on the order of 50 – 80 kcal/mol (2.2 – 3.5 eV or $\lambda \sim 600 - 360$ nm for a single photon). Thus, from energetic considerations alone, protonated PAHs should be able to dissociate even from the absorption of visible or near-UV photons. In Chapter 3, the energies for the excited states will be calculated, with Chapters 5 and 6 turning to experimental analyses of the photostability and spectra of protonated PAHs.

2.6.4 Interstellar H_2 Formation

Molecular hydrogen is abundant in the interstellar medium. The mechanisms of H_2 formation are still debated in the literature, especially in warm regions such as diffuse or translucent clouds where dust grain synthesis models have a very difficult time generating sufficient rates of molecular hydrogen production. One possible 'out' is through reactions of PAHs with atomic hydrogen since the effective 'surface area' is increased dramatically. From the bond dissociation energies and barrier heights calculated for benzene and naphthalene [117], it is thought that hydrogen atom association reactions with PAH cations and dehydrogenated cations do not have a barrier. From these calculations, it was also suggested that H_2 abstraction by H atoms from protonated PAHs might occur efficiently. This mechanism was later extended to anthracene and pyrene molecules [121], and the general cycle would be:

$$\begin{cases} \mathrm{PAH}^+ + \mathrm{H} \longrightarrow \mathrm{H\text{–}PAH}^+ \\ \mathrm{H\text{–}PAH}^+ + \mathrm{H} \longrightarrow \mathrm{PAH}^+ + \mathrm{H}_2 \end{cases}$$

The first step in this mechanism proceeds almost at collision rate, but the rate for the second step is not known. It should only be a fraction of the collision rate, even if it is almost barrierless since the reaction will proceed only if the hydrogen atom approaches the 'right' carbon at a proper angle.

Another way to form molecular H_2 is via protonated PAH dissociation to generate the dehydrogenated PAH cation, as has been suggested in discussions of PAH cation reactivity with H atoms (for benzene and naphthalene [76]). The cycle for this mechanism would be:

$$\begin{cases} \mathrm{PAH}^+_{-H} + \mathrm{H} \longrightarrow \mathrm{PAH}^+ \\ \mathrm{PAH}^+ + \mathrm{H} \longrightarrow \mathrm{H\text{–}PAH}^+ \\ \mathrm{H\text{–}PAH}^+ \longrightarrow \mathrm{PAH}^+_{-H} + \mathrm{H}_2 \end{cases}$$

The first two steps in this reaction are exothermic and fast (they occur at nearly the collision rate), but the last step is endothermic. Thus, it is the rate-determining step in this cycle and depends largely on the external sources of protonated PAH excitation in the ISM. The absorption of UV photons may provide a viable option in diffuse clouds or near luminous young stars [90]. Chapter 5 discusses this in greater detail.

Whichever of the two mechanisms that predominates will depend on the rate for the second step in the first mechanism and the UV flux in the second cycle. Most likely, the first mechanism would be preferred since protonated PAHs were found to be photostable (Chapter 5).

One additional way to make molecular hydrogen would be through the H_2 loss channel by hydrogenated PAHs, formed in protonated PAH electron recombination. This channel is only 5.5 – 6.0 kcal/mol above the H atom loss channel. It should be energetically accessible since such dissociative recombination reaction for protonated PAHs should be exothermic by ∼100 kcal/mol. Dehydrogenated PAHs formed in this reaction would be ionized and would acquire hydrogen atoms to reform the protonated PAHs:

$$\begin{cases} \mathrm{PAH}^{+}_{-H} + \mathrm{H} \longrightarrow \mathrm{PAH}^{+} \\ \mathrm{PAH}^{+} + \mathrm{H} \longrightarrow \mathrm{H{-}PAH}^{+} \\ \mathrm{H{-}PAH}^{+} + e^{-} \longrightarrow \mathrm{PAH}_{-H} + \mathrm{H}_2 \\ \mathrm{PAH}_{-H} + h\nu \longrightarrow \mathrm{PAH}^{+}_{-H} + e^{-} \end{cases}$$

Such a cycle would be especially effective for smaller PAHs and would be facilitated by relatively high electron densities such as those found in diffuse clouds where the fractional electron abundance of $f(e^-) = n(e^-)/n(H) \sim 10^{-4}$ is maintained by atomic carbon photoionization.

2.7 Summary

The above calculations show that protonated PAHs are stable species. They are formed by proton binding to a carbon atom and not the C–C bond or the whole aromatic ring. In the ISM, PAHs are likely to be in protonated form.

Protonated PAHs have a stronger and more complicated IR spectrum than neutral PAHs. Some of the strong IR frequencies are located near UIR bands in the mid-IR range. CH_2 stretch vibrations are located in the red wing region of 3.3 μm UIR feature and may account for part of it.

The two lowest dissociation channels are loss of an H atom and an H_2 molecule from the protonation site. The dissociation energies are in the range 50 – 80 kcal/mol and in principle may be accessed by near UV or visible photons. The H_2 loss channel may be responsible for molecular hydrogen production in the ISM.

Vibrationally excited protonated PAHs can isomerize without dissociation. The proton can migrate almost everywhere on the outside rim of the PAH molecule. This would lead to broader electronic spectra and possibly to the thermodynamic distribution of the isomers in the ISM.

Chapter 3

Excited States Calculations for Protonated PAHs

3.1 Introduction

Protonated PAHs are closed shell ions. Their electronic structure should therefore be similar to that of neutral PAHs, but as is shown in this chapter, the electronic transitions of protonated PAHs are shifted to the red. The red shift occurs because the HOMO – LUMO gap is reduced due to rehybridization of the protonated carbon atom. Thus, one may expect that even small protonated PAHs would absorb in the visible wavelength range, that is, where the diffuse interstellar bands are located. Based on the assumption that protonated PAHs may be a class of DIB carriers, the experimental measurement of their electronic spectra is an important goal. Before undertaking such experiments, a survey of the expected protonated PAHs excited states could be used to guide the choice of molecules for study, based on the predicted proximity to observed DIBs. *Ab initio* calculations may be very helpful in making such predictions, as well as providing better knowledge of the electronic structure of protonated PAHs. However, it must be realized that such calculations are far from being precise and are best viewed as a guide for further research. Here, the S_1 states are the objects of interest as they participate in the longest wavelength absorption from the ground electronic state.

3.2 Methodology

To calculate the energies of the excited states for neutral and protonated PAHs, the same hardware and software (GAUSSIAN 98, Revision A.9 [98]) were used as in the ground state calculations (Chapter 2). All excited state calculations were performed on geometries that were first optimized at the B3LYP 6–311++G** level.

3.2.1 Theory Level and Basis Set

A number of methods have been used to calculate excited states of neutral PAHs and their cations [122–127]. The methods for calculating excited states are not as precise as for the ground state, indeed, they are currently an active area of research. Some are rather complicated and require a careful choice of the orbitals to be considered. The goal of the calculations carried out here is not to predict the positions of each excited state precisely, but rather to estimate where they are located. In addition, information about the *relative* energetics of the same state but in different isomers of protonated PAHs would be very useful as a guide to experiments.

The Configuration Interaction – Singles (CIS) method [122] was used here to perform calculations. This is the least precise excited state method, since it is an analog for the ground state Hartree-Fock method, but it does not require a prior knowledge about the electronic structure of the molecule and is reasonably stable for most molecules. Since protonated PAHs are closed shell species, the CIS method may be applied to them as well.

The choice of calculation parameters was based on the benzene calculation discussed in exercise 9.4 of [128]. The full call for the excited states calculation was:

```
# rCIS=(Direct,Singlets,NStates=12)/6–311++G(2d,2p) Density=Current
                                             IOp(9/40=2) Pop=Full
```

The 6–311++G(2d,2p) basis set was chosen based on the convergence analysis described in 3.2.2. Only singlet states were considered (*Singlets* keyword) as relevant to one-photon electronic absorption spectroscopy. The first twelve singlet excited states were calculated (*NStates=12*). Such a large number was not required, but used to avoid missing any degenerate or forbidden transitions. *Density=Current* was used for better estimates of the oscillator strengths for each transition. *Pop=Full* ensured that all orbitals were considered in the orbital population analysis, and *IOp(9/40=2)* specified which wavefunction coefficients were to be included in the output. The *Direct* keyword was used to avoid problems with disk space for larger molecules.

3.2.2 Convergence Tests

The accuracy of the excited states calculation depends on the basis set and the geometry optimization. To investigate the effect of both factors on the first singlet excited state, a number of tests were performed on neutral and protonated naphthalene. A summary of the results is presented in Table 3.1. A general trend is the increase in the wavelength with the increase in the CIS basis set. However, even with the biggest basis set used, the photon energy was overestimated because the experimental value for neutral naphthalene is known to be at a much longer wavelength (312 nm).

For the geometry optimization, tests were carried out with and without diffuse functions, but the difference was found to be negligible (0.06%). The effect of the basis set on CIS energies is seen to be more noticeable. In particular, the addition of both polarized (d,p) and diffuse (+) functions in the basis set improves the performance. The calculated wavelengths

Table 3.1: Convergence dependence on the basis set for the $S_1 \leftarrow S_0$ transition wavelength (nm) calculations in neutral and protonated naphthalene.

CIS basis set	B3LYP 6–311G(d,p) geom		B3LYP 6–311++G(d,p) geom		
	$C_{10}H_8$	2–$C_{10}H_9^+$	$C_{10}H_8$	1–$C_{10}H_9^+$	2–$C_{10}H_9^+$
3–21G	225.75	329.02			
4–31G	227.82	331.00	228.07	287.02	331.20
6–31G	229.37	332.66	229.62	288.29	332.87
6–31G(d,p)			236.21	294.69	338.55
6–31+G(d,p)			242.13	297.68	341.35
6–31++G(d,p)			242.14	297.80	341.64
6–311G	231.94	334.60	232.20	290.15	334.81
6–311G(d)	239.94	341.31			
6–311G(d,p)	240.24	341.04	240.50	297.08	341.25
6–311+G(d)			243.56	298.48	342.96
6–311+G(d,p)	243.71	342.54	243.97	298.79	342.76
6–311++G(d,p)	243.72	342.66	243.98	298.84	342.88
6–311++G(2d,2p)			245.86	300.55	345.45

appear to group together for minor basis set changes and experience a ‘nudge’ towards smaller energies upon more significant changes. The basis set changes explored were 4–31G ⟶ 6–31G, 6–31G ⟶ 6–311G, the addition of polarized functions [105] (either d or d,p), a change in the level of polarized functions (from d,p to 2d,2p), and the addition of at least one diffuse function [106]. With each change, the calculated values move toward the experimental values. From these tests, the 6–31+G(d) basis set appears to be the minimum required for CIS calculations on neutral and protonated PAHs. Here, the 6–311++G(2d,2p) was selected for excited states calculations. This basis set is relatively large, but at the same time, CIS calculations are still significantly faster than geometry optimizations. Typically, 4 hours were needed to calculate the singlet energies and about another 20 hours to perform the population analysis on the P4–2.7 system.

3.2.3 Scaling Factors

Clearly, the CIS calculations tend to overestimate the excited states energies. The easiest way to compensate for this in a homologous suite of compounds is an empirical approach, that is, scaling the calculated results to better match experimental values. Fortunately, the gas phase $S_1 \leftarrow S_0$ transition wavelengths have been measured for many small neutral aromatics (benzene [129], naphthalene [70], anthracene [69], phenanthrene [130,131], pyrene [131,132]). The ratios of the calculated and experimental values are presented in Table 3.2. They lie mainly in the range 0.77 ± 0.01 for all molecules considered, except anthracene (0.846). Based on this result, the scaling factor for protonated PAHs should be somewhere in the 0.75 – 0.85 range. Here, the scaling factors obtained from the respective neutral molecule calculations are used.

Table 3.2: Scaling factors for the $S_1 \leftarrow S_0$ transitions in neutral aromatic hydrocarbons.

Molecule	$S_1 \leftarrow S_0$ wavelength (nm)		Scaling factor
	Calculated	Experimental	
Benzene (C_6H_6)	206.22	262.56	0.78542
Naphthalene ($C_{10}H_8$)	243.98	312.30	0.78123
Anthracene ($C_{14}H_{10}$)	305.39	361.17	0.84556
Phenanthrene ($C_{14}H_{10}$)	258.26	340.99	0.75738
Pyrene ($C_{16}H_{10}$)	282.19	367.43	0.76801

The validity of scaling down the calculated values may be questioned, especially whether the factor for the neutral molecule can be applied to its protonated versions. To date, experimental data are available only for protonated benzene [89,90]. Calculated but scaled wavelengths for the $C_6H_7^+$ $S_1 \leftarrow S_0$ transition (349.77 nm in Table 3.3) is slightly red-shifter from the experimentally measured band maximum at ∼335 nm. The scaled predicted and experimental values also turn out to be very close for isomer 1 of protonated anthracene, and somewhat red-shifted for isomer 2 (Chapter 6).

3.3 Valence Molecular Orbitals

In neutral aromatic molecules, the transitions from the ground to the first few excited electronic states are $\pi - \pi^*$ transitions. The electronic structure of protonated PAHs should therefore not differ drastically from neutral PAHs. In particular, their $S_1 \leftarrow S_0$ transitions should be $\pi - \pi^*$ as well. To illustrate the changes in the molecular π orbitals upon protonation, the benzene molecule is first considered as an example system.

3.3.1 Protonated Benzene

The benzene molecule is one of the most popular benchmark systems in chemistry. Its molecular orbital system is well-studied and is described in nearly every general chemistry textbook. The molecular π orbitals of neutral benzene based on Hückel theory are shown in Figure 3.1. These are the *NaturalOrbitals* from an energy calculation (HF STO–3G) on previously optimized geometries (B3LYP 6–311++G**) and visualized in Chem3D [133].

Upon protonation, the hybridization of one of the carbon atoms changes from sp^2 to sp^3 (Figure 3.2). As a result, its p_z orbital is not a part of the aromatic system and the ring is no longer aromatic. The p_z orbitals of the other five carbon atoms remain unchanged and still form a conjugated system, as can best be seen in the $2b_2$ orbital that is lying just below the HOMO.

Because of this reduction in symmetry, the orbitals of protonated benzene are no longer degenerate. Two out of the six benzene orbitals (one e_{1g} and one e_{2u}) do not overlap with the protonation site, and therefore have the same appearance in protonated benzene (two a_2 orbitals), with energies that are barely perturbed by protonation. The other four orbitals, however, are altered substantially by the protonation process and become a hybrid of carbon p_z orbitals and hydrogen s orbitals (four b_2 orbitals), since the C–H bonds at

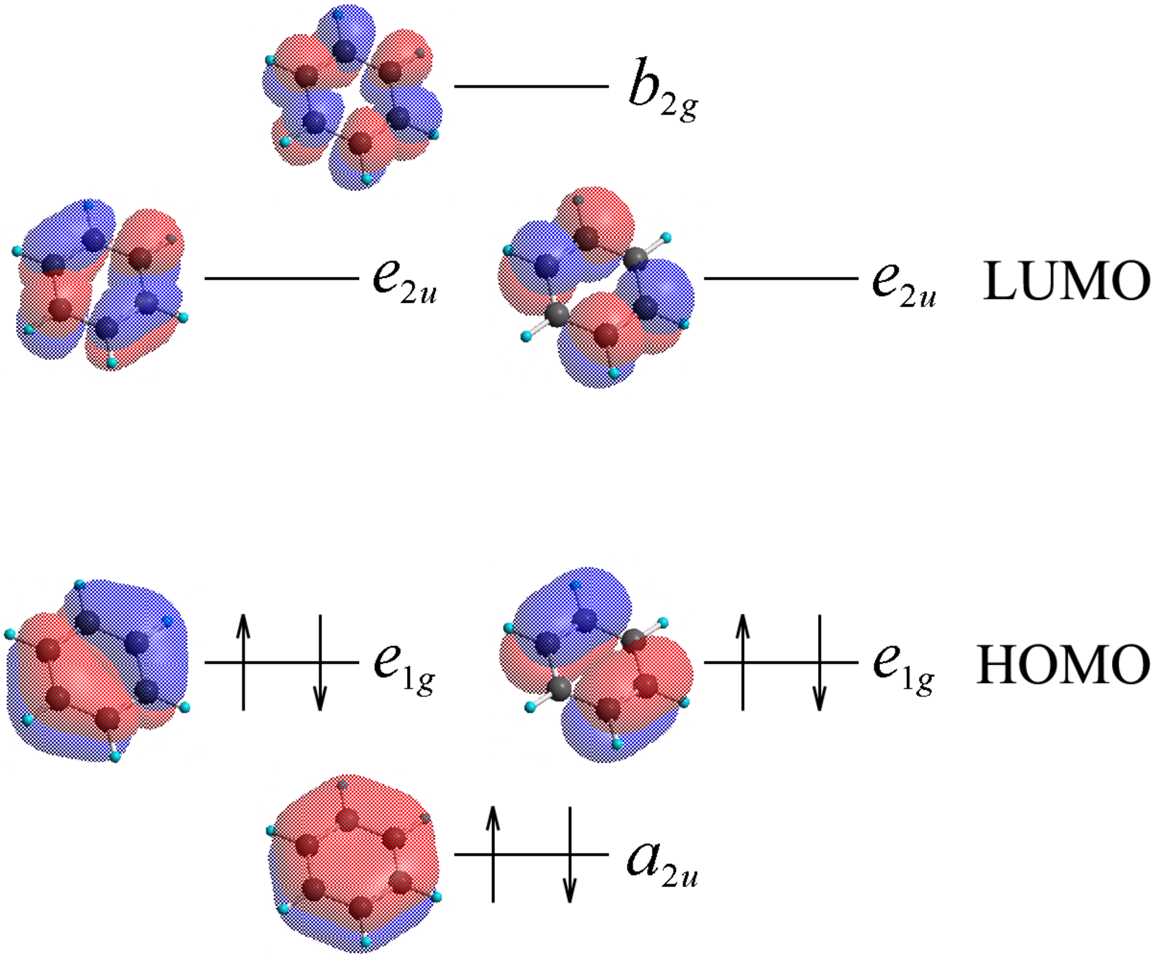

Figure 3.1: The π molecular orbitals of benzene.

the CH_2 site are σ bonds. As a result, their energies are lowered with respect to neutral benzene orbitals (solid *vs.* dashed lines in Figure 3.2). Since the HOMO is unaffected, this reduces the HOMO – LUMO gap, which leads to a red shift in the absorption spectrum.

3.3.2 Other Protonated Aromatics

When a molecule with more than one ring is protonated, the changes in orbitals are similar to benzene, that is, the aromaticity is lost only in the ring with the protonation site while other rings remain aromatic. Unlike the benzene molecule, the HOMOs and

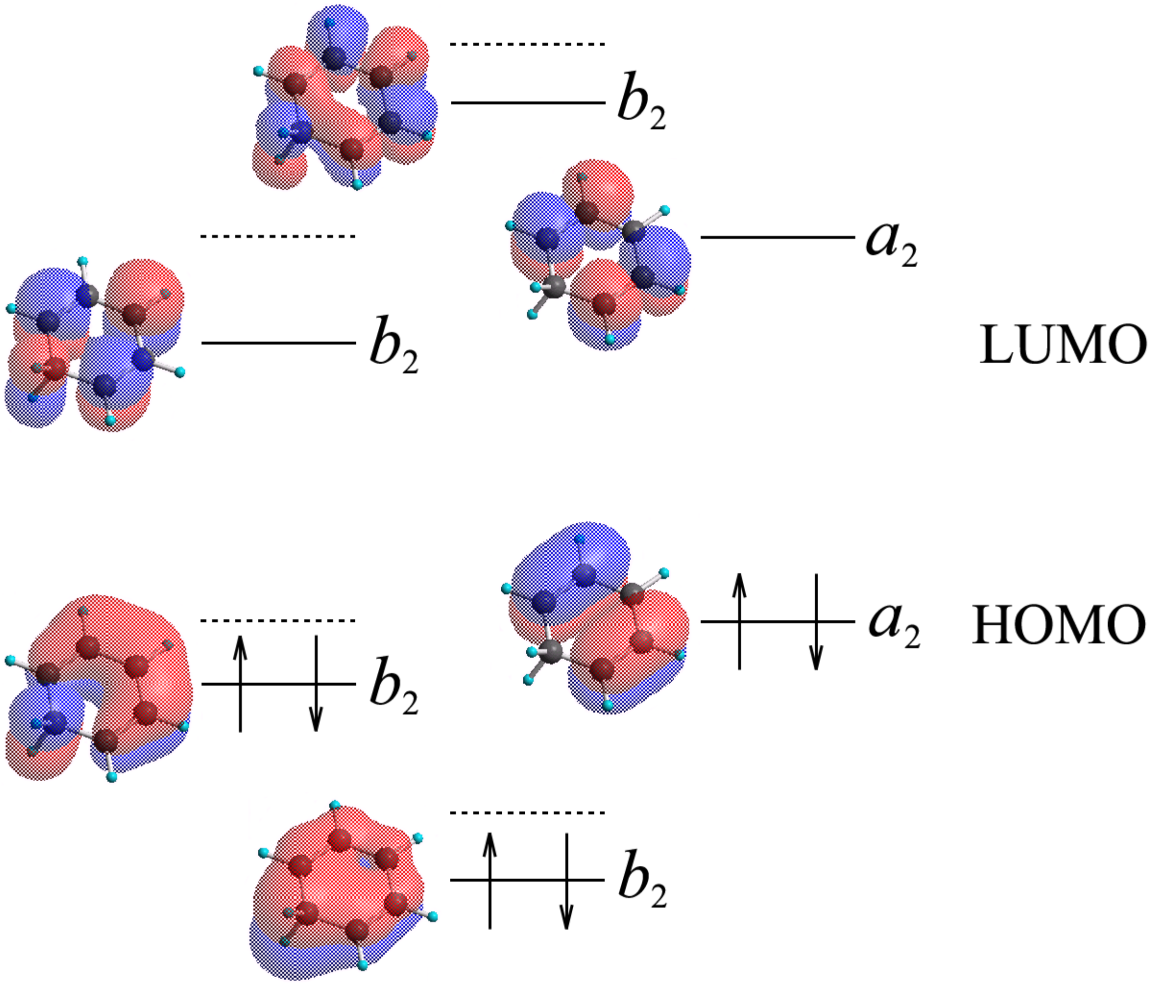

Figure 3.2: The π molecular orbitals of protonated benzene.

LUMOs of neutral polycyclic aromatic molecules are non-degenerate and remain that way after protonation. Orbital images of the HOMOs and LUMOs of neutral and protonated PAHs are shown in Appendix A, Table A.39.

3.3.3 Electronic States Assignment

The assignment of electronic states is based on the molecular orbital symmetry [134]. Among neutral PAHs, benzene belongs to the D_{6h} symmetry group, naphthalene, anthracene and pyrene to the D_{2h} group, and phenanthrene to the C_{2v} group. The symmetry is reduced in protonated PAHs. Protonated benzene, isomer 9 of protonated anthracene and isomer 2 of protonated pyrene are members of the C_{2v} symmetry group, while the rest have C_s symmetry.

The exact assignment of the orbital symmetry depends on the choice of the orthogonal coordinate system. Here, for all non-C_{2v} symmetric molecules, the Z axis is set to be normal to the molecular plane by analogy with neutral benzene (Figure 3.3 **1**). In molecules with C_{2v} symmetry, the Z axis is selected as the rotational C_2 symmetry axis (Figure 3.3 **2**), with the X axis set orthogonal to the Z axis in the molecular plane and in the prolate direction. The Y axis is orthogonal to the X and Z axes. It is therefore in the molecular plane for non-C_{2v} symmetric molecules. This coincides with the coordinate system used in studies of the valence states of polyacenes [127].

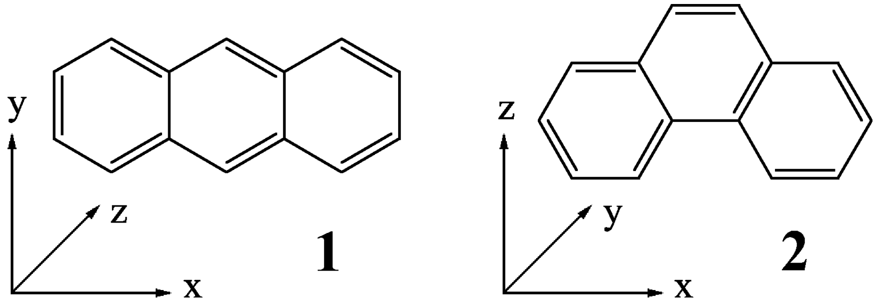

Figure 3.3: Orthogonal axis selection for molecules with different symmetry.

Based on this coordinate system, the ground and the first singlet electronic states, as well as electronic configurations, were assigned (Appendix A, Table A.38). The total number of π orbitals was the same as the number of carbon atoms. The symmetries of orbitals were determined by visual inspection. The electronic states were then labeled using the symmetry of HOMO and LUMO orbitals (the ones that have x and y electrons in Table A.38).

C_s-symmetric molecules (the majority of protonated PAHs) present the simplest case. For them, all orbitals have a'' symmetry. Thus, the ground state (S_0) is $\widetilde{X}\ ^1A'$ and the first singlet excited state (S_1) is $\widetilde{A}\ ^1A'$. For C_{2v}-symmetric molecules, the HOMOs and LUMOs have a_2 and b_2 symmetry, leading to $\widetilde{X}\ ^1A_1$ ground states and to $\widetilde{A}\ ^1B_1$ for S_1 states. The orbital symmetries become more diverse for D_{xh}-symmetric molecules. Molecules with D_{2h} symmetry have $\widetilde{X}\ ^1A_g\ \ S_0$ states and $\widetilde{A}\ ^1B_{\mathrm{xu}}$ (x = 1, 2 or 3) S_1 states. For the benzene molecule (D_{6h}), it is well known that the S_0 state is $\widetilde{X}\ ^1A_{1g}$ and the S_1 state is $\widetilde{A}\ ^1E_{1u}$.

3.4 Excited States Energies

The first singlet excited state energies and $S_1 \leftarrow S_0$ transition wavelengths were calculated for the neutral and stable isomers of protonated benzene, naphthalene, anthracene, phenanthrene, and pyrene. A short overview of the results is presented in Table 3.3, and the full version is presented in Appendix A, Table A.37. The wavelengths in both tables are scaled by the neutral PAHs experimental values. The scaling in Table A.37 ranges for 0.75 – 0.85.

As one would expect, the $S_1 \leftarrow S_0$ wavelengths for protonated PAHs are shifted to the red, as compared to their neutral PAH precursors. There is a wide range of red shifts, from 15 nm for isomer 9 of protonated anthracene to just over 200 nm for isomer 2 of protonated pyrene. The majority are significant, on the order of 100 nm (Appendix A, Table A.37).

The $S_1 \leftarrow S_0$ transitions for small neutral PAHs lie at UV wavelengths range, and so are not important to the DIBs. With the exception of protonated benzene, however, all of the protonated versions of small PAHs have isomers that should absorb visible wavelength photons. In fact, all isomers of protonated phenanthrene and pyrene absorb in the visible. Roughly, it appears that the closer the protonation site is to the center-of-mass of the

Table 3.3: Scaled calculated $S_1 \leftarrow S_0$ wavelengths for neutral and protonated PAHs.

Molecule	$S_1 \leftarrow S_0$ Wavelength (nm)
Benzene	
C_6H_6	262.56
$C_6H_7^+$	349.77
Naphthalene	
$C_{10}H_8$	312.30
1–$C_{10}H_9^+$	382.53
2–$C_{10}H_9^+$	438.90
Anthracene	
$C_{14}H_{10}$	361.17
1–$C_{14}H_{11}^+$	443.09
2–$C_{14}H_{11}^+$	490.41
9–$C_{14}H_{11}^+$	376.47
Phenanthrene	
$C_{14}H_{10}$	340.99
1–$C_{14}H_{11}^+$	477.20
2–$C_{14}H_{11}^+$	497.78
3–$C_{14}H_{11}^+$	460.81
4–$C_{14}H_{11}^+$	493.13
9–$C_{14}H_{11}^+$	479.36
Pyrene	
$C_{16}H_{10}$	367.43
1–$C_{16}H_{11}^+$	442.82
2–$C_{16}H_{11}^+$	569.30
4–$C_{16}H_{11}^+$	499.23

molecule, the shorter the wavelength of the $S_1 \leftarrow S_0$ transition. For polyacenes (naphthalene, anthracene), this also correlates with isomer ground state stability; more stable isomers absorb at shorter wavelengths.

The photon energies for the $S_1 \leftarrow S_0$ transitions are close to the ground state dissociation thresholds for protonated PAHs calculated in Chapter 2 (Table 3.4). After absorbing a UV/visible photon, the protonated PAH ion ends up in an electronically excited state that may undergo an internal conversion to the ground electronic state. The photon energy in this case would be converted into vibrations via intramolecular vibrational energy redistribution (IVR). This means that protonated benzene, naphthalene and anthracene would, in principle, have enough energy to dissociate even when excited to the S_1 electronic state. Larger protonated PAHs would have enough energy to dissociate when excited to higher electronic states. Thus, it may be possible to record absorption spectra of protonated PAHs by resonance-enhanced dissociation method. Such an attempt is made in Chapter 5. At the same time, this casts a shadow on the prospective of protonated PAHs survival in the interstellar medium.

Protonated PAHs are expected to be strong absorbers, since the calculated oscillator strengths for the $S_1 \leftarrow S_0$ transitions are in the 0.14 – 0.7 range (Appendix A, Table A.37). Depending on the isomer, some of them may absorb better than their neutral cousins.

Table 3.4: Comparison of the calculated $S_1 \leftarrow S_0$ wavelengths and ground state dissociation energies for protonated PAHs, in kcal/mol.

Molecule	$S_1 \leftarrow S_0$ Wavelength	Dissociation Energy
Benzene		
$C_6H_7^+$	81.74	63.22
Naphthalene		
1–$C_{10}H_9^+$	74.32	62.41
2–$C_{10}H_9^+$	64.66	59.51
Anthracene		
1–$C_{14}H_{11}^+$	64.53	52.41
2–$C_{14}H_{11}^+$	58.30	49.36
9–$C_{14}H_{11}^+$	75.95	61.06
Phenanthrene		
1–$C_{14}H_{11}^+$	59.92	59.53
2–$C_{14}H_{11}^+$	57.44	57.53
3–$C_{14}H_{11}^+$	62.05	58.98
4–$C_{14}H_{11}^+$	57.98	58.46
9–$C_{14}H_{11}^+$	59.64	59.33
Pyrene		
1–$C_{16}H_{11}^+$	64.57	60.78
2–$C_{16}H_{11}^+$	50.22	46.57
4–$C_{16}H_{11}^+$	57.27	50.52

3.4.1 Comparison with DIB spectrum

Since protonated PAHs are predicted to be strong absorbers of visible wavelength photons, it is interesting to compare calculated $S_1 \leftarrow S_0$ transition wavelengths with the spectrum of the diffuse interstellar bands. The DIB synthetic absorption spectrum is calculated based on extensive DIB surveys [31–33] that were compiled from many different astronomical sources [1]. In Figure 3.4, the black solid line is the synthetic DIB spectrum; vertical colored dashed lines are the scaled $S_1 \leftarrow S_0$ wavelengths; and the horizontal colored solid lines are the scaled wavelengths ranges for each transition.

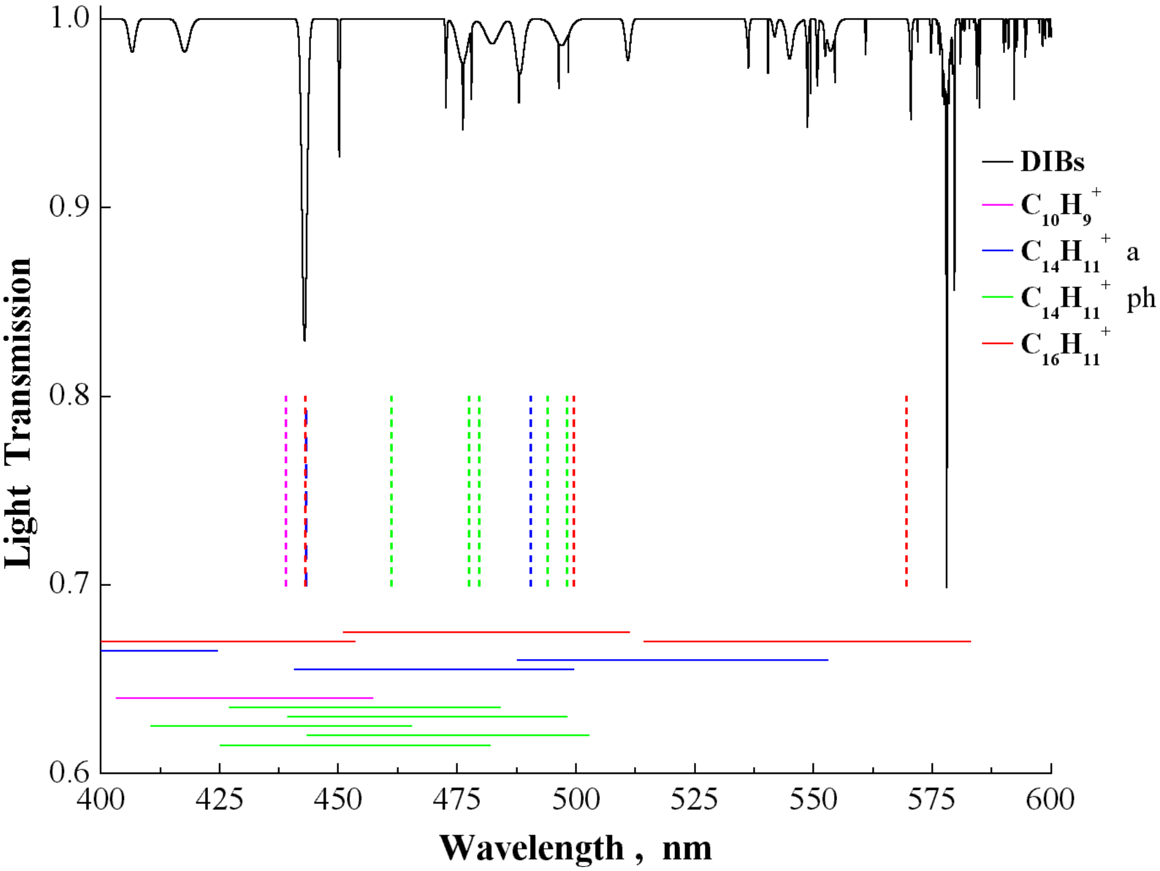

Figure 3.4: Diffuse interstellar bands and calculated $S_1 \leftarrow S_0$ wavelengths for protonated PAHs.

Since protonated PAHs are relatively large molecular ions, their absorption bands should be broader than for small molecules. Hence, if protonated PAHs are the DIB carriers, they should contribute to broad DIB features (1 – 3 nm wide). There are three different protonated PAH isomers (from naphthalene, anthracene and pyrene) that absorb near the strong 443 nm band. Four isomers of protonated phenanthrene and one from protonated anthracene and pyrene should absorb in 470 – 520 nm range, where five broad bands are located. One isomer of protonated pyrene is in the vicinity of the 578 nm band. The proximity of the calculated transitions to the broad DIBs makes a good argument in favor of protonated PAHs as DIB carriers, however, it should be tested experimentally. The UV/visible absorption spectra of protonated PAHs in the gas phase need to be measured. This issue is addressed in Chapters 5 and 6.

3.5 Summary

$S_1 \leftarrow S_0$ transition wavelengths were calculated for neutral and protonated PAHs with CIS method. The symmetries of the ground and the first singlet excited states were assigned together with their electronic configurations. It was determined that most protonated PAHs have $\widetilde{X}\ ^1A'$ ground state and $\widetilde{A}\ ^1A'$ excited S_1 state.

The $S_1 \leftarrow S_0$ transitions for most protonated PAHs are estimated to be in the visible, where the DIBs are located. They are fairly close to a number of the broad DIB features. This is encouraging news for the theory that protonated PAHs are DIB carriers. For species with a few isomers in the DIB range, the match of a few experimentally measured bands with DIBs would be solid proof for such a theory.

The energy differences between LUMO and HOMO in protonated PAHs are close to their dissociation thresholds. In the absence of IVR, this makes them potentially unstable in the ISM, but as the size of the molecule gets larger, IVR has a profound effect on the stabilization of PAHs. As was found in Chapter 5, even relatively small protonated PAHs may be photostable in the ISM.

Chapter 4

Experimental Setup

4.1 Introduction

To measure the electronic spectra of protonated PAHs, appropriate protonation and detection methods need to be selected. In general, protonated PAHs can be produced in a hydrogen discharge of some kind, or by a proton transfer from other protonated molecules. The method for recording the spectrum may strongly depend on the way the protonation has been performed, and so should be considered in tandem with the production techniques.

In afterglow discharge experiments [75], for example, the reactions of PAH cations with hydrogen were studied. As a result of these reactions, the cations of aromatic molecules (benzene, naphthalene and pyrene) acquired hydrogen atoms, making protonated PAHs with nearly 100% efficiency. For this fairly high pressure method, the protonated PAH spectra would have to be recorded in direct absorption. Even with multipass configurations for the laser beam, the sensitivity of such methods is usually low. The absorption strength would strongly depend on the concentration of protonated PAHs, but high concentrations are not easily achievable for multi-ring PAHs due to their low vapor pressures. The sample and possibly the flow cell would therefore need to be heated to increase the amount of absorbing ions, and the high temperatures and collision frequency would broaden the spectrum significantly.

In the IR cluster photodissociation experiments on $C_6H_7^+$ [3, 96], protonated benzene was created by proton transfer from the H_3^+ produced as a result of H_2 molecule ionization by an electron gun. This method produced protonated benzene that was sufficiently cold to cluster with Ar, N_2, etc. Such a protonation method requires high pressure at the pulsed valve throat which can be achieved by increasing the carrier gas pressure behind the pulsed valve (i.e. the backing pressure) to ∼10 atm. This creates a significant load on vacuum pumps and requires multiple differential pumping stages with good ion guides. It is possible to decrease the gas load on the pumps by shortening the gas pulse duration, but the piezo-based pulsed valves must be used in this case. Piezo valves cannot be heated above 80 − 100 °C and would be useful only when working with benzene and naphthalene, but not larger PAHs.

Alternatively, PAHs may be protonated in a longitudinal pulsed discharge source (pinhole or slit). Discharge sources of this kind have been used successfully to create a wide array of species, including neutral, cationic and anionic carbon chains, and miscellaneous radicals [40, 135–137]. These discharge sources do not require high gas backing pressure and are easy to operate. When heated, they may be used with large PAHs as well, although it must be noted that the ions produced are typically vibrationally warmer than the ones from electron gun ionization-based sources.

A suitable way to record the spectra needs to be selected once the production method is set. Absorption or photodissociation would be the most appropriate methods for the gas phase spectroscopy of positive ions. As mentioned earlier, a typical absorption experiment requires a large number of protonated PAH molecules to be produced, even if some kind of multipass scheme for the light is implemented. The most sensitive of such methods –

cavity ringdown spectroscopy – has been used successfully to record absorption spectra of PAH cations (naphthalene, pyrene) produced in a slit pulsed discharge source [62–64]. It was estimated that with our discharge source, the cavity ringdown method would barely be able to detect any absorption due to the low number of protonated PAH ions and was therefore discarded.

An alternative method would be to conduct photodissociation measurements on protonated ions. Resonance Enhanced Multiphoton Dissociation (REMPD) was used previously to record the electronic spectra of the naphthalene [67], anthracene and phenanthrene [138] cations. Photodissociation was also used for protonated benzene [89,90] as well. The central problem with this method lies in its multiphoton character, therefore either high radiation intensity or long interaction time between the ions and photons are needed.

In our experiments, a longitudinal pinhole pulsed discharge source was used for PAH protonation due to its robustness and compatibility with existing equipment. Laser photodissociation was chosen to record spectra, and a reflectron time-of-flight mass spectrometer was used as a detection method.

4.2 Pulsed Discharge Source

4.2.1 Design

The pulsed discharge source was based on the Thaddeus group design used for the Fourier-transform microwave spectroscopy of carbon chains [40]. It was modified for use with the time-of-flight mass spectrometer, but the electronic circuitry was kept the same. The design for our source is shown in Figure 4.1 (see Appendix B, Figures B.1–B.7 for detailed shop drawings). The discharge source consisted of two electrodes mounted on a Parker General

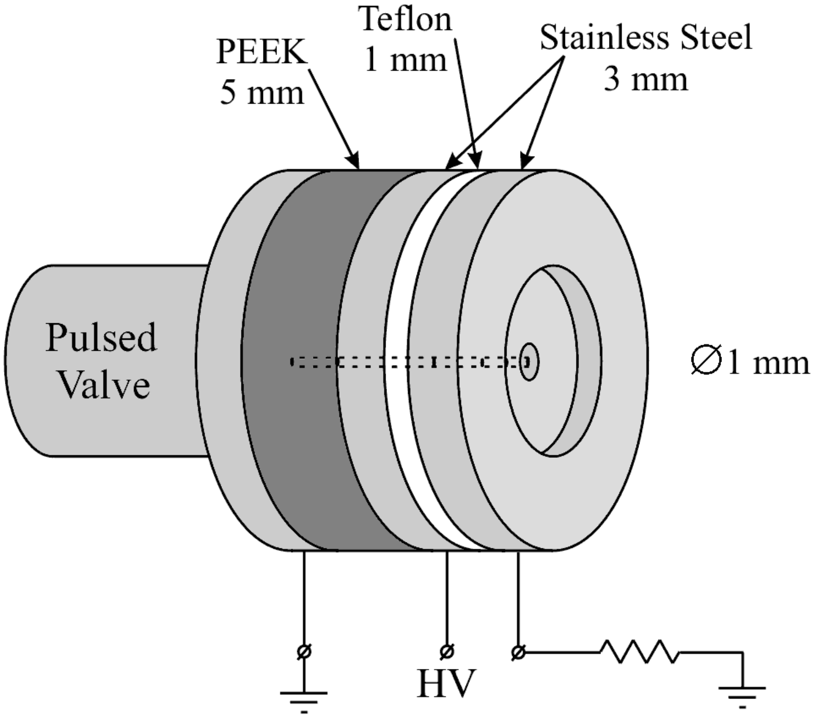

Figure 4.1: The pulsed discharge source design.

Valve series 9 pulsed valve, separated from the valve and each other by insulating spacers. A small channel for the gas flow was drilled in the center of the electrodes and spacers. The diameter of the channel was 1.0 mm. This value was optimized for the best discharge conditions which consisted of balancing the preferably low pressure for the discharge with the preferably high pressure for gas cooling during the expansion into vacuum. The diameter of the pulsed valve orifice was 0.7 mm. To avoid a parasitic volume next to the pulsed valve, the face of the valve body was flat, that is, there was no standard cone around the orifice. The outside diameter of the electrodes and spacers was the same as for the pulsed valve body – 1.33″ (33.9 mm). The spacer between the electrodes was made of teflon and was 1.0 mm thick. The spacer between the pulsed valve and the inside electrode was made of PEEK (poly-ether-ether ketone) to insulate the heated pulsed valve thermally from the rest of the discharge assembly. Either a 5.0 or 7.0 mm thick spacer was used. Electrodes were made of stainless steel to prevent their sputtering by the discharge. High voltage rated (up to 5 kV) electric wires were attached to the side of the electrodes with 0–80 screws. Ideally, the electrodes should be as thin as possible (down to 0.5 mm) to avoid plasma neutralization by the electrodes. In our case, they were 2.54 mm thick due to the size of wire lugs and screw heads. The middle part of the outside electrode was made 1.7 mm thick and had a 90° cone to improve the quality of the gas jet flow. Electrodes and wires were wrapped with teflon tape to prevent arcing between electrodes outside the discharge channel. The entire assembly was held together with four screws, insulated electrically from the electrodes by teflon inserts and washers.

In principle, high voltage could be applied to both electrodes in the discharge. In order to avoid ion deflection by the electrode potential after the plasma left the discharge, the outside electrode was held at almost ground potential. It was connected to ground with a 10 Ω, 10 W current monitoring resistor. The negative DC high voltage pulse (up to –2.0 kV) was applied to the inside electrode, and the pulsed valve body was grounded. The discharge would occur between the electrodes and not between the inside electrode and the valve body due to the large difference in the thickness of the PEEK and teflon spacers.

The pulsed valve was operated at 5 – 7 Hz repetition rate by a driver circuit (Appendix B, B.2.2) that applied a 400 μs long pulse to open the valve with a setting of 160 – 180 V on the capacitors C_1. After two to three days of continuous operation, the inside channel of the discharge had to be cleaned of a carbonaceous deposit. The need for cleaning was determined by a decline in the ion signal and an increased surface arcing in the discharge.

4.2.2 Voltage and Current Profiles

The negative high voltage pulse was typically applied to the inside electrode 250 μs after opening the pulsed valve. The duration of the high voltage pulse was 1200 μs to cover the full gas pulse delivered by the valve. Typical voltage and current curves for the discharge are shown in Figure 4.2. In this example, a –560 V pulse was applied. In the absence of gas between discharge electrodes (the front and the tail of the pulse), no discharge occurs. When the gas from the pulsed valve reaches the electrodes, the discharge starts, resulting in the high voltage drop and current flow observed. A dim blue glow was observed at

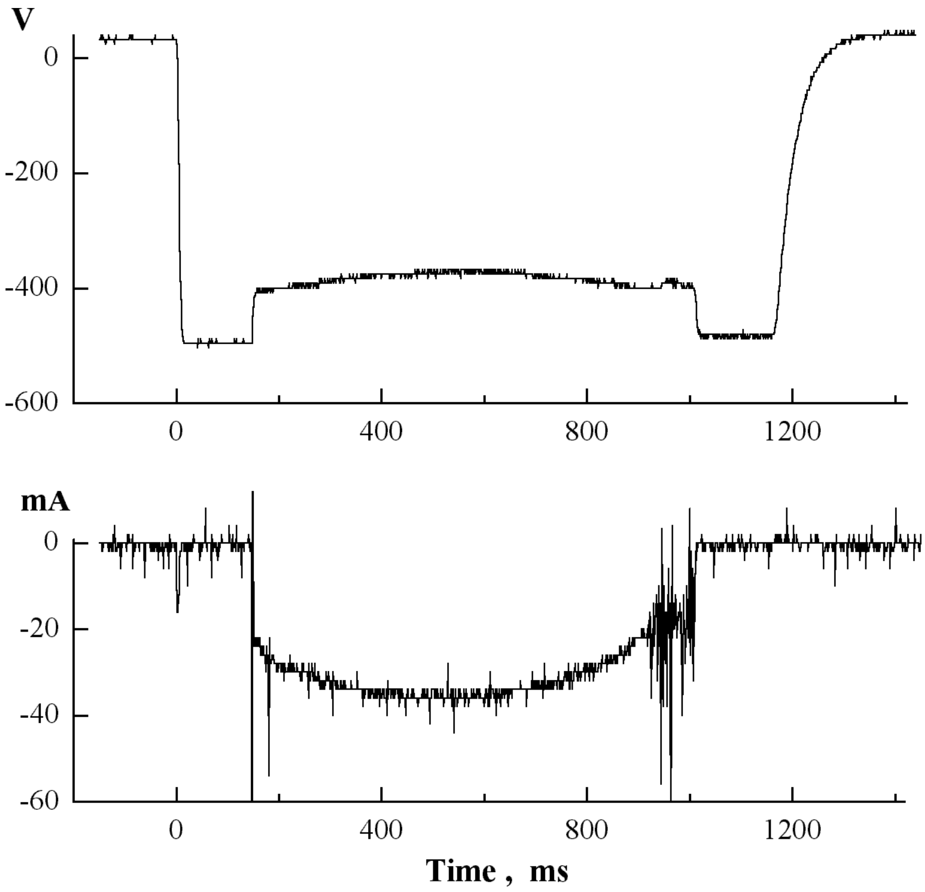

Figure 4.2: Pulsed nozzle discharge voltage and current profiles.

the discharge throat when plasma was expanding into the vacuum chamber of the mass spectrometer. Under these conditions, the discharge is stable and tracks the gas pulse well, as shown in the V(t) and I(t) curves in Figure 4.2.

In the case of an unstable discharge, the discharge start time would fluctuate significantly (by a few hundred microseconds). Sometimes, the discharge would not happen at all when it was 'poisoned' by the carbonaceous deposit inside the channel, or if the concentration of PAH molecules was too high. The latter would happen mostly for C_6H_6. In such cases, the discharge would occur mostly along the surface and not through the gas, resulting in large random spikes in the voltage and current profiles.

4.2.3 Protonation Mechanism and Efficiency

The protonation of PAHs has been performed in discharges with H_2 as the carrier gas ($P_{H_2} = 1 - 2.5$ atm) and a low concentration of PAH molecules (at their nominal vapor pressure for heated samples). Mass spectra for an anthracene discharge with He and H_2 as carrier gases are presented in Figure 4.3. In He, the discharge produced only anthracene cations (m/z = 178 a.m.u.), and the cation signal was relatively weak. However, when He was replaced with H_2, a cation signal with almost the same strength was produced, along with a new peak at (m/z = 179 a.m.u.) that is much stronger and corresponds to protonated anthracene. The intensity ratio for the protonated and cation mass peaks ranged from 1 : 1 to 20 : 1, with 8 : 1 being a typical value.

The protonation of PAH molecules in the hydrogen discharge was expected to happen through the mechanism of proton transfer from H_3^+ [3]:

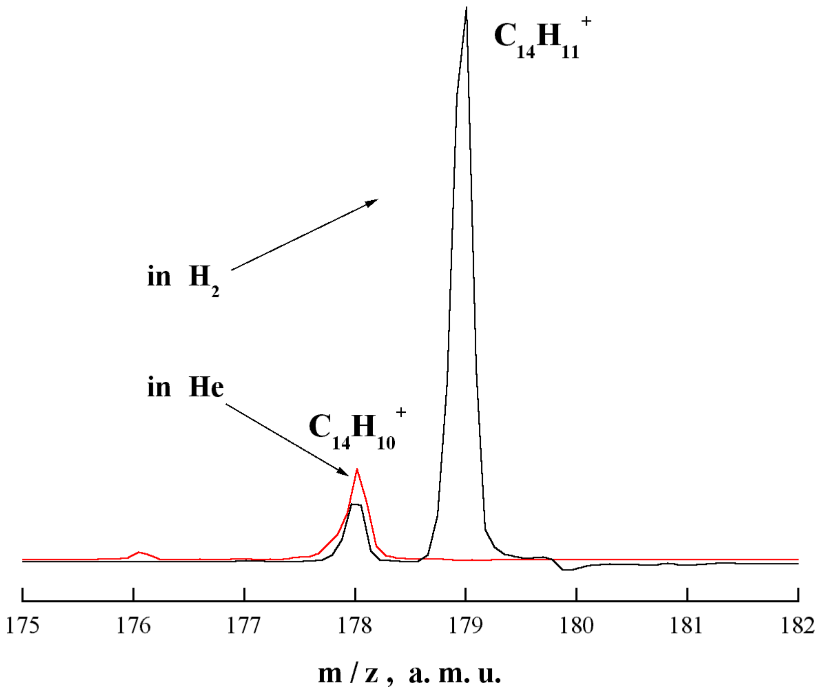

Figure 4.3: Mass spectra of anthracene and protonated anthracene in He *vs.* H_2 discharges.

$$\left\{\begin{aligned} & H_2 + e^- \longrightarrow H_2^+ + 2e^- \\ & H_2^+ + H_2 \longrightarrow H_3^+ + H \\ & H_3^+ + \text{PAH} \longrightarrow \text{H-PAH}^+ + H_2 \end{aligned}\right.$$

Indeed, in the mass spectrum of a pure H_2 discharge, the following mass peaks were observed: H^+, H_2^+ and H_3^+ (m/z = 1, 2 and 3 a.m.u. in Figure 4.4).

The threshold voltage for the discharge to start was –800–900 V in pure H_2. Whenever PAH molecules were added into the discharge, that value dropped to –530–560 V. Simultaneously, the H_3^+ peak disappeared from the mass spectrum. One explanation for this behavior would be that all the H_3^+ ions were scavenged by PAH molecules. However, a more realistic mechanism for PAH protonation is likely via PAH ionization by discharge electrons, followed either by association with H atoms or by PAH cation hydrogen abstraction from the H_2 carrier gas:

$$\begin{cases} \mathrm{PAH} + e^- \longrightarrow \mathrm{PAH}^+ + 2e^- \\ \mathrm{PAH}^+ + \mathrm{H} \longrightarrow \text{H-PAH}^+ \end{cases}$$

$$\begin{cases} \mathrm{PAH} + e^- \longrightarrow \mathrm{PAH}^+ + 2e^- \\ \mathrm{PAH}^+ + \mathrm{H}_2 \longrightarrow \text{H-PAH}^+ + \mathrm{H} \end{cases}$$

This would easily explain the threshold voltage drop, and the first process is known to be fast [75]. The second was not observed at room temperature due to a barrier in the hydrogen abstraction reaction, but may be possible at higher temperatures in the discharge, or with internal excitation of the PAH.

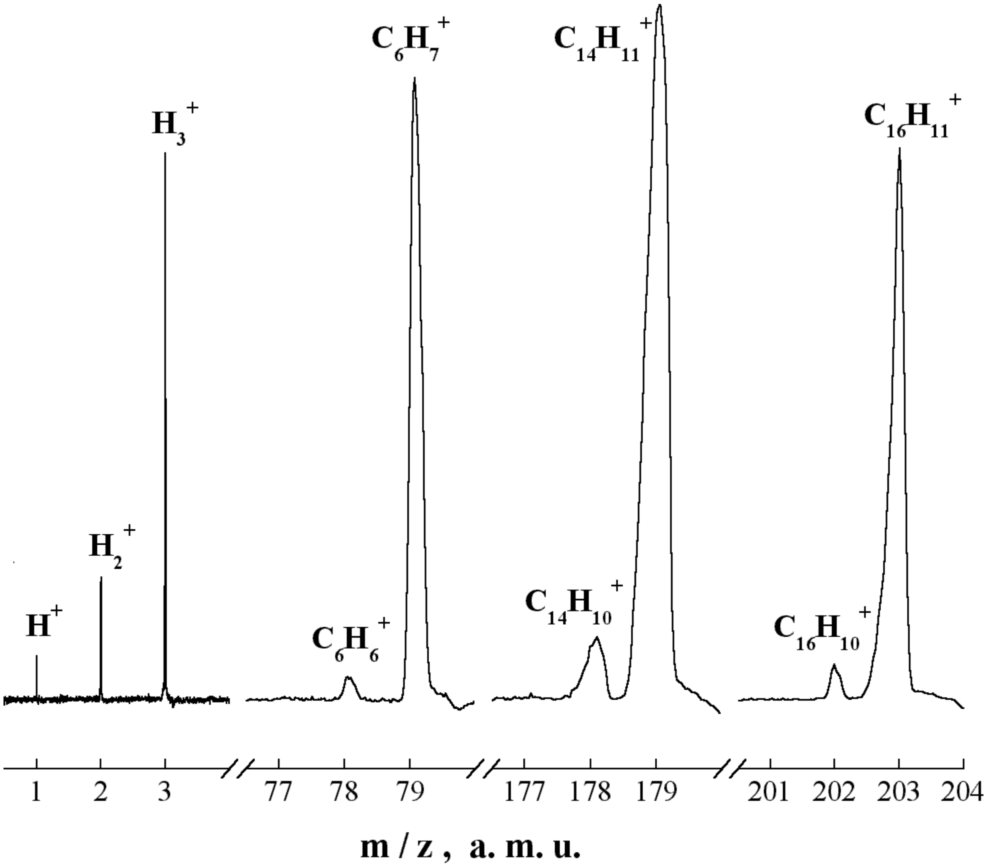

Figure 4.4: H_3^+ formation and the protonation of different aromatic molecules (benzene, anthracene and pyrene) in hydrogen discharges.

The protonation of benzene, anthracene and pyrene has been optimized in a discharge (Figure 4.4). In the case of anthracene and pyrene, ~5 – 10 g of the crystalline solid (Aldrich, 99% purity) was placed into an aluminium sample holder tube and connected to the pulsed valve with stainless steel tubing, with carrier gas (H_2) supplied to the tubing as well. The pulsed valve and sample holder were placed in thermal contact with, and heated by, electric heating cartridges. The stainless steel tubing was heated by heating tape wrapped around it. Temperatures were measured by K-type thermocouples and controlled by temperature controllers (Omega 7600CN). Typical temperatures used in the experiments were:

$$\mathrm{T_{sample}} = 130\ ^\circ\mathrm{C},\ \ \mathrm{T_{tubing}} = 137\ ^\circ\mathrm{C},\ \ \mathrm{T_{valve}} = 145\ ^\circ\mathrm{C}\ \ \text{for anthracene; and}$$

$$\mathrm{T_{sample}} = 168\ ^\circ\mathrm{C},\ \ \mathrm{T_{tubing}} = 174\ ^\circ\mathrm{C},\ \ \mathrm{T_{valve}} = 180\ ^\circ\mathrm{C}\ \ \text{for pyrene.}$$

The pulsed valve was kept 15 °C warmer than the sample to reduce sample recrystallization on the inside of the valve faceplate due to its cooling from the gas flow into vacuum.

For protonated benzene, ~10 – 20 mL of benzene were placed into a stainless steel container and hydrogen was bubbled though it. For such an operation, the high concentration of benzene sometimes caused discharge instability. To reduce this instability, the walls of the gas line tubing were passivated with benzene for ~10 minutes and then the bubbler was disconnected. The passivated benzene evaporated slowly and sustained a stable signal for 1 – 2 hours, after which the procedure was repeated.

The signal produced from protonated PAHs was quite strong. For example, 10^5 protonated anthracene ions per shot were estimated to be detected in the mass spectrometer. The high ion density led to noticeable broadening of mass peaks, thereby reducing the mass resolution. However, the deterioration of mass resolution was not an issue for the ions studied.

4.3 Cluster Source

4.3.1 Design

The cluster source used for making clusters of protonated anthracene with water consisted of the discharge source described above and another pulsed valve for delivering cluster partner molecules (Figure 4.5, see Appendix B, Figures B.3–B.10 for the drawings). The

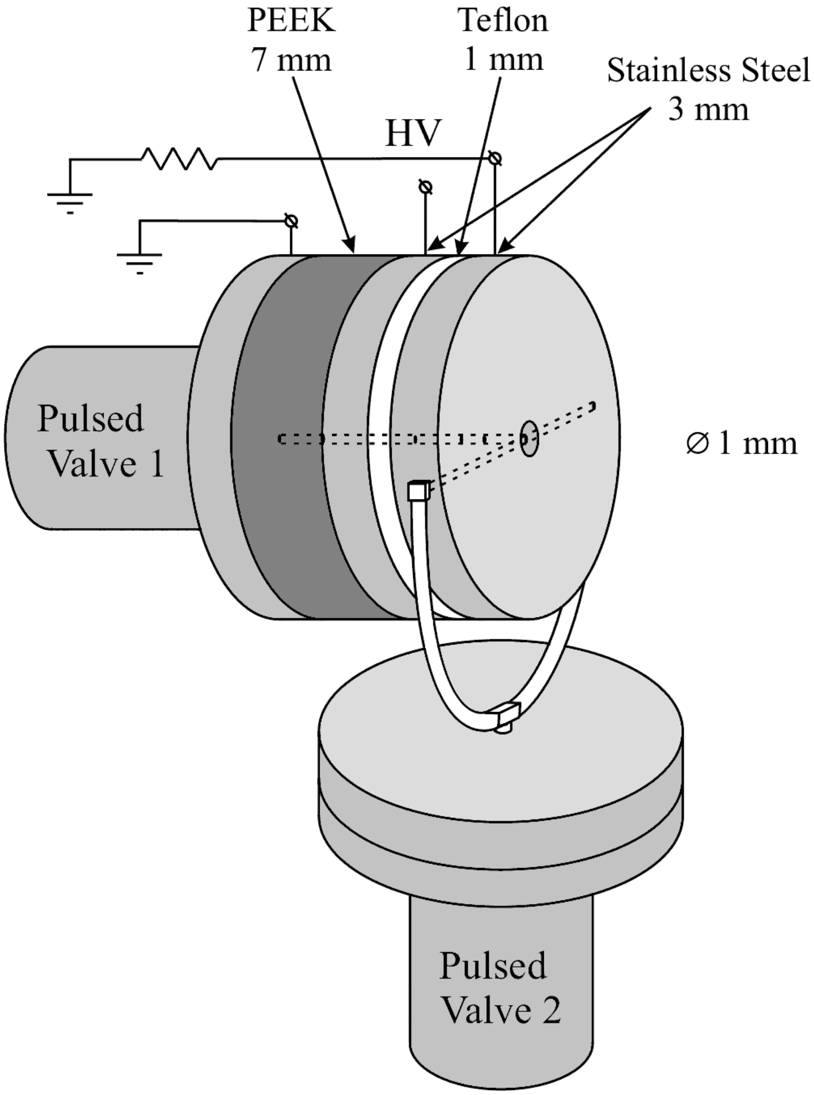

Figure 4.5: Pulsed discharge cluster source with two pulsed valves.

outside electrode of the discharge was modified to be 3 mm thick and had the same thickness in the middle and on the outside. A long 1.0 mm diameter channel was made in the middle of the electrode parallel to the disk plane, crossing the discharge channel at a right angle. The second valve was used for delivering atoms or molecules to create clusters at the discharge exit. Such a design was intended to prevent cluster partner molecules from entering the discharge. On the other hand, clustering occurs most efficiently in high gas pressure regions so clusters must be made at the discharge exit. In our case, PAH molecules are first protonated in the discharge, and as they are about to expand into vacuum, they collide with other molecules.

The second pulsed valve (Parker General Valve series 9) was placed as close as practical to the discharge. It had a faceplate adapter for a gas line. The adapter was equipped with a T-shaped nylon fitting. Similarly, the L-shaped elbow fittings were placed on the side ends of the discharge. Teflon tubing with a 1/16″ inner diameter connected the fittings in a 'stethoscope' configuration. When the valve was open, the gas would flow through that tubing and enter the discharge region symmetrically from the opposing sides, thus maintaining the pointing of the gas jet.

It should be pointed out that this source is different from another ion cluster mixing source [139], in which clusters of molecular anions with rare gas atoms are first formed in the high pressure expansion. Cluster ligands are then substituted with another molecule in a low pressure cell, filled by the opening of a second pulsed valve.

4.3.2 Operation

Both pulsed valves of the cluster source were operated at a 0.9 Hz repetition rate, limited by the pumping speed available in the mass spectrometer chamber. At higher repetition rates, the pressure in the flight tube of the time-of-flight mass spectrometer was above 10^{-6} Torr, which could potentially damage the MCP detectors. When photodissociation spectra of clusters were recorded, the laser had to be operated at 10 Hz. To reduce the operating repetition rate for the pulsed valves, a TTL frequency divider circuit (Appendix B, B.2.4) was used with a dividing ratio of 11 : 1.

The second pulsed valve must be opened before the discharge valve, since time is needed for the gas to reach the mixing region of the discharge. Delay times were optimized for the maximum cluster signal by 2–D scanning of the delays between the two pulsed valves, and between the valves and the ion extraction pulse in the mass spectrometer.

4.4 Mass Spectrometer

A Wiley-McLaren time-of-flight mass spectrometer (TOF MS) [140] with a reflectron [141, 142], manufactured by R.M.Jordan Co., was used to detect and analyze positive ions from the discharge (Figure 4.6). It was previously described in detail [143, 144]. The mass-spectrometer chamber consisted of three independently pumped regions for differential pumping. The first chamber was designed to house the pulsed valve, while the second chamber was designed for ion extraction. The skimmer between the first and second chambers was removed in order to move the discharge as close to the extraction ion optics as feasible. The ion optics were enclosed in an extension of a third chamber and were connected to the second chamber via a skimmer (Beam Dynamics, 1 mm diameter) from the discharge side and an orifice (8 mm diameter) on the opposite side to provide an exit for the molecular beam. The third chamber served as the field free ion flight tube. The reflectron was placed close to the end of the flight tube. Microchannel plate (MCP) detectors were placed at both ends of the flight tube to detect ions in the linear and reflectron operation modes of

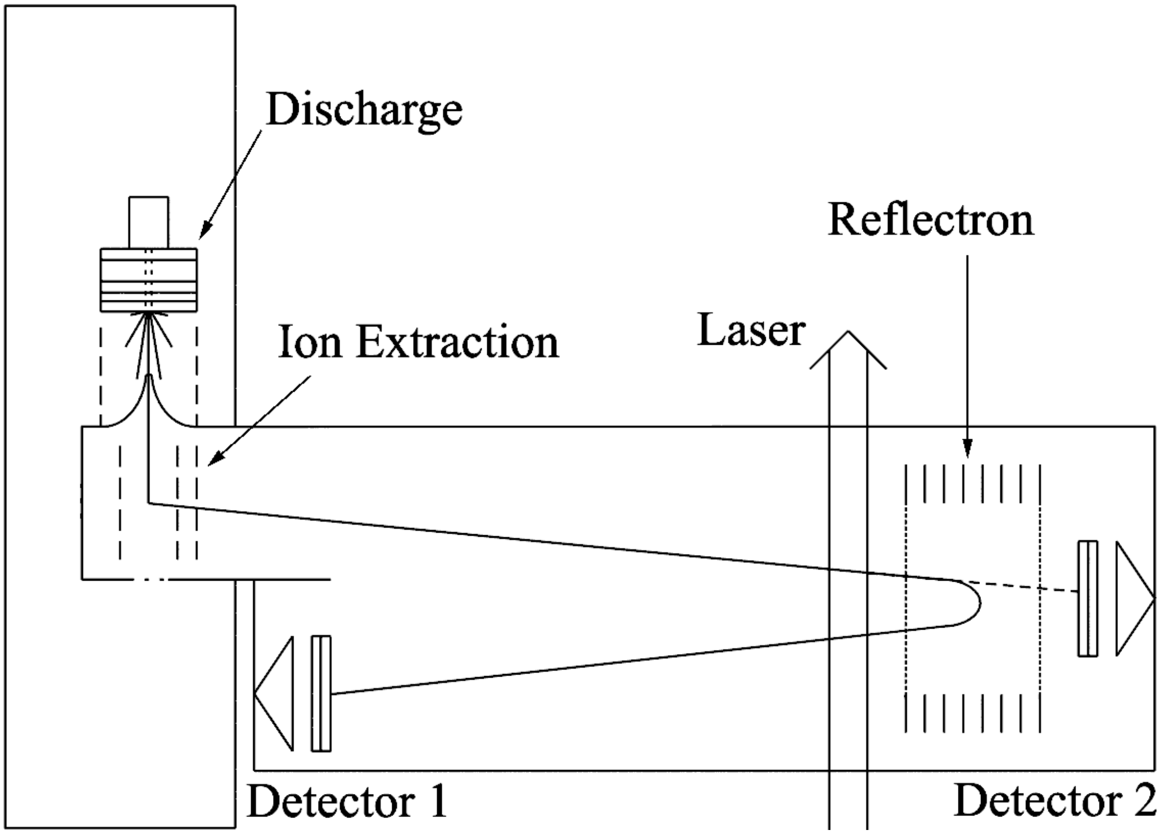

Figure 4.6: The time-of-flight mass spectrometer setup for photodissociation experiments (top view).

the mass-spectrometer.

4.4.1 Ion Shielding

Electrically neutral plasma exited the discharge at almost the thermal supersonic jet velocity, for which the kinetic energy of ions was estimated to be 0.1 eV. Special precautions had to be taken to protect such slow ions from any stray and static voltages inside the chamber.

The discharge source needed to be located as close to the skimmer as possible, and was placed 15 mm from the skimmer. A grounded wire mesh cylinder ($1.3''$ diameter) was placed around the supersonic jet along its path to the skimmer. Wires that delivered high voltage to ion optics were ground shielded whenever possible.

All of these measures were not enough, however, since the discharge plasma was creating surface charges on the skimmer and mesh surfaces. To improve the conductivity of the metal surfaces, the face of the discharge source, the skimmer, and the wire mesh were coated with carbon black film (Acheson Aquadag paste dissolved in acetone). This improved the detected ion signal dramatically and enabled ion extraction from any part of the discharge pulse.

4.4.2 Ion Extraction

Positively charged ions were pushed by a repeller grid A_1 (at 3150 V) to an extraction grid A_2 (at 2850 V), and then accelerated to the grounded grid in the direction perpendicular to the molecular beam. An Eisnel lens (at 120 V) was used to focus the ion beam, while two XY deflector plates (typically, at 75 – 120 V) were used to accelerate ions in the horizontal direction parallel to the molecular beam to guide the ion beam onto the MCPs.

When the mass spectrometer was operated in the linear mode, the reflectron was kept at ground potential. In the reflectron mode, reflectron voltages were set to 1900 V and 3300 V, respectively. Voltages on the repeller and the extractor could be static when working with a neutral molecular beam and creating ions by photoionization. When working with ions created in the discharge source, these grids must first be grounded to allow unaccelerated plasma to enter the space between the repeller and the extractor. High voltages must then be applied simultaneously to these grids by a two-channel pulser, described in Appendix B, B.2.3.

High voltages for the ion optics and reflectron MCP detector were provided by a R.M.Jordan AREF power supply (5 kV, 1 mA maximum), for the Eisnel lens by a Hewlett–

Packard 6525A power supply, and for the linear MCP detector by a Stanford Research Systems PS325 power supply, equipped with a voltage divider.

4.4.3 Reflectron Mode

The mass spectrometer was operated in the reflectron mode when photodissociation experiments were performed for two reasons. First, the reflectron helped to improve the mass resolution. For example, the TOF peaks from anthracene cation (178 a.m.u.) and protonated anthracene (179 a.m.u.) produced in the discharge were only partially resolved in the linear mode. In the reflectron mode, they were separated by at least the peak's full width at half maximum (Figure 4.4). The mass resolution in the mass spectrometer depended on the ion density and was lower for ions created by the discharge as compared to the photoionization. When the cluster discharge source was used for making ions, the ion density was lower and the mass resolution was therefore higher.

Second, the use of the reflectron in the photodissociation experiment gave the ability to monitor both parent ion signal depletion and neutral product formation. In the absence of the laser beam, all ions were turned by the reflectron to the reflectron MCP (detector 1). In the photodissociation experiment, the laser beam intercepted the ions before they entered the reflectron. When the ions absorbed laser radiation and dissociated, at least one ion and one neutral product were formed. The ions would still be turned by the reflectron, but the neutral photodissociation product would strike the linear MCP (detector 2). The depletion of the parent ion peak and possibly, the formation of the ion product would be observed with the reflectron detector. The signal-to-noise ratio on detector 1 was fairly poor, since the low dissociation yields could be buried in the intensity fluctuations of the parent ion peak.

On the other hand, the neutral product channel provided a good alternative to ion channel detection. The velocity of the neutral product would be close to the original velocity of the parent ion which had ∼3.0 keV kinetic energy. Thus, the neutral product retained sufficient kinetic energy to produce a measurable signal on the linear detector. Unlike the signal on the reflectron detector, the neutral product signal had very little background and thus a much better signal-to-noise ratio.

4.4.4 Detectors

Each TOF MS detector consisted of two stacked Galileo MCPs. The diameter of the MCPs was 25 mm for the linear detector and 50 mm for the reflectron detector. The gain was regulated by applying up to 1000 V voltage to each MCP. The signal was collected by a conical electrode and sent to a preamplifier. The amplified signal was read by a digital oscilloscope. An EG&G ORTEC 9301 fast preamplifier (gain 10, ±0.7 V output range) was used with the linear detector, while an EG&G ORTEC VT120C fast-timing preamplifier (gain 20, 0 to –5 V output range) was used with the reflectron detector.

4.4.5 Vacuum System

The first chamber was pumped by a 10″ Varian VHS–10 diffusion pump (Dow Corning 705 oil); the second chamber was pumped by a 6″ Varian VHS–6 diffusion pump (Santovac–5 oil); and the flight tube was equipped with a 4″ Edwards Diffstack 100 diffusion pump (Santovac–5 oil). The 10″ and 6″ pumps were baffled by water-cooled baffles, and the 4″ pump had a built-in baffle. Each pump had gate valves on both the intake and exhaust ports. The diffusion pumps were backed by an Edwards EM2-275 mechanical pump.

The pressure in the TOF MS chambers was measured by three MKS cold cathode pressure gauges, and the backing pressure was measured by a MKS Pirani pressure gauge. With the pulsed valves off, the residual pressure in the chambers was $5{\cdot}10^{-6}$ Torr, $3{\cdot}10^{-7}$ and $2{\cdot}10^{-8}$ Torr, respectively. The backing pressure was $2{\cdot}10^{-3}$ Torr. With the pulsed valve on, the pressure in the second chamber was $6{\cdot}10^{-5}$ Torr and in the flight tube $1{\cdot}10^{-6}$ Torr. Under operating conditions the backing pressure rose to $6{\cdot}10^{-3}$ – $1{\cdot}10^{-2}$ Torr.

The diffusion pump cooling water was supplied by a closed loop Neslab Coolflow System II Liquid/Liquid recirculator. The mechanical pump was cooled by a Neslab Coolflow CFT–75 refrigerated recirculator.

The system was equipped with an interlock circuit (Appendix B in [143]) that was used to monitor the water flow through diffusion pumps and the backing pressure (set to be below 0.1 Torr). When tripped, it would turn off diffusion pump heaters, close pneumatic gate valves between mass spectrometer chambers and diffusion pumps, and turn off the high voltage power supplies connected to the ion optics and MCP detectors.

4.5 Laser Systems

4.5.1 Excimer Laser

A Lambda Physik LPX–120i excimer laser with NovaTube technology was used to generate UV radiation at 193 and 248 nm. The maximum pulse energy was 200 mJ for a 25 × 9 mm beam. The beam was passed through a 9 mm pinhole, retaining 25% of the original pulse energy, then guided with a system of 193 nm dielectric-coated mirrors into the TOF MS chamber. The size of the clipped, unfocused beam inside the flight tube was set to 10 × 15 mm for better spatial overlap with the ion cloud. The pulse energy was adjusted by the discharge voltage in the laser. The laser was triggered externally and synchronized with the pulsed valve.

A mixture of 0.22% F_2, 8.33% Ar, 4.12% He and 87.33% Ne at a total pressure of 3000 mbar was used to produce $\lambda = 193$ nm, while the $\lambda = 248$ nm pulses were produced in a mixture of 0.19% F_2, 4.84% Kr, 3.68% He and 91.29% Ne at the total pressure of 3300 mbar.

4.5.2 Nd:YAG Lasers

Two nanosecond Nd:YAG lasers were used to pump the OPOs. Both lasers were triggered by an external delay generator to provide synchronization with the experiment. The first, a Coherent Infinity 40–100, had a 4.5 ns long pulse and a singe mode beam profile ∼5 mm in diameter. Its frequency was tripled to 355 nm and operated at the maximum energy of 225 mJ/pulse at the fundamental wavelength (1064 nm) to yield 100 mJ/pulse in the third harmonic. The repetition rate of the laser could be adjusted from 0.1 to 100 Hz at 0.1 Hz increments without significant change in the beam profile or pulse energy.

The second Nd:YAG laser, a Spectra–Physics Quanta–Ray GCR–16S, had a 12 ns long pulse and a beam ∼7 mm in diameter. The maximum used pulse energy in the third harmonic (355 nm) was 135 mJ. Although the laser repetition rate could be adjusted from 0 – 15 Hz, the optimal frequency was 10 Hz. The pulse energy would drop noticeably when the repetition rate was changed more than ±1 Hz from that value due to variations in thermal lensing.

4.5.3 BBO Type II OPO

A simple type II β–BaB_2O_4 (BBO) optical parametric oscillator (OPO) described in detail previously [144–146] was used to perform some initial experiments. Two identical

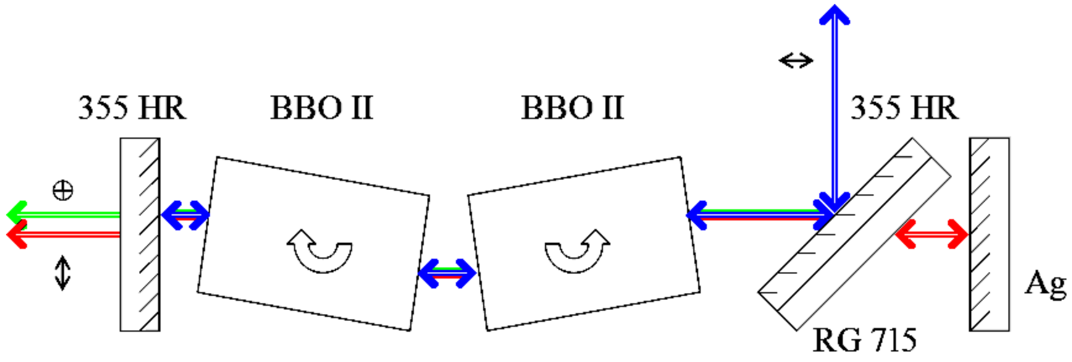

Figure 4.7: A top view of the BBO type II OPO.

type II BBO crystals (6.3 × 12.2 × 12.1 mm, $\Theta = 36°$, $\phi = 45°$) were used in the counter-rotating configuration (Figure 4.7). The OPO cavity, formed by a silver-coated mirror and an output coupler coated with a 355 nm high reflective (HR) coating, was pumped at 30° by the third harmonic of the Coherent Infinity Nd:YAG laser. A long wavelength pass filter (Schott Glass Technologies, RG715) behind a 45° 355 nm HR mirror was used to absorb the visible (signal) wave, but allowed the IR (idler) wave to resonate.

The working wavelength range for the signal wave was 418 – 630 nm. When it was necessary to employ tunable UV radiation, the signal beam was frequency-doubled in a type I BBO crystal (10.0 × 7.0 × 6.1 mm, $\Theta = 56°$, $\phi = 0°$). A Pellin–Broca fused silica prism was used to separate the second harmonic beam from the rest (signal, idler and residual pump). The usable wavelength range for the second harmonic (at least 0.2 mJ/pulse) was 212 – 280 nm.

Both OPO crystals, the second harmonic crystal, and the prism were placed on rotation stages driven by Newport 850F series linear actuators, controlled by the BGSpecT software (Appendix C) via Precision MicroControl DCX–PC100 or DC2–PC100 motion control boards.

4.6 Hybrid BBO OPO with a Rotated Prism Cavity

The OPO described above is robust and simple in operation, but it has a few drawbacks. Most significantly, the OPO conversion efficiency is low when approaching the degeneracy point (2λ or 710 nm for 355 nm pumped OPOs). Indeed, very little or no energy is produced by the type II OPO in the $640 - 800$ nm wavelength range. This problem is due to the optical properties of the type II BBO crystals and could, in principle, be solved by replacing the type II BBO with some other crystals – for example, a type I BBO – but doing so would generate new problems.

Another issue is the beam shape. In the blue part of the signal spectrum (420 – 460 nm), the beam is nicely round. At longer wavelengths, however, the beam divergence increases in the non-dispersive direction and the beam profile elongates up to a $7:1$ aspect ratio. This problem is inherent to such a simple cavity design. To circumvent this behavior, image-rotating OPO cavities have recently been implemented [147,148] that incorporate prisms to rotate the image and waveplates to compensate for the phase mismatch introduced. These image-rotating cavities produce beams of nearly round shape, even at wavelengths where the non-rotating cavities have highly elongated beam profiles. The cavity design in [147] is similar to the simple type II BBO OPO (4.5.3) in that it is also a 355 nm pumped type II BBO OPO with only one crystal. It utilizes the same double pass pump scheme, but instead of the metal-coated mirror, it uses a right angle prism rotated at $\alpha = 45^\circ$ in a back reflector geometry. A $\lambda/2$ waveplate was placed into the cavity to maintain the polarization of the signal wave. Such a design solves the beam profile issue, but not the efficiency around the degeneracy point. In addition, the waveplate has to be rotated as the wavelength is tuned.

To further improve the performance of the OPO, the cavity of the simple type II BBO

OPO was modified as described below.

4.6.1 New Cavity Design

The new cavity design is shown in Figure 4.8. In a similar fashion to the image-rotating cavity [147], the metal-coated mirror in the old cavity was replaced with a fused silica right angle prism. The difference was that the back sides of the prism were coated with aluminium to change the phase rotating properties of the prism. Two BBO crystals were used in the new OPO: one type II and one type I. No waveplates were used and the long wavelengths pass filter was retained to resonate the idler.

The new design may at first seem to be not very logical, but in fact, it has some advantages. Let us take a closer look at its operating principles.

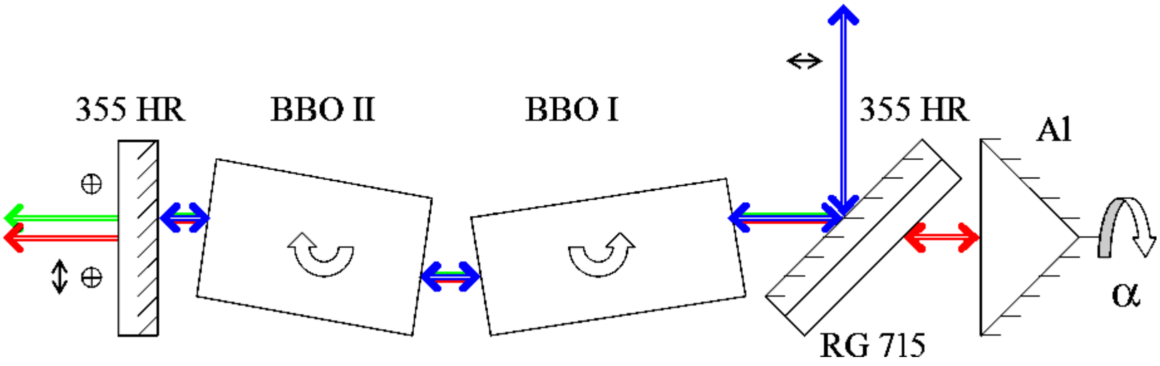

Figure 4.8: A top view of the BBO type I and II hybrid OPO with rotated prism cavity.

4.6.2 Phase Matching

The prism in the cavity introduces a new phase delay to the idler wave. When only the geometric image rotation is considered (Figure 4.9), the general expression for the wave polarization of the original S and P polarized light during prism rotation by α degrees is:

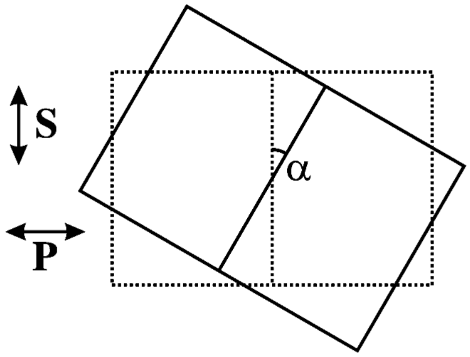

Figure 4.9: A rotated right angle prism.

$$\text{Polarization Rotation} = \begin{cases} 90^\circ(1 + cos(2\alpha)) & , \quad \text{for P polarization} \\ 90^\circ(1 - cos(2\alpha)) & , \quad \text{for S polarization} \end{cases}$$

If the prism is not rotated (its 90° angle edge is parallel to the crystal rotation axis), the image is mirrored in the vertical plane. When the prism is rotated 90°, the image is mirrored in the horizontal plane. At $\alpha = 45^\circ$, both the S and P polarizations are rotated by 90°.

Another factor is the phase delay due to reflections on the prism surfaces. This delay is zero for the non-coated prism and 180° per each internal reflection for the metal coated prism. Delays from the prism refractive index wavelength dependence must also be considered. The overall phase change due to these factors combined is shown in Figure 4.10 for the example of an Al-coated BK–7 glass right angle prism. In the operational range of the OPO, the delay for P polarization is 335 – 350 degrees, which is close to the needed 360° phase shift. For S polarization, it is close to 180 degrees (mirror imaging).

When the prism is rotated by $\alpha = 45^\circ$, the net effect is a 90° polarization rotation with almost complete phase matching. It it possible to achieve better phase matching by slightly rotating the prism. Thus, there is no need for the waveplate. The analysis would change if

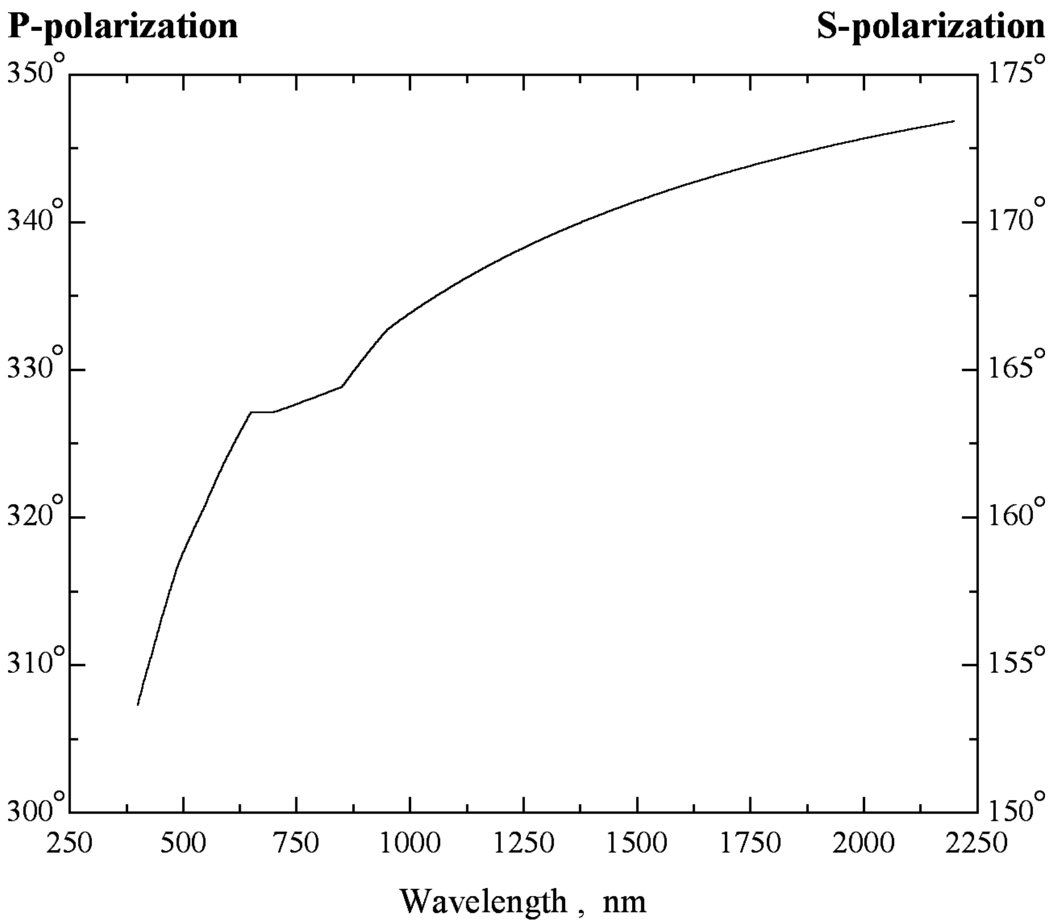

Figure 4.10: The additional phase delay caused by an Al-coated BK–7 right angle prism. Calculated by Foreal Spectrum Co.

the prism were not coated or if the signal wave was resonated.

A polarization rotation of 90° makes the wave unusable for the next pass through the *same* crystal. This may be circumvented by the careful selection of OPO crystals, as described next.

4.6.3 The Choice of Crystals

Crystals used in OPOs must be able to match the group velocities for the pump and signal/idler waves. This is easily achieved in birefringent crystals. For the radiation propagating in such crystals, the polarization has two components (Figure 4.11). The ordinary

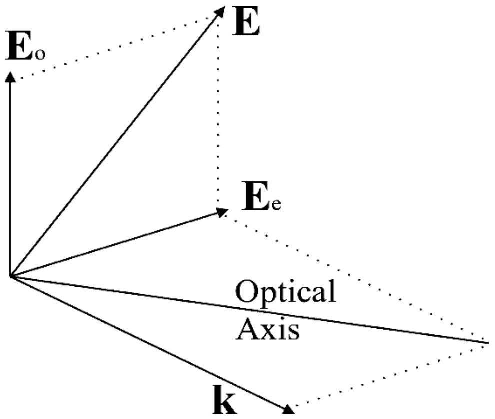

Figure 4.11: Light polarizations in a birefringent nonlinear crystal.

polarization is normal to the plane, formed by the light k–vector and the crystal optical axis, and the extraordinary polarization is in that plane. The refractive index of the ordinary wave does not depend on the angle between the k–vector and the optical axis, but the refractive index of the extraordinary wave does depend on it.

The proper OPO polarizations for BBO crystals are shown in Table 4.1. For both type I and type II BBO, the signal wave polarization is perpendicular to the pump wave polarization, but the idler polarization varies with the crystal type – a fact we exploit in our image/polarization rotating cavity. For the old, non-rotating cavity, the best performance could be achieved only when crystals of the same type are used. For the rotated prism OPO, however, when there are crystals of both types in the cavity, the idler polarization is rotated after each pass and is sequentially amplified by one of the crystals.

Table 4.1: OPO wave polarizations for BBO type I and II crystals.

Wave	BBO I	BBO II
Pump	e	e
Signal	o	o
Idler	o	e

This new OPO, with both BBO type I and type II crystals housed in the cavity, inherits many of the advantages of each crystal. BBO type I, for example, has better performance around the degeneracy point and a better overall conversion efficiency compared to type II crystals. Hence, in our cavity it serves as the main amplifying crystal. Alternatively, BBO type II has higher $d\lambda/d\Theta$, which means a smaller acceptance angle and narrower bandwidth. In our cavity it therefore serves as a bandpass filter for the type I crystal.

Thus, the new cavity is expected to have a much better beam profile (due to the image rotation by the prism) with as good a linewidth as the old BBO type II only OPO (BBO type II filtering), much better performance around the degeneracy point, and perhaps, higher pulse energy (BBO type I gain).

4.6.4 Hybrid Cavity Performance

The performance of the new OPO has been characterized for $\alpha \simeq 45°$ rotation of the prism. The beam shape in the blue part of the signal wave spectrum is unchanged and circular. In the red part of the signal spectrum, the beam has a shape of the cross with nearly all of the energy concentrated in a small spot at the center of the beam (Figure 4.12). This is similar to the beam shapes from other image-rotating cavities. The measured beam divergence is ≤ 3 mrad at 2 m.

The signal wave was linearly polarized in the direction perpendicular to the pump polarization, which is the same as in the old cavity. The idler wave, however, was elliptically polarized. Thus, the efficiency of the OPO depended on the prism rotation angle α. When it was set to exactly 45°, the pulse energy dependence *vs.* wavelength was similar to the old BBO type II cavity. The pulse energy maximized at 435 nm and steadily dropped as the wavelength was tuned to the red. This behavior most likely resulted from incomplete phase matching. To alleviate this problem, the prism was rotated to $\alpha \simeq 30 - 35°$, which

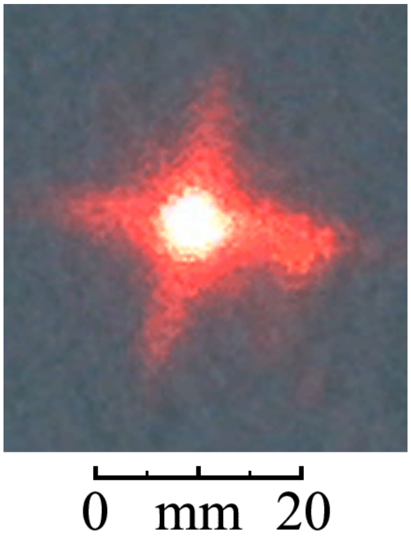

Figure 4.12: Beam shape for the mixed BBO type I and II prism cavity OPO.

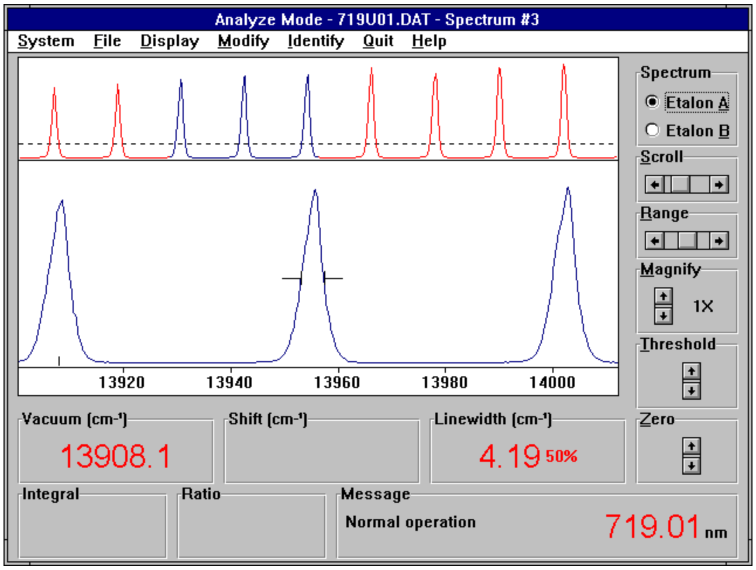

Vacuum (cm-¹): 13908.1

Linewidth (cm-¹): 4.19 50%

Message: Normal operation

719.01 nm

Figure 4.13: Hybrid cavity OPO wavemeter reading at $\lambda_{\text{idler}} = 719$ nm.

drastically improved the efficiency near the degeneracy point. Indeed, tuning to signal wavelengths as long as 710 nm was straightforward, with good efficiency in both the signal and idler beams. Furthermore, the linewidth did not deteriorate significantly around the degeneracy point as is seen in type I OPOs. The idler wave linewidth at 719 nm was ~4 cm^{-1} (Figure 4.13), for example, which is close to the 2 – 3 cm^{-1} measured for the signal wave linewidth far from the degeneracy point.

4.7 Other Hardware

The wavelength of the OPO signal wave was measured by a Burleigh WA–4500 pulsed wavemeter in order to calibrate the OPOs. The OPO linewidth was measured by a Burleigh PLSA–3500 pulsed laser spectrum analyzer.

The OPO pulse energy was measured by a Newport model 818J–25 pyroelectric energy meter detector. Pulse energies of the excimer laser and Nd:YAG lasers were measured by a Newport model 818T–150 high power thermopile detector. The outputs of both detectors were read with a Newport model 1825–C power/energy meter.

Two Stanford Research Systems DG535 pulse/delay generators were used to trigger all devices used in the experiments and to set the appropriate delay times. All delay generator parameters could be controlled from a PC via a GPIB interface.

A GaGe CompuScope 85G digital oscilloscope PC plug-in card was used to read the signal from both mass spectrometer detectors. A GaGe CompuScope 1450 digital oscilloscope card was used to read the signal from the pyroelectric detector that measured the OPO pulse energy. Both cards were plugged into PCI slots of a personal computer and were controlled by software described at length in Appendix C. A Tektronix TDS 210 digital oscilloscope was used to monitor the discharge voltage and current profiles, and was accessible from a PC via a GPIB interface.

4.8 Data Acquisition

The data acquisition for all experiments was conducted by the PC that also controlled all necessary devices. The following was installed in the PC: both GaGe oscilloscope cards, a National Instruments PCI–GPIB card for remote control of GPIB devices, and a Precision MicroControl DCX-PC100 card for OPO wavelength tuning.

Software written for these experiments remotely controlled both delay generators and laser delays, read out the TOF mass spectra and OPO pulse energy traces from oscilloscopes, and analyzed the data, saving the spectrum to a file on the PC hard drive.

4.8.1 Blake Group Spectroscopy Tools Software

The Blake Group Spectroscopy Tools (BGSpecT) is designed to be a multipurpose spectrometer software package. For flexibility, it has a modular structure. On the device module level it performs the remote control (GPIB, RS232, PC plug-in cards) of numerous devices that are used in the experiment. For example, when scanning a spectrum, BGSpecT tunes the laser wavelength and reads the signal from a digital oscilloscope. A separate spectrometer module uses the device modules to perform the actual scan. The advantage of such a system is that the spectrometer module does not need to know any device-specific commands (differences between the models of the same device type, etc.) since it works at a higher software level. Thus, the spectrometer module can be used for different experiments simply by changing the software configuration, but not the code behind it.

The device modules may be used to control devices independently, almost as if the user was turning knobs on the device itself. In addition, they allow communication with multiple devices of the same kind. For example, reading the waveforms from multiple 2-channel oscilloscopes simultaneously is essentially the same as reading them from one 4- or

8-channel oscilloscope. In some cases, this helps to conduct affordable experiments with the existing equipment.

BGSpecT is written and compiled in Microsoft Visual Basic. When the modules were first coded, the available computers were slow and there was a noticeable speed difference between software designed in LabView and Basic or C++. Nowadays, the bottleneck is usually in the speed of the experiment itself or the data transfer from the device to the computer. Historically, Visual Basic was used to ensure interoperability with other software developed by the group.

4.8.2 Choice of Delay Times

It was important to carefully select delay times for experimental synchronization. First, since protonation was performed in a hydrogen discharge (4.2), it was necessary to adjust the delay time between the valve opening (discharge start) and ion extraction to maximize the intensity of the protonated ion peak. The long term stability of this signal was ensured by first 'seasoning' the discharge for 0.5 – 1 hour. Usually, ions produced in the beginning of the discharge were used. The ion beam was then intercepted with an intense pulse from the excimer laser ($\lambda = 193$ nm, E = 25 – 35 mJ/pulse, 10×15 mm spot size) to dissociate the molecular ions. The delay time for the excimer laser was adjusted to maximize the photodissociation of ions of a selected mass, usually protonated PAHs. This delay then was fixed.

When an OPO was used to scan the spectrum, the delay time for the OPO pump Nd:YAG laser was adjusted for optimum temporal overlap with the excimer pulse as measured by a fast photodiode.

During the spectral scan, the ion signal without the laser was collected as well, nearly in real time. For each OPO wavelength, the MCP signals with the laser was acquired. The laser delay time was then increased by more than 50 μs (longer than the mass spectrum time range) and the 'background' signal was acquired. Finally, the laser delay was returned to its original position.

Typical delay generator parameters were:

Delay generator #1. Internal triggering mode at 5 Hz rate.

$$\left\{\begin{array}{lll}
\mathrm{T}_0 & = 0\ \mu\mathrm{s} & ,\ \text{open pulsed valve (400 }\mu\text{s)} \\
\mathrm{A} & = \mathrm{T}_0 + 320.00\ \mu\mathrm{s} & ,\ \text{turn discharge On; trigger delay generator \#2;} \\
 & & \ \ \text{trigger Tektronix TDS 210 oscilloscope (discharge monitor)} \\
\mathrm{B} & = \mathrm{A} + 460.00\ \mu\mathrm{s} & ,\ \text{turn discharge Off} \\
\mathrm{C} & = \mathrm{D} - 260.00\ \mu\mathrm{s} & ,\ \text{turn Coherent Infinity Nd:YAG lamp On} \\
\mathrm{D} & = \mathrm{A} + 198.61\ \mu\mathrm{s} & ,\ \text{turn Coherent Infinity Nd:YAG Q-switch On (OPO);} \\
 & & \ \ \text{trigger GaGe CS 1450 oscilloscope (OPO pulse energy)}
\end{array}\right.$$

Delay generator #2. External triggering mode, triggered by delay generator #1.

$$\left\{\begin{array}{lll}
\mathrm{T}_0 & = 0\ \mu\mathrm{s} & \text{– from DG \#1, line A} \\
\mathrm{A} & = \mathrm{B} - 1.09\ \mu\mathrm{s} & ,\ \text{trigger Lambda Physik excimer laser} \\
\mathrm{B} & = \mathrm{C} + 18.54\ \mu\mathrm{s} & ,\ \text{actual excimer pulse produced, for protonated anthracene} \\
 & \phantom{= \mathrm{C} +\ } 20.13\ \mu\mathrm{s} & ,\ \phantom{\text{actual excimer pulse produced, }}\text{for protonated pyrene} \\
 & \phantom{= \mathrm{C} +\ } 12.56\ \mu\mathrm{s} & ,\ \phantom{\text{actual excimer pulse produced, }}\text{for protonated benzene} \\
\mathrm{C} & = \mathrm{T}_0 + 180.00\ \mu\mathrm{s} & ,\ \text{TOF MS ion extraction pulse On (7 }\mu\text{s)} \\
\mathrm{D} & = \mathrm{C} + 0.35\ \mu\mathrm{s} & ,\ \text{trigger GaGe CS 85G oscilloscope (TOF MS spectra)}
\end{array}\right.$$

When the cluster discharge source was used (4.3), there was an additional pulsed valve to trigger. In that case, typical delay times were:

Delay generator #1. Internal triggering mode at 10 Hz rate.

$$\begin{cases} \mathrm{T}_0 & = 0\ \mu\mathrm{s} & \text{, send to TTL frequency divider, to trigger delay generator \#2} \\ \mathrm{A} & = \mathrm{B} - 0.95\ \mu\mathrm{s} & \text{, trigger Lambda Physik excimer laser} \\ \mathrm{B} & = \mathrm{D} + 0.47\ \mu\mathrm{s} & \text{, actual excimer pulse produced} \\ \mathrm{C} & = \mathrm{D} - 120.00\ \mu\mathrm{s} & \text{, turn Spectra–Physics GCR Nd:YAG lamp On} \\ \mathrm{D} & = \mathrm{T}_0 + 789.44\ \mu\mathrm{s} & \text{, turn Spectra–Physics GCR Nd:YAG Q-switch On (OPO)} \end{cases}$$

Delay generator #2. External triggering mode, triggered by TTL frequency divider at 0.91 (10/11) Hz.

$$\begin{cases} \mathrm{T}_0 & = 0\ \mu\mathrm{s} & \text{, open } \mathrm{H_2O} \text{ pulsed valve (400 } \mu\text{s)} \\ \mathrm{A} & = \mathrm{T}_0 + 280.00\ \mu\mathrm{s} & \text{, open discharge pulsed valve (400 } \mu\text{s)} \\ \mathrm{B} & = \mathrm{C} + 240.00\ \mu\mathrm{s} & \text{, TOF MS ion extraction pulse On (7 } \mu\text{s);} \\ & & \text{trigger GaGe CS 1450 oscilloscope (OPO pulse energy)} \\ \mathrm{C} & = \mathrm{A} + 250.00\ \mu\mathrm{s} & \text{, turn discharge On (1200 } \mu\text{s);} \\ & & \text{trigger Tektronix TDS 210 oscilloscope (discharge monitor)} \\ \mathrm{D} & = \mathrm{B} + 0.35\ \mu\mathrm{s} & \text{, trigger GaGe CS 85G oscilloscope (TOF MS spectra)} \end{cases}$$

4.8.3 Data Analysis

Raw data were processed by the software as soon as it was acquired. After each discharge pulse, the oscilloscope traces were read by the software and then analyzed. For the mass spectra, there was always a mass peak produced by the discharge whose intensity could be monitored. For example, while recording the cluster photodissociation spectrum, the intensity of the protonated PAH peak was monitored. The dynamic range option from the Oscilloscope panel of BGSpecT was used to make sure that the intensity of the desired peak from each shot was within a user selected range. If the signal at that mass was too weak (too few ions) or too strong (saturated), all data from that shot were discarded. 'Good' traces were then averaged, typically up to 60 or 100 traces per wavelength. Averaged mass spectra were then baselined by subtracting a linear fit and saved onto the hard drive for the future analysis, if needed.

The signal for mass spectra was the area under a peak of selected mass. A few masses could be monitored simultaneously. For the OPO pulse energy, the signal was the difference between the maximum and the minimum of the pyroelectric detector signal.

The results were saved into an ASCII file with several columns: laser wavelength, laser pulse energy, and one column per each monitored mass peak. Two files were created: one for the data with the laser, and one without.

After the scan was completed, the data underwent further manual processing. For the neutral dissociation product peak, the value without the laser was subtracted from the value with the laser to improve the baselining. The parent ion and neutral product peaks were then normalized by the parent signal in the absence of the laser to adjust for long term discharge source intensity fluctuations, and then normalized by the OPO pulse energy to yield a final spectrum.

Chapter 5

Laser Dissociation of Protonated PAHs

5.1 Experiments

The photodissociation experiments were performed with protonated PAHs using different laser sources. The calculations from Chapter 3 indicated that it might be energetically feasible to dissociate protonated PAHs with visible/near UV photons from the OPO in one- or two-photon process. The original goal was therefore to measure visible electronic spectra of protonated PAHs by one-photon photodissociation. Thanks to the photostability of protonated PAHs described below, a combined excimer laser and OPO experiment has been performed to yield better results.

Most experiments were performed with protonated anthracene, and some with protonated pyrene and protonated benzene. Protonated anthracene was selected as the smallest protonated PAH molecule since it had a predicted absorption in the visible wavelength region, where 355 nm -pumped OPOs have several mJ of pulse energy. Protonated pyrene is heavier and has lower vapor pressure; therefore, it was the second molecule of choice. The S_2 state of protonated benzene lies within reach of frequency-doubled BBO OPOs and its spectrum, although broad, was measured previously [90]. The S_1 state of protonated benzene and protonated naphthalene, as well as neutral naphthalene, anthracene and pyrene, are all located between 300 – 400 nm and therefore, could not be accessed either by the fundamental or second harmonic of our OPO. It would be possible to generate such photons by sum frequency mixing of the OPO signal with the fundamental from the Nd:YAG laser (1064 nm) or by doubling a 532 nm pumped OPO, but neither of these methods has yet been implemented to extend the OPO wavelength range.

The single-valve hydrogen discharge source was used to protonate neutral aromatic molecules (Chapter 4, 4.2), and the delay times for the discharge and ion extraction were optimized to produce the maximum protonated ion signal. The laser delay time was then adjusted to selectively dissociate the protonated ions. The signals from both the reflectron (parent ion depletion) and linear (neutral product formation) detectors were recorded.

5.1.1 The Type II BBO OPO as a Laser Photodissociation Source

Our first attempt to the photodissociation spectrum of protonated anthracene used the signal (visible) beam from the BBO type II OPO (Chapter 4, 4.5.3). The wavelength range covered was 418 – 600 nm, with a of resolution 0.1 nm and a pulse energy from 0.3 to 5 mJ/pulse at the intersection with the ion beam. The laser beam was unfocused and had a round spot with diameter of 5 mm at $\lambda = 425$ nm and a 7×18 mm (vertical × horizontal) spot at $\lambda = 600$ nm.

No dissociation was observed for protonated anthracene. That is, the parent ion signal on the reflectron detector was within the fluctuation limits and the neutral products signal on the linear detector remained within the noise level. After this first attempt, the OPO signal beam was focused into the TOF MS chamber either into a dot with a spherical lens (fused silica, $f = 250$ mm), or into a horizontal line with a cylindrical lens (fused silica,

$f = 250$ mm) . Again, no dissociation was observed.

Finally, the OPO signal frequency was doubled (209 – 280 nm, with a resolution of 0.05 nm) to search for more highly excited states. Still, no dissociation was recorded for protonated anthracene, and a similar attempt to record the spectrum of the S_2 state of protonated benzene around 250 nm (as was found previously [90]) resulted in no observed dissociation.

5.1.2 Two-color Dissociation – OPO and Excimer Laser

The OPO scan demonstrated that more intense pulses may be needed to dissociate protonated PAHs on nanosecond timescales; therefore, the dissociation experiment was performed with pulses from two lasers. The idea was to perform $1 + 1'$ resonance-enhanced multiphoton dissociation. The first photon (1) from the OPO (visible wavelengths) would excite the protonated PAH ion electronically. Then, the second photon ($1'$) from the excimer laser ($\lambda = 193$ nm) would provide the additional energy needed to dissociate the excited ion. The excimer pulse energy was kept below ~10 mJ/pulse to ensure that the dissociation was produced by both lasers and not the excimer laser alone. The pulse duration for the OPO was ~2.5 – 3.5 ns while that for the excimer laser was 20 ns. The time delay between the two lasers was synchronized with a fast photodiode, and set either to have the OPO pulse arrive 1 ns ahead of the excimer pulse or during its maximum intensity. As in the case of the OPO only scans, the neutral fragment signal did not depend on the OPO wavelength and thus, no $1 + 1'$ protonated anthracene dissociation was observed.

5.1.3 Dissociation Yield with Excimer Laser

In order to better understand the lack of dissociation in the OPO and OPO with excimer experiments, additional high energy excimer studies at $\lambda = 193$ and 248 nm were performed on protonated anthracene, pyrene and benzene. Good depletion signals were observed once the delay time of the laser was set in order to dissociate ions of the appropriate mass. Typical mass spectra for protonated pyrene (Figure 5.2), protonated anthracene (Figure 5.1) and the neutral product from protonated anthracene (Figure 5.3) are shown below. Figure 5.4 demonstrates that the neutral product signal arises from protonated anthracene dissociation because it has the same flight time as the parent ion in the linear TOF MS mode. A strong and narrow peak was produced on the linear detector (neutral channel) by the excimer laser and was not RF induced (Figure 5.3). This peak was present even when there were no ions (that is, with the discharge turned off) and it moved in time when the laser delay was changed, but disappeared when the beam was blocked. No signal was produced by UV photons striking the reflectron detector or by visible photons on either detector.

The dependence of the dissociation yield on the UV pulse energy was measured for protonated anthracene and protonated pyrene by recording the signal at every laser intensity with the laser ON and OFF (blocked beam) for normalization purposes. The laser delay was chosen to maximize the depletion of the parent ion peak in the mass spectrum, and the signals from both reflectron and linear detectors were recorded. When the data were plotted, the curves for parent ion depletion and neutral products showed similar behavior, but the neutral products data were less noisy and therefore used in the subsequent analysis.

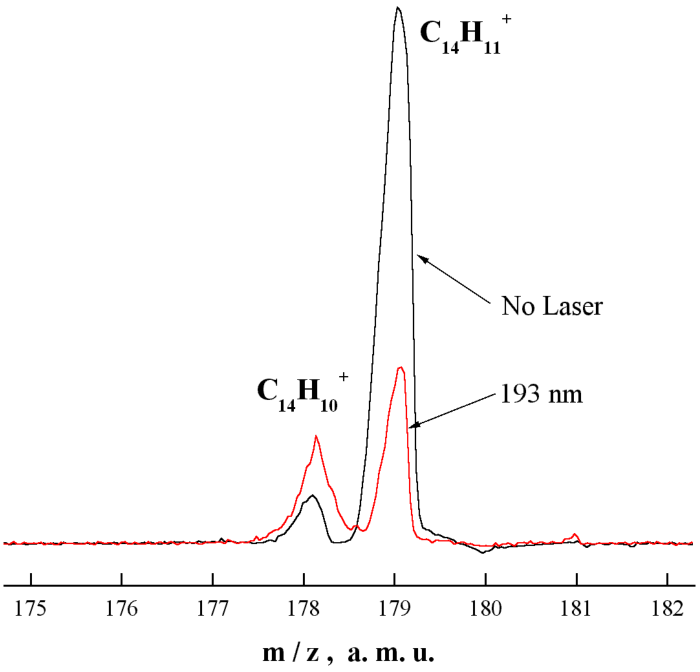

Figure 5.1: An ion channel mass spectrum of protonated anthracene photodissociation with $\lambda = 193$ nm excimer laser pulses.

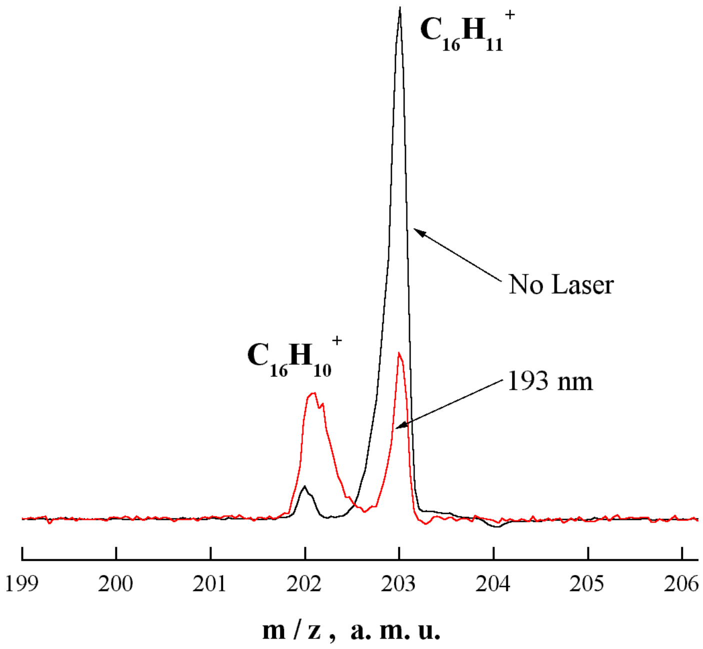

Figure 5.2: An ion channel mass spectrum of protonated pyrene photodissociation with $\lambda = 193$ nm excimer laser pulses.

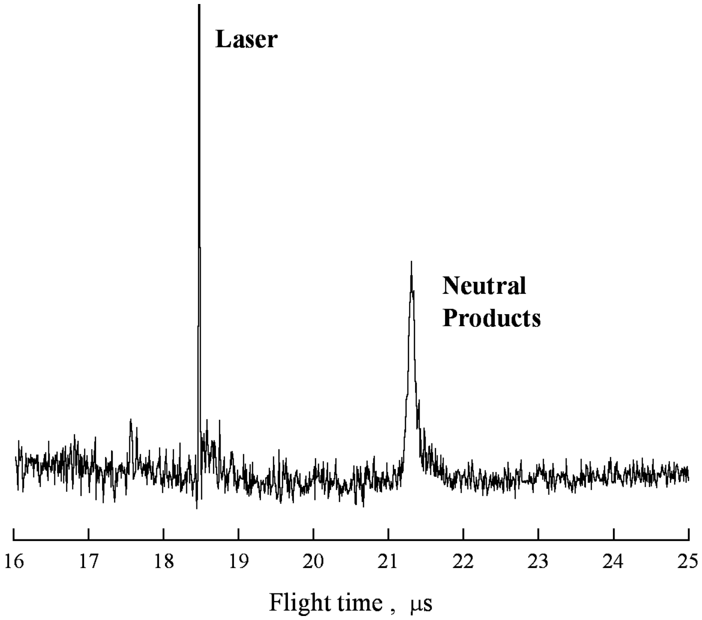

Figure 5.3: Mass spectrum of the neutral products from protonated anthracene photodissociation.

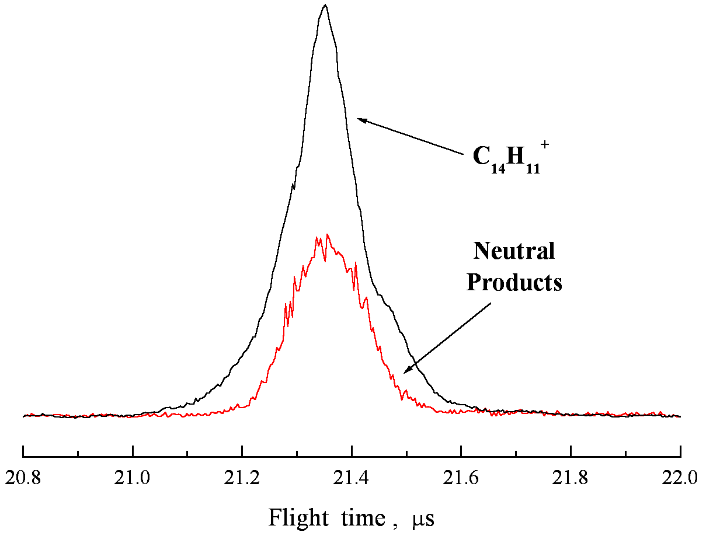

Figure 5.4: Comparison of the linear mode mass spectra for protonated anthracene and its neutral photodissociation products.

5.2 Observed Results

Under our experimental conditions, protonated anthracene and protonated benzene did not dissociate from low energy (<10 mJ/pulse) pulses produced by nanosecond visible and UV lasers. However, all studied ions (protonated anthracene, protonated pyrene and protonated benzene) dissociated after interaction with $10 \leq \mathrm{E} \leq 35$ mJ pulses. This implies the dissociation is multiphoton in nature.

5.2.1 Photodissociation Products

No experiments were conducted to determine the exact nature of the neutral photodissociation products, although some information may be derived from the ion mass spectra in the reflectron channel. Ground state DFT calculations (Chapter 2) have shown that the two lowest dissociation channels should be the loss of a hydrogen atom or the hydrogen molecule, and so these are expected to be the primary neutral dissociation products. Primary ion dissociation products (the cation and dehydrogenated cation) may undergo further dissociation in intense laser fields. Since the laser intercepts the ion beam before it enters the reflectron, only neutral products can pass through the reflectron to produce the signal on the linear detector. The ion dissociation products (ions with positive charge), however, cannot penetrate the reflectron and are deflected toward the reflectron detector. Ions from fast dissociation with small recoil velocities will be collected efficiently by the reflectron and produce reasonably narrow enough mass peaks at the reflectron detector.

The only observed changes in the ion mass spectrum under high intensity laser pulses were the decrease in the intensity of the parent ion peak for protonated PAHs ($\mathrm{m/z} = \mathrm{M} + 1$) and a concomitant increase in the intensity of the cation peak ($\mathrm{m/z} = \mathrm{M}$) (see Figures 5.1, 5.2). No other new peaks appeared in the mass spectrum when the laser was used.

The decrease in the parent ion peak intensity is due to protonated PAH dissociation, and can be as high as 90%. The complete depletion of this peak depends on the spatial overlap of the laser beam with the mass M + 1 ion packet and may be less than 100%. The intensity increase in the cation peak is significantly smaller than the observed protonated ion loss. This suggests that either the dissociation is not sufficiently prompt or that secondary, tertiary, etc. dissociations are possible. One way to test this idea would be to intercept the ions as soon as they are extracted into the mass spectrometer field-free flight region. Unfortunately, this has to be done very close to the reflectron detector which is saturated by the scattered UV light from the laser for an extended time period (more than 100 μs), making it impossible to draw a conclusion. On the other hand, the neutral products signal changes with laser intensity. This may mean that the dissociation is sufficiently fast for the neutral products to be concentrated into a small solid angle.

The intensity increase in the cation peak does not mean that the dissociation happens through the H atom loss channel. In fact, it indicates that the primary dissociation channel is the loss of an H_2 molecule (or two H atoms). This is due to the fact that the dissociation occurs approximately in the middle of the ion flight. In this case, the ions that produce the additional cation signal have mass M + 1 before dissociation (about half of the flight time) and mass M − 1 after (second half of the flight), averaging to mass M. For the H atom loss channel, the ion peak shift would be only 0.5 a.m.u., not the observed 1 a.m.u. The shift would be 2 a.m.u. if the dissociation was performed immediately after the ions were extracted into the mass spectrometer from the discharge.

The loss of two H atoms or the H_2 molecule is in good agreement with the previously observed products in the photodissociation of protonated benzene [90] and the coronene cation [120].

5.2.2 Yield Dependence on the Pulse Energy

In general, photodissociation product yields with respect to the light intensity (pulse energy) can be expected as a power law relationship with exponent γ:

$$S \propto I^{\gamma}$$

The slope of the S *vs.* I curve on a log–log plot gives γ, which corresponds approximately to the number of photons in the process. Data for the photodissociation of protonated anthracene with 193 and 248 nm photons are plotted in Figures 5.5 and 5.6, those for

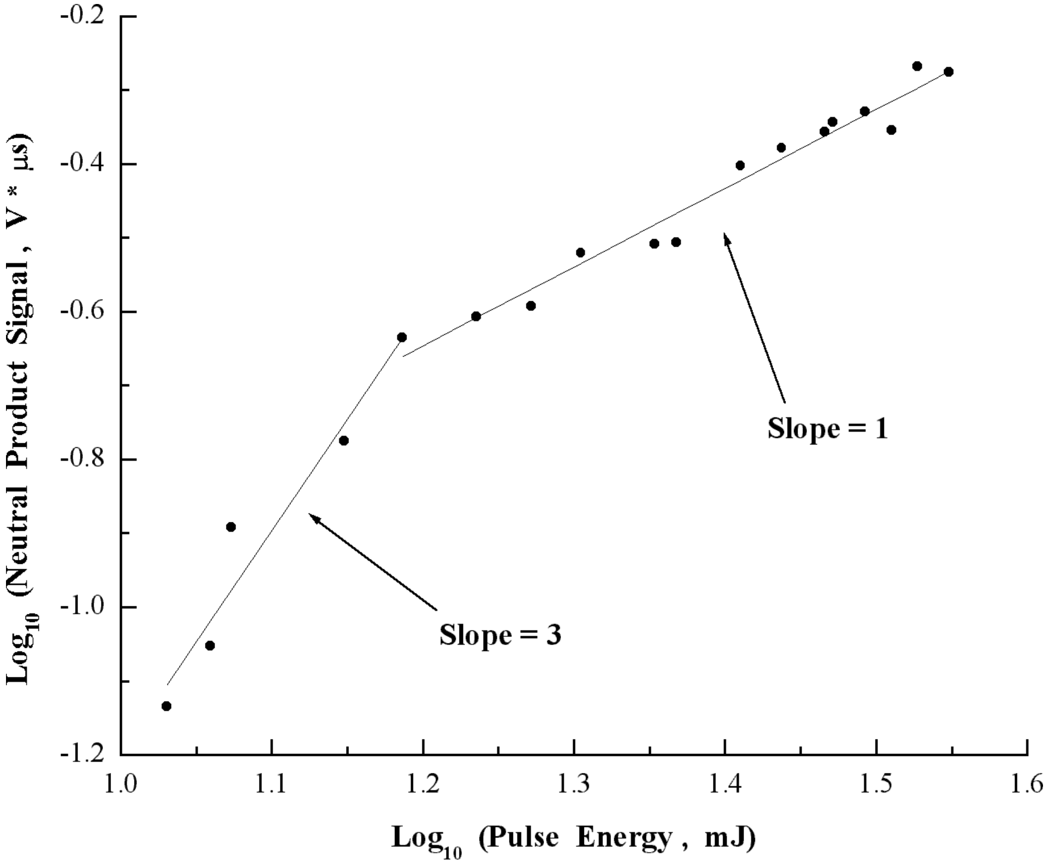

Figure 5.5: Protonated anthracene photodissociation with $\lambda = 193$ nm excimer laser pulses. The dependence of neutral products yield on the pulse energy is indicated by the linear fits in this and subsequent log-log plots.

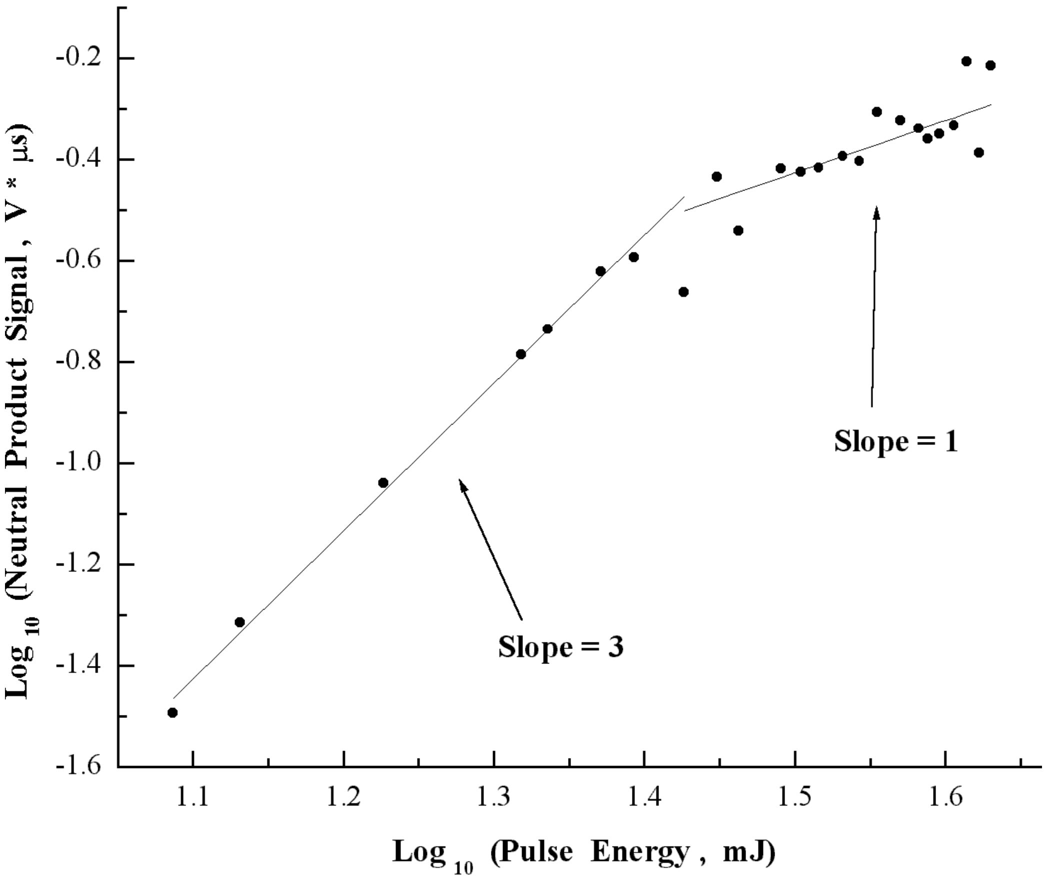

Figure 5.6: Protonated anthracene photodissociation with $\lambda = 248$ nm excimer laser pulses.

protonated pyrene with 193 nm photons in Figure 5.7.

At low pulse energies, the curves for protonated anthracene have a slope of 3. This means that nonresonant dissociation at both 193 and 248 nm is a three-photon process. Both curves have a slope of 1 at higher pulse energies due to the saturation of some of the dissociation steps.

For protonated pyrene, the slope at low intensities was 11. There were two reasons for this unphysical result. First, the pulse energy fluctuations were quite high in this experiment, increasing the uncertainty. Second, protonated pyrene clearly dissociates noticeably easier than does protonated anthracene. This indicates that the transition to one of its

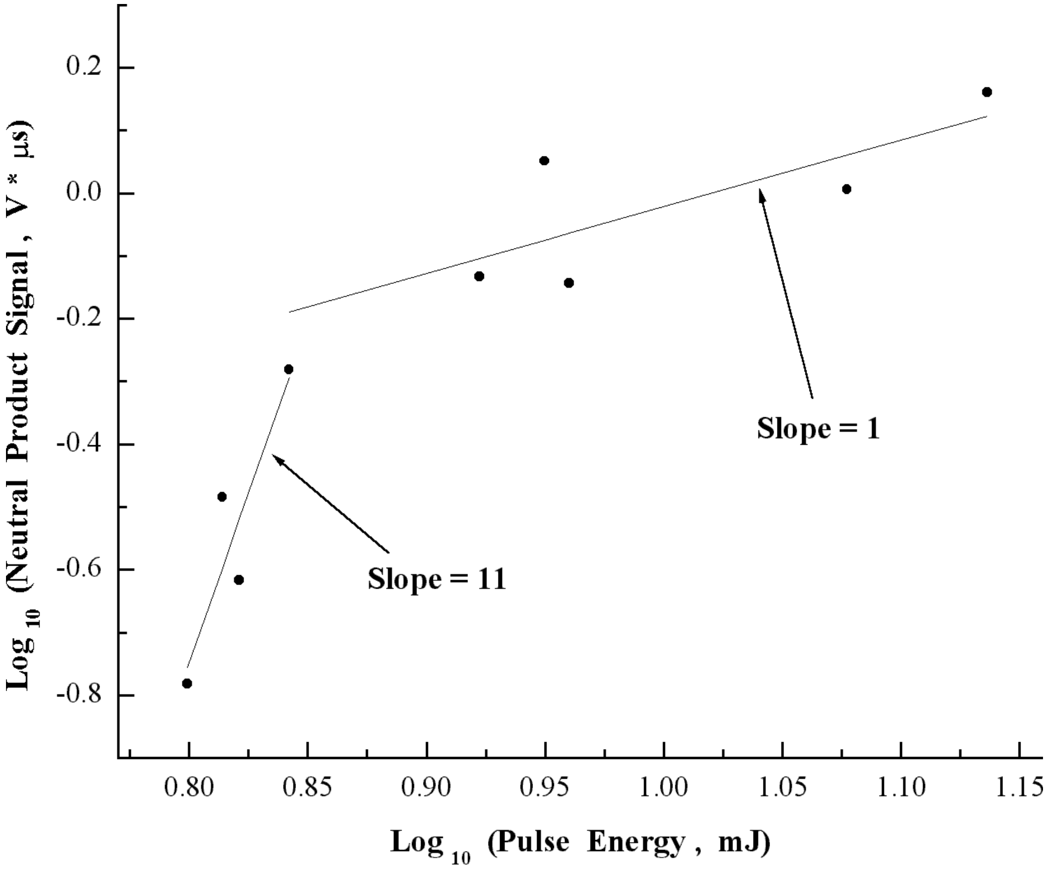

Figure 5.7: Protonated pyrene photodissociation with $\lambda = 193$ nm excimer laser pulses.

excited states lies close to 193 nm, and that the dissociation efficiency was influenced by the proximity to a resonance. The overall nature of dissociation was still multiphoton, but the direct relationship of the slope to the number of photons needed no longer applies.

The observed behavior for protonated benzene was similar to protonated anthracene, although the detailed dissociation yield versus energy was not measured accurately.

5.3 Discussion

5.3.1 Multiphoton Nature of the Photodissociation

The excimer experiments show that the UV photodissociation of protonated PAHs is clearly multiphoton. For protonated anthracene, it is possible to estimate the internal energy required for dissociation (Figure 5.8). Since both 193 and 248 nm dissociation is a three photon process, protonated anthracene dissociates rapidly after absorbing three photons, but not from two photons. Three 248 nm photons therefore establish the upper limit for the dissociation energy while two 193 nm photons determine the lower limit.

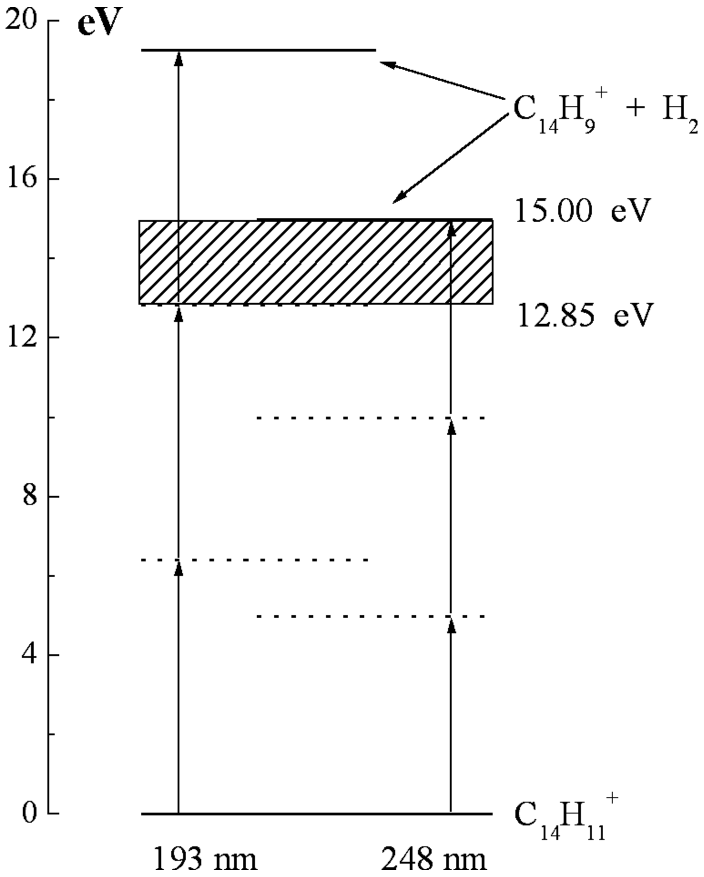

Figure 5.8: Estimates of dissociation energy for protonated anthracene by multiphoton nanosecond laser excitation.

Thus, when using a nanosecond laser, one needs to place 12.85 – 15.00 eV (296.3 – 345.9 kcal/mol) of internal energy into the protonated anthracene ion for it to dissociate in these nanosecond experiments. This is the total amount of energy required and not that needed thermodynamically to break the bonds. Indeed, it is much higher than the dissociation energies (60 – 70 kcal/mol) calculated in Chapter 2. The excess energy goes mostly into the vibrational degrees of freedom of the products, especially in the heavy ion produced. Intramolecular vibrational energy redistribution (IVR) plays a crucial role here.

Two-photon dissociation has been observed in the dissociation of the benzene [149] and naphthalene [67] cations. Here, IVR was also seen to lead to the broadening of the absorption bands in the spectrum. The spectral broadening grew very fast with the number of vibrational modes in the molecule and similar effects may make it impossible to record the photodissociation spectra of large PAHs or PAH cations.

A picture of the dissociation that explains the experimental results is as follows: photons are absorbed quickly during the laser pulse (a few nanoseconds) simultaneously, sequentially, or a combination of both. Then, an electronically excited molecule returns to the ground electronic state potential energy surface via internal conversion and IVR, in the process becoming vibrationally excited. The vibrational energy is distributed over the many different vibrations in the molecule. When the vibrational excitation is sufficiently high, the molecule dissociates. For protonated anthracene, this requires on the order of 4.6 kcal/mol (1620 cm^{-1}) per vibrational mode, which is calculated by dividing the estimated dissociation threshold by the total number of vibrational modes.

This explains why one-photon and $1 + 1'$ two-photon dissociation was not observed with lower energy laser pulses. For example, the dissociation of protonated anthracene with visible nanosecond pulses would be a five-photon process. To observe any noticeable dissociation signal with the visible wavelength photons, the light intensity needs to be much higher than was available here. Such intensities are achievable using much shorter pulses (picosecond or femtosecond duration), but it is not possible to produce enough energy with widely tunable nanosecond lasers (OPOs, dye, etc.) such as those used in the current setup.

To circumvent such pulse energy limitations with high spectral resolution lasers, the experiment needs to be modified. One possibility is to increase the interaction time of the ions with laser radiation by placing the ions into a trap. Photodissociation experiments of this type used a FT ICR trap for protonated benzene [90] and the coronene cation [120], and an RF trap for the anthracene and phenanthrene cations [138]. Alternatively, clusters of protonated PAHs with rare gas atoms or volatile molecules can be made. In this case, the approach would be to measure the one-photon dissociation spectrum of the cluster. This approach is described in Chapter 6 for the specific case of clusters of protonated anthracene with water.

5.3.2 Photostability and Implications for ISM

The observed photostability of protonated PAHs makes it very difficult to record their electronic absorption spectra in TOF systems. On the other hand, this is a very good argument towards the existence of protonated PAHs in the interstellar medium. The ground state calculations described in Chapter 2 have shown that if PAHs exist in the ISM, at least a sizable fraction would exist in the protonated form. The calculations for the excited states from Chapter 3 predict that most protonated PAHs will absorb in the visible and near-UV regions. Our attempts to record photodissociation spectra of protonated PAHs demonstrate that they are extremely resilient against single visible and UV photon dissociation

The estimated single photon dissociation energy of protonated anthracene is close to 13.6

eV. Thanks to the high abundance of hydrogen in a gas of solar composition, most radiation with photon energies above 13.6 eV is absorbed by the ISM and hence is unavailable to dissociate or ionize atoms and molecules. If species do not dissociate through photons with wavelength longer than 912 Å, they are photostable in the ISM. The radiation fluxes in interstellar clouds are not nearly sufficient for multiphoton absorption to occur.

Thus, should protonated PAHs exist in the diffuse ISM, their life cycle would be as follows. An ion in the ground state absorbs a visible or UV photon; it does not dissociate but rather, becomes vibrationally excited. The excess vibrational energy is then emitted at IR wavelengths over a period of milliseconds to seconds, the radiative lifetime for vibrational states. Cold ions can cycle through this loop for long time, and since the UV photon absorption interval is much larger than the IR emission lifetime, most protonated PAHs will exist in their ground states. Such a picture is in perfect agreement with the theory that PAHs (or protonated PAHs) are the species that emit the 3.3 – 11.3 μm UIRs. The question of whether protonated PAHs are DIB carriers still remains to be answered.

Removal mechanisms for protonated PAHs in the ISM include the absorption of more than one photon (highly unlikely), undergoing a chemical reaction, neutralization by dissociative electron recombination, or destruction by high energy particles (e.g. cosmic rays).

5.4 Summary

Several attempts were made to record single- and two-color visible and UV photodissociation spectra of protonated PAHs, but were not successful. Protonated PAHs were found, however, to dissociate under sufficiently intense UV laser pulse excitation. The photodissociation yield measurements demonstrate that nanosecond dissociation is multiphoton in nature. For protonated anthracene, dissociation is a three-photon process at 193 and 248 nm.

The photodissociation energy of protonated anthracene was estimated to be 12.85 – 15.00 eV, a value much higher than the thermodynamic threshold predicted in calculations reported in Chapter 2. Thus, even small protonated PAHs are very photostable, likely due to rapid IVR in the excited states.

This pronounced photostability of protonated PAHs argues in favor of their existence in interstellar clouds.

Chapter 6

Cluster Predissociation Spectroscopy of Protonated Anthracene

6.1 Introduction

As determined in Chapter 5, protonated PAHs are very photostable – a fact that makes recording their direct dissociation spectra with nanosecond lasers quite difficult. To enable single photon experiments to be conducted, the spectra of van der Waals clusters of protonated PAHs with volatile atoms or molecules may be recorded. Since van der Waals interactions are much weaker than chemical bonds, even the vibrational excitation of intramolecular bonds in the components can lead to dissociation. Recording the photodissociation of the cluster gives the predissociation spectrum of the chromophore molecule or ion in the cluster. The spectral lines of the cluster are shifted from the gas phase values of the chromophore due to its interaction with the cluster partner. For clusters with rare gases, the shift is usually within 100 cm^{-1}.

The cluster photodissociation method has been successfully used in the past to record the vibrational [3, 96, 150–154] and electronic [71–74] spectra of clusters of protonated benzene and PAH cations with rare gases. Here it is used to record the visible spectrum of protonated anthracene.

6.2 Experiment

Ideally, for optimum cluster production, the partner gas should be mixed with protonated PAHs in the discharge under high pressure and then expanded into vacuum. In most experiments, the number of molecules for this gas significantly exceeds the number of PAH molecules. The single-valve discharge source (Chapter 4, 4.2) that has been used to protonate PAHs has an inconvenient property in this regard. Whenever a third gas is added to the hydrogen:PAH mixture, it changes the discharge charge transfer characteristics because the cluster partner competes with PAH molecules for protonation. As a result, the PAH protonation efficiency is decreased. For example, no protonation was observed for anthracene when the discharge was run with 1% of argon added to mixture.

To avoid this problem, the third gas can be mixed into the discharge flow after the protonation has already happened. This may be done either in a crossed molecular beam setup, or as the ions expand into vacuum. The latter method also helps to cool the clusters and therefore, was selected here. In particular, the clusters of protonated anthracene with water were made in the two-valve discharge source described in Chapter 4 (4.3) with the second pulsed valve used to deliver the cluster partner into the discharge through two symmetric channels in the last electrode. When the pressure and delay times were adjusted properly, the third gas was picked up by the discharge stream and carried into vacuum without entering the discharge.

Argon, krypton and xenon were first tested as the cluster partner, but they did not produce any clusters with protonated anthracene. Apparently, the discharge was too hot and the pressure at the mixing point was not high enough to provide the cooling needed for cluster formation. A molecule that would create a stronger bound cluster is needed.

Water and ammonia are well known for their ability to cluster with other molecules and were therefore tested as well. One important consideration here is the effect of the cluster partner on the protonated PAHs. The proton affinities of PAHs are in 190 – 210 kcal/mol range and that for H_2O and NH_3 is 165 kcal/mol and 204 kcal/mol, respectively [113]. Since the proton affinity of water is lower than that for PAHs, it will not significantly affect the protonation level of ground state PAH molecules. Ammonia, on the other hand, may attract the proton, thus making a cluster of a neutral PAH and protonated ammonia instead of protonated PAH and ammonia. For this reason, ammonia was discarded.

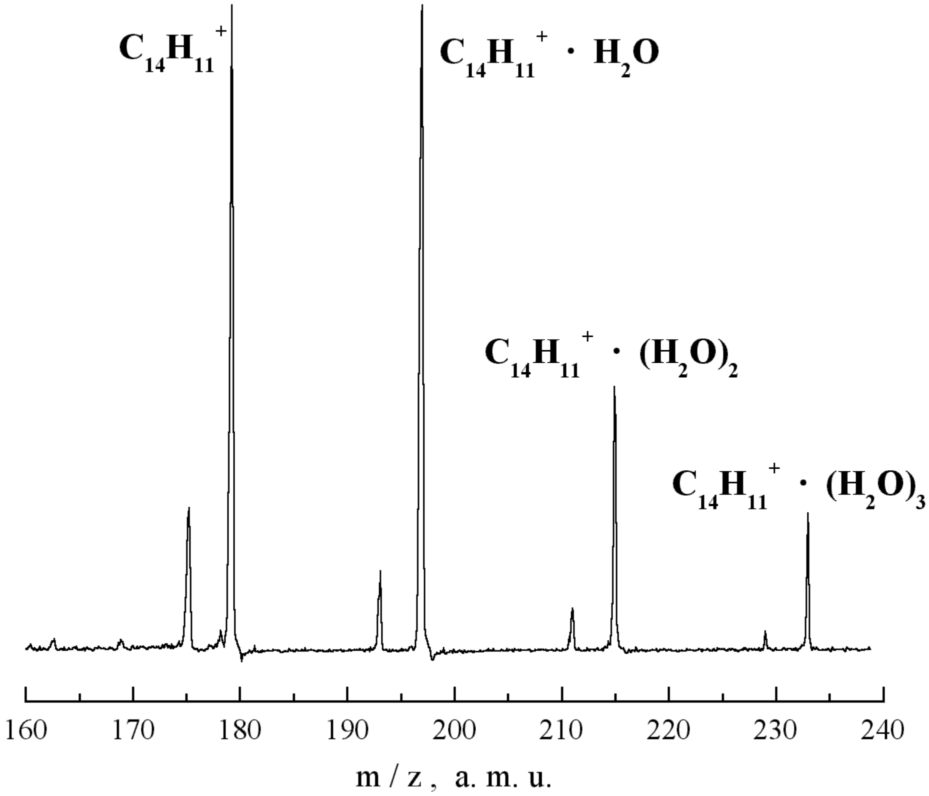

Figure 6.1: A mass spectrum of the two-nozzle source of protonated anthracene–water clusters.

Hydrogen was flowed over the surface of distilled water and used as a carrier gas to deliver H_2O molecules to the discharge. This method was preferred over hydrogen bubbling through water since it assured more stable pressure for the H_2O/H_2 mixture. With this setup, the water mixing ratio and the total pressure in the mixing region was high enough to allow clustering. Indeed, water was found to cluster with protonated anthracene very efficiently. Clusters with up to three water molecules were observed (Figure 6.1). Spectroscopy could be performed with any of these clusters, but $C_{14}H_{11}^{+} \cdot H_2O$ was selected as it possessed the strongest and most stable signal.

The experiments were performed in the same way as that outlined for the photodissociation of protonated PAHs in Chapter 5, with the OPO with mixed BBO Type I and II rotated prism cavity (Chapter 4, 4.6) used as the laser source.

6.3 Results and Discussion

6.3.1 Cluster Geometry

The geometry of PAH $\cdot$ H_2O clusters is determined by the balance of the electrostatic interaction and repulsive forces between the cluster partners. For example, in $C_6H_6 \cdot H_2O$

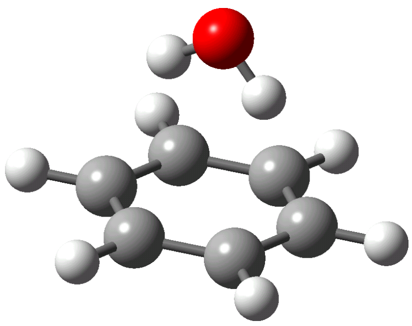

Figure 6.2: The benzene–water ($C_6H_6 \cdot H_2O$) dimer geometry.

(Figure 6.2), the water molecule binds with its hydrogens pointed toward the π aromatic system of benzene [155], thanks to the electrostatic interaction of the water molecule dipole moment with the quadrupole moment of the benzene molecule.

The picture is different in the case of protonated PAHs since they are a positively charged species. To zeroth order, the electrostatic interaction is dominated by charge-dipole forces. As a result, water prefers to bind via the oxygen side and can no longer bind to the aromatic system of protonated PAH due to the repulsion between the aromatic π system electrons and the oxygen lone pairs. Hence, water binds in the PAH plane. To be more precise, it will bind to the site with the largest positive charge: the CH_2 site hydrogens. The cluster geometry for isomer 1 of protonated anthracene was optimized at a low level of theory and is shown in Figure 6.3. The geometry is similar to that of the protonated benzene–water cluster [156], although for $C_6H_7^+ \cdot H_2O$, the isomer of the cluster with the bridged stricture was estimated to be more stable.

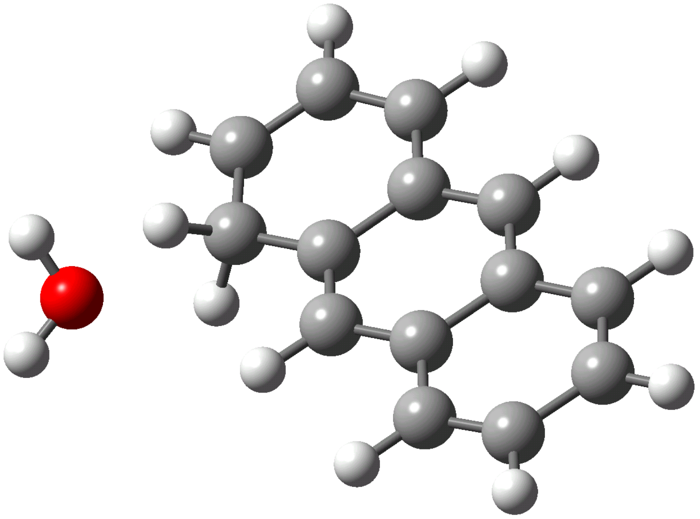

Figure 6.3: Protonated anthracene–water ($1\text{–}C_{14}H_{11}^+ \cdot H_2O$) cluster geometry.

It is not known whether successive water molecules bind to the PAH protonation site or to other H_2O molecules in the cluster. This question, however, is not considered further as no results were acquired for $C_{14}H_{11}^+ \cdot (H_2O)_n$, $n \geq 2$.

6.3.2 Measured Spectrum

The photodissociation spectrum of the $C_{14}H_{11}^+ \cdot H_2O$ cluster was recorded in the 422 – 540 nm range with a resolution of 0.1 nm. Longer wavelengths were not scanned because no excited states for protonated anthracene were predicted to lie at such low energies. The predicted dissociation products are protonated anthracene and water, but this could not be verified experimentally. The neutral product (presumably H_2O) signal was normalized by the value of the cluster signal without the laser, and by the laser pulse energy. The resulting absorption spectrum is shown as the upper trace in Figure 6.4.

At longer wavelengths, there is no measurable absorption. As the wavelength is decreased, the cluster begins to absorb with a threshold wavelength of ∼490 nm. The absorption continually increases toward the blue and is never saturated. The maximum cluster dissociation occurred at 435 nm, where the dissociation efficiency reached 50% due to higher OPO pulse energies.

At first glance, the spectrum appears nearly exponential. A more careful inspection reveals two noticeable bumps that we assign to the excited electronic states of protonated anthracene isomers. The spectrum can be fit nicely by an exponential (grey curve) and two Gaussian or Lorentzian (blue and green curves) functions, resulting in the red curve. The lower trace in Figure 6.4 is the spectrum at the top with the exponential dependence removed for better contrast in the remaining features. Here, the red curve displays the fit of the two Lorentzians alone (fits with Gaussians are quite similar).

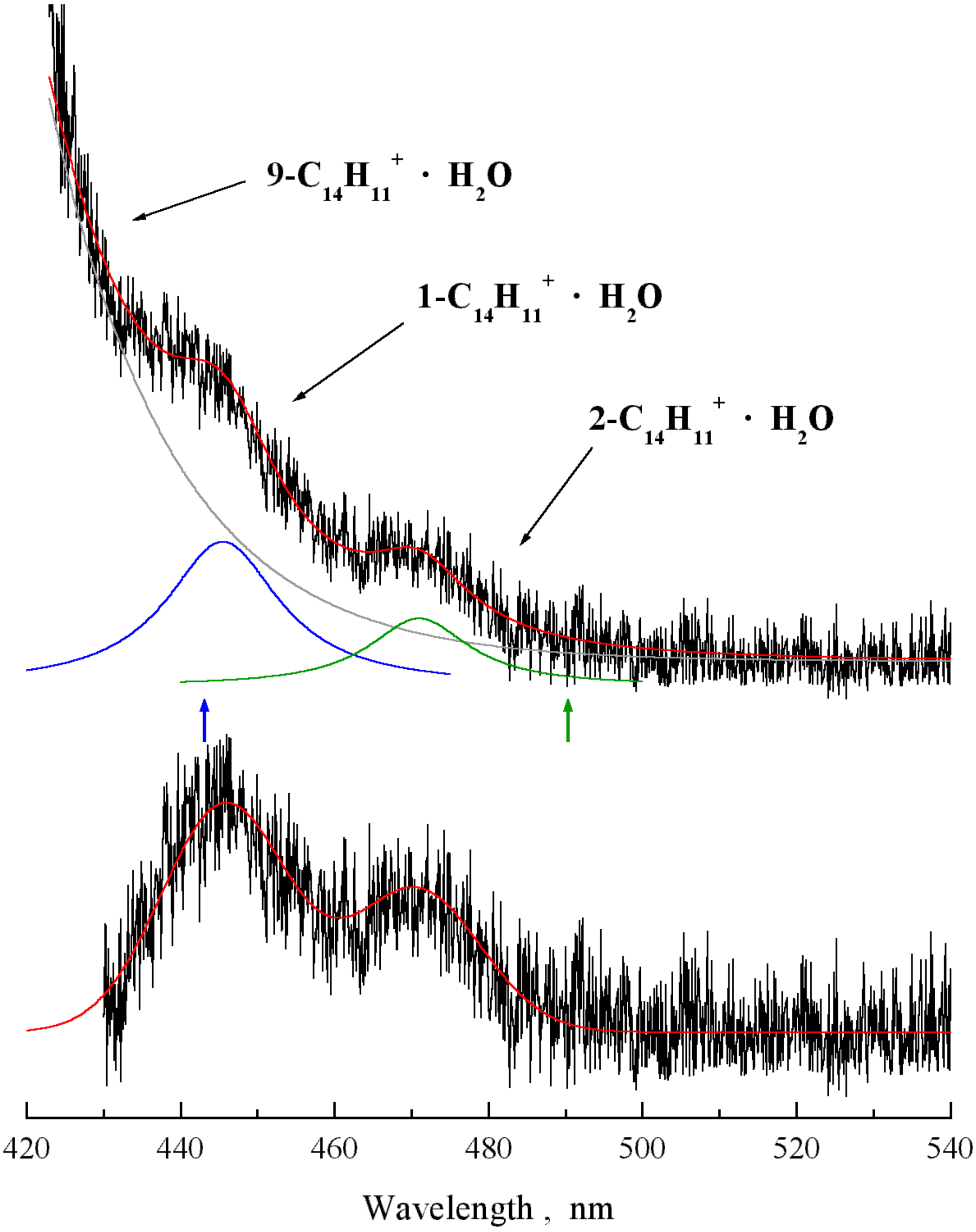

Figure 6.4: Protonated anthracene–water ($C_{14}H_{11}^{+} \cdot H_2O$) cluster photodissociation spectrum. Top: The recorded spectrum and exponential+Lorentzian fit. Bottom: Data with the exponential rise to short wavelengths removed.

We base our assignment of the observed bands to the $S_1 \leftarrow S_0$ transition for protonated anthracene based on the excited state calculations presented in Chapter 3. The longer wavelength band corresponds to isomer 2 of protonated anthracene, while the shorter wavelength band corresponds to isomer 1. The overall exponential increase at short wavelengths is most likely due to the most stable isomer, isomer 9, but a final assignment of this blue increase may only be accomplished when the spectrum down to ∼350 nm is recorded.

Isomer 9 is more stable than the other two isomers by ∼10 kcal/mol and isomer 1 is more stable than isomer 2 by 3 kcal/mol. If the clusters are in thermodynamic equilibrium, the majority of them will be in the form of isomer 9. Similarly, the oscillator strength for isomer 9 is twice as large as for isomer 1, which in turn, has a larger oscillator strength than isomer 2 (Table A.37 in Appendix A). The combined effects of the isomer population distribution and the inherent strengths of the bands may explain the steep rise in absorption at short wavelengths.

6.3.3 Band Positions and Widths

In the fit to the measured spectrum, the two gaussian curves have their maxima at 445.8 nm and 470.7 nm, with full width at half maxima (FWHM) of 19.6 nm. For Lorentzian fits to the data, band positions of 445.5 and 471.0 nm are derived with FWHM of 17.2 and 16.0 nm, respectively. In either case, the band origins (that is, the wavelength of the feature maximum) are about 445.6 nm for isomer 1 and 471 for isomer 2. The predicted transition wavelengths (443.1 nm and 490.4 nm) are shown in Figure 6.4 as vertical arrows. The predicted transition wavelength for isomer 1 is remarkably close to the band origin in the measured spectrum (443.1 nm *vs.* 445.6 nm), while for isomer 2 the experimental value is shifted to the blue by ∼19 nm from that predicted.

At the available signal-to-noise ratio, no internal structure is seen in the bands. The spectra are either vibrationally or lifetime broadened. The vibrational broadening of the excited state leads to band blue shift, while the vibrational broadening of the ground state and the lifetime broadening are expected to work in both directions from the band origin.

6.3.4 Comparison with Spectra of Other Clusters

The measured $C_{14}H_{11}^+ \cdot H_2O$ cluster spectrum should be compared to the spectra of similar clusters in order to draw any conclusions about the cluster properties and especially about the spectrum of bare protonated anthracene. The dissociation spectrum for the naphthalene cation–argon cluster [71, 73] is red-shifted from the gas phase spectrum of the naphthalene cation [62] by 2 nm (50 cm^{-1}), but has similar widths (25 – 30 cm^{-1} FWHM) of the vibronic features therein. For the phenanthrene–argon cluster [72, 73], the red shift is 13 cm^{-1}. REMPI spectral lines for the anthracene–argon cluster [69] are also very narrow (10 cm^{-1} FWHM) and the red shift is 47 cm^{-1}. However, these shifts are for clusters with argon, whose spectra do not have as large a red shift as those with polar molecules. For clusters of anthracene with water [157] and methanol [158], the band widths increase slightly compared to those with Ar but are no more than 30 – 40 cm^{-1}, and the red shifts remain tolerably small at 100 – 150 cm^{-1}.

Based on these data, one would expect the absorption bands for the protonated anthracene–water cluster to be no more than 50 cm^{-1} wide, versus the measured value of 1100 cm^{-1}. The red shift in the protonated anthracene gas phase spectrum would be about 100 – 200 cm^{-1} (4 nm) if it behaved similarly to PAHs and PAH cations. The comparison of the calculated $S_1 \leftarrow S_0$ transition wavelength (as in Chapter 3) for isomer 1 of protonated anthracene and its cluster with water gives a similar shift value. Using these shifts and the measured band origins, the photodissociation spectrum for the $C_{14}H_{11}^{+} \cdot H_2O$ cluster should look similar to that shown in Figure 6.5. Clearly, this is not the case. Thus, absorption bands as measured experimentally must be broadened by either a property intrinsic to protonated anthracene or created by the cluster environment.

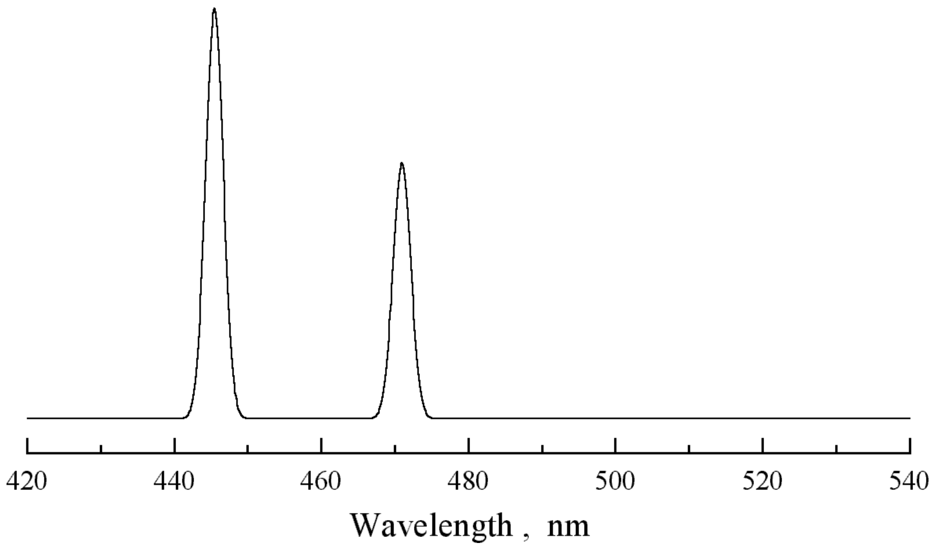

Figure 6.5: The expected protonated anthracene–water cluster photodissociation spectrum from comparisons with PAH and PAH^{+} clusters.

6.3.5 Effect of Proton Mobility on the Spectral Width

To answer the important question, “What causes the widths of measured bands to be as high as 1100 cm^{-1} (FWHM)?”, several scenarios must be considered. Is it due to some experimental procedure, or is it due to a property of the cluster or of protonated anthracene itself?

As was found in Chapter 2, protonated aromatics have one thing in common that neutral PAHs and their cations do not: an ability to isomerize by proton hopping from one carbon atom to another. This dramatically increases the density of vibrational states for the highly excited protonated PAHs, increase that is largely due to the contribution of all isomers since they are coupled to each other. No such coupling exists for neutral PAHs and their cations, and although they have nearly the same number of atoms (and hence the number of vibrational modes) as protonated PAHs, only one isomer is possible.

When a protonated PAH absorbs a visible or UV photon and becomes excited electronically, it can non-radiatively transfer to the ground electronic potential energy surface via internal conversion. The density of vibrational states on the ground state at an excitation of 10,000 – 25,000 cm^{-1} is the crucial consideration. Higher densities of vibrational states lead to faster internal conversion, shorter excited state lifetimes and broader spectral features. This lifetime broadening mechanism will not depend on whether the protonated PAH exists freely or as a member of a cluster, and explain why the protonated benzene photodissociation spectrum [90] is as broad as the protonated anthracene–water bands observed here.

6.3.6 Other Factors

If protonated anthracene in a cluster retains vibrational excitation, additional spectral broadening of the predissociation spectrum can result. Since protonated anthracene was made in a discharge, it is expected to be vibrationally warm, thanks to the high electron temperature of such environments. This is the likely explanation for why the attempts to generate protonated PAH clusters with rare gases were unsuccessful. On the other hand, the clusters cannot be too hot because clusters with up to three water molecules were produced. Based on this observation, one would expect the vibrational temperature of the clusters be somewhere in the range of 50 – 150 K. At these temperatures, intermolecular and the very lowest intramolecular modes could be populated, but it is unlikely they could cause the level of broadening observed or create a spectral profile that is as smooth as that measured experimentally.

Another thing that may lead to spectral broadening is C–H bond softening at the protonation site through interactions with the water molecule. For the protonated benzene–water dimer, for example, the energy difference between the two protonation sites (one on benzene, the other on water) was calculated to be only 2.6 kcal/mol [156] with a barrier to proton transfer of only 2.5 kcal/mol, despite the fact that the proton affinity of benzene is 14.3 kcal/mol larger than in water. The effect should be not as noticeable in the protonated anthracene–water cluster since the proton affinity of anthracene is higher than for benzene by another 20 – 30 kcal/mol, depending on the protonated isomer (1, 2, or 9).

6.3.7 Comparison with the DIBs

There is a strong diffuse interstellar band at 4430 Å (FWHM = 1.15 nm) which is very close to the expected band origin of the transition for isomer 2 of protonated anthracene (Chapter 3, Figure 3.4). There are also four broad diffuse interstellar bands in the 470 – 500 nm region, one of which (λ_{max} = 476.2 nm, FWHM = 2.36 nm) red-shifted by ∼6 – 10 nm from the expected band origin of the isomer 2 transition. This is a rather large discrepancy for a good match, but given the uncertainties in the cluster spectrum, the coincidence is worth considering further if additional experimental data are generated. Little can be said at present about isomer 9. Further, even the broadest currently known DIB features are one order of magnitude narrower than the measured bands. Thus, it is most likely that protonated anthracene is not a DIB carrier. Such broad electronic transitions do make protonated PAHs excellent 'harvesters' of interstellar visible and UV photons, however, and this combined with the high photostability makes them excellent candidates for UIR emitters.

If other protonated PAHs have electronic absorption spectra with bands that are similarly broadened, they are equally unlikely to be DIB carriers. This depends largely on the spectral broadening nature. If the proton mobility is a major factor to that, then the isomerization within one PAH ring is a larger contributor then the isomerization across the ring fusion, because such process has a higher barrier. This may lead to narrower absorption band widths in species like coronene. If the vibrational temperatures of protonated PAHs in the ISM are lower than those in laboratory experiments, interstellar absorption bands may be even narrower. The cumulative effect of these factors may bring the expected interstellar band widths close to those for wide DIBs.

6.4 Summary

The visible photodissociation spectrum of the protonated anthracene–water ($C_{14}H_{11}^{+} \cdot H_2O$) cluster was recorded using our modified BBO OPO type I and type II cavity. The two absorption bands observed were assigned to isomers 1 and 2 of protonated anthracene. The origin of one of these bands was very close to the predicted value, but the observed absorption bands were very broad: FWHM were close to $\simeq$ 20 nm or 1100 cm^{-1}. The smooth nature of the bands suggests that a substantial component of the broadening is most likely due to the increase in the density of vibrational states resulting from the proton mobility in protonated anthracene. Internal vibrational excitation of the anthracene or of the cluster intermolecular modes may contribute as well, as may proton transfer interactions with the water molecule.

The measured absorption bands are 10 times wider than even the broadest diffuse interstellar bands. While there is a DIB next to the band origin for isomer 1 of protonated anthracene, no such close coincidence exists for isomer 2. Protonated anthracene is therefore unlikely to be a DIB carrier. If all protonated PAHs share the dynamical properties of $C_{14}H_{11}^+$ inferred from the predissociation spectrum, there role as DIB carriers is suspect as well. The excellent photostability of these species, along with their vibrational band positions, however, means that they would be very efficient sources of UIR emission.

Chapter 7

Summary

Several of the properties of protonated PAHs that are important to their abundance and photophysics in the interstellar medium have been explored in this thesis. The key findings are outlined below.

7.1 Structures and Reaction Pathways

In Chapter 2, the results of extensive density functional calculations on protonated benzene, naphthalene, anthracene, phenanthrene and pyrene in their ground electronic state were presented. The original goal of these calculations was to determine the relative energies for protonated PAH isomers and to find their most likely dissociation channels. Loss of a hydrogen atom or a hydrogen molecule from the protonation site were identified as the two lowest energy dissociation channels. The former channel was found to be lower in energy for molecules with a few aromatic rings, although the energy difference between these two channels is not very large. In photodissociation experiments in both [90] and Chapter 5, the mass spectra of the ion product showed the loss of 2 a.m.u., which can be explained either by the loss of H_2 or the sequential loss of two H atoms. The former channel is significantly lower in energy, and is therefore more likely. This photodissociation channel of protonated PAHs would provide a way to generate interstellar molecular hydrogen if the single photon vacuum-UV yield is comparable to that measured in the near-UV multiphoton experiments.

Along with the dissociation channels, barrier heights for unimolecular isomerization of protonated PAHs have been calculated. It was determined that with sufficient vibrational excitation, protonated PAHs may isomerize freely. This process can occur well below the dissociation energy, and is not limited by only one aromatic ring. Indeed, the proton may migrate on the outside rim of PAH molecule, 'hopping' from one carbon atom to another. On cosmic time scales, such proton hopping events would lead to a complete statistical scrambling of the different isomers, and the system would therefore lose all memory about the manner in which it was created.

One significant spectroscopic outcome of the proton mobility in protonated PAHs is a dramatically increased density of vibrational states as is described below.

7.2 Molecular Orbitals and Electronic Transitions

Chapter 3 was devoted to understanding the changes of PAH molecular orbitals upon protonation, and estimating the $S_1 \leftarrow S_0$ transition wavelengths for all isomers of a given protonated PAH. In case of the benzene molecule, all π and π^* orbitals have been considered. The protonation of one of its carbon atoms leads to a change from sp^2 to sp^3 hybridization at this site. Those molecular orbitals of protonated benzene that do not overlap with the protonation site have the same energies as in the benzene molecule; energies of the rest of the orbitals shift to lower values (that is, they are more stable) due to the stabilizing effect induced by the hybridization of the proton σ orbital with the carbon p_z orbital. The immediate result of such changes is to reduce the HOMO – LUMO gap, which leads to a red shifting of electronic absorption bands.

For larger PAHs, the changes in HOMO and LUMO orbitals were more pronounced, although it was still possible to trace their origins to changes in the orbitals of their neutral PAH precursors. Based on the orbital symmetry, the ground and the first singlet excited electronic states of protonated PAHs were assigned. Most protonated PAHs have C_s symmetry, resulting in $\widetilde{X}\ ^1A'$ and $\widetilde{A}\ ^1A'$ ground and first excited states.

Wavelengths for the $S_1 \leftarrow S_0$ transitions have been calculated for both neutral and protonated PAHs using the CIS method. The calculated values had a $\sim$25% discrepancy with the experimental data for neutral PAHs, a data set that was used to establish scaling factors for the excited electronic states of protonated PAHs, much as the fairly low level *ab initio* calculations of vibrational spectra must be scaled to agree with experiment. While this manipulation of the predicted energies has no rigorous physical basis, the scaled *ab initio* wavelengths were somewhat red-shifted from experimentally measured values for protonated benzene and isomer 2 of protonated anthracene while being very close to the experimental band position for isomer 1 of protonated anthracene. Such proximity of predicted and experimental wavelengths lend credence to the approach for other aromatic systems.

The predicted red shifts from the analogous transitions in neutral PAHs were some 15 – 200 nm, with a median shift of more than 100 nm. All protonated aromatic hydrocarbons except protonated benzene were found to have strong transitions at visible wavelengths. Many of the calculated values were close to broad bands in the DIB spectrum, a result that encourages the further investigation of protonated PAHs as possible DIB carriers. Although the predicted wavelengths are not sufficiently precise to make conclusions about any exact matches with known DIBs, they do serve as a relatively good guide for laboratory searches for these electronic transitions.

The calculated $S_1 \leftarrow S_0$ transition energies of protonated PAHs turned out to be very close to the predicted thermodynamic threshold for dissociation at the protonated site.

Thus, one might expect them to be photophysically unstable. The opposite behavior has been determined experimentally, as is described next.

7.3 Photostability of Protonated PAHs

Chapter 5 focuses on attempts to record the photodissociation spectra of bare protonated benzene, anthracene and pyrene. The protonation of neutral PAH molecules was performed in a hydrogen discharge source, and mass selected ions were allowed to interact with the pulses from tunable visible/UV nanosecond OPO and excimer lasers. Both the depletion of the parent ion signal and photodissociation products were detected in a reflectron time-of-flight mass spectrometer. No photodissociation by low energy laser pulses was observed, but high energy nanosecond pulses from the excimer laser were found to significantly deplete the protonated PAH ion signal.

The measurements of the photodissociation yield versus radiation intensity revealed the dissociation process to be multiphoton in nature. In the case of protonated anthracene, nanosecond photodissociation required three photons at both 193 and 248 nm. This fact allowed the nanosecond dissociation energy of protonated anthracene to be constrained to 13 – 15 eV. This is significantly higher than the predicted thermodynamic threshold of $\sim$60 kcal/mol, and shows that the lowest excited electronic states of protonated PAHs have poor Franck-Condon overlap with states that lead to C–H bond cleavage.

Rapid internal conversion and intramolecular vibrational energy redistribution processes are likely responsible for the high photostability observed for protonated PAHs. Thus, even small systems of this type have an excellent probability of surviving the UV radiation field in diffuse and translucent interstellar clouds. This is another factor in support of the presence of protonated PAHs in the ISM.

7.4 Visible Spectrum of Protonated Anthracene

The photodissociation spectrum of clusters of protonated anthracene with water was recorded in the visible wavelength region in Chapter 6. Protonated anthracene served as the chromophore, with the cluster method serving to circumvent the high photostability of bare protonated PAHs and enable single photon experiments. Although the cluster spectrum is not identical to that of bare protonated anthracene, the expected shifts are small and the overall nature of the spectrum is expected to be preserved.

The measured spectrum had two very broad ($\sim$1100 cm^{-1} FWHM) absorption bands that were assigned to isomers 1 and 2 of protonated anthracene based on the *ab initio* predictions from Chapter 3. The widths of these bands were quite similar to that measured for protonated benzene in a continuous wave ion trap dissociation experiment [90]. For both species, the broadening may well arise from the extremely high density of vibrational states induced by the proton mobility in such systems, although the degree of internal vibrational excitation in the clusters has not been determined and must be considered as well.

While there is a strong DIB feature near the band origin for the isomer 1 of protonated anthracene, no such close features have been seen in the vicinity of the expected band origin for the isomer 2. Furthermore, the widths of the observed bands were an order of magnitude larger than widest DIB features currently known. Thus, it is unlikely that protonated anthracene is a DIB carrier unless the conditions of our experiment are vastly different than those in the ISM. For larger PAHs, the vibrational density of states and hence, the vibrational energy redistribution rates would be even larger, so the general case for protonated PAHs as DIB carriers would seem to be weakened by our results.

7.5 Conclusions

Perhaps the most important result of this thesis is the high measured photostability of protonated PAHs under nanosecond laser pulse illumination. Thus, if they are created efficiently in the ISM as is suggested by laboratory kinetics experiments [75,82], the chances of their removal by UV radiation are very small. This provides another strong argument in favor of the presence of protonated PAHs in the ISM.

The measured photodissociation spectrum of protonated anthracene – water cluster had very broad absorption bands, however, with only one being in even reasonable proximity to a known DIB. This indicates that protonated anthracene, and by extension the entire class of small protonated PAHs, are not the carriers of the diffuse interstellar bands. The observed spectral widths can naturally be explained by the proton mobility in protonated PAHs.

7.6 Future Research Directions

To further investigate protonated PAHs and to clarify unresolved questions raised by this thesis, a number of experiments or observations come to mind. In the laboratory, more spectra of protonated PAHs should be recorded in the same fashion as that outlined in Chapter 6. This involves measuring the spectrum of protonated anthracene at shorter wavelengths to determine whether isomer 9 contributes to the blue absorption seen, as well as recording the spectra of other protonated PAHs (e.g. protonated naphthalene, phenanthrene, pyrene, and coronene). Protonated coronene would be an especially interesting species to study because it has a larger size, but like benzene, has only one stable isomer. The relative proportion of ring fusion hopping steps needed to scan the PAH periphery is also rather larger than in the small protonated PAHs studied here, and the effect of this on the excited state dynamics could play an important role in the spectral broadening of large protonated PAHs in the ISM.

To minimize the potential broadening due to internal vibrational excitation of protonated PAHs in the discharge source, additional experiments should be performed at cryogenic temperatures. The best way to do this would be to perform visible/UV spectroscopy of protonated PAHs in liquid helium nanodroplets. In such an environment, protonated PAHs would have a temperature 0.38 K, along with a minimal amount of perturbation by the surrounding helium atoms which would permit a better measurement of the band origin positions of the electronic absorption bands. This would be a challenging experiment to perform, and as an easier first step, protonated PAHs could be deposited into rare gas matrices (argon or neon). In this case, the proton may well be confined to only one carbon atom. As a result, the absorption band profiles may be quite different from those in the gas phase or in nanodroplets.

If protonated PAHs do exist in diffuse interstellar clouds, they may produce DIBs that are wider than those measured with current astronomical surveys that are limited to a maximum spectral width of 50 Å for robust feature extraction from complex stellar spectra. Targeted DIB surveys can be conducted that are sensitive to even wider DIB features. Another interesting trend to follow would be to measure the dependence of the DIB width versus environment. For example, DIB profiles from different parts of the same diffuse cloud that are at different temperatures or exposed to different levels of UV radiation could be compared in order to draw conclusions about the rigidity/stability of the absorbing species.

Protonated PAHs have relatively large permanent dipole moments and therefore should be detectable via pure rotational techniques. Indeed, laboratory microwave spectra should in principle be measurable for a wide range of protonated PAHs, including those that are deuterated or that contain heteroatoms. The data obtained may be used in the search for protonated PAHs in the ISM by radio astronomy tools, and the measured frequencies may be compared to those predicted theoretically for improved structure determinations. At the highest resolution achievable, it may even be possible to observe spectral line shifts or splittings that would provide insight into the importance of proton mobility in the electronic ground state of protonated PAHs.

Theoretically, the distribution of the different isomers of protonated PAHs in actual interstellar environments can be calculated based on their relative energies, proton mobilities, UV excitation and IR emission rates. This would permit more accurate estimates of intensity ratios for different protonated PAH isomers that could be compared to astronomical observations. Other effects such as deuteration, dissociative electron recombination, and chemical reactions may be considered as well.

Appendix A

GAUSSIAN 98 Results

A.1 Geometries

Table A.1: Symmetry Groups, Dipole Moments, Rotational Constants.

Molecule	Symmetry Group	Dipole Moment (Debye)	Rotational Constants (GHz)		
			A	B	C
Benzene					
C_6H_6	D_{6h}	0.0000	5.70390	5.70358	2.85187
$C_6H_7^+$	C_{2v}	0.8729	5.44292	5.31711	2.73189
Naphthalene					
$C_{10}H_8$	D_{2h}	0.0000	3.12608	1.23304	0.88426
1–$C_{10}H_9^+$	C_s	2.0089	3.02746	1.19994	0.86371
2–$C_{10}H_9^+$	C_s	1.9098	3.00985	1.20301	0.86381
Anthracene					
$C_{14}H_{10}$	D_{2h}	0.0004	2.15007	0.45211	0.37356
1–$C_{14}H_{11}^+$	C_s	3.6691	2.09822	0.44507	0.36799
2–$C_{14}H_{11}^+$	C_s	2.9302	2.09404	0.44523	0.36795
9–$C_{14}H_{11}^+$	C_{2v}	18.0182	2.09785	0.44552	0.36829
Phenanthrene					
$C_{14}H_{10}$	C_{2v}	0.0148	1.61849	0.55146	0.41132
1–$C_{14}H_{11}^+$	C_s	3.6954	1.60553	0.53656	0.40312
2–$C_{14}H_{11}^+$	C_s	3.5894	1.56116	0.54831	0.40675
3–$C_{14}H_{11}^+$	C_s	2.9631	1.60847	0.53527	0.40256
4–$C_{14}H_{11}^+$	C_s	3.5209	1.56388	0.54928	0.40749
9–$C_{14}H_{11}^+$	C_s	2.6637	1.56907	0.54629	0.40618
Pyrene					
$C_{16}H_{10}$	D_{2h}	0.0006	1.01227	0.55629	0.35900
1–$C_{16}H_{11}^+$	C_s	0.9957	1.01056	0.54208	0.35356
2–$C_{16}H_{11}^+$	C_{2v}	3.5447	0.98544	0.55087	0.35408
4–$C_{16}H_{11}^+$	C_s	3.3564	0.98697	0.55073	0.35422

A.1.1 Z-Matrices

Table A.2: Benzene (C_6H_6) Z-Matrix.

Atom 1	Atom 2	Bond, Å	Atom 3	Angle, °	Atom 4	Dihedral Angle, °
C						
C	1	1.394654				
C	2	1.394666	1	120.001991		
C	3	1.394666	2	119.996074	1	0.000000
C	4	1.394654	3	120.001976	2	0.000000
C	1	1.394667	2	120.001971	3	0.000000
H	1	1.084426	2	119.998426	3	180.000000
H	2	1.084425	1	119.999042	6	180.000000
H	3	1.084418	2	120.001991	1	180.000000
H	4	1.084426	3	119.998977	2	180.000000
H	5	1.084426	4	119.998467	3	180.000000
H	6	1.084418	1	120.002023	2	180.000000

Table A.3: Protonated benzene ($C_6H_7^+$) Z-Matrix.

Atom 1	Atom 2	Bond, Å	Atom 3	Angle, °	Atom 4	Dihedral Angle, °
C						
C	1	1.368727				
C	2	1.410091	1	119.091029		
C	3	1.410091	2	122.978924	1	0.000000
C	4	1.368727	3	119.091029	2	0.000000
C	1	1.468723	2	120.870021	3	0.000000
H	1	1.085006	2	120.934222	3	180.000000
H	2	1.082815	1	121.103374	6	180.000000
H	3	1.086011	2	118.510538	1	180.000000
H	4	1.082815	3	119.805596	2	180.000000
H	5	1.085006	4	120.934222	3	180.000000
H	6	1.107768	1	109.582298	2	-125.565642
H	6	1.107768	1	109.582298	2	125.565642

Table A.4: Naphthalene ($C_{10}H_8$) Z-Matrix.

Atom 1	Atom 2	Bond, Å	Atom 3	Angle, °	Atom 4	Dihedral Angle, °
C						
C	1	1.374287				
C	2	1.419949	1	120.859505		
C	3	1.431358	2	118.849618	1	0.000000
C	4	1.419949	3	118.849618	2	0.000000
C	5	1.374287	4	120.859505	3	0.000000
H	3	2.162862	2	96.213583	1	180.000000
H	1	1.084246	2	120.105825	3	180.000000
H	2	1.085201	1	120.354128	6	180.000000
C	3	1.419949	2	122.300764	1	180.000000
C	4	1.419949	3	118.849618	2	180.000000
H	5	1.085201	4	118.786367	3	180.000000
H	6	1.084246	5	120.105825	4	180.000000
C	11	1.374287	4	120.859505	3	0.000000
C	10	1.374287	3	120.859505	2	180.000000
H	11	1.085201	4	118.786367	3	180.000000
H	14	1.084246	11	120.105825	4	180.000000
H	15	1.084246	10	120.105825	3	180.000000

Table A.5: Protonated naphthalene ($1\text{–}C_{10}H_9^+$) Z-Matrix.

Atom 1	Atom 2	Bond, Å	Atom 3	Angle, °	Atom 4	Dihedral Angle, °
C						
C	1	1.474279				
C	2	1.494690	1	116.787133		
C	3	1.431159	2	119.092662	1	0.000000
C	4	1.404226	3	119.070231	2	0.000000
C	1	1.364716	2	122.183322	3	0.000000
H	3	2.150313	2	96.202424	1	180.000000
H	1	1.085343	2	117.497804	3	180.000000
H	2	1.103342	1	108.112234	6	-124.958072
C	3	1.389728	2	122.030912	1	180.000000
C	4	1.422179	3	120.071957	2	180.000000
H	5	1.086579	4	118.059944	3	180.000000
H	6	1.082676	1	121.003188	2	180.000000
C	11	1.375768	4	119.879439	3	0.000000
C	10	1.393535	3	120.053953	2	180.000000
H	11	1.083991	4	119.251121	3	180.000000
H	14	1.082707	11	120.532382	4	180.000000
H	15	1.084106	10	119.200021	3	180.000000
H	2	1.103342	1	108.112269	6	124.958072

Table A.6: Protonated naphthalene (2–$C_{10}H_9^+$) Z-Matrix.

Atom 1	Atom 2	Bond, Å	Atom 3	Angle, °	Atom 4	Dihedral Angle, °
C						
C	1	1.467137				
C	2	1.375120	1	122.320057		
C	3	1.453306	2	118.929699	1	0.000000
C	4	1.437357	3	119.984361	2	0.000000
C	5	1.351281	4	121.171920	3	0.000000
H	3	2.176465	2	95.396030	1	180.000000
H	1	1.105786	2	108.533743	3	125.434348
H	2	1.086393	1	117.910108	6	180.000000
C	3	1.435418	2	121.261956	1	180.000000
C	4	1.400581	3	118.151009	2	180.000000
H	5	1.083869	4	118.198098	3	180.000000
H	6	1.083716	5	120.954631	4	180.000000
C	11	1.386258	4	120.326676	3	0.000000
C	10	1.367430	3	120.103584	2	180.000000
H	11	1.083408	4	119.625693	3	180.000000
H	14	1.084505	11	119.119868	4	180.000000
H	15	1.082661	10	120.737318	3	180.000000
H	1	1.105787	2	108.533724	3	-125.434348

Table A.7: Anthracene ($C_{14}H_{10}$) Z-Matrix.

Atom 1	Atom 2	Bond, Å	Atom 3	Angle, °	Atom 4	Dihedral Angle, °
C						
C	1	1.367410				
C	2	1.429250	1	120.967249		
C	3	1.443006	2	118.582161	1	0.000000
C	4	1.429172	3	118.590960	2	0.000000
C	5	1.367437	4	120.968419	3	0.000000
C	3	1.398763	2	122.305297	1	180.000000
C	4	1.398832	3	119.107531	2	180.000000
C	8	1.398760	4	121.779438	3	0.000000
C	7	1.398812	3	121.778585	2	180.000000
C	10	1.429139	7	122.297882	3	180.000000
H	11	1.085123	10	118.562270	7	0.000000
C	11	1.367419	10	120.972114	7	180.000000
C	13	1.424931	11	120.437315	10	0.000000
C	14	1.367412	13	120.450640	11	0.000000
H	7	1.085938	3	119.114219	2	0.000000
H	1	1.084221	2	120.150061	3	180.000000
H	2	1.085119	1	120.470108	6	180.000000
H	5	1.085112	4	118.566980	3	180.000000
H	6	1.084213	5	120.156221	4	180.000000
H	8	1.085940	4	119.106858	3	180.000000
H	13	1.084214	11	120.159346	10	180.000000
H	14	1.084218	13	119.397937	11	180.000000
H	15	1.085113	14	120.470891	13	180.000000

Table A.8: Protonated anthracene (1–$C_{14}H_{11}^{+}$) Z-Matrix.

Atom 1	Atom 2	Bond, Å	Atom 3	Angle, °	Atom 4	Dihedral Angle, °
C						
C	1	1.479937				
C	2	1.504130	1	116.134837		
C	3	1.446275	2	118.713966	1	0.000000
C	4	1.397695	3	119.648300	2	0.000000
C	1	1.361794	2	122.814749	3	0.000000
C	3	1.367795	2	122.450139	1	180.000000
C	4	1.411540	3	120.113776	2	180.000000
C	8	1.392425	4	121.097815	3	0.000000
C	7	1.423370	3	121.704778	2	180.000000
C	10	1.410808	7	121.877995	3	180.000000
H	11	1.083777	10	119.373319	7	0.000000
C	11	1.378894	10	120.411623	7	180.000000
C	13	1.418182	11	121.286124	10	0.000000
C	14	1.368859	13	120.060713	11	0.000000
H	7	1.085400	3	120.148250	2	0.000000
H	1	1.085497	2	117.205039	3	180.000000
H	2	1.101786	1	107.799292	6	-124.661354
H	5	1.086207	4	118.348002	3	180.000000
H	6	1.082671	1	120.880352	2	180.000000
H	8	1.085112	4	119.110324	3	180.000000
H	13	1.083867	11	119.567690	10	180.000000
H	14	1.082946	13	119.532146	11	180.000000
H	15	1.084048	14	120.796350	13	180.000000
H	2	1.101786	1	107.799292	6	124.661354

Table A.9: Protonated anthracene (2–$C_{14}H_{11}^{+}$) Z-Matrix.

Atom 1	Atom 2	Bond, Å	Atom 3	Angle, °	Atom 4	Dihedral Angle, °
C						
C	1	1.470852				
C	2	1.373405	1	122.499303		
C	3	1.461045	2	119.639274	1	0.000000
C	4	1.446288	3	118.819264	2	0.000000
C	5	1.345776	4	121.680143	3	0.000000
C	3	1.425471	2	120.538285	1	180.000000
C	4	1.376667	3	118.384766	2	180.000000
C	8	1.417533	4	121.864294	3	0.000000
C	7	1.383412	3	121.227119	2	180.000000
C	10	1.432854	7	121.737433	3	180.000000
H	11	1.084028	10	118.843158	7	0.000000
C	11	1.366052	10	120.256134	7	180.000000
C	13	1.421761	11	119.983428	10	0.000000
C	14	1.377650	13	121.548968	11	0.000000
H	7	1.085283	3	118.800838	2	0.000000
H	1	1.104819	2	108.298282	3	125.207578
H	2	1.086639	1	117.878499	6	180.000000
H	5	1.084132	4	117.885071	3	180.000000
H	6	1.083467	5	120.850716	4	180.000000
H	8	1.084449	4	119.633165	3	180.000000
H	13	1.082870	11	120.529047	10	180.000000
H	14	1.084041	13	118.987048	11	180.000000
H	15	1.083601	14	120.244026	13	180.000000
H	1	1.104819	2	108.298282	3	-125.207578

Table A.10: Protonated anthracene (9–$C_{14}H_{11}^{+}$) Z-Matrix.

Atom 1	Atom 2	Bond, Å	Atom 3	Angle, °	Atom 4	Dihedral Angle, °
C						
C	1	1.394050				
C	2	1.390144	1	120.384604		
C	3	1.426659	2	118.563098	1	0.000000
C	4	1.421758	3	120.213063	2	0.000000
C	5	1.376545	4	120.061211	3	0.000000
C	3	1.500143	2	121.279835	1	180.000000
C	4	1.405851	3	119.297043	2	180.000000
C	8	1.405754	4	124.242978	3	0.000000
C	9	1.426652	8	119.299897	4	0.000000
C	10	1.390096	9	118.567217	8	180.000000
H	11	1.084358	10	120.019811	9	180.000000
C	11	1.394074	10	120.385302	9	0.000000
C	13	1.405176	11	121.406514	10	0.000000
C	14	1.376488	13	119.373490	11	0.000000
H	7	1.098956	3	108.760842	2	56.468647
H	1	1.084108	2	119.220050	3	180.000000
H	2	1.084337	1	119.602837	6	180.000000
H	5	1.084148	4	119.192679	3	180.000000
H	6	1.082638	5	120.608464	4	180.000000
H	8	1.087236	4	117.880126	3	180.000000
H	13	1.084112	11	119.225093	10	180.000000
H	14	1.082633	13	120.022690	11	180.000000
H	15	1.084158	14	120.752494	13	180.000000
H	7	1.098957	3	108.760828	2	-56.468647

Table A.11: Phenanthrene ($C_{14}H_{10}$) Z-Matrix.

Atom 1	Atom 2	Bond, Å	Atom 3	Angle, °	Atom 4	Dihedral Angle, °
C						
C	1	1.378471				
C	2	1.413354	1	121.099608		
C	3	1.424475	2	119.606717	1	0.000000
C	4	1.413263	3	117.893357	2	0.000000
C	5	1.380988	4	121.472309	3	0.000000
C	3	1.434162	2	120.693861	1	180.000000
C	4	1.456723	3	119.103793	2	180.000000
C	8	1.424418	4	119.119975	3	0.000000
C	7	1.357291	3	121.194763	2	180.000000
C	9	1.413327	8	119.617736	4	180.000000
H	11	1.085131	9	118.616545	8	180.000000
C	11	1.378483	9	121.099180	8	0.000000
C	13	1.405687	11	119.543123	9	0.000000
C	14	1.380987	13	120.384090	11	0.000000
H	7	1.085024	3	118.339687	2	0.000000
H	1	1.084076	2	120.342319	3	180.000000
H	2	1.085155	1	120.282458	6	180.000000
H	5	1.082285	4	119.966771	3	180.000000
H	6	1.084211	5	119.725356	4	180.000000
H	10	1.085012	7	120.474034	3	180.000000
H	13	1.084075	11	120.345031	9	180.000000
H	14	1.084214	13	119.895385	11	180.000000
H	15	1.082261	14	118.565856	13	180.000000

Table A.12: Protonated phenanthrene (1–$C_{14}H_{11}^+$) Z-Matrix.

Atom 1	Atom 2	Bond, Å	Atom 3	Angle, °	Atom 4	Dihedral Angle, °
C						
C	1	1.475058				
C	2	1.495222	1	117.156059		
C	3	1.429831	2	119.928125	1	0.000000
C	4	1.397021	3	117.632924	2	0.000000
C	1	1.357960	2	121.068904	3	0.000000
C	3	1.396177	2	119.977555	1	180.000000
C	4	1.458290	3	119.954821	2	180.000000
C	8	1.429284	4	117.985263	3	0.000000
C	7	1.381595	3	120.200220	2	180.000000
C	9	1.416074	8	120.091030	4	180.000000
H	11	1.083990	9	118.970714	8	180.000000
C	11	1.376454	9	120.402602	8	0.000000
C	13	1.405888	11	119.610147	9	0.000000
C	14	1.384319	13	121.074294	11	0.000000
H	7	1.083982	3	119.908381	2	0.000000
H	1	1.084605	2	117.932331	3	180.000000
H	2	1.102707	1	108.543914	6	-124.640168
H	5	1.083506	4	118.850365	3	180.000000
H	6	1.082766	1	121.086017	2	180.000000
H	10	1.085082	7	119.266283	3	180.000000
H	13	1.082956	11	120.436629	9	180.000000
H	14	1.083552	13	119.585358	11	180.000000
H	15	1.082101	14	118.206244	13	180.000000
H	2	1.102707	1	108.543914	6	124.640168

Table A.13: Protonated phenanthrene (2–$C_{14}H_{11}^{+}$) Z-Matrix.

Atom 1	Atom 2	Bond, Å	Atom 3	Angle, °	Atom 4	Dihedral Angle, °
C						
C	1	1.468189				
C	2	1.371631	1	123.007747		
C	3	1.453814	2	119.369366	1	0.000000
C	4	1.438253	3	118.739306	2	0.000000
C	5	1.352055	4	121.934392	3	0.000000
C	3	1.443040	2	120.413984	1	180.000000
C	4	1.425593	3	118.728614	2	180.000000
C	8	1.438723	4	119.093138	3	0.000000
C	7	1.351442	3	120.404293	2	180.000000
C	9	1.404716	8	119.290368	4	180.000000
H	11	1.083654	9	119.084496	8	180.000000
C	11	1.382611	9	120.739391	8	0.000000
C	13	1.408608	11	120.515032	9	0.000000
C	14	1.374795	13	120.140008	11	0.000000
H	7	1.083471	3	118.420100	2	0.000000
H	1	1.104947	2	109.117261	3	-124.872435
H	2	1.085882	1	117.712241	6	180.000000
H	5	1.080344	4	119.305093	3	180.000000
H	6	1.083960	5	120.448393	4	180.000000
H	10	1.083716	7	120.591244	3	180.000000
H	13	1.083774	11	119.841247	9	180.000000
H	14	1.082905	13	119.841770	11	180.000000
H	15	1.080833	14	118.558351	13	180.000000
H	1	1.104947	2	109.117261	3	124.872435

Table A.14: Protonated phenanthrene (3–$C_{14}H_{11}^{+}$) Z-Matrix.

Atom 1	Atom 2	Bond, Å	Atom 3	Angle, °	Atom 4	Dihedral Angle, °
C						
C	1	1.349837				
C	2	1.437289	1	121.504799		
C	3	1.455246	2	120.547628	1	0.000000
C	4	1.368844	3	117.608897	2	0.000000
C	5	1.472927	4	123.494302	3	0.000000
C	3	1.402309	2	119.988905	1	180.000000
C	4	1.469299	3	119.529611	2	180.000000
C	8	1.426660	4	118.228638	3	0.000000
C	7	1.378836	3	120.535509	2	180.000000
C	9	1.413852	8	120.233021	4	180.000000
H	11	1.083994	9	119.042150	8	180.000000
C	11	1.378811	9	120.359355	8	0.000000
C	13	1.403063	11	119.474904	9	0.000000
C	14	1.388080	13	121.075577	11	0.000000
H	7	1.083173	3	119.380933	2	0.000000
H	1	1.083877	2	121.020169	3	180.000000
H	2	1.083861	1	120.641768	6	180.000000
H	5	1.083615	4	120.416548	3	180.000000
H	6	1.104827	5	108.822075	4	124.978246
H	10	1.085435	7	119.108259	3	180.000000
H	13	1.082886	11	120.465931	9	180.000000
H	14	1.083608	13	119.631552	11	180.000000
H	15	1.082239	14	118.231429	13	180.000000
H	6	1.104827	5	108.822075	4	-124.978246

Table A.15: Protonated phenanthrene (4–$C_{14}H_{11}^{+}$) Z-Matrix.

Atom 1	Atom 2	Bond, Å	Atom 3	Angle, °	Atom 4	Dihedral Angle, °
C						
C	1	1.414522				
C	2	1.400366	1	124.034567		
C	3	1.425577	2	119.275536	1	0.000000
C	4	1.496064	3	118.412385	2	0.000000
C	1	1.359082	2	118.975596	3	0.000000
C	3	1.434704	2	120.212430	1	180.000000
C	4	1.415902	3	119.543093	2	180.000000
C	8	1.438788	4	118.792358	3	0.000000
C	7	1.357530	3	120.045392	2	180.000000
C	9	1.409865	8	119.139024	4	180.000000
H	11	1.083749	9	119.007502	8	180.000000
C	11	1.378720	9	120.716313	8	0.000000
C	13	1.413083	11	120.540746	9	0.000000
C	14	1.372471	13	120.247478	11	0.000000
H	7	1.083473	3	118.883919	2	0.000000
H	1	1.082629	2	119.722248	3	180.000000
H	2	1.086326	1	118.232708	6	180.000000
H	5	1.101896	4	110.145502	3	123.648080
H	6	1.084860	1	120.841278	2	180.000000
H	10	1.083752	7	120.510711	3	180.000000
H	13	1.083638	11	119.922542	9	180.000000
H	14	1.083081	13	119.677417	11	180.000000
H	15	1.082535	14	118.943540	13	180.000000
H	5	1.101896	4	110.145502	3	-123.648080

Table A.16: Protonated phenanthrene (9–$C_{14}H_{11}^+$) Z-Matrix.

Atom 1	Atom 2	Bond, Å	Atom 3	Angle, °	Atom 4	Dihedral Angle, °
C						
C	1	1.387024				
C	2	1.395878	1	120.545143		
C	3	1.418994	2	120.003489	1	0.000000
C	4	1.414289	3	118.352881	2	0.000000
C	5	1.380516	4	120.916427	3	0.000000
C	3	1.495940	2	119.564894	1	180.000000
C	4	1.453414	3	119.668931	2	180.000000
C	8	1.454793	4	120.291054	3	0.000000
C	9	1.372561	8	119.859447	4	0.000000
C	9	1.438144	8	120.542370	4	180.000000
H	11	1.084022	9	118.423935	8	180.000000
C	11	1.364187	9	120.472239	8	0.000000
C	13	1.416186	11	118.825375	9	0.000000
C	14	1.384560	13	122.337737	11	0.000000
H	7	1.103694	3	110.793487	2	56.406843
H	1	1.083425	2	119.929275	3	180.000000
H	2	1.084633	1	119.854537	6	180.000000
H	5	1.081033	4	120.497171	3	180.000000
H	6	1.083025	5	119.875098	4	180.000000
H	10	1.086570	9	119.285883	8	180.000000
H	13	1.082451	11	121.136248	9	180.000000
H	14	1.084548	13	118.908638	11	180.000000
H	15	1.080279	14	118.314757	13	180.000000
H	7	1.103694	3	110.793487	2	-56.406843

Table A.17: Pyrene ($C_{16}H_{10}$) Z-Matrix.

Atom 1	Atom 2	Bond, Å	Atom 3	Angle, °	Atom 4	Dihedral Angle, °
C						
C	1	1.391972				
C	2	1.402633	1	120.739411		
C	3	1.426444	2	119.022027	1	0.000000
C	4	1.426438	3	119.872623	2	0.000000
C	1	1.391990	2	120.604218	3	0.000000
C	3	1.436672	2	122.403096	1	180.000000
C	4	1.425474	3	120.063823	2	180.000000
C	8	1.426442	4	120.061143	3	0.000000
C	7	1.359189	3	121.363114	2	180.000000
C	9	1.402616	8	119.026347	4	180.000000
H	11	1.084904	9	119.192936	8	180.000000
C	11	1.391981	9	120.732880	8	0.000000
C	13	1.391970	11	120.604589	9	0.000000
C	14	1.402620	13	120.740171	11	0.000000
C	15	1.436675	14	122.405817	13	180.000000
C	16	1.359181	15	121.363180	14	180.000000
H	17	1.085067	16	120.309077	15	180.000000
H	16	1.085075	15	118.340550	14	0.000000
H	7	1.085085	3	118.339160	2	0.000000
H	1	1.084285	2	119.695651	3	180.000000
H	2	1.084924	1	120.065041	6	180.000000
H	6	1.084910	1	120.073577	2	180.000000
H	10	1.085068	7	120.310576	3	180.000000
H	13	1.084278	11	119.697237	9	180.000000
H	14	1.084911	13	120.063643	11	180.000000

Table A.18: Protonated pyrene (1–$C_{16}H_{11}^{+}$) Z-Matrix.

Atom 1	Atom 2	Bond, Å	Atom 3	Angle, °	Atom 4	Dihedral Angle, °
C						
C	1	1.484870				
C	2	1.495981	1	116.069518		
C	3	1.414417	2	119.884321	1	0.000000
C	4	1.433524	3	120.512709	2	0.000000
C	1	1.348258	2	122.403726	3	0.000000
C	3	1.405577	2	120.558883	1	180.000000
C	4	1.419838	3	119.807855	2	180.000000
C	8	1.419956	4	120.025833	3	0.000000
C	7	1.379499	3	120.814162	2	180.000000
C	9	1.412935	8	119.069663	4	180.000000
H	11	1.084554	9	119.124196	8	180.000000
C	11	1.389014	9	120.955320	8	0.000000
C	13	1.393620	11	120.082406	9	0.000000
C	14	1.407498	13	120.899101	11	0.000000
C	15	1.421901	14	122.171238	13	180.000000
C	16	1.377167	15	121.470626	14	180.000000
H	17	1.083416	16	120.008081	15	180.000000
H	16	1.084811	15	118.824382	14	0.000000
H	7	1.084157	3	119.425269	2	0.000000
H	1	1.084400	2	117.236511	3	180.000000
H	2	1.101319	1	109.050961	6	-123.962510
H	6	1.083807	1	120.603305	2	180.000000
H	10	1.084577	7	119.796588	3	180.000000
H	13	1.082770	11	119.992475	9	180.000000
H	14	1.084523	13	119.870945	11	180.000000
H	2	1.101319	1	109.050961	6	123.962510

Table A.19: Protonated pyrene (2–$C_{16}H_{11}^{+}$) Z-Matrix.

Atom 1	Atom 2	Bond, Å	Atom 3	Angle, °	Atom 4	Dihedral Angle, °
C						
C	1	1.470333				
C	2	1.370219	1	122.014273		
C	3	1.449838	2	119.169522	1	0.000000
C	4	1.449797	3	120.877687	2	0.000000
C	5	1.370208	4	119.187924	3	0.000000
C	3	1.444090	2	121.766917	1	180.000000
C	4	1.404630	3	119.557230	2	180.000000
C	8	1.436828	4	120.047808	3	0.000000
C	7	1.353812	3	120.807526	2	180.000000
C	9	1.396269	8	118.875480	4	180.000000
H	11	1.083632	9	119.501513	8	180.000000
C	11	1.394449	9	120.551358	8	0.000000
C	13	1.394442	11	121.238994	9	0.000000
C	14	1.396281	13	120.563951	11	0.000000
C	15	1.437984	14	121.863348	13	180.000000
C	16	1.353803	15	121.250554	14	180.000000
H	17	1.083581	16	120.875361	15	180.000000
H	16	1.083857	15	118.337050	14	0.000000
H	7	1.083598	3	118.324929	2	0.000000
H	1	1.105615	2	109.416144	3	124.925482
H	2	1.084883	1	117.889640	6	180.000000
H	6	1.084883	5	120.094581	4	180.000000
H	10	1.083847	7	120.424528	3	180.000000
H	13	1.083778	11	119.379209	9	180.000000
H	14	1.083611	13	119.928590	11	180.000000
H	1	1.105614	2	109.416162	3	-124.925482

Table A.20: Protonated pyrene (4–$C_{16}H_{11}^{+}$) Z-Matrix.

Atom 1	Atom 2	Bond, Å	Atom 3	Angle, °	Atom 4	Dihedral Angle, °
C						
C	1	1.403163				
C	2	1.383145	1	120.462718		
C	3	1.424514	2	119.424834	1	0.000000
C	4	1.430585	3	119.996056	2	0.000000
C	1	1.385091	2	120.932708	3	0.000000
C	3	1.500997	2	121.360907	1	180.000000
C	4	1.418265	3	120.735705	2	180.000000
C	8	1.452571	4	121.170269	3	0.000000
C	9	1.372498	8	119.175629	4	0.000000
C	9	1.430775	8	119.986412	4	180.000000
H	11	1.084010	9	118.930752	8	180.000000
C	11	1.373249	9	120.150324	8	0.000000
C	13	1.406652	11	119.749260	9	0.000000
C	14	1.402902	13	122.902081	11	0.000000
C	15	1.435077	14	121.963798	13	180.000000
C	16	1.358524	15	120.464711	14	180.000000
H	17	1.083899	16	120.295556	15	180.000000
H	16	1.083575	15	118.776176	14	0.000000
H	7	1.103321	3	110.887915	2	56.559860
H	1	1.083491	2	119.316120	3	180.000000
H	2	1.084600	1	119.468008	6	180.000000
H	6	1.083747	1	120.135217	2	180.000000
H	10	1.086607	9	119.435423	8	180.000000
H	13	1.082628	11	120.614238	9	180.000000
H	14	1.085420	13	118.748334	11	180.000000
H	7	1.103321	3	110.887948	2	-56.559860

A.2 Vibrational Frequencies

The scaling factors are determined to be 0.9619 for C–H stretching vibrations (frequencies above 2000 cm^{-1}) and 0.9815 for lower frequency vibrations by comparing gas phase experimental and B3LYP 6–311++G(d,p) calculated frequencies for neutral benzene and anthracene (Tables A.21, A.22).

Table A.21: Scaling of the benzene molecule vibrational frequencies.

Mode	Symmetry	Experimental, cm^{-1}	Calculated, cm^{-1}
ν_{16}	e_{2u}	398.131	409.2508
ν_6	e_{2g}	608.13	622.2075
ν_{11}	a_{2u}	673.9747	686.4609
ν_4	b_{2g}	702.24	719.2481
ν_{10}	e_{1g}	847.1062	863.6909
ν_{17}	e_{2u}	967.98	980.5364
ν_5	b_{2g}	992.93	1010.6745
ν_1	a_{1g}	993.071	1011.0642
ν_{12}	b_{1u}	1013.74	1022.4331
ν_{18}	e_{1u}	1038.267	1058.9918
ν_{15}	b_{2u}	1147.6751	1174.6646
ν_9	e_{2g}	1177.776	1197.1716
ν_{14}	b_{2u}	1309.4	1335.6178
ν_3	a_{2g}	1350	1380.8794
ν_{19}	e_{1u}	1483.9854	1510.0520
ν_8	e_{2g}	1609.518	1633.1875
ν_{20}	e_{1u}	3047.908	3154.9144
ν_{13}	b_{1u}	3057	3181.3283
ν_7	e_{2g}	3057.04	3181.6125
ν_2	a_{1g}	3073.942	3191.8678

Experimental data taken from [111].

Table A.22: Scaling of the anthracene molecule vibrational frequencies.

Mode	Symmetry	Experimental, cm^{-1}	Calculated, cm^{-1}
ν_{64}	b_{3u}	465.2	476.961
ν_{49}	b_{2u}	601.4	617.0831
ν_{63}	b_{3u}	725.3	739.3821
ν_{48}	b_{2u}	794.8	820.8065
ν_{62}	b_{3u}	876.7	864.1561
ν_{30}	b_{1u}	907.8	911.1968
ν_{61}	b_{3u}	954.2	972.5292
ν_{47}	b_{2u}	996	1026.1756
ν_{46}	b_{2u}	1128	1159.9346
ν_{29}	b_{1u}	1150.4	1172.6212
ν_{45}	b_{2u}	1165.5	1189.8674
ν_{28}	b_{1u}	1271.3	1290.8509
ν_{27}	b_{1u}	1316.5	1338.2374
ν_{44}	b_{2u}	1341.7	1377.5670
ν_{43}	b_{2u}	1396.8	1416.7486
ν_{26}	b_{1u}	1450	1480.8151
ν_{42}	b_{2u}	1476	1486.1868
ν_{41}	b_{2u}	1539.6	1578.3891
ν_{25}	b_{1u}	1626	1667.6092
ν_{24}	b_{1u}	3028	3157.7870
ν_{23}	b_{1u}	3052	3165.7045
ν_{22}	b_{1u}	3061	3189.7013
ν_{39}	b_{2u}	3067	3190.0427

Experimental data taken from [112].

Table A.23: Benzene and protonated benzene: scaled vibrational frequencies and IR intensities.

C_6H_6		$C_6H_7^+$	
ν, cm^{-1}	IR int	ν, cm^{-1}	IR int
401.6797	0.0000	207.0374	12.1219
402.4736	0.0013	323.8184	0.0000
610.6967	0.0000	406.2831	1.5535
610.7172	0.0000	579.2896	5.4868
673.7614	122.0287	584.4683	0.0265
705.9420	0.0000	647.6300	57.2190
845.1487	0.0000	791.8260	0.0000
847.7126	0.0000	832.6574	16.0955
961.0158	0.0000	882.0701	13.8096
962.3965	0.0041	971.7421	16.5344
991.9770	0.0004	982.5926	0.4828
992.3595	0.0000	992.5469	0.0000
1003.5181	0.0000	995.5653	0.2352
1039.0731	6.3651	1027.9043	0.0152
1039.4005	6.3744	1048.1727	2.5553
1152.9333	0.0000	1129.6961	0.3245
1175.0239	0.0001	1131.1016	0.0000
1175.2203	0.0001	1183.2846	19.5856
1310.9089	0.0002	1190.0769	23.3059
1355.3331	0.0000	1257.4158	113.9668
1482.1160	7.1996	1336.8588	14.3341
1482.3507	7.1487	1393.8416	6.8657
1602.9325	0.0002	1448.8265	175.8423
1602.9735	0.0005	1457.2509	26.4624
3034.7122	0.0463	1541.7174	2.1079
3044.9359	0.0051	1608.1701	74.4622
3045.1460	0.0073	2833.8540	24.0384
3060.1197	36.9916	2839.2640	62.5214
3060.3931	37.1709	3059.5157	0.1546
3070.2576	0.0343	3067.5970	2.5411
		3068.8847	5.5714
		3086.0872	6.7612
		3088.2879	1.7803

Table A.24: Naphthalene and protonated naphthalene: scaled vibrational frequencies and IR intensities.

$C_{10}H_8$		1–$C_{10}H_9^+$		2–$C_{10}H_9^+$	
ν, cm^{-1}	IR int	ν, cm^{-1}	IR int	ν, cm^{-1}	IR int
169.4145	2.8104	115.0238	0.4088	134.2035	5.7151
181.4778	0.0000	169.8269	1.5821	166.2855	0.7202
358.3695	1.8304	242.3699	11.6633	260.9555	1.8114
388.2838	0.0003	350.0190	0.9599	355.7677	2.4700
469.5430	0.0001	399.2639	0.0106	371.0291	1.1248
479.2424	24.1588	427.0042	13.0135	439.1710	3.9478
509.1167	0.0051	486.2705	0.1248	481.1385	21.2405
510.1492	0.0007	492.1717	0.4450	493.5473	4.0892
619.6614	0.0000	495.1976	16.5382	500.4934	0.6442
623.4749	3.2877	599.8496	2.0755	607.4839	1.3968
715.1633	0.0022	662.0221	0.0075	660.0737	2.2940
758.1406	0.0001	730.8713	28.0030	733.5593	4.2081
767.6320	0.0001	735.0980	4.4553	767.5992	34.0881
782.9871	122.5348	776.5801	61.6570	770.8273	4.1169
793.5282	0.3215	783.9355	0.2020	789.7835	12.6599
832.9490	0.0000	849.4712	7.4023	799.7599	20.4370
878.2911	0.0049	909.1840	0.9372	894.4784	9.5482
932.8070	0.0038	912.8521	1.3963	911.6343	25.0571
943.7688	0.0013	953.7979	12.8250	920.3033	0.1440
962.1320	3.5108	979.7361	0.0494	941.7730	20.2299
971.4251	0.0004	1002.8414	5.0216	992.8974	2.6962
979.6829	0.0053	1016.2134	0.3066	1005.8365	1.0672
1015.1555	11.0855	1023.1885	0.0330	1018.1834	2.4280
1025.6051	0.0006	1028.7145	2.5254	1018.9470	0.9761
1129.0893	6.7544	1091.1212	8.4447	1032.6991	14.6466
1147.6323	0.7540	1133.5737	6.1211	1140.4693	5.1158
1149.4143	0.0008	1159.2722	0.8416	1142.4153	0.0952
1163.2484	0.0001	1169.3644	32.8669	1161.8284	20.6217
1208.3148	0.7037	1177.0096	9.5891	1180.2637	18.5647
1245.7875	0.0106	1194.0854	9.3836	1212.1639	5.6154
1262.7006	7.3088	1244.4128	23.9391	1246.2730	6.5326
1364.6736	0.9743	1272.7489	23.7537	1282.3671	68.8119
1371.7347	0.0051	1320.2167	111.1756	1300.1806	109.8671
1390.5500	4.2261	1348.3846	43.0687	1353.4166	34.2552
1461.1824	0.0000	1367.6470	57.7761	1392.1690	98.5422
1461.4239	0.0081	1419.0089	37.1812	1403.9551	8.0366
1517.4368	7.9027	1442.8935	1.8160	1438.3395	1.1747
1581.8685	0.0049	1458.4152	130.5548	1472.0554	126.0498

— continued on the next page —

$C_{10}H_8$		$1\text{–}C_{10}H_9^+$		$2\text{–}C_{10}H_9^+$	
ν, cm^{-1}	IR int	ν, cm^{-1}	IR int	ν, cm^{-1}	IR int
1606.6887	2.6276	1512.8755	237.3922	1504.3483	30.6534
1636.8155	0.0100	1553.5685	14.5643	1544.3416	4.1690
3036.0010	0.0268	1577.4620	64.4722	1606.5400	29.5076
3037.8480	7.0148	1622.2347	89.2320	1629.3655	241.6182
3040.1955	0.3076	2863.1685	26.2422	2846.5401	10.2962
3042.1915	0.0292	2868.2406	6.8228	2848.6604	53.4301
3053.1975	0.0257	3051.0111	0.3846	3052.8251	0.7085
3054.3243	58.9447	3059.7462	0.1149	3063.5692	0.1470
3065.3029	42.4607	3062.4287	1.4124	3066.1493	1.1471
3066.5056	0.0044	3066.9603	0.0700	3068.5941	0.1373
		3072.3632	0.1745	3077.0909	0.2662
		3086.2220	2.8842	3081.3179	0.5111
		3086.8465	0.1351	3088.0533	0.4251

Table A.25: Anthracene and protonated anthracene: scaled vibrational frequencies and IR intensities.

$C_{14}H_{10}$		$1\text{–}C_{14}H_{11}^{+}$		$2\text{–}C_{14}H_{11}^{+}$		$9\text{–}C_{14}H_{11}^{+}$	
ν, cm^{-1}	IR int	ν, cm^{-1}	IR int	ν, cm^{-1}	IR int	ν, cm^{-1}	IR int
90.6821	1.3556	70.4991	0.2308	81.0081	3.5138	52.4500	0.0381
118.9177	0.0007	102.3111	2.5679	107.3786	0.1345	103.8544	0.0005
231.6094	1.4742	165.4247	3.6131	187.9503	0.2570	176.0060	6.0420
233.5255	0.0002	228.8075	1.2144	230.6508	2.8025	221.8039	0.0036
261.1006	0.0000	251.6879	0.0927	242.4070	0.3530	230.7709	0.2675
382.1054	0.0382	275.5286	2.6684	296.2451	1.6753	314.6469	9.1203
388.3877	0.0003	380.2106	0.2830	382.0541	0.2912	374.6915	0.2133
390.2435	0.0001	388.4608	7.3321	383.8827	1.7159	377.8337	2.9451
468.1372	25.9027	403.2874	5.4686	388.9133	1.4807	407.4422	8.9731
476.2223	0.5999	425.4458	7.6603	436.2109	13.3598	439.2496	0.1560
501.7094	0.0089	474.1534	11.6914	461.6315	14.5126	484.6544	0.0271
525.3630	0.0002	503.7022	0.0121	504.2975	0.1064	512.6018	0.8791
580.9104	0.0002	513.3926	28.7446	516.0975	4.5531	524.3009	32.7964
605.6671	8.4296	576.6563	1.0079	592.2181	4.6479	595.7877	2.9941
629.9297	0.0001	618.1799	2.5412	618.1121	0.3902	607.6497	17.4426
649.0252	0.5412	642.7178	0.2692	639.5392	7.7584	658.2665	19.3567
725.7035	90.3199	644.6349	5.7943	640.5587	18.3765	661.9430	0.1347
745.6664	0.0142	717.5431	25.3305	730.8010	3.4168	723.8486	0.3923
749.4274	0.0005	735.3701	7.6471	748.2718	6.5237	731.5772	0.0516
755.8735	0.0009	750.8957	13.2480	756.6004	44.7187	768.4203	93.4549
770.9059	0.0006	759.2296	29.6253	769.5847	0.0027	778.3522	0.4468
805.6216	0.1077	792.5464	3.5126	793.7256	3.8758	800.0035	5.4294
824.4049	0.0002	846.0901	1.4324	794.6408	3.7219	845.0529	0.6468
848.1692	0.0018	875.3600	3.4960	860.9030	0.1399	881.7706	0.0239
881.2327	63.5914	890.7972	1.6421	884.0419	25.6619	884.7373	0.1553
894.3397	0.0219	902.0789	0.8655	897.7396	9.7448	899.2555	0.1569
901.7842	1.9277	907.9225	40.0565	898.3674	10.7665	922.8449	12.8563
912.1253	0.0001	925.3737	0.3822	908.2952	15.8457	967.2480	0.7584
954.5374	0.0337	947.9224	24.6308	914.5663	22.3771	979.1555	0.0272
959.1014	5.6996	979.9649	1.2422	953.5934	30.7861	997.8273	10.6462
974.8280	0.0001	996.0797	4.1938	982.9509	4.0744	1013.2228	0.1865
976.7700	0.0070	1006.9014	0.1624	995.2328	0.5992	1013.5434	0.6463
1007.1914	8.6096	1013.1386	0.8739	1008.2669	0.3509	1032.8158	1.7735
1011.6642	0.0010	1018.7456	1.1545	1014.8512	4.8722	1033.3012	2.0425
1105.1936	0.0002	1063.8511	14.4432	1022.7683	10.2104	1105.2782	0.0017
1138.4758	1.8229	1133.4439	3.0242	1127.2229	4.0393	1138.4095	8.9628
1150.9277	7.9588	1159.3612	4.5993	1152.4063	0.0641	1164.8411	84.5565
1166.8837	1.7153	1171.8186	2.7104	1160.1667	1.5577	1176.2010	7.9884

— continued on the next page —

$C_{14}H_{10}$		$1\text{–}C_{14}H_{11}^{+}$		$2\text{–}C_{14}H_{11}^{+}$		$9\text{–}C_{14}H_{11}^{+}$	
ν, cm^{-1}	IR int	ν, cm^{-1}	IR int	ν, cm^{-1}	IR int	ν, cm^{-1}	IR int
1167.8549	0.0002	1175.8036	0.6944	1173.9367	39.6052	1184.2331	18.9987
1188.4965	0.0001	1179.1241	22.3166	1186.1471	7.9572	1191.4008	0.1469
1265.5488	0.0279	1194.2698	90.3276	1198.2107	65.5581	1193.5940	0.8249
1266.9702	5.4406	1242.5586	56.7125	1242.0685	19.2167	1207.8722	58.1882
1270.4910	0.0009	1272.3748	11.8002	1277.4508	12.1036	1254.2262	0.6617
1313.4800	4.8217	1295.1931	4.4584	1292.8219	6.1357	1287.8226	0.6233
1352.0820	3.8821	1296.2105	3.5787	1308.6672	69.3597	1294.9944	25.4321
1387.4732	0.0004	1346.1972	129.9891	1329.1923	121.4536	1338.0471	191.5836
1390.5388	1.7148	1356.3985	35.2136	1353.7433	23.5427	1368.0035	22.5466
1402.4687	0.0010	1380.9868	139.6458	1392.6826	192.7469	1372.2968	36.3942
1453.4200	1.0785	1397.3178	15.2257	1401.5619	0.9555	1376.1459	38.1824
1458.6923	1.4026	1423.8461	12.4377	1409.8216	43.3518	1429.4762	43.0552
1488.2130	0.0002	1442.5450	11.4800	1437.0955	19.6411	1460.4157	27.6703
1549.1889	6.8078	1455.4923	315.2885	1467.9159	72.9368	1461.4459	172.5045
1564.2774	0.0021	1492.5786	1.2990	1487.6098	24.0765	1498.1171	17.7025
1592.2151	0.0011	1516.6483	432.8844	1533.6015	25.3365	1526.9723	333.9746
1636.7584	2.2566	1545.5191	99.6921	1552.3349	53.5095	1562.7378	12.4701
1638.1398	1.9693	1579.8629	99.3710	1596.8177	62.0961	1567.1575	37.8833
3035.5251	6.2658	1616.2389	13.6839	1621.4964	468.4955	1606.6280	465.5735
3037.4753	0.0070	1630.0135	239.0029	1641.9146	147.5208	1621.2268	22.8080
3039.0372	0.0228	2869.2120	13.6976	2851.7368	4.2058	2889.8988	5.3718
3040.1899	14.3112	2876.6619	2.2066	2853.1486	45.1824	2909.4276	2.3259
3043.4351	0.0195	3047.7182	1.4657	3049.2952	0.0527	3043.5688	0.2756
3045.0912	0.0036	3052.0445	1.4101	3057.8757	0.0645	3059.6297	0.4408
3056.5217	0.8022	3056.7136	0.2753	3059.8703	0.0859	3060.0267	0.3601
3056.8791	58.1490	3058.7498	0.3353	3062.2724	1.9275	3065.2655	0.5332
3068.1737	51.2160	3059.7848	0.2688	3063.4827	0.7386	3066.3259	0.4517
3068.5021	0.0259	3063.2490	0.2375	3066.8913	0.0191	3074.0746	0.3602
		3073.2910	2.0092	3076.7803	1.1404	3075.0717	0.2486
		3083.8449	1.3084	3079.1873	0.5177	3088.7548	0.2418
		3084.6358	0.2419	3087.1170	0.4328	3089.0265	0.1823

Table A.26: Phenanthrene and protonated phenanthrene: scaled vibrational frequencies and IR intensities.

$C_{14}H_{10}$		1–$C_{14}H_{11}^{+}$		2–$C_{14}H_{11}^{+}$	
ν, cm^{-1}	IR int	ν, cm^{-1}	IR int	ν, cm^{-1}	IR int
94.1967	0.0033	66.8310	0.4078	77.8542	3.0516
99.2912	0.9067	98.6964	2.0581	89.8509	0.7524
223.1468	4.1778	157.7058	0.4744	186.4559	0.2077
238.5203	0.0003	213.0964	4.1247	218.4536	4.4060
242.9889	0.4580	235.8947	1.5378	246.0627	1.1656
394.2872	0.0018	279.8484	10.7683	295.4089	2.3895
403.6186	0.5392	384.2937	0.2044	366.0720	1.1431
428.9911	8.0648	394.0992	3.8387	402.5492	4.2092
437.9531	1.9032	428.4114	3.0333	416.8031	12.4927
496.5687	1.0243	434.9084	3.8347	433.9158	0.6284
497.6790	5.6189	486.5031	1.0467	481.1466	1.6061
533.9579	0.0116	487.3224	1.9428	486.4599	0.5875
546.5301	0.2733	499.0529	4.5097	535.6937	2.7991
587.0511	0.0002	542.7338	17.2577	536.0105	0.3361
631.9821	5.3449	602.1786	0.6744	599.7317	8.3489
709.4696	0.0716	627.1811	9.3719	633.1490	4.1356
710.2180	2.1936	685.6043	1.7118	689.6513	8.2423
713.3346	2.0777	705.8554	0.0620	700.6441	1.2351
733.4026	89.9634	717.6209	22.3442	724.6895	9.5247
753.8650	0.0422	738.6946	3.0845	751.1034	52.1083
784.0600	0.0082	759.9602	47.8919	791.2935	12.8500
812.8769	60.4701	821.7176	4.6482	795.6133	18.9122
827.3557	0.0612	829.0989	39.3086	812.6907	7.2791
860.4947	0.1014	867.3581	2.1852	818.3090	9.8546
865.2298	10.6824	871.1894	4.2033	852.1372	1.9636
871.2405	2.0618	888.7542	3.2588	877.6763	10.0076
942.2343	0.0220	941.6789	15.1545	922.0052	27.8659
950.5919	3.0042	967.1783	0.1676	933.6127	20.6802
966.1769	0.0196	984.7964	2.1972	972.2705	1.6940
976.5710	0.0134	994.5599	5.8541	984.7952	0.4064
977.9282	0.0138	994.6051	0.5520	988.7993	7.9596
997.7435	2.5449	1004.5687	0.4170	999.5386	0.9301
1040.5756	7.2705	1008.5462	0.5162	1008.7296	0.4787
1041.1145	1.6881	1040.8573	1.5861	1026.0300	14.9448
1093.7494	2.2897	1063.0781	1.8768	1041.6504	5.7341
1143.4660	2.2286	1120.9165	4.4267	1110.0456	11.0717
1151.6246	0.0295	1158.1179	24.2629	1143.4355	0.0053

— continued on the next page —

$C_{14}H_{10}$		1–$C_{14}H_{11}^{+}$		2–$C_{14}H_{11}^{+}$	
ν, cm^{-1}	IR int	ν, cm^{-1}	IR int	ν, cm^{-1}	IR int
1163.9952	0.1991	1161.9644	1.1146	1158.8326	6.4067
1167.0895	0.4953	1169.4978	1.1270	1167.1523	23.8018
1201.5408	1.8410	1180.2455	4.3025	1179.6339	12.7273
1218.6117	0.5131	1203.2989	8.9504	1206.5033	1.3420
1242.3857	10.2436	1233.7048	20.7813	1220.6362	20.7024
1279.9567	0.0045	1250.8571	79.8095	1257.3717	26.2570
1299.8082	2.5612	1282.9118	11.3405	1282.2228	11.3503
1342.7728	0.1215	1302.4900	5.8559	1308.3848	127.4549
1349.2786	0.7828	1326.1043	217.1552	1330.7162	90.1603
1417.3657	0.4096	1346.5572	312.6771	1355.1865	14.7231
1423.0397	1.2301	1359.6256	6.8524	1369.6733	112.5547
1442.6138	3.5413	1390.9642	200.7722	1406.3337	41.5622
1461.7055	10.5507	1423.9572	14.8492	1420.4206	4.1091
1505.2961	5.9138	1449.6666	1.1361	1440.4158	10.4778
1531.6928	1.8858	1456.8742	31.9259	1467.0203	108.8570
1576.6635	0.0790	1507.4256	51.1561	1477.4480	107.8114
1610.3195	1.8366	1530.5348	204.1641	1532.6130	10.1197
1622.4005	0.0971	1546.2847	27.3673	1551.0334	23.5177
1627.2943	0.1731	1574.5060	135.7502	1599.7978	224.8536
3036.2905	0.1077	1609.9637	1.0527	1618.4424	94.9944
3039.0293	3.3461	1616.2117	49.5613	1627.6335	108.0935
3040.0193	1.7506	2867.0308	30.7786	2852.5979	7.0315
3048.6770	0.0697	2874.0203	5.3546	2853.1429	49.0977
3049.8867	13.4446	3055.1147	0.0577	3054.3693	0.2865
3055.5026	33.1547	3061.9167	0.7137	3061.8476	0.2341
3061.6454	37.5327	3064.4682	2.2472	3063.9347	0.2851
3064.6472	0.8129	3066.6230	0.4275	3069.8651	0.9510
3071.4832	14.1301	3068.6839	0.3912	3072.5380	0.2769
3083.3012	19.3960	3073.4131	0.9389	3077.5952	0.5478
		3081.1743	1.9590	3080.6354	0.6591
		3085.4837	0.4133	3091.2866	0.4981
		3088.5864	0.6645	3108.2634	0.5539

— continued on the next page —

3–$C_{14}H_{11}^+$		4–$C_{14}H_{11}^+$		9–$C_{14}H_{11}^+$	
ν, cm^{-1}	IR int	ν, cm^{-1}	IR int	ν, cm^{-1}	IR int
67.9947	0.7722	82.5920	0.0418	68.4213	0.3489
98.5772	1.0773	102.3673	0.9208	89.4593	0.1729
185.4722	8.4139	170.6658	6.4054	174.6351	8.9753
226.1071	0.0598	215.7809	2.0827	218.9379	3.2365
237.5229	0.3890	229.2664	1.0655	242.6537	1.8744
282.0925	0.0002	273.5060	7.1988	265.0713	0.8130
394.5469	4.3574	396.4172	3.8341	393.6559	6.6158
396.6824	2.8436	401.1307	10.8642	412.8374	7.7328
407.0016	3.7319	431.5685	0.7363	428.1788	0.0147
433.7555	0.9466	434.8214	0.1069	429.8925	0.7838
490.8570	4.4328	487.4470	1.7129	465.2069	0.8464
491.7979	6.8949	487.8313	1.5712	488.8239	2.4661
511.4307	3.3446	518.8698	3.2033	517.9534	3.3654
538.4446	5.7051	532.6294	5.4806	537.3154	0.2199
601.7457	4.1965	597.4887	0.7408	612.2059	2.6280
640.5680	23.0381	628.3979	0.7553	670.3057	1.5372
695.1468	0.3791	684.2585	17.2016	689.4227	4.3614
706.4309	3.5485	706.1690	3.2121	694.8828	11.7230
726.6655	0.7419	712.6530	47.0578	716.3663	23.0627
759.7846	45.3178	745.0416	21.3160	759.9382	11.6892
778.3826	0.0059	767.9317	8.7694	772.8323	82.6562
803.6541	0.0376	809.7642	29.2338	800.2659	6.2465
815.6690	1.4822	822.1024	0.7905	806.1470	2.5926
858.3347	25.2080	845.0012	0.1111	851.0204	0.3472
861.5825	1.0793	874.0899	19.6783	868.8398	5.9128
880.2520	20.1095	884.7413	12.0839	878.5173	0.0033
913.7954	31.5725	951.8956	13.2277	951.8135	1.9611
937.7633	22.0480	971.6525	0.1309	970.4054	0.0149
969.1507	2.3836	981.7815	1.5604	988.5470	0.7264
988.7445	3.9067	992.2869	5.3997	993.5013	4.1198
997.5475	0.0105	993.6547	1.4459	1005.9900	0.3402
1004.8626	0.1122	1004.2919	0.3685	1014.9348	0.4616
1006.0397	0.0095	1014.7714	0.0003	1025.2669	13.7296
1033.8640	4.3175	1032.3690	1.3793	1035.3078	14.4911
1045.6648	0.2482	1060.9424	6.8796	1047.9238	4.0291
1114.7411	2.0098	1121.6351	11.1129	1106.5516	1.0762
1149.2280	0.0014	1159.6033	7.4670	1149.3712	20.2114
1157.7243	20.0859	1162.1242	0.0922	1159.7551	1.2183
1166.3319	40.8071	1174.0277	5.3250	1176.8140	22.0567

— continued on the next page —

$3\text{–}C_{14}H_{11}^+$		$4\text{–}C_{14}H_{11}^+$		$9\text{–}C_{14}H_{11}^+$	
ν, cm^{-1}	IR int	ν, cm^{-1}	IR int	ν, cm^{-1}	IR int
1178.6581	5.0714	1178.0795	13.8555	1181.3182	43.9946
1221.7659	96.2017	1186.1501	9.4292	1187.1326	0.2769
1238.0347	22.3805	1220.7042	4.8264	1219.4820	5.5773
1259.8949	41.4472	1241.4692	19.3288	1256.6658	69.6261
1286.2212	8.5068	1274.6392	5.5811	1283.6424	1.8351
1296.0576	4.4107	1326.9125	6.5054	1308.1174	69.9866
1319.6674	155.1110	1356.5073	50.8937	1325.4735	111.5601
1344.9203	94.3402	1391.4536	44.1385	1332.7650	89.0793
1362.0603	33.0623	1391.4536	209.8578	1363.6392	13.3516
1404.3831	163.6224	1399.9653	118.6090	1389.2988	73.3719
1428.8197	0.6698	1415.0769	23.6905	1419.9175	16.1036
1441.5497	15.2252	1435.9622	56.1361	1453.8930	197.3566
1465.3018	82.1274	1455.9324	58.6101	1464.9969	23.4654
1513.9608	232.0720	1480.6514	227.3070	1480.3588	90.3283
1524.3456	12.7466	1520.5825	82.3635	1532.0905	39.3648
1552.5484	45.0630	1546.0982	32.9404	1551.1872	5.2345
1579.5118	224.7362	1587.9698	17.2206	1578.6360	24.8403
1606.8414	36.2921	1613.3280	41.8340	1611.4547	54.4120
1638.6240	94.8078	1626.2855	113.2273	1622.8728	222.2757
2851.5043	5.0708	2872.6139	12.8384	2858.2511	30.7022
2852.3017	35.5274	2882.1236	5.1109	2862.3105	5.1553
3056.5632	0.1851	3051.3575	0.8473	3049.2919	0.4121
3063.1680	0.4819	3061.8519	0.3702	3174.8125	1.4671
3064.1178	1.1686	3064.4351	0.2226	3063.9745	0.1645
3066.8565	0.0052	3065.4902	0.9536	3068.0785	0.0523
3073.6479	0.8403	3068.8017	0.0042	3069.9035	0.3538
3077.4879	0.0715	3076.7139	1.0855	3080.2951	0.7615
3079.8730	0.2102	3078.5850	1.2314	3088.2247	0.1210
3082.8876	1.2366	3085.7359	0.9976	3090.4592	0.6643
3087.9075	0.7155	3087.6694	0.5761	3106.8336	0.6655

Table A.27: Pyrene and protonated pyrene: scaled vibrational frequencies and IR intensities.

$C_{16}H_{10}$		1–$C_{16}H_{11}^{+}$		2–$C_{16}H_{11}^{+}$		4–$C_{16}H_{11}^{+}$	
ν, cm^{-1}	IR int	ν, cm^{-1}	IR int	ν, cm^{-1}	IR int	ν, cm^{-1}	IR int
97.1181	0.5821	95.5462	1.5344	83.3823	3.5085	78.6657	0.0415
148.5445	0.0009	110.9925	1.0065	138.6492	0.0001	127.2766	1.6657
208.6291	10.4254	188.6274	2.5206	202.0453	0.8603	183.3704	8.2686
243.5924	0.0001	195.5718	8.9718	213.1682	15.4343	208.5666	8.7083
257.3209	0.0005	249.6784	0.5228	228.6481	0.0007	244.5676	0.0549
351.8438	1.8199	324.7912	2.4638	287.7624	3.2037	271.6604	1.1672
395.9707	0.0005	343.7002	1.8267	350.8490	4.9552	347.2684	1.4075
404.1908	0.0001	400.9396	4.8102	371.2372	0.0001	395.5658	5.0511
453.7523	0.0002	402.3490	1.0714	399.3193	2.2867	419.7240	0.4333
490.5197	2.2572	449.6438	4.3214	443.9150	1.7838	446.2471	0.5545
498.3130	0.0058	463.9985	0.9676	483.6031	0.8495	464.4044	0.0058
498.5643	3.2297	487.7195	0.5154	488.2543	0.0325	488.5639	3.1973
503.7334	0.0570	494.2288	3.7523	493.2542	0.1501	496.6897	0.8321
527.9526	0.0030	497.7693	1.5129	495.2806	0.1378	499.9849	2.2666
544.0087	2.5088	528.3905	1.3358	508.4643	0.0004	518.7121	0.9348
571.7413	0.0002	538.3323	0.5091	537.9310	0.6465	537.6307	2.5327
583.7679	0.0003	584.1907	1.1131	571.2952	2.1281	570.9713	2.0852
674.3892	0.0311	631.8460	15.0741	645.8913	1.3784	599.6938	0.1137
690.5622	0.0155	661.6750	8.0910	662.9864	0.0320	676.8108	2.6968
708.3842	43.8722	674.3356	0.2393	673.6081	1.1642	692.5809	28.5727
735.3980	0.0001	700.6681	12.1358	715.8940	23.6626	715.2946	0.8365
742.5187	17.8701	720.2445	2.0603	728.0312	3.2390	720.0007	1.9308
761.0679	0.3744	765.5098	6.1663	757.1292	10.8156	766.4817	14.5960
799.5707	0.0001	790.1094	0.2612	773.9228	0.1563	785.8267	11.1992
799.8627	0.0442	790.3971	0.0173	782.9817	0.8948	786.3504	1.9686
802.9084	0.6643	816.9432	0.6102	793.1654	0.0045	793.8929	0.2380
818.1137	4.1177	828.3045	16.8187	803.7679	1.5999	804.6890	0.1777
841.0556	111.8551	863.5597	86.5014	841.4280	83.1074	840.2639	89.1334
891.9943	0.0027	901.3692	0.6784	854.2992	0.0000	915.5988	0.2863
904.0837	0.0013	934.3861	15.6847	926.0139	0.0059	933.1823	8.0193
960.5316	0.0040	948.0922	0.0934	946.8781	12.3960	947.0653	4.3745
961.7593	0.0023	966.5755	5.8640	947.3105	3.5174	964.7524	0.0256
967.0518	0.1565	985.0209	0.0753	948.6760	28.7649	981.7520	0.0323
967.3023	1.1345	992.2696	0.0411	984.9485	0.0484	990.4956	1.7576
975.6922	0.0000	993.1250	8.1706	985.8101	0.1118	998.4249	0.4085
995.3900	1.9656	998.5797	1.1418	998.5920	19.7050	1001.1393	0.1302
1069.2168	0.0004	1003.9566	0.0026	1004.0496	0.3997	1040.9955	15.9617
1092.1416	8.5560	1083.9496	0.4941	1057.6170	27.0444	1070.4810	11.7216

— continued on the next page —

$C_{16}H_{10}$		$1\text{–}C_{16}H_{11}^{+}$		$2\text{–}C_{16}H_{11}^{+}$		$4\text{–}C_{16}H_{11}^{+}$	
ν, cm^{-1}	IR int	ν, cm^{-1}	IR int	ν, cm^{-1}	IR int	ν, cm^{-1}	IR int
1105.3650	0.0000	1127.3516	10.2833	1083.0996	0.2665	1092.7238	1.9344
1144.0798	0.4214	1146.1586	30.9353	1107.5940	2.7481	1100.6467	9.3081
1146.6601	0.0001	1162.9392	10.1137	1131.1866	0.0000	1159.1800	18.6460
1175.9907	0.0001	1174.4712	0.9650	1151.7842	9.8735	1162.8441	1.2149
1182.4068	14.3182	1175.8038	3.1648	1172.8496	8.4850	1179.1170	11.4306
1208.2526	0.0040	1191.7900	3.3840	1186.2498	21.0161	1187.6893	0.7535
1238.0825	0.0008	1204.2396	34.0111	1213.5664	5.3738	1203.7399	18.9939
1240.3292	0.0001	1229.3335	81.7602	1238.2736	3.9808	1234.5776	20.1997
1244.2157	2.1748	1234.6502	83.4711	1245.7966	5.0913	1237.7360	18.5845
1317.7591	5.2586	1252.4066	26.7257	1251.1884	12.2932	1252.9277	9.3160
1325.5821	0.0007	1322.5934	11.0836	1293.6961	158.2851	1325.6396	112.2704
1373.1458	0.0003	1357.3778	78.4578	1346.0674	103.5324	1334.6865	11.1933
1399.1937	0.0018	1362.0484	55.3707	1346.5580	7.5443	1335.4976	24.6094
1407.3476	0.0008	1364.3560	70.0057	1355.3209	23.3295	1370.0729	9.2170
1429.4404	3.2860	1383.6554	87.0799	1407.3655	1.3157	1380.6631	154.5740
1431.5310	6.9852	1410.7907	27.1735	1407.5246	18.1018	1407.1274	12.5503
1454.9869	1.2825	1420.8215	4.2517	1425.5012	80.1772	1424.0572	65.6510
1485.0450	3.1353	1432.8487	4.7756	1427.3118	6.4131	1429.4466	4.6571
1504.9519	0.0003	1450.7626	0.2849	1442.4997	14.6186	1440.0267	15.5180
1563.0586	0.0005	1487.1203	54.2065	1472.8360	58.1742	1479.1663	48.3764
1593.7654	0.0003	1504.2297	2.0058	1513.0355	46.2821	1513.1456	51.4439
1602.4305	12.1115	1538.2747	153.1500	1562.9437	115.5723	1549.9078	4.2840
1611.9029	1.5195	1572.0022	84.3038	1564.1022	3.3750	1565.5552	23.6833
1637.0552	0.0007	1584.9714	116.3863	1607.1853	4.0784	1595.0864	75.7052
3036.7044	2.6658	1610.7141	266.9465	1607.7609	33.5238	1604.1307	36.8072
3037.0646	0.0445	1633.3277	33.9505	1624.1268	87.4592	1629.3258	159.0258
3039.5478	0.0097	2874.3037	21.0480	2848.5199	7.9957	2859.6963	30.1848
3040.1169	0.0993	2883.7229	1.4680	2849.8495	44.5904	2864.3705	4.3288
3046.7735	16.0856	3056.6725	0.0690	3060.6343	0.1379	3048.3867	0.1898
3047.5586	0.0445	3058.2026	0.0572	3060.8045	0.0862	3053.8725	1.4159
3055.2178	12.3247	3059.2597	0.4489	3062.1924	0.0519	3056.2523	0.5670
3055.2749	52.6730	3060.9412	0.0809	3062.7257	0.6191	3060.3166	0.3360
3063.0471	53.4440	3064.5143	0.1818	3063.6648	2.1822	3064.0593	1.0369
3063.6080	2.7379	3069.8436	0.6518	3069.4393	1.0050	3067.5172	0.4729
		3073.0496	0.1959	3076.0615	1.1421	3074.8974	1.5060
		3075.1417	1.1855	3076.1686	1.1011	3079.7530	1.2761
		3084.0800	0.3097	3079.4115	0.7470	3086.2294	0.0157

A.3 Vibrational Spectra

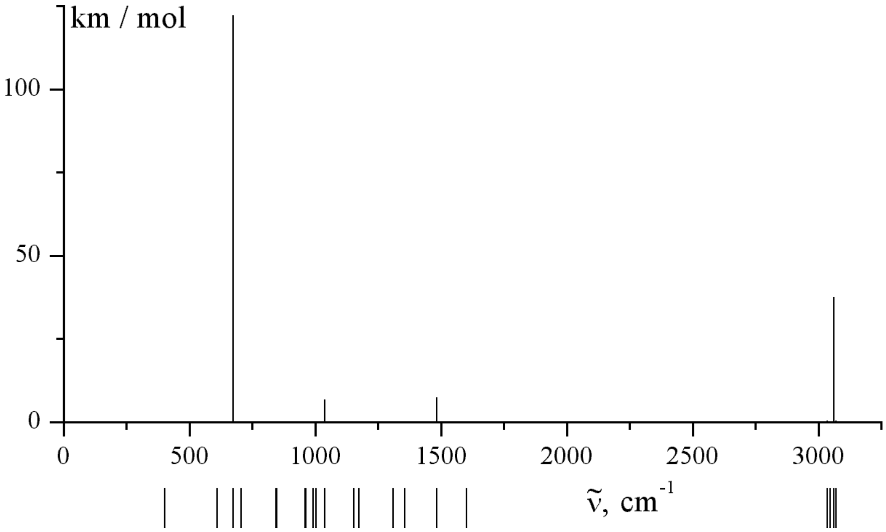

Figure A.1: Calculated benzene C_6H_6 IR vibrational spectrum.

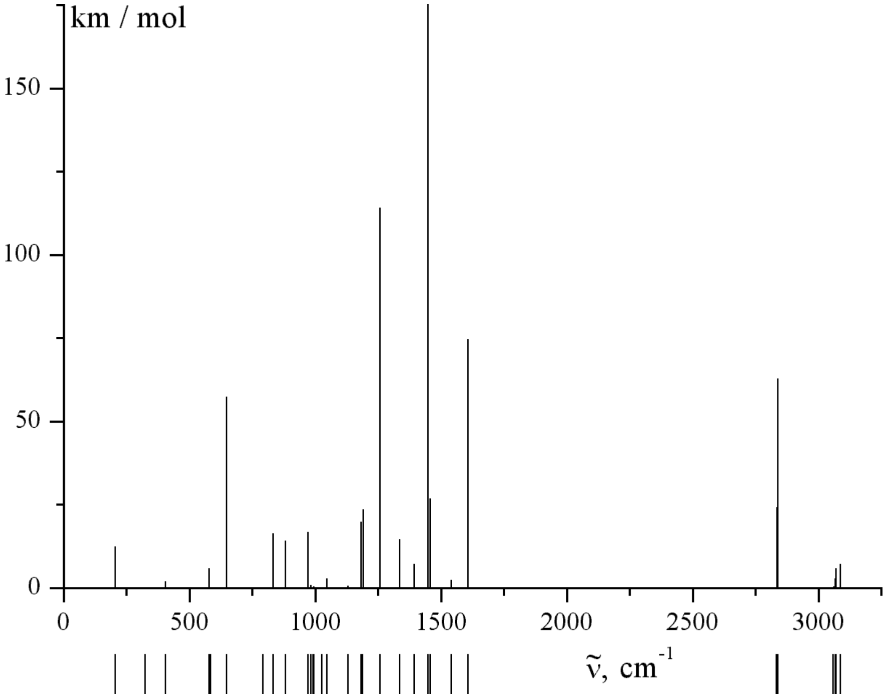

Figure A.2: Calculated protonated benzene $C_6H_7^+$ IR vibrational spectrum.

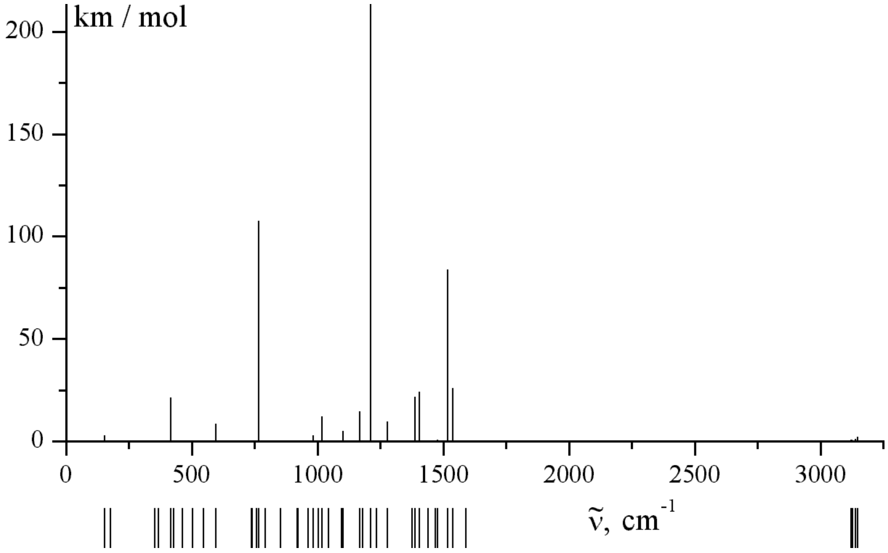

Figure A.3: Calculated naphthalene $C_{10}H_8$ IR vibrational spectrum.

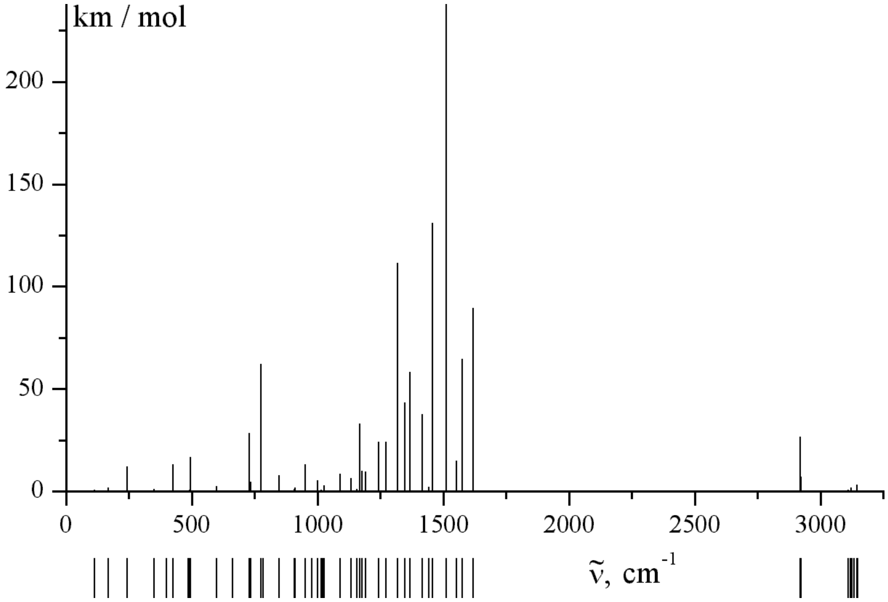

Figure A.4: Calculated protonated naphthalene 1–$C_{10}H_9^+$ IR vibrational spectrum.

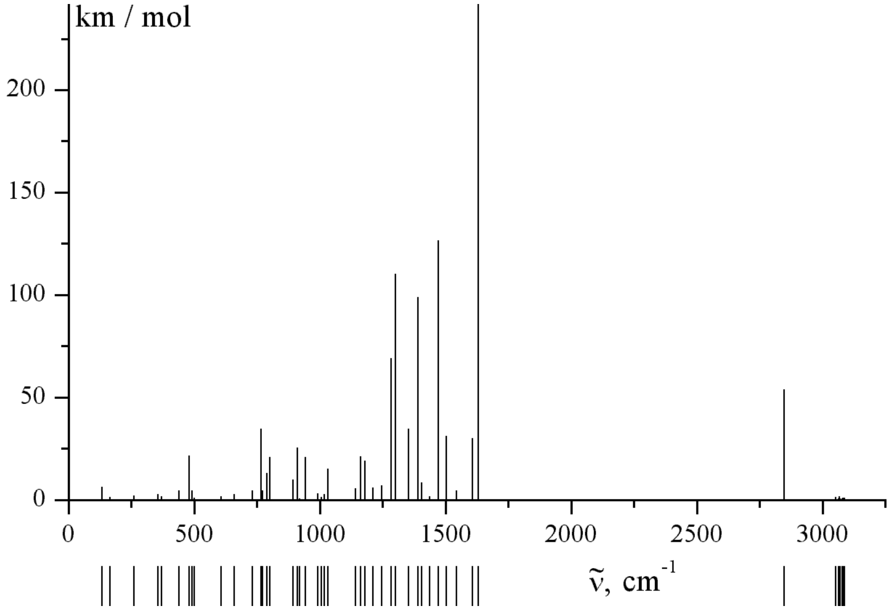

Figure A.5: Calculated protonated naphthalene 2–$C_{10}H_9^+$ IR vibrational spectrum.

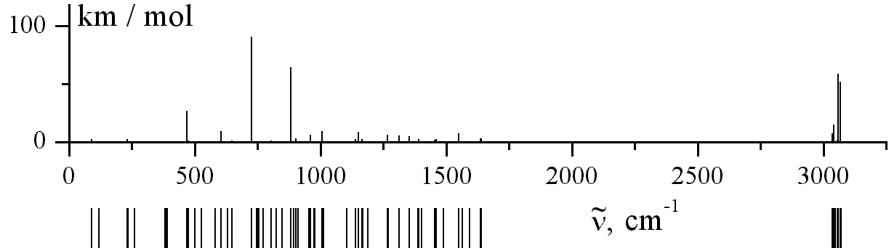

Figure A.6: Calculated anthracene $C_{14}H_{10}$ IR vibrational spectrum.

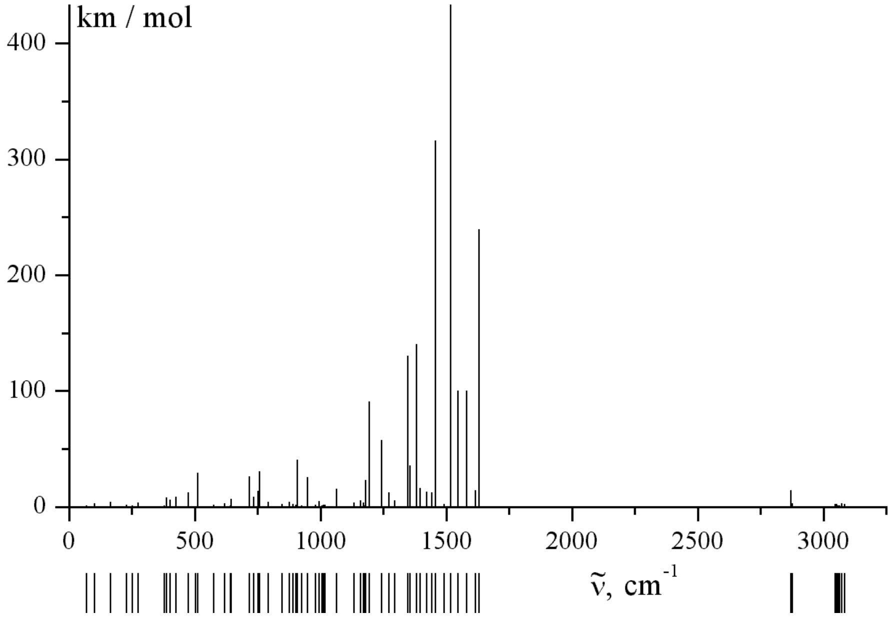

Figure A.7: Calculated protonated anthracene 1–$C_{14}H_{11}^{+}$ IR vibrational spectrum.

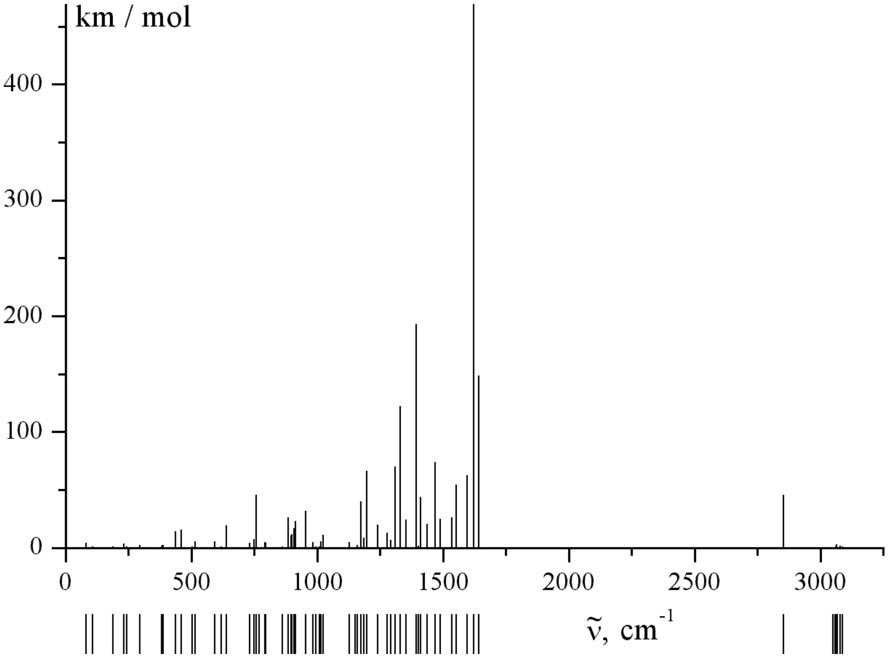

Figure A.8: Calculated protonated anthracene 2–$C_{14}H_{11}^{+}$ IR vibrational spectrum.

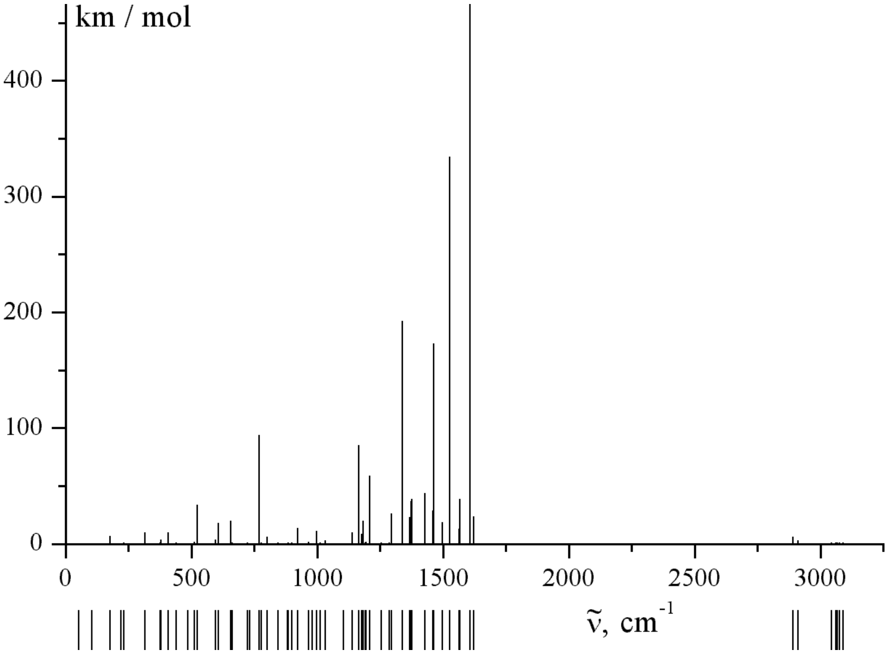

Figure A.9: Calculated protonated anthracene 9–$C_{14}H_{11}^{+}$ IR vibrational spectrum.

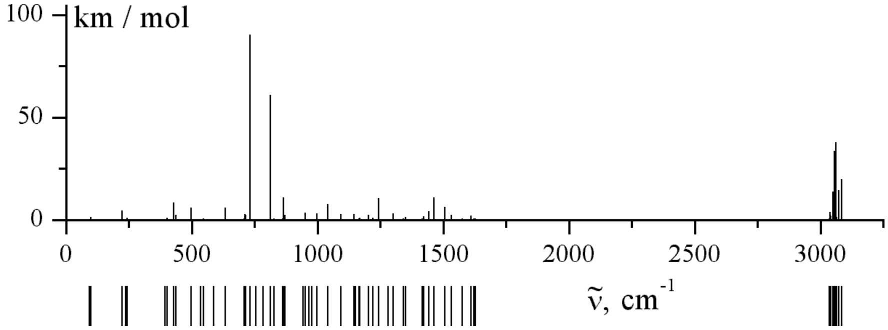

Figure A.10: Calculated phenanthrene $C_{14}H_{10}$ IR vibrational spectrum.

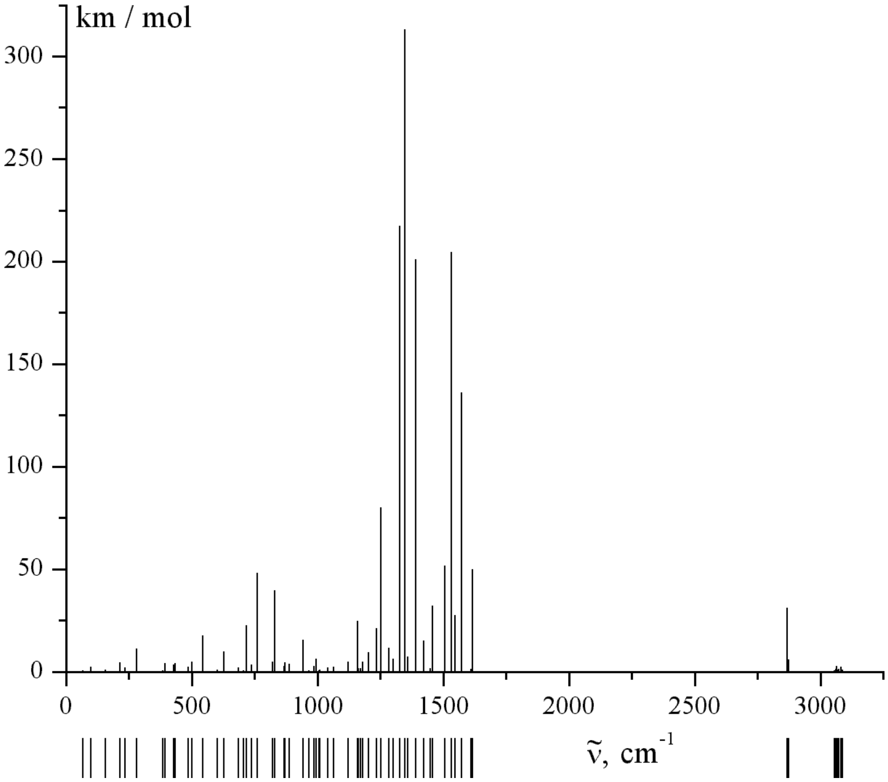

Figure A.11: Calculated protonated phenanthrene 1–$C_{14}H_{11}^{+}$ IR vibrational spectrum.

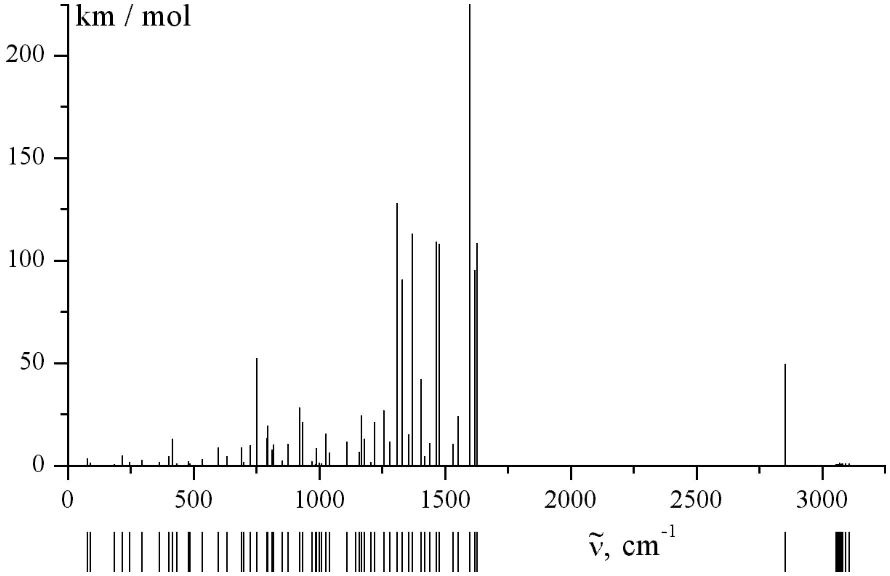

Figure A.12: Calculated protonated phenanthrene 2–$C_{14}H_{11}^{+}$ IR vibrational spectrum.

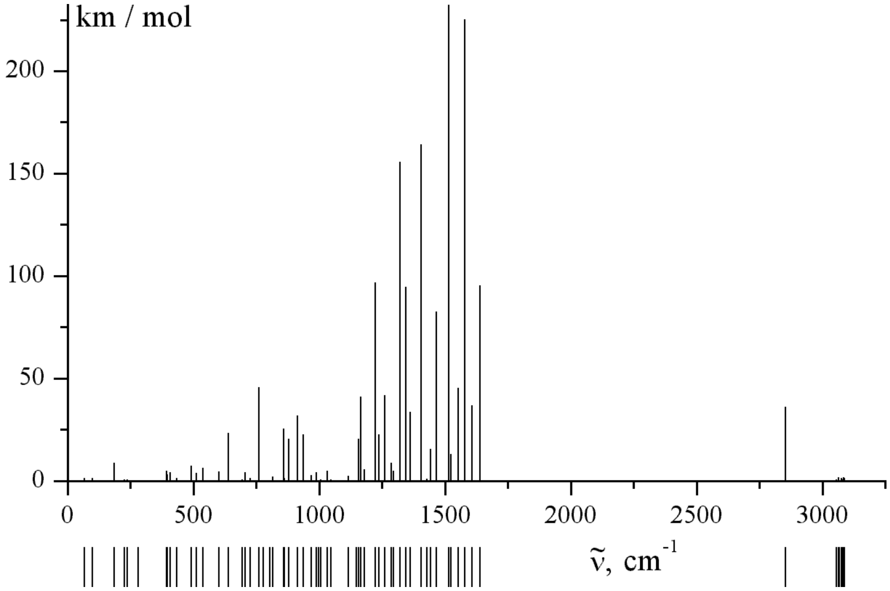

Figure A.13: Calculated protonated phenanthrene 3–$C_{14}H_{11}^{+}$ IR vibrational spectrum.

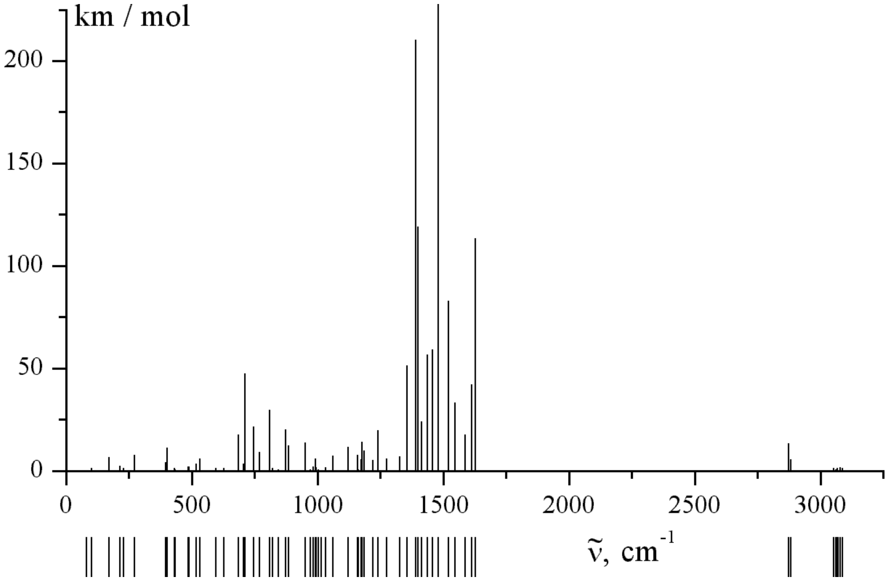

Figure A.14: Calculated protonated phenanthrene 4–$C_{14}H_{11}^{+}$ IR vibrational spectrum.

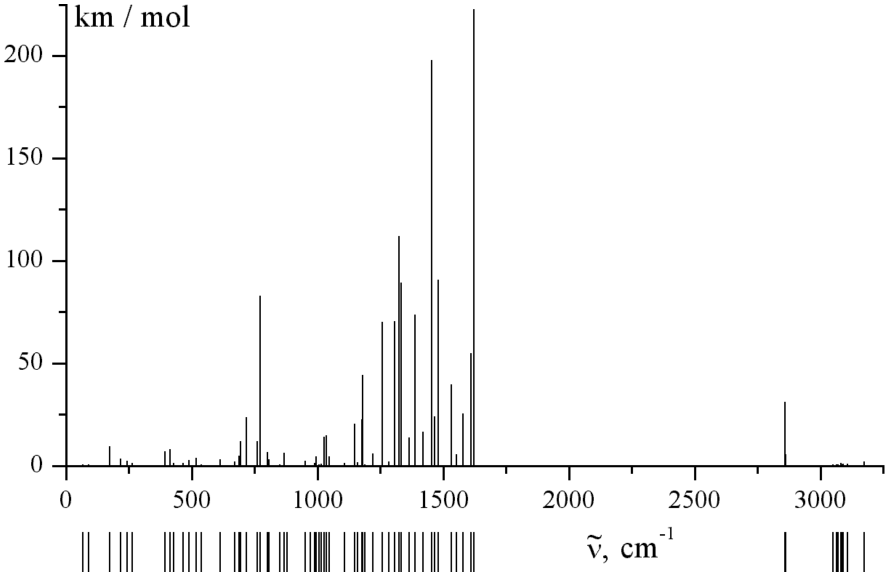

Figure A.15: Calculated protonated phenanthrene 9–$C_{14}H_{11}^{+}$ IR vibrational spectrum.

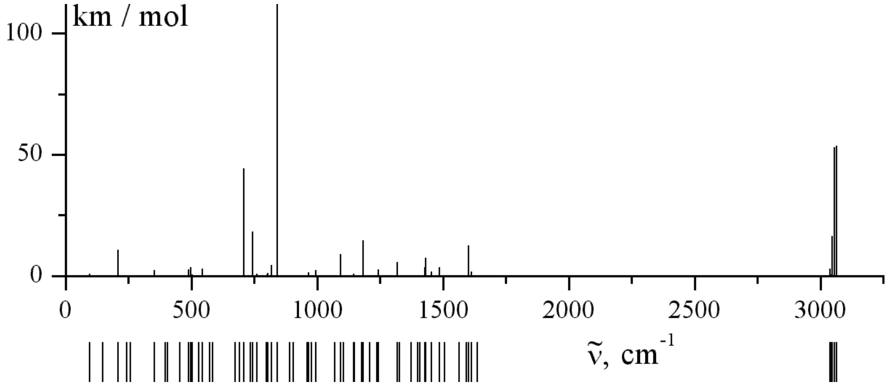

Figure A.16: Calculated pyrene $C_{16}H_{10}$ IR vibrational spectrum.

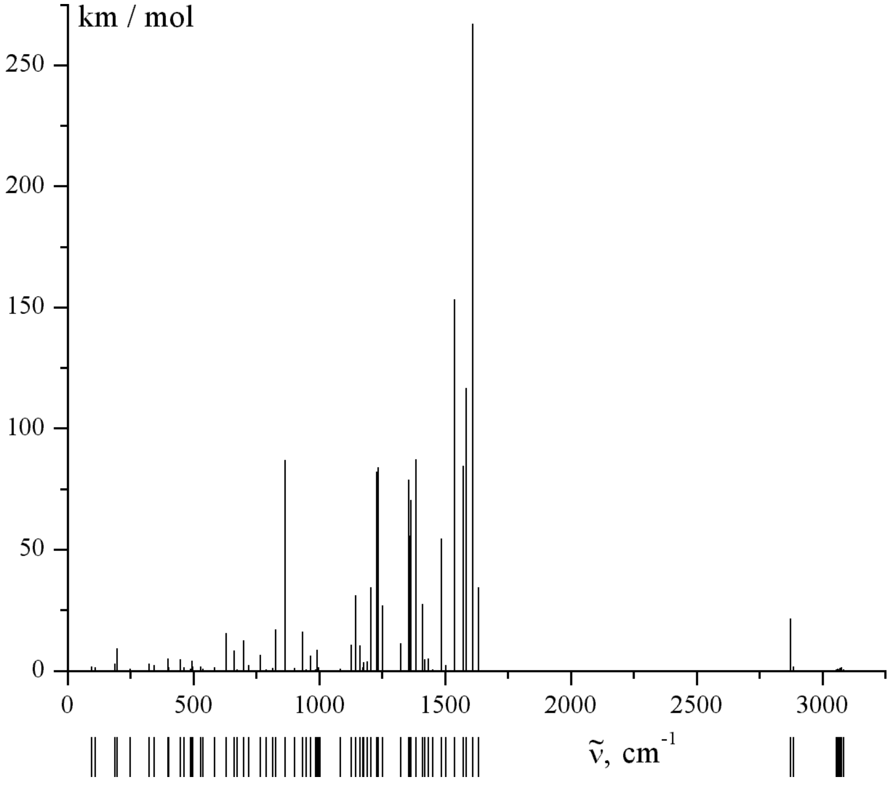

Figure A.17: Calculated protonated pyrene 1–$C_{16}H_{11}^{+}$ IR vibrational spectrum.

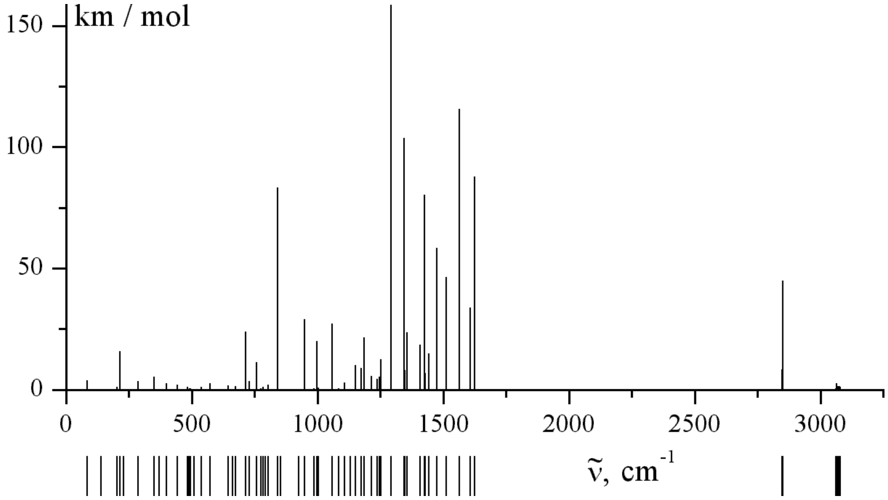

Figure A.18: Calculated protonated pyrene 2–$C_{16}H_{11}^{+}$ IR vibrational spectrum.

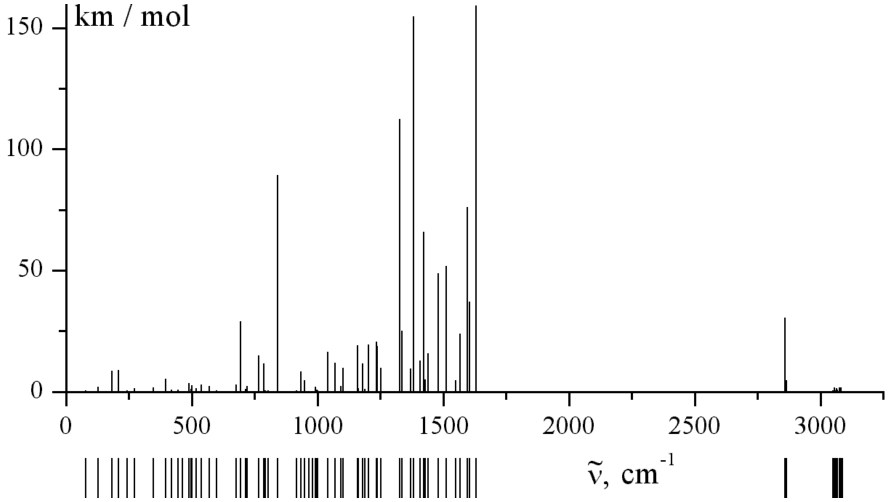

Figure A.19: Calculated protonated pyrene 4–$C_{16}H_{11}^{+}$ IR vibrational spectrum.

A.4 Energy Landscapes for Protonated PAHs

Table A.28: Protonated benzene energy landscape.

	Energy (kcal/mol)	Description
$C_6H_7^+$	-63.22	Stable isomer
1–2 $C_6H_7^+$	-51.90	1–2 isomerization transition state
$C_6H_5^+ + H_2$	0.00	Dissociation via H_2 loss from CH_2 site
$C_6H_6^+ + H$	12.63	Dissociation via H loss from CH_2 site
$C_6H_5^+ + 2H$	103.55	Dissociation via 2 H atoms loss, one from CH_2 site
$C_6H_6 + H^+$	118.97	Dissociation via H^+ loss from CH_2 site

Table A.29: Protonated naphthalene energy landscape.

	Energy (kcal/mol)	Description
1–$C_{10}H_9^+$	-62.41	Stable isomer (C 1)
2–$C_{10}H_9^+$	-59.51	Stable isomer (C 2)
9–$C_{10}H_9^+$	-43.47	Unstable isomer (C 9)
1–2 $C_{10}H_9^+$	-47.35	1–2 isomerization transition state
2–3 $C_{10}H_9^+$	-42.43	2–3 isomerization transition state
1–9 $C_{10}H_9^+$	-38.78	1–9 isomerization transition state
9–10 $C_{10}H_9^+$	-35.79	9–10 isomerization transition state
$C_{10}H_8^+ + H$	0.00	Dissociation via H loss from CH_2 site
1–$C_{10}H_7^+ + H_2$	7.28	Dissociation via H_2 loss from CH_2 site (C 1)
2–$C_{10}H_7^+ + H_2$	8.58	Dissociation via H_2 loss from CH_2 site (C 2)
1–$C_{10}H_7^+ + 2H$	110.84	Dissociation via 2 H atoms loss, one from CH_2 site (C 1)
2–$C_{10}H_7^+ + 2H$	112.14	Dissociation via 2 H atoms loss, one from CH_2 site (C 2)
$C_{10}H_8 + H^+$	133.79	Dissociation via H^+ loss from CH_2 site
2→1 $C_{10}H_8^+ + H$	48.34	Dissociation via H loss from C 2 in isomer 1
3→1 $C_{10}H_8^+ + H$	50.23	Dissociation via H loss from C 3 in isomer 1
4→1 $C_{10}H_8^+ + H$	47.75	Dissociation via H loss from C 4 in isomer 1
5→1 $C_{10}H_8^+ + H$	49.53	Dissociation via H loss from C 5 in isomer 1
6→1 $C_{10}H_8^+ + H$	49.97	Dissociation via H loss from C 6 in isomer 1
7→1 $C_{10}H_8^+ + H$	48.78	Dissociation via H loss from C 7 in isomer 1
8→1 $C_{10}H_8^+ + H$	49.17	Dissociation via H loss from C 8 in isomer 1
1→2 $C_{10}H_8^+ + H$	50.70	Dissociation via H loss from C 1 in isomer 2
3→2 $C_{10}H_8^+ + H$	52.34	Dissociation via H loss from C 3 in isomer 2
4→2 $C_{10}H_8^+ + H$	52.05	Dissociation via H loss from C 4 in isomer 2
5→2 $C_{10}H_8^+ + H$	52.76	Dissociation via H loss from C 5 in isomer 2
6→2 $C_{10}H_8^+ + H$	51.44	Dissociation via H loss from C 6 in isomer 2
7→2 $C_{10}H_8^+ + H$	52.98	Dissociation via H loss from C 7 in isomer 2
8→2 $C_{10}H_8^+ + H$	52.40	Dissociation via H loss from C 8 in isomer 2

Table A.30: Protonated anthracene energy landscape.

	Energy (kcal/mol)	Description
1–$C_{14}H_{11}^+$	-52.41	Stable isomer (C 1)
2–$C_{14}H_{11}^+$	-49.36	Stable isomer (C 2)
9–$C_{14}H_{11}^+$	-61.06	Stable isomer (C 9)
11–$C_{14}H_{11}^+$	-31.70	Unstable isomer (C 11)
1–2 $C_{14}H_{11}^+$	-34.87	1–2 isomerization transition state
2–3 $C_{14}H_{11}^+$	-28.16	2–3 isomerization transition state
1–11 $C_{14}H_{11}^+$	-24.57	1–11 isomerization transition state
9–11 $C_{14}H_{11}^+$	-29.33	9–11 isomerization transition state
11–12 $C_{14}H_{11}^+$	-21.23	11–12 isomerization transition state
$C_{14}H_{10}^+$ + H	0.00	Dissociation via H loss from CH_2 site
1–$C_{14}H_9^+$ + H_2	19.17	Dissociation via H_2 loss from CH_2 site (C 1)
2–$C_{14}H_9^+$ + H_2	18.58	Dissociation via H_2 loss from CH_2 site (C 2)
9–$C_{14}H_9^+$ + H_2	19.67	Dissociation via H_2 loss from CH_2 site (C 9)
1–$C_{14}H_9^+$ + 2H	122.73	Dissociation via 2 H atoms loss, one from CH_2 site (C 1)
2–$C_{14}H_9^+$ + 2H	122.14	Dissociation via 2 H atoms loss, one from CH_2 site (C 2)
9–$C_{14}H_9^+$ + 2H	123.23	Dissociation via 2 H atoms loss, one from CH_2 site (C 9)
$C_{14}H_{10}$ + H^+	151.44	Dissociation via H^+ loss from CH_2 site

Table A.31: Protonated phenanthrene energy landscape.

	Energy (kcal/mol)	Description
1–$C_{14}H_{11}^+$	-59.53	Stable isomer (C 1)
2–$C_{14}H_{11}^+$	-57.53	Stable isomer (C 2)
3–$C_{14}H_{11}^+$	-58.98	Stable isomer (C 3)
4–$C_{14}H_{11}^+$	-58.46	Stable isomer (C 4)
9–$C_{14}H_{11}^+$	-59.33	Stable isomer (C 9)
$C_{14}H_{10}^+$ + H	0.00	Dissociation via H loss from CH_2 site
$C_{14}H_{10}$ + H^+	140.27	Dissociation via H^+ loss from CH_2 site

Table A.32: Protonated pyrene energy landscape.

	Energy (kcal/mol)	Description
1–$C_{16}H_{11}^+$	-60.78	Stable isomer (C 1)
2–$C_{16}H_{11}^+$	-46.57	Stable isomer (C 2)
4–$C_{16}H_{11}^+$	-50.52	Stable isomer (C 4)
$C_{16}H_{10}^+$ + H	0.00	Dissociation via H loss from CH_2 site
$C_{16}H_{10}$ + H^+	150.46	Dissociation via H^+ loss from CH_2 site

A.5 Energy Landscapes for Hydrogenated PAHs

Table A.33: Hydrogenated benzene energy landscape.

	Energy (kcal/mol)	Description
C_6H_7	-22.53	Stable isomer
C_6H_7 fr	-19.68	Stable isomer, frozen $C_6H_7^+$ geometry
C_6H_6 + H	0.00	Dissociation via H loss from CH_2 site
$C_6H_5 + H_2$	5.57	Dissociation via H_2 loss from CH_2 site
C_6H_5 + 2H	109.12	Dissociation via 2 H atoms loss, one from CH_2 site
$C_6H_7^+ + e^-$	132.99	Ionization

Table A.34: Hydrogenated naphthalene energy landscape.

	Energy (kcal/mol)	Description
1–$C_{10}H_9$	-30.26	Stable isomer (C 1)
2–$C_{10}H_9$	-25.49	Stable isomer (C 2)
1–$C_{10}H_9$ fr	-27.31	Stable isomer (C 1), frozen 1–$C_{10}H_9^+$ geometry
2–$C_{10}H_9$ fr	-22.45	Stable isomer (C 2), frozen 2–$C_{10}H_9^+$ geometry
$C_{10}H_8$ + H	0.00	Dissociation via H loss from CH_2 site
1–$C_{10}H_7 + H_2$	5.69	Dissociation via H_2 loss from CH_2 site (C 1)
2–$C_{10}H_7 + H_2$	5.65	Dissociation via H_2 loss from CH_2 site (C 2)
1–$C_{10}H_7$ + 2H	109.25	Dissociation via 2 H atoms loss, one from CH_2 site (C 1)
2–$C_{10}H_7$ + 2H	109.21	Dissociation via 2 H atoms loss, one from CH_2 site (C 2)
1–$C_{10}H_9^+ + e^-$	118.97	Ionization (C 1)
2–$C_{10}H_9^+ + e^-$	121.87	Ionization (C 2)

Table A.35: Hydrogenated anthracene energy landscape.

	Energy (kcal/mol)	Description
1–$C_{14}H_{11}$	-34.13	Stable isomer (C 1)
2–$C_{14}H_{11}$	-29.91	Stable isomer (C 2)
9–$C_{14}H_{11}$	-40.63	Stable isomer (C 9)
1–$C_{14}H_{11}$ fr	-31.00	Stable isomer (C 1), frozen 1–$C_{14}H_{11}^{+}$ geometry
2–$C_{14}H_{11}$ fr	-26.67	Stable isomer (C 2), frozen 2–$C_{14}H_{11}^{+}$ geometry
9–$C_{14}H_{11}$ fr	-38.04	Stable isomer (C 9), frozen 9–$C_{14}H_{11}^{+}$ geometry
$C_{14}H_{10}$ + H	0.00	Dissociation via H loss from CH_2 site
1–$C_{14}H_9$ + H_2	5.66	Dissociation via H_2 loss from CH_2 site (C 1)
2–$C_{14}H_9$ + H_2	5.65	Dissociation via H_2 loss from CH_2 site (C 2)
9–$C_{14}H_9$ + H_2	5.93	Dissociation via H_2 loss from CH_2 site (C 9)
1–$C_{14}H_9$ + 2H	109.22	Dissociation via 2 H atoms loss, one from CH_2 site (C 1)
2–$C_{14}H_9$ + 2H	109.21	Dissociation via 2 H atoms loss, one from CH_2 site (C 2)
9–$C_{14}H_9$ + 2H	109.49	Dissociation via 2 H atoms loss, one from CH_2 site (C 9)
1–$C_{14}H_{11}^{+}$ + e^{-}	111.33	Ionization (C 1)
2–$C_{14}H_{11}^{+}$ + e^{-}	114.37	Ionization (C 2)
9–$C_{14}H_{11}^{+}$ + e^{-}	102.68	Ionization (C 9)

A.6 Ionization Energies

Table A.36: Ionization energies for PAHs, hydrogenated and dehydrogenated PAHs.

Molecule	Calculated (eV)	Experimental (eV)
C_6H_6	9.0562	9.24378
$C_{10}H_8$	7.8655	8.1442
$C_{14}H_{10}$ anthracene	7.1002	7.4233
$C_{14}H_{10}$ phenanthrene	7.5845	7.891
$C_{16}H_{10}$ pyrene	7.1427	7.426
Hydrogenated		
C_6H_7	6.7439	
1–$C_{10}H_9$	6.4713	
2–$C_{10}H_9$	6.3900	
1–$C_{14}H_{11}$ anthracene	6.3078	
2–$C_{14}H_{11}$ anthracene	6.2568	
9–$C_{14}H_{11}$ anthracene	6.2144	
Dehydrogenated		
C_6H_5	8.2670	
1–$C_{10}H_7$	7.9347	
2–$C_{10}H_7$	7.9927	
1–$C_{14}H_9$ anthracene	7.6861	
2–$C_{14}H_9$ anthracene	7.6607	
9–$C_{14}H_9$ anthracene	7.6960	

A.7 Excited States

Table A.37: Calculated first singlet excited states of neutral and protonated PAHs. S_1 state energies, $S_1 \leftarrow S_0$ wavelengths, red shifts, oscillator strengths.

Molecule	S_1 (eV)	$S_1 \leftarrow S_0$ wavelength (nm)			Red shift (nm)	Oscillator strength
	Calculated		Scaled	Scaled range		
Benzene						
C_6H_6	6.0122	206.22	**262.56**			0.0000
$C_6H_7^+$	4.5130	274.72	**349.77**	323.20 – 366.29	87.21	0.1737
Naphthalene						
$C_{10}H_8$	5.0429	243.98	**312.30**			0.0825
1–$C_{10}H_9^+$	4.1253	298.84	**382.53**	351.58 – 398.45	70.22	0.4090
2–$C_{10}H_9^+$	3.5890	342.88	**438.90**	403.39 – 457.17	126.60	0.1714
Anthracene						
$C_{14}H_{10}$	4.0598	305.39	**361.17**			0.1399
1–$C_{14}H_{11}^+$	3.3092	374.66	**443.09**	440.78 – 499.55	81.92	0.3459
2–$C_{14}H_{11}^+$	2.9899	414.67	**490.41**	487.85 – 552.89	129.24	0.1862
9–$C_{14}H_{11}^+$	3.8949	318.33	**376.47**	374.51 – 424.44	15.30	0.7120
Phenanthrene						
$C_{14}H_{10}$	4.8007	258.26	**340.99**			0.0318
1–$C_{14}H_{11}^+$	3.4305	361.42	**477.20**	425.20 – 481.89	136.21	0.4661
2–$C_{14}H_{11}^+$	3.2886	377.01	**497.78**	443.54 – 502.68	156.79	0.1205
3–$C_{14}H_{11}^+$	3.5525	349.01	**460.81**	410.60 – 465.35	119.82	0.3068
4–$C_{14}H_{11}^+$	3.3196	373.49	**493.13**	439.40 – 497.99	152.14	0.1984
9–$C_{14}H_{11}^+$	3.4149	363.06	**479.36**	427.13 – 484.08	138.37	0.2854
Pyrene						
$C_{16}H_{10}$	4.3936	282.19	**367.43**			0.3643
1–$C_{16}H_{11}^+$	3.6456	340.09	**442.82**	400.11 – 453.45	75.39	0.3338
2–$C_{16}H_{11}^+$	2.8356	437.23	**569.30**	514.39 – 582.97	201.87	0.1419
4–$C_{16}H_{11}^+$	3.2337	383.41	**499.23**	451.07 – 511.21	131.80	0.1464

Table A.38: Symmetry and S_0, S_1 electronic states assignment for neutral and protonated PAHs.

Molecule	Symm group	State Symbol		Orbital Symmetry and Electronic Configuration.
		S_0	S_1	(x,y) = (2,0) for S_0, (1,1) for S_1
Benzene				
C_6H_6	D_{6h}	$\widetilde{X}\ {}^1A_{1g}$	$\widetilde{A}\ {}^1E_{1u}$	$(1a_{2u})^2(1e_{1g})^x(1e_{2u})^y(1b_{2g})^0$, here (x,y) = (4,0) for S_0, (3,1) for S_1
$C_6H_7^+$	C_{2v}	$\widetilde{X}\ {}^1A_1$	$\widetilde{A}\ {}^1B_1$	$(1b_2)^2(2b_2)^2(1a_2)^x(3b_2)^y(2a_2)^0(4b_2)^0$
Naphthalene				
$C_{10}H_8$	D_{2h}	$\widetilde{X}\ {}^1A_g$	$\widetilde{A}\ {}^1B_{2u}$	$(1b_{1u})^2(1b_{3g})^2(1b_{2g})^2(2b_{1u})^2(1a_u)^x(2b_{2g})^y(2b_{3g})^0(3b_{1u})^0(2a_u)^0(3b_{3g})^0$
1–$C_{10}H_9^+$	C_s	$\widetilde{X}\ {}^1A'$	$\widetilde{A}\ {}^1A'$	$(1a'')^2(2a'')^2(3a'')^2(4a'')^2(5a'')^x(6a'')^y(7a'')^0(8a'')^0(9a'')^0(10a'')^0$
2–$C_{10}H_9^+$	C_s	$\widetilde{X}\ {}^1A'$	$\widetilde{A}\ {}^1A'$	$(1a'')^2(2a'')^2(3a'')^2(4a'')^2(5a'')^x(6a'')^y(7a'')^0(8a'')^0(9a'')^0(10a'')^0$
Anthracene				
$C_{14}H_{10}$	D_{2h}	$\widetilde{X}\ {}^1A_g$	$\widetilde{A}\ {}^1B_{2u}$	$(1b_{1u})^2(1b_{2g})^2(1b_{3g})^2(2b_{1u})^2(2b_{2g})^2(1a_u)^2(2b_{3g})^x(3b_{1u})^y(2a_u)^0(3b_{2g})^0(3b_{3g})^0(4b_{1u})^0(3a_u)^0...$
1–$C_{14}H_{11}^+$	C_s	$\widetilde{X}\ {}^1A'$	$\widetilde{A}\ {}^1A'$	$(1a'')^2(2a'')^2(3a'')^2(4a'')^2(5a'')^2(6a'')^2(7a'')^x(8a'')^y(9a'')^0(10a'')^0(11a'')^0(12a'')^0(13a'')^0(14a'')^0$
2–$C_{14}H_{11}^+$	C_s	$\widetilde{X}\ {}^1A'$	$\widetilde{A}\ {}^1A'$	$(1a'')^2(2a'')^2(3a'')^2(4a'')^2(5a'')^2(6a'')^2(7a'')^x(8a'')^y(9a'')^0(10a'')^0(11a'')^0(12a'')^0(13a'')^0(14a'')^0$
9–$C_{14}H_{11}^+$	C_{2v}	$\widetilde{X}\ {}^1A_1$	$\widetilde{A}\ {}^1B_1$	$(1b_2)^2(2b_2)^2(1a_2)^2(3b_2)^2(2a_2)^2(4b_2)^2(3a_2)^x(5b_2)^y(4a_2)^0(6b_2)^0(5a_2)^0(7b_2)^0(6a_2)^0(8b_2)^0$
Phenanthrene				
$C_{14}H_{10}$	C_{2v}	$\widetilde{X}\ {}^1A_1$	$\widetilde{A}\ {}^1B_1$	$(1b_2)^2(1a_2)^2(2b_2)^2(3b_2)^2(2a_2)^2(3a_2)^2(4b_2)^x(4a_2)^y(5b_2)^0(6b_2)^0(5a_2)^0(6a_2)^0(7b_2)^0(7a_2)^0$
1–$C_{14}H_{11}^+$	C_s	$\widetilde{X}\ {}^1A'$	$\widetilde{A}\ {}^1A'$	$(1a'')^2(2a'')^2(3a'')^2(4a'')^2(5a'')^2(6a'')^2(7a'')^x(8a'')^y(9a'')^0(10a'')^0(11a'')^0(12a'')^0(13a'')^0(14a'')^0$
2–$C_{14}H_{11}^+$	C_s	$\widetilde{X}\ {}^1A'$	$\widetilde{A}\ {}^1A'$	$(1a'')^2(2a'')^2(3a'')^2(4a'')^2(5a'')^2(6a'')^2(7a'')^x(8a'')^y(9a'')^0(10a'')^0(11a'')^0(12a'')^0(13a'')^0(14a'')^0$
3–$C_{14}H_{11}^+$	C_s	$\widetilde{X}\ {}^1A'$	$\widetilde{A}\ {}^1A'$	$(1a'')^2(2a'')^2(3a'')^2(4a'')^2(5a'')^2(6a'')^2(7a'')^x(8a'')^y(9a'')^0(10a'')^0(11a'')^0(12a'')^0(13a'')^0(14a'')^0$
4–$C_{14}H_{11}^+$	C_s	$\widetilde{X}\ {}^1A'$	$\widetilde{A}\ {}^1A'$	$(1a'')^2(2a'')^2(3a'')^2(4a'')^2(5a'')^2(6a'')^2(7a'')^x(8a'')^y(9a'')^0(10a'')^0(11a'')^0(12a'')^0(13a'')^0(14a'')^0$
9–$C_{14}H_{11}^+$	C_s	$\widetilde{X}\ {}^1A'$	$\widetilde{A}\ {}^1A'$	$(1a'')^2(2a'')^2(3a'')^2(4a'')^2(5a'')^2(6a'')^2(7a'')^x(8a'')^y(9a'')^0(10a'')^0(11a'')^0(12a'')^0(13a'')^0(14a'')^0$
Pyrene				
$C_{16}H_{10}$	D_{2h}	$\widetilde{X}\ {}^1A_g$	$\widetilde{A}\ {}^1B_{3u}$	$(1b_{1u})^2(2b_{2g})^2(1b_{3g})^2(2b_{1u})^2(1a_u)^2(3b_{1u})^2(2b_{2g})^2(2b_{3g})^x(2a_u)^y(4b_{1u})^0(3b_{2g})^0(3b_{3g})^0(4b_{2g})^0...$
1–$C_{16}H_{11}^+$	C_s	$\widetilde{X}\ {}^1A'$	$\widetilde{A}\ {}^1A'$	$(1a'')^2(2a'')^2(3a'')^2(4a'')^2(5a'')^2(6a'')^2(7a'')^2(8a'')^x(9a'')^y(10a'')^0(11a'')^0(12a'')^0(13a'')^0...$
2–$C_{16}H_{11}^+$	C_{2v}	$\widetilde{X}\ {}^1A_1$	$\widetilde{A}\ {}^1B_1$	$(1b_2)^2(2b_2)^2(1a_2)^2(3b_2)^2(2a_2)^2(4b_2)^2(5b_2)^2(3a_2)^x(6b_2)^y(4a_2)^0(7b_2)^0(8b_2)^0(5a_2)^0(9b_2)^0(6a_2)^0...$
4–$C_{16}H_{11}^+$	C_s	$\widetilde{X}\ {}^1A'$	$\widetilde{A}\ {}^1A'$	$(1a'')^2(2a'')^2(3a'')^2(4a'')^2(5a'')^2(6a'')^2(7a'')^2(8a'')^x(9a'')^y(10a'')^0(11a'')^0(12a'')^0(13a'')^0...$

Table A.39: Highest occupied (HOMO) and lowest unoccupied (LUMO) molecular orbitals of neutral and protonated PAHs.

HOMO	LUMO
Benzene, C_6H_6	
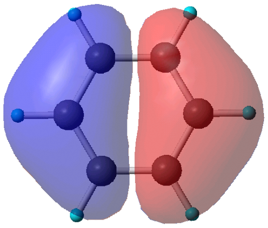 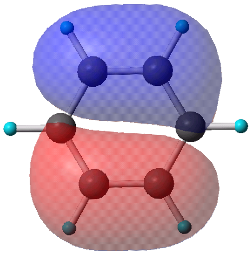	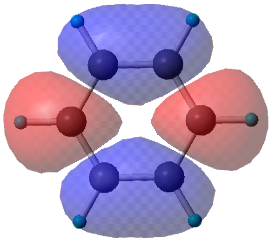 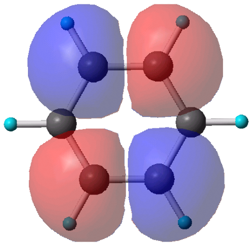
Protonated Benzene, $C_6H_7^+$	
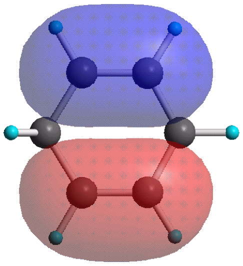	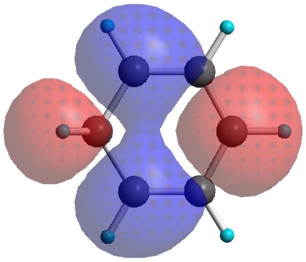
Naphthalene, $C_{10}H_8$	
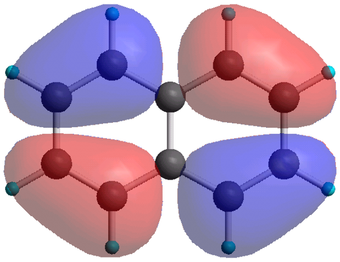	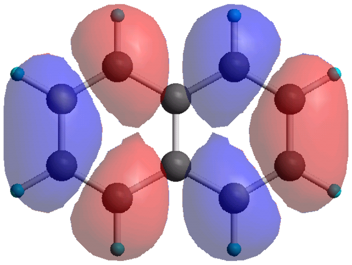
Protonated Naphthalene, 1–$C_{10}H_9^+$	
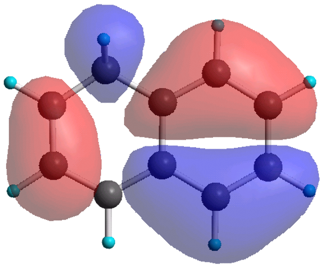	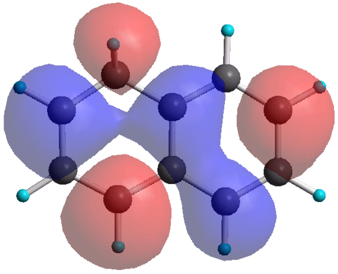

— continued on the next page —

HOMO	LUMO

Protonated Naphthalene, 2–$C_{10}H_9^+$

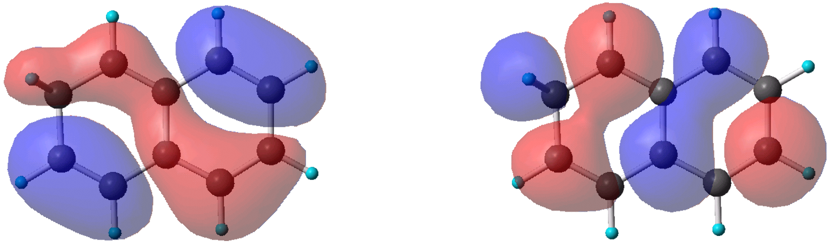

Anthracene, $C_{14}H_{10}$

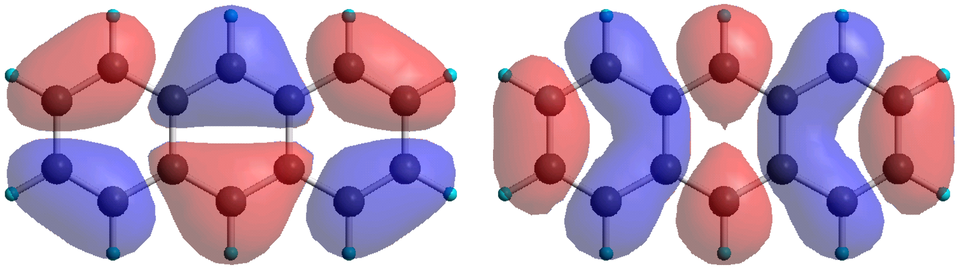

Protonated Anthracene, 1–$C_{14}H_{11}^+$

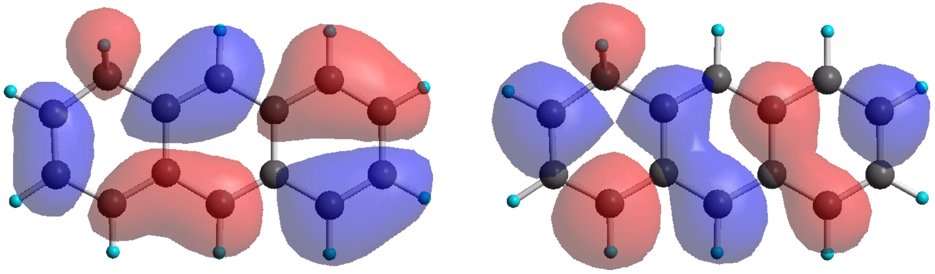

Protonated Anthracene, 2–$C_{14}H_{11}^+$

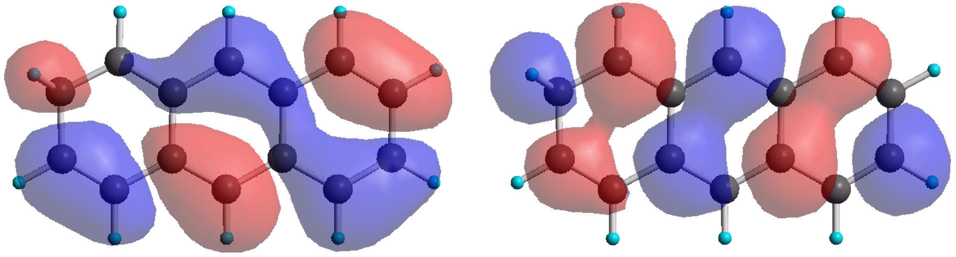

— continued on the next page —

HOMO LUMO

Protonated Anthracene, 9–$C_{14}H_{11}^{+}$

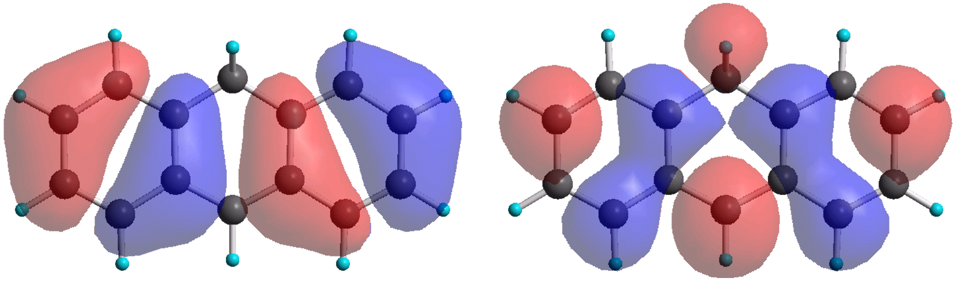

Phenanthrene, $C_{14}H_{10}$

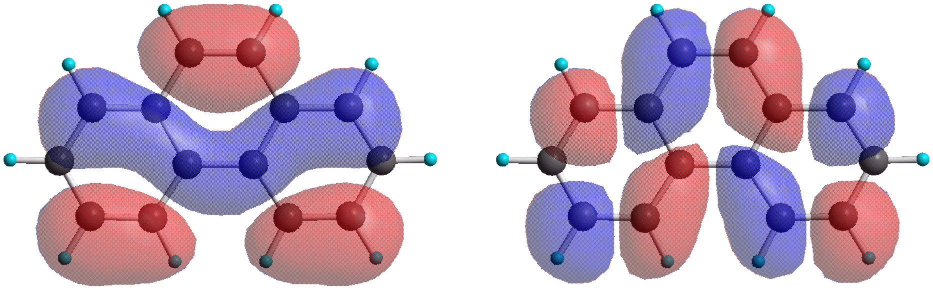

Protonated Phenanthrene, 1–$C_{14}H_{11}^{+}$

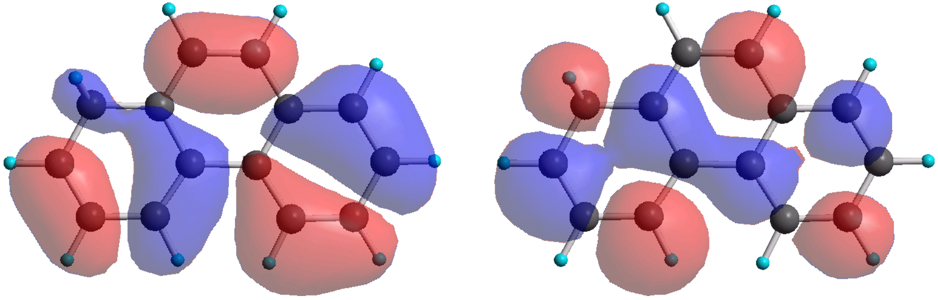

Protonated Phenanthrene, 2–$C_{14}H_{11}^{+}$

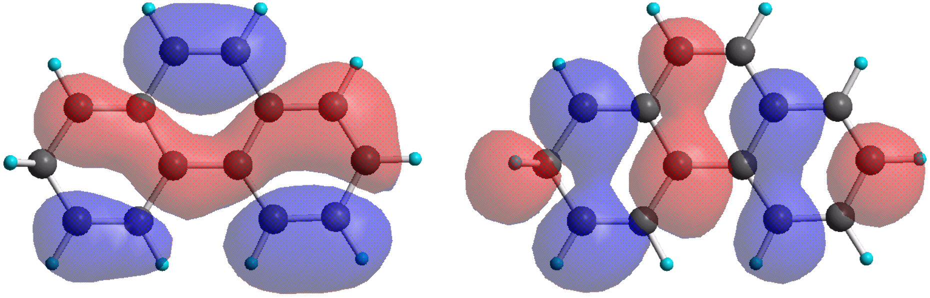

— continued on the next page —

HOMO LUMO

Protonated Phenanthrene, 3–$C_{14}H_{11}^{+}$

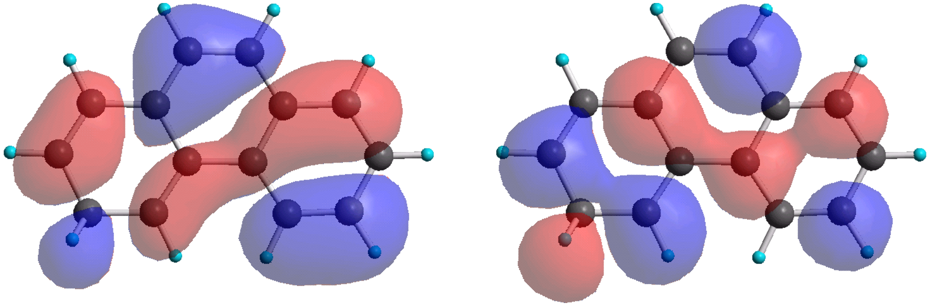

Protonated Phenanthrene, 4–$C_{14}H_{11}^{+}$

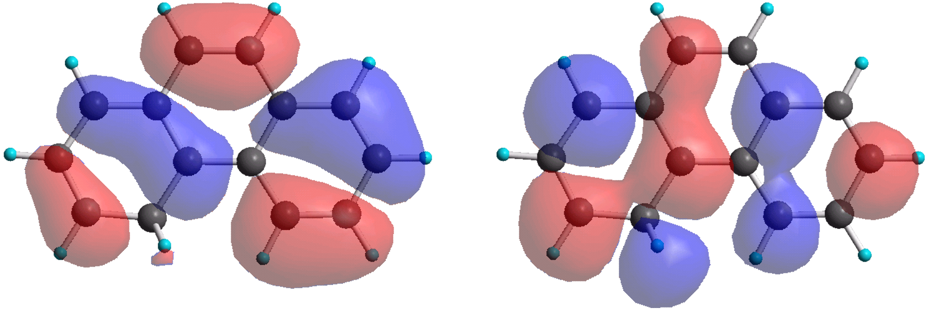

Protonated Phenanthrene, 9–$C_{14}H_{11}^{+}$

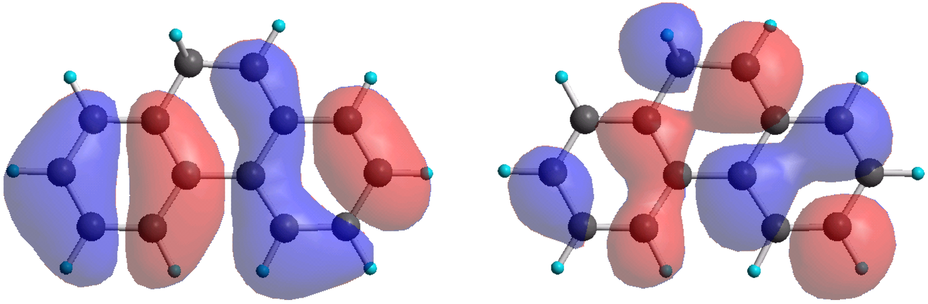

Pyrene, $C_{16}H_{10}$

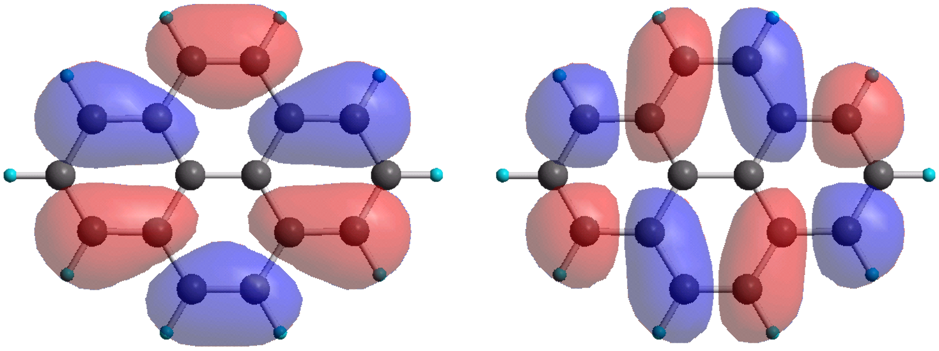

— continued on the next page —

HOMO LUMO

Protonated Pyrene, 1–$C_{16}H_{11}^{+}$

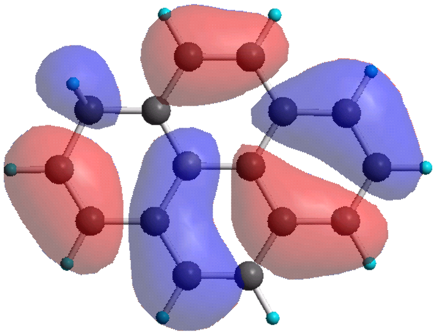

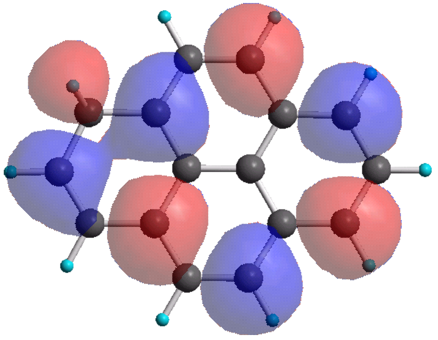

Protonated Pyrene, 2–$C_{16}H_{11}^{+}$

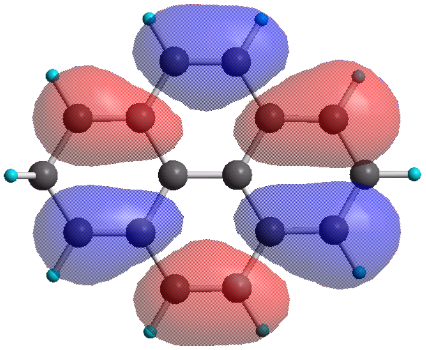

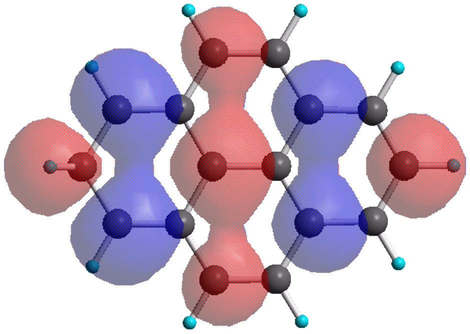

Protonated Pyrene, 4–$C_{16}H_{11}^{+}$

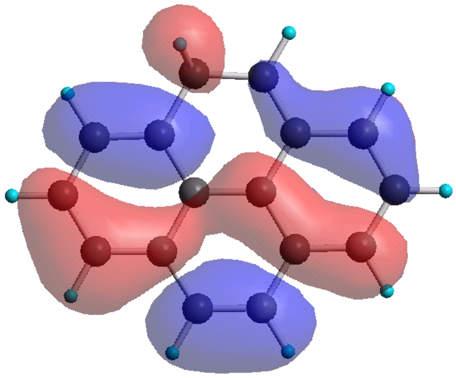

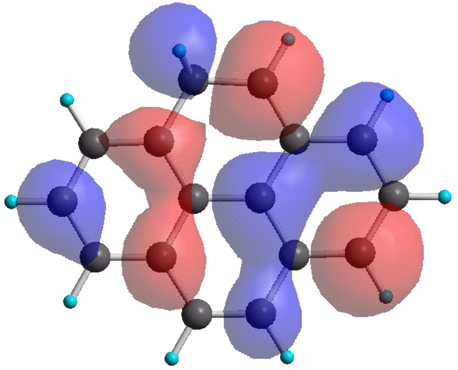

Appendix B

Experimental Setup Descriptions

B.1 Discharge

B.1.1 Pulsed Discharge Source

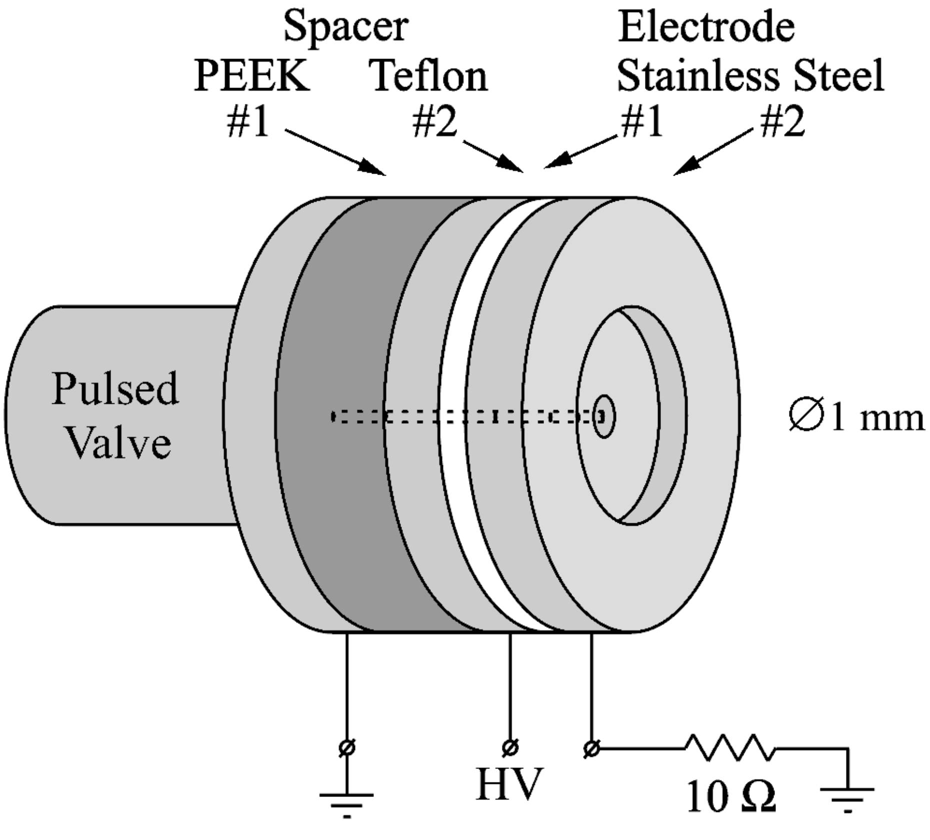

Figure B.1: Pulsed discharge source.

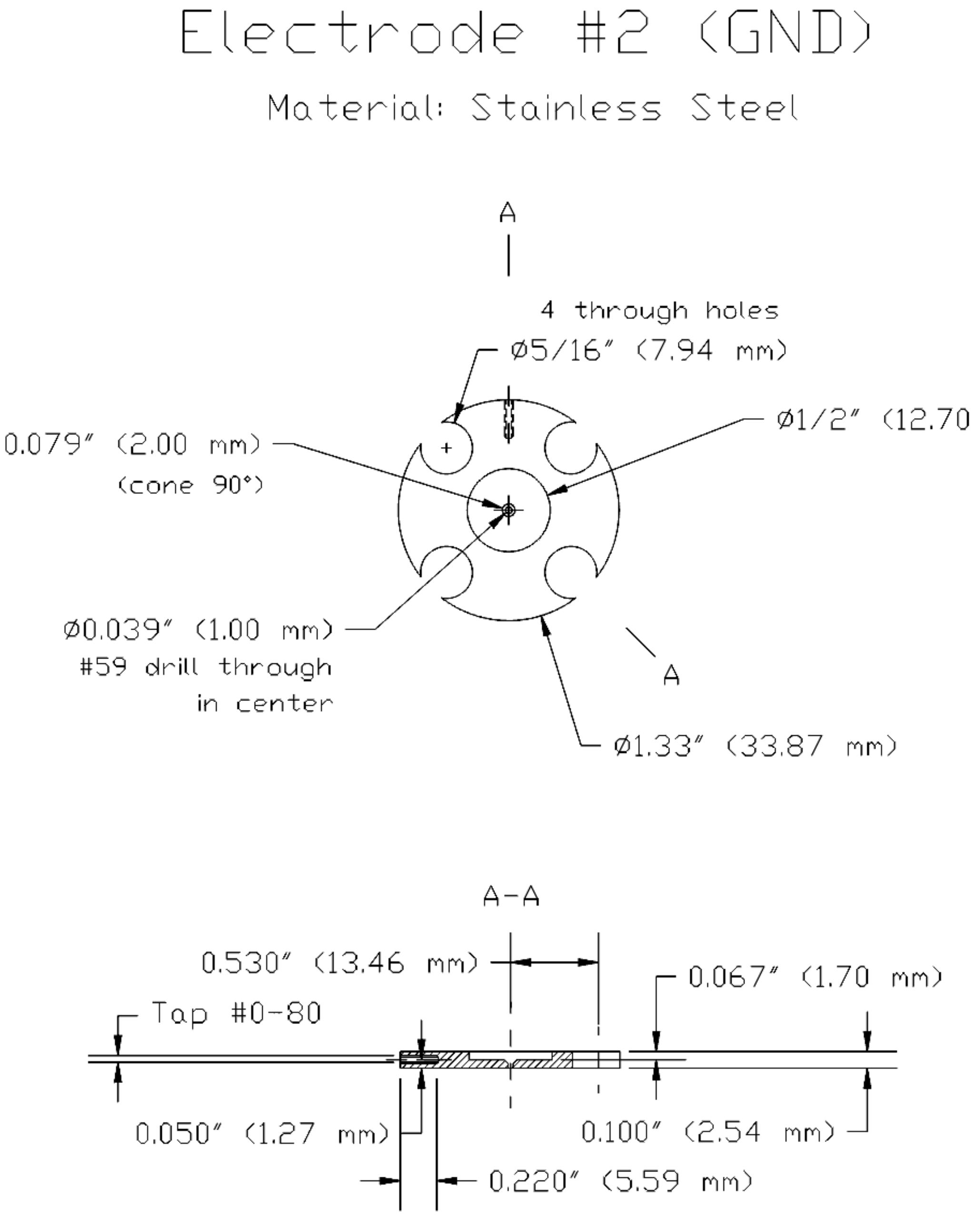

Figure B.2: Ground (outside) pulsed discharge electrode.

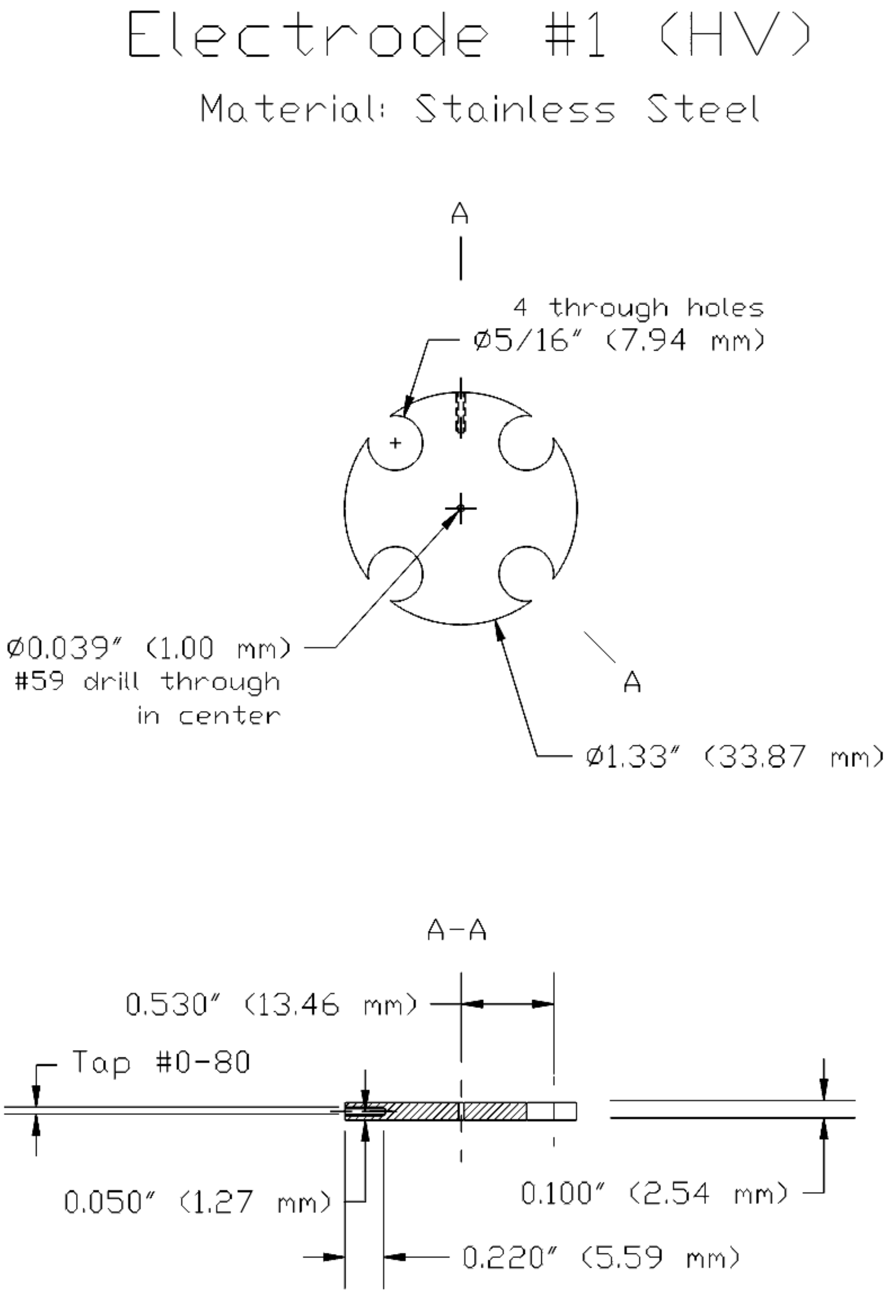

Figure B.3: High voltage (inside) pulsed discharge electrode.

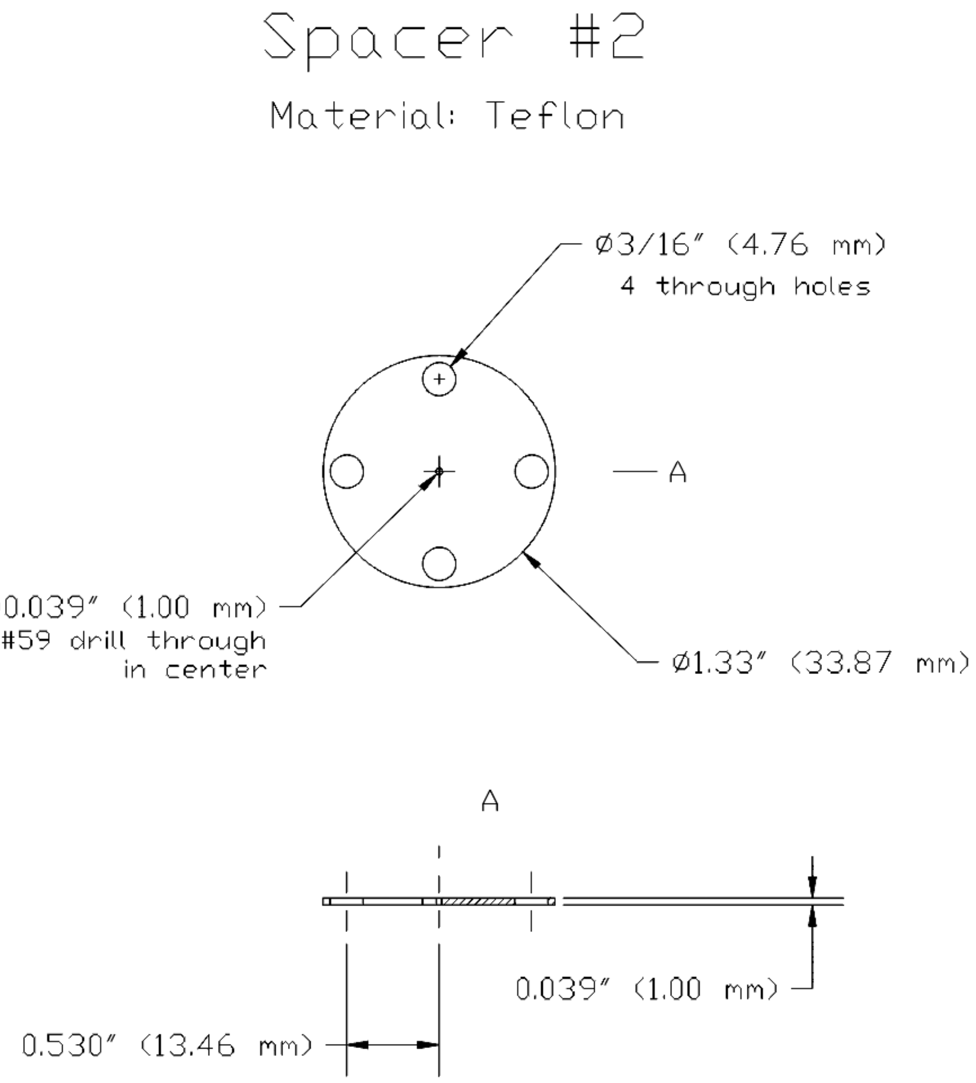

Figure B.4: Teflon insulating spacer between discharge electrodes.

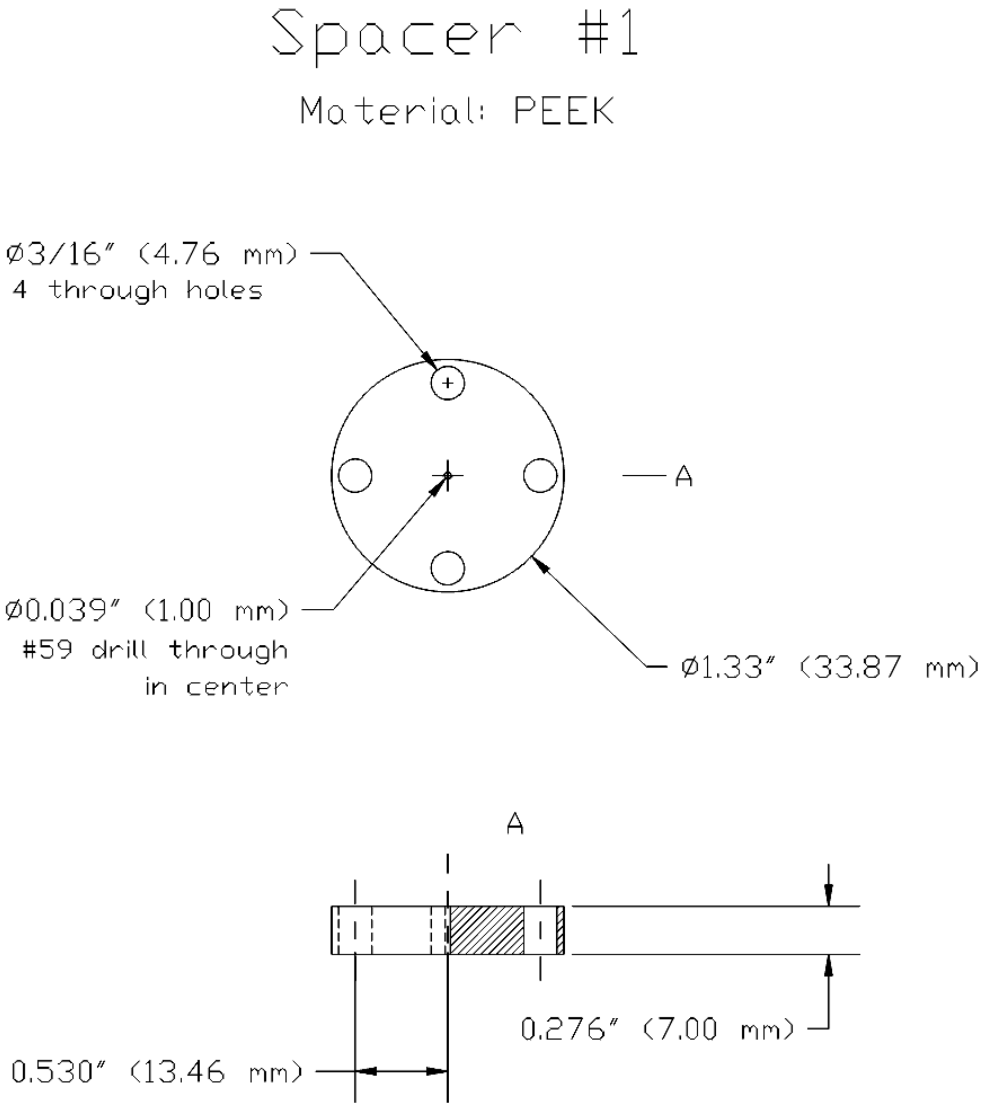

Figure B.5: PEEK insulating spacer between inside electrode and pulsed valve.

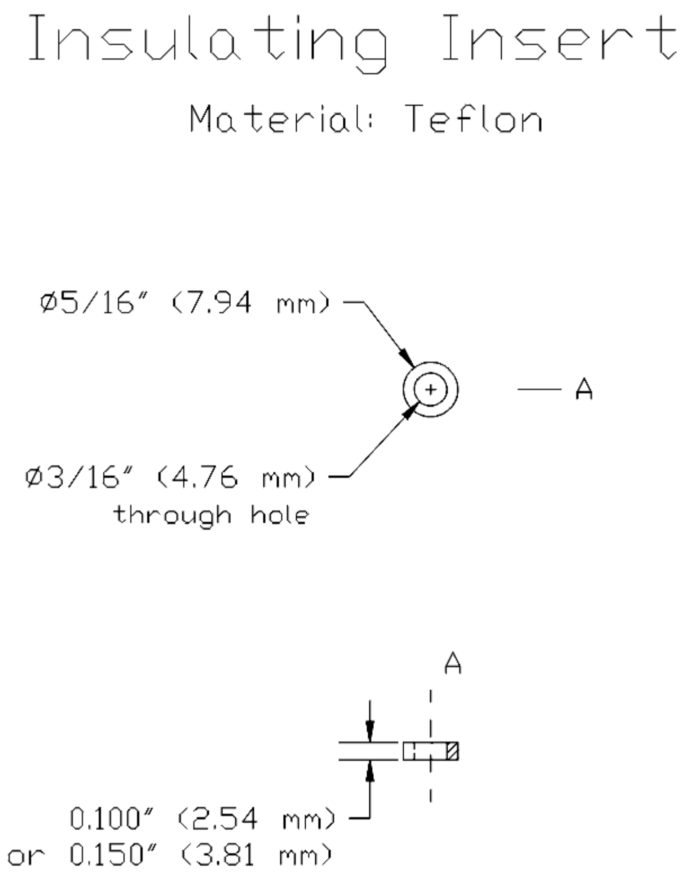

Figure B.6: Electrode inserts for screw insulation.

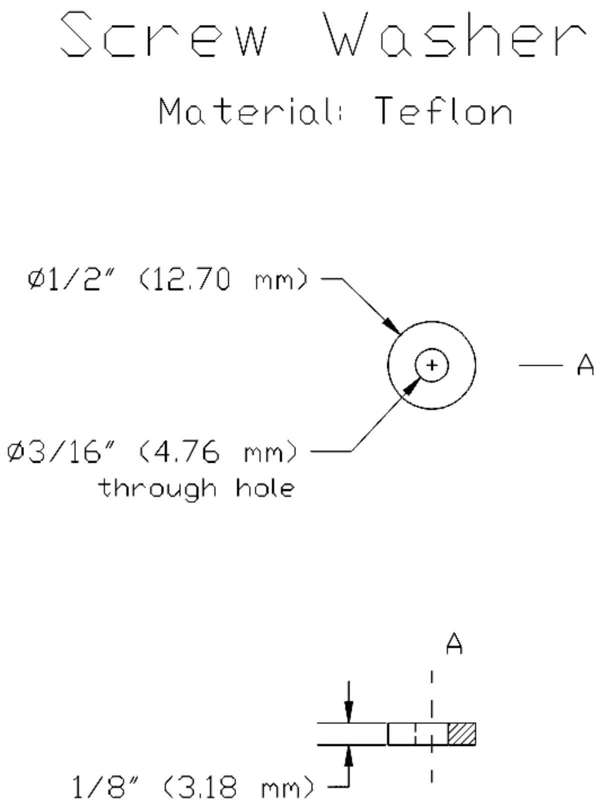

Figure B.7: Screw washer for insulation form outside electrode.

B.1.2 Pulsed Discharge Cluster Source

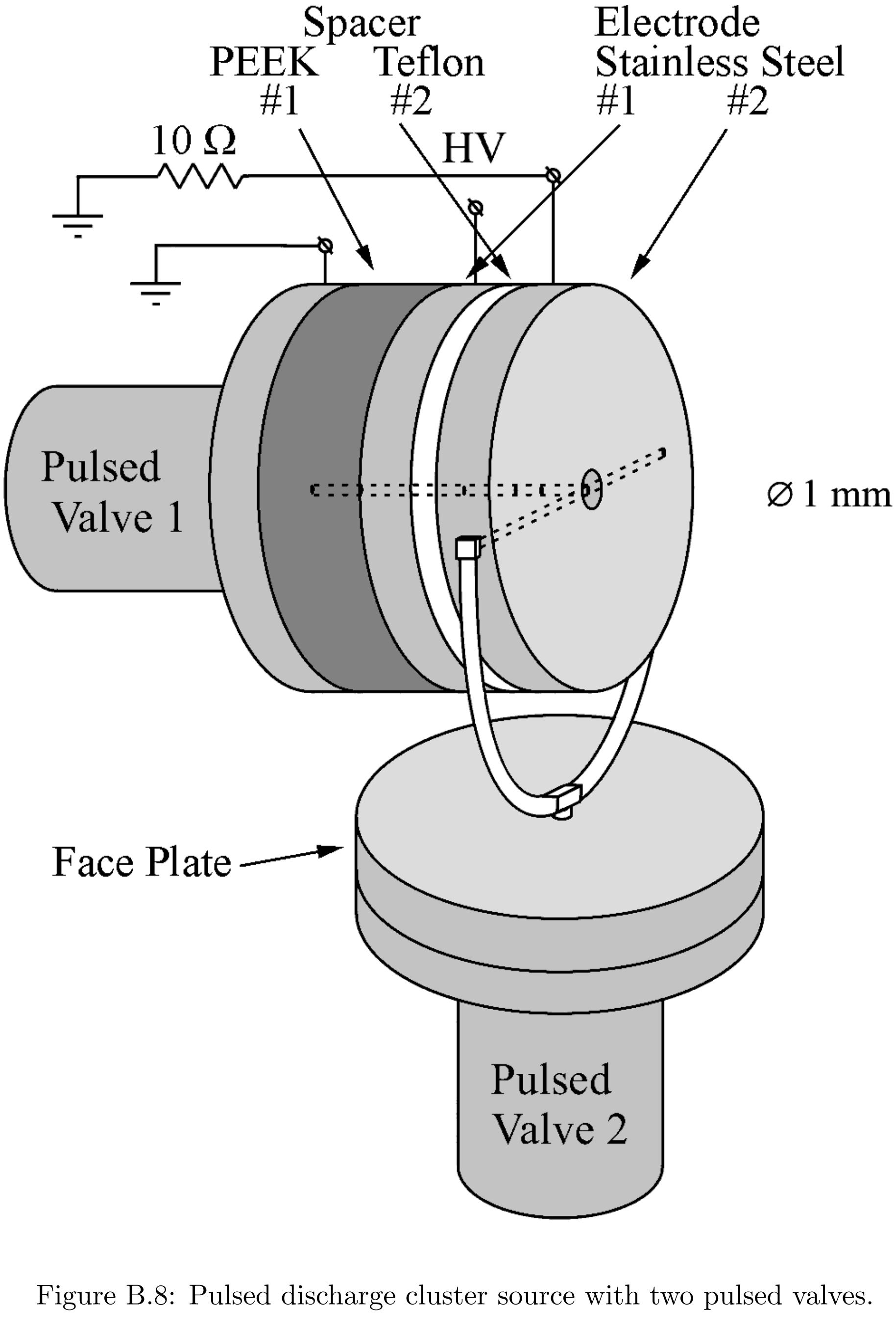

Figure B.8: Pulsed discharge cluster source with two pulsed valves.

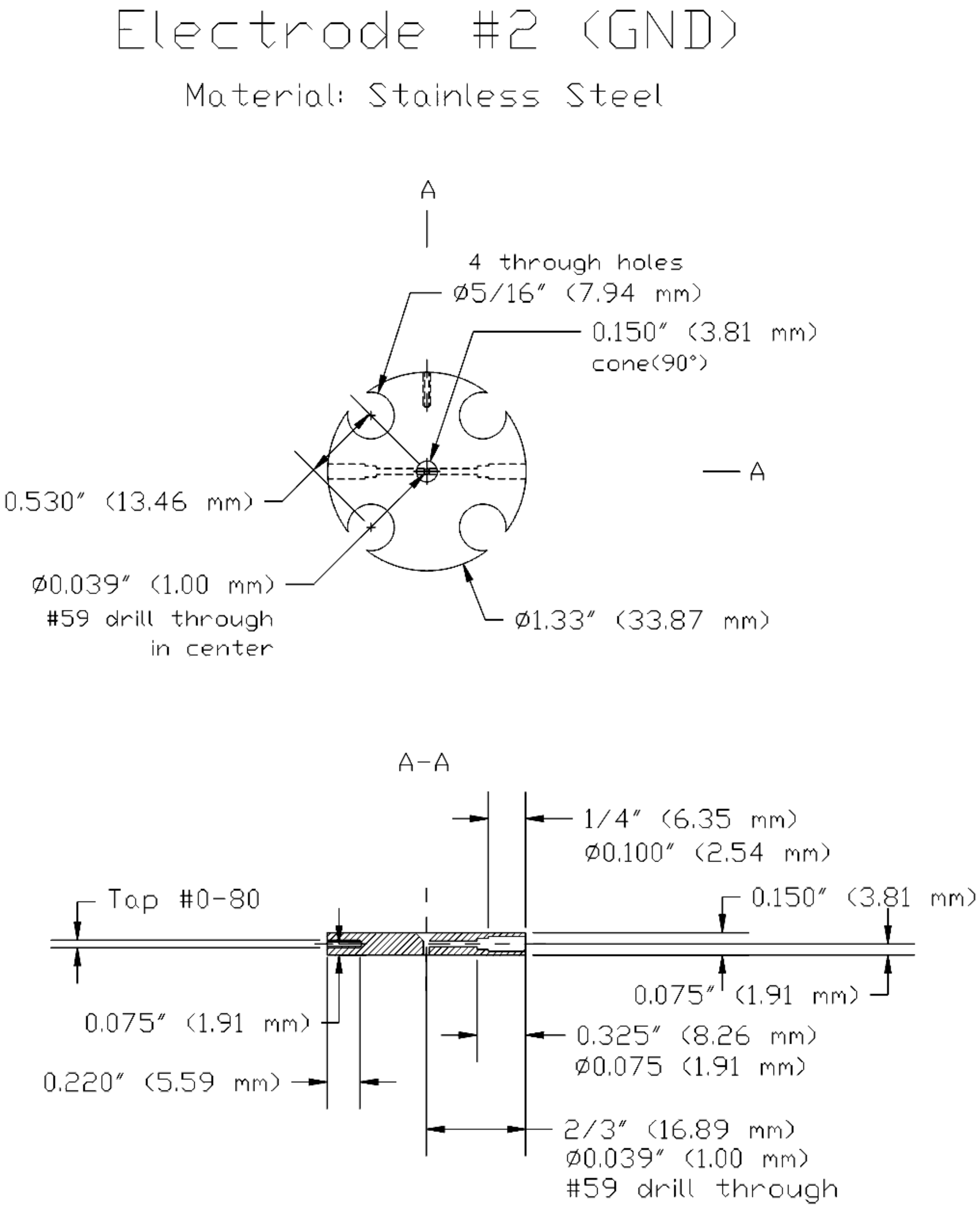

Figure B.9: Ground (outside) discharge electrode for cluster production.

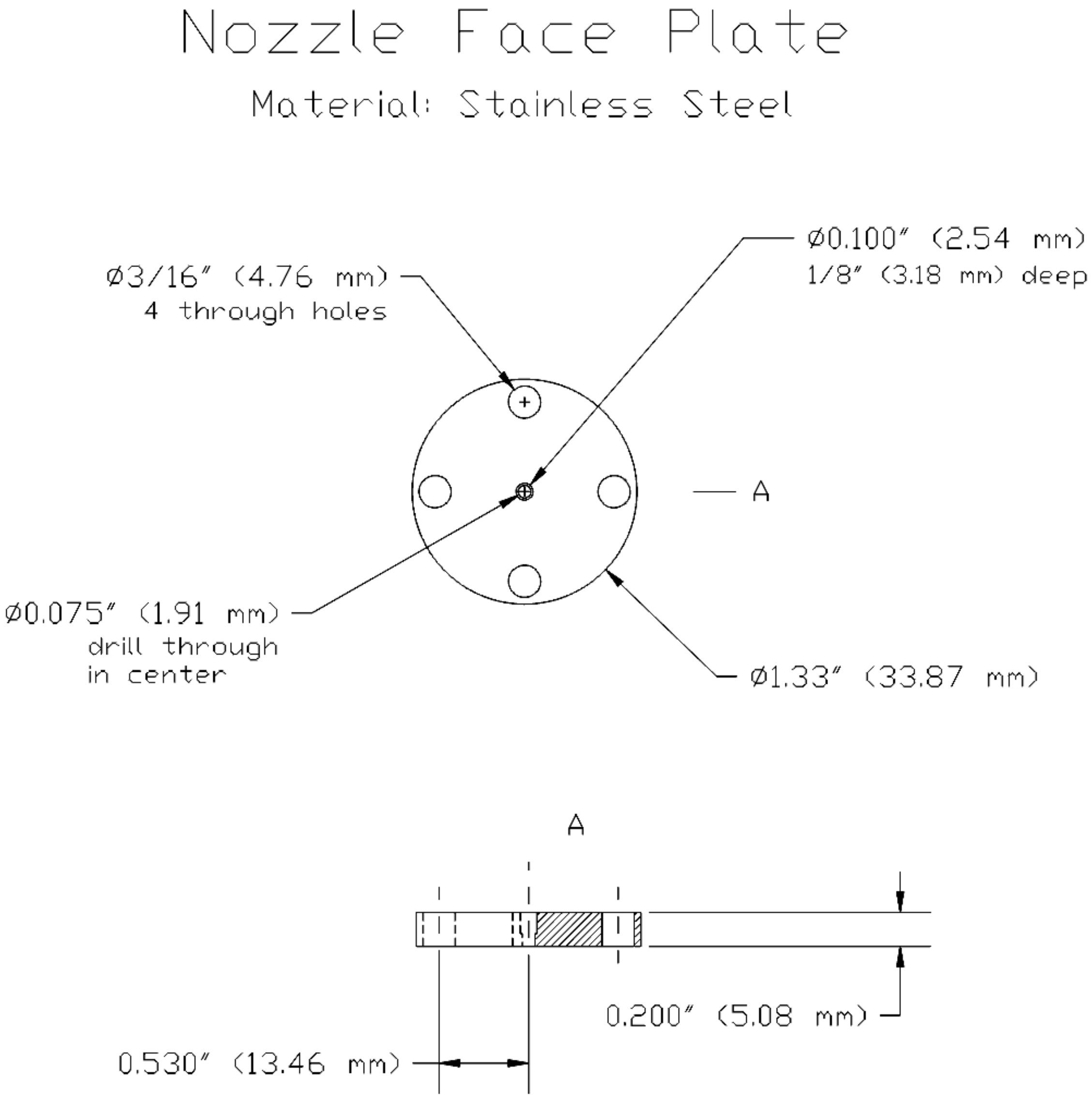

Figure B.10: Non-discharge pulsed valve faceplate flange for cluster production.

B.2 Circuits

B.2.1 TTL Pulse Width Selector

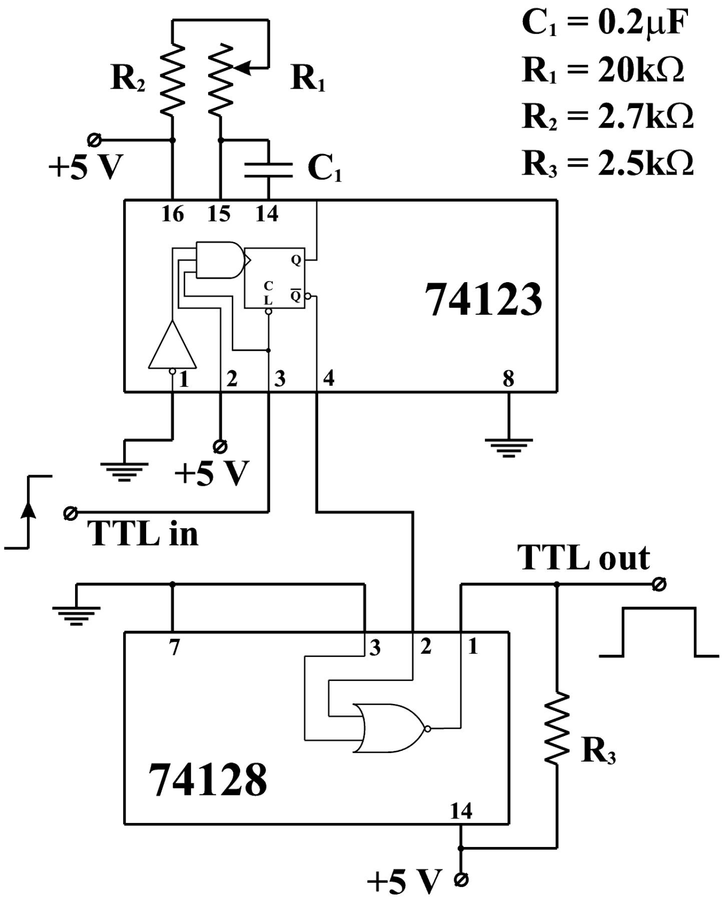

Figure B.11: TTL pulse width selector circuit, triggered by a TTL pulse rising front.

This circuit is triggered by the rising front of a TTL pulse and is used to produce a rectangular TTL pulse of desired duration (up to a few milliseconds). This helps to limit the number of triggering delay lines needed from a commonly used SRS 535 pulsed delay generator to only one. The pulse is produced by a retriggerable monostable multivibrator (74123). The pulse duration is determined by the $(R_1 + R_2)C_1$ time constant, and may be adjusted by the R_1 trim pot. The inverter (74128) is used to invert the pulse to the proper polarity and to isolate the input (delay generator) from the output (high voltage circuit).

B.2.2 Pulsed Valve Driver

The pulsed valve driver (Figure B.12) is based on a 2N6768 power MOSFET transistor. It applies high voltage to a solenoid pulsed valve whenever the transistor is opened. High voltage (up to 400 V) was produced by charging the C_1 capacitors in a voltage doubling arrangement. The voltage was regulated by a Variac, isolated from the rest of the circuit by a transformer. The R_1 resistor is used to discharge these capacitors when the circuit is turned off. The 1 kΩ, 25 W resistor was used to limit the current through the valve solenoid coil.

The high voltage transistor was opened by the TTL pulse width selector circuit (B.2.1). The necessary +5 V should be provided by a regulated +5 V power supply (300 mA or better).

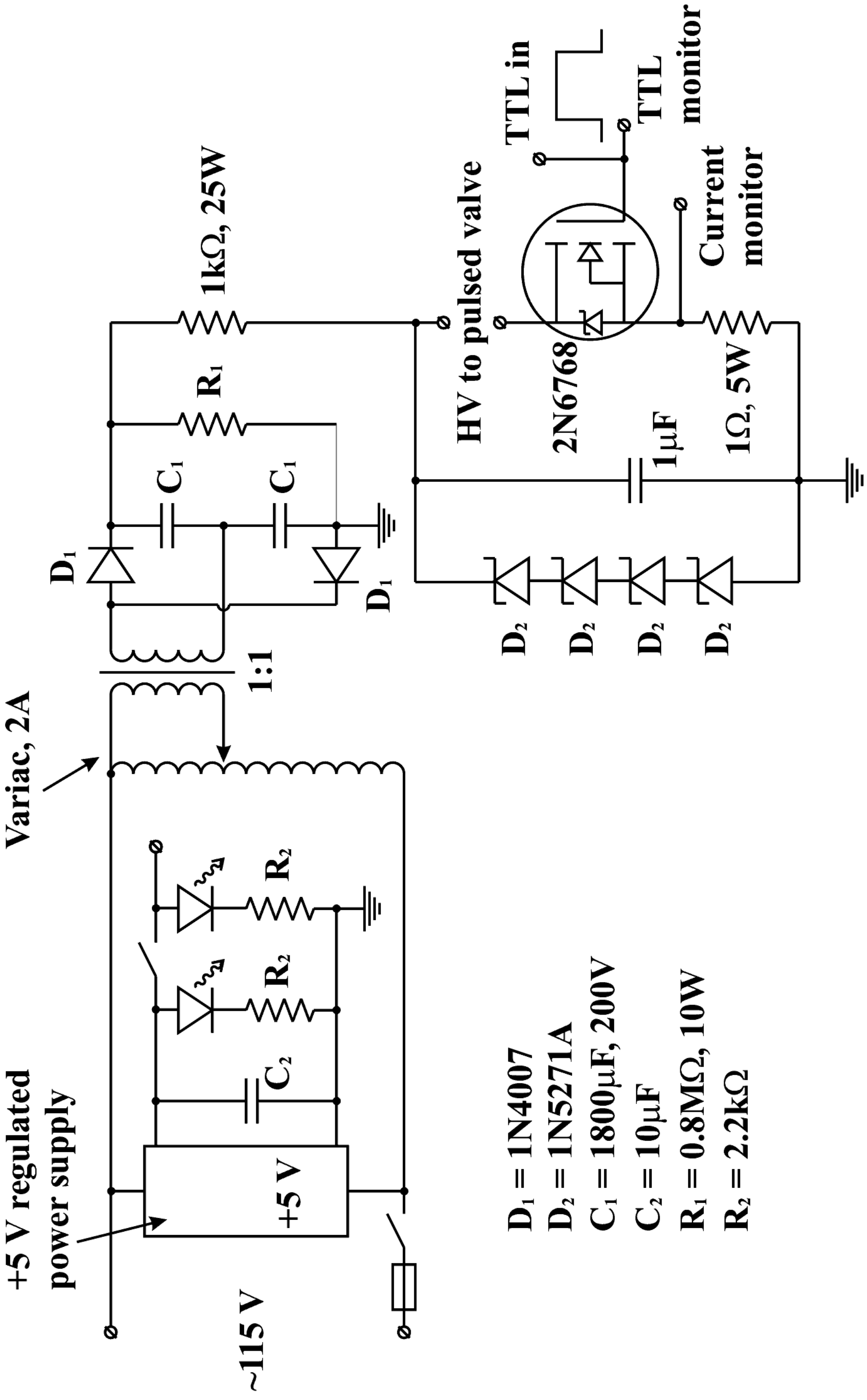

Figure B.12: Pulsed valve driver circuit.

B.2.3 TOF MS High Voltage Pulser

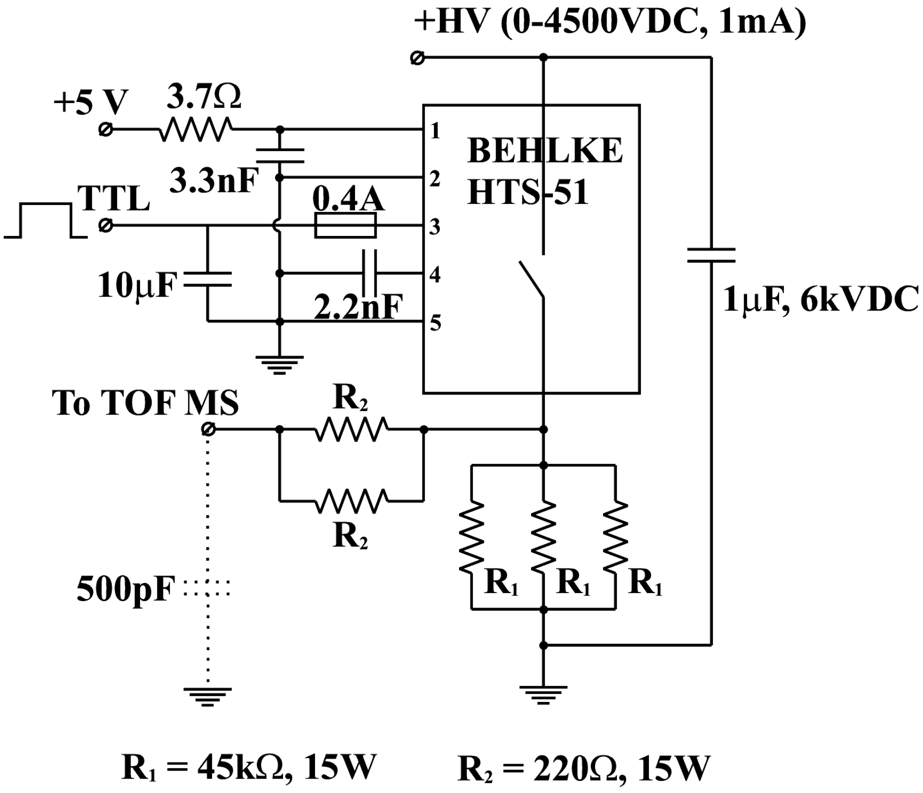

Figure B.13: One channel of the TOF MS high voltage pulser.

The pulser for high voltage ion extraction and acceleration in the time-of-flight mass spectrometer has two identical channels (Figure B.13). Each channel is based on a fast high voltage, high current switch HTS–51 (upto 5 kV, 30 A), manufactured by BEHLKE ELECTRONIC GmbH.

The high voltage capacitor was made of metalized polyester film rated up to 6 kV DC, custom made by Dearborn Electronics, Inc. It has been selected to be as large as possible to compensate for the low current from the power supply (1 mA maximum). It was therefore not possible to completely compensate for the high voltage overshoot at the beginning of

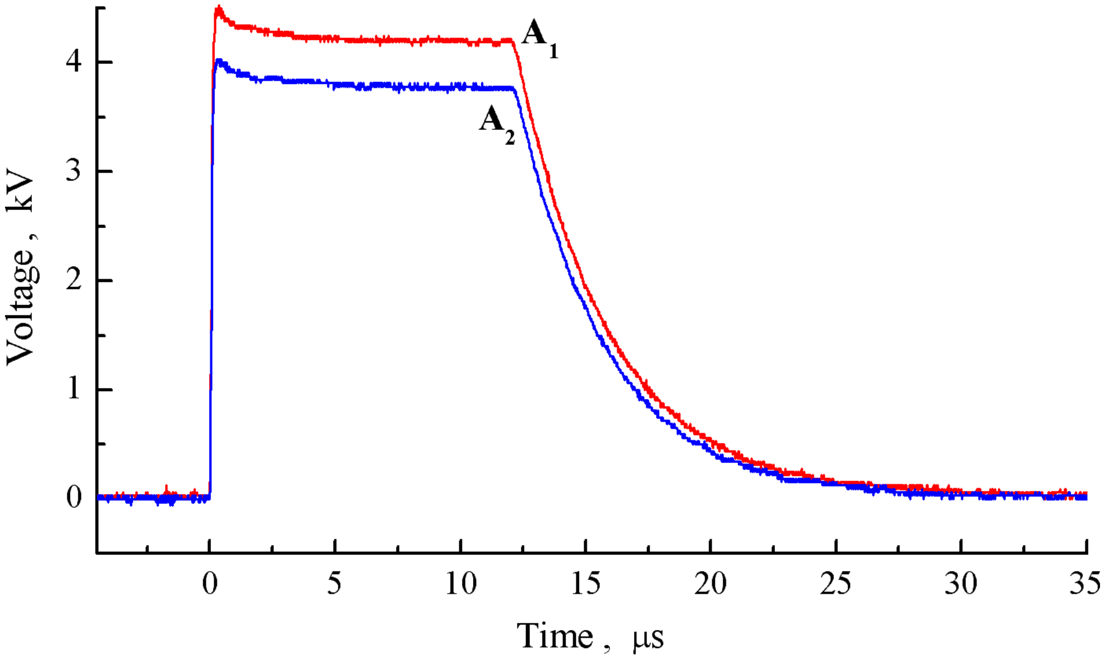

Figure B.14: TOF MS pulser high voltage pulse profile (full).

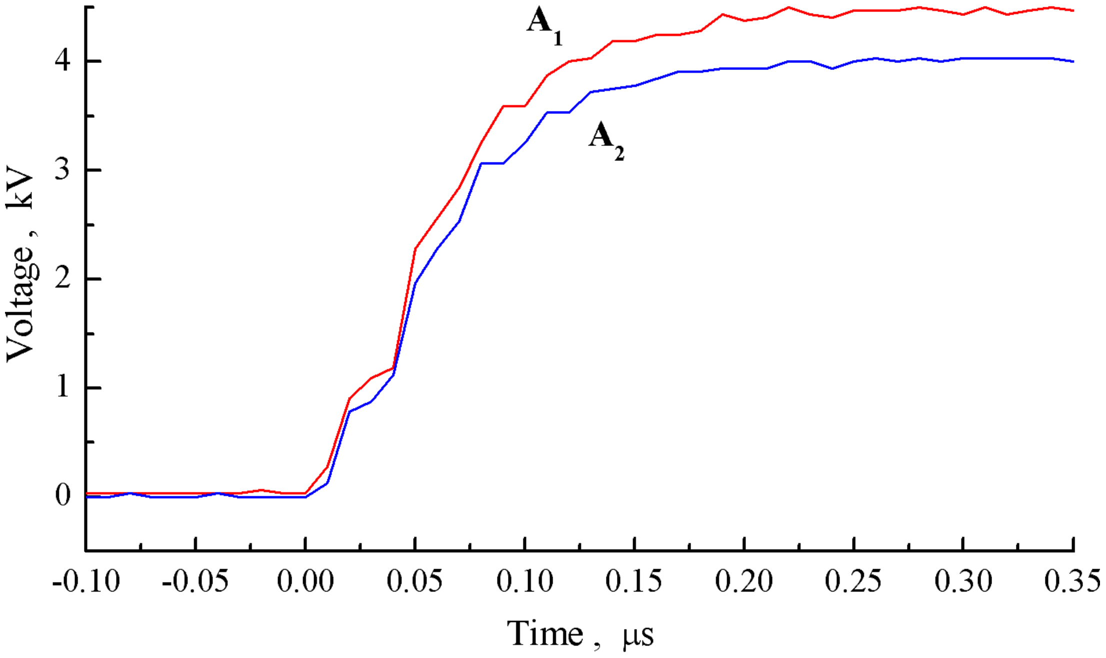

Figure B.15: TOF MS pulser high voltage pulse profile (front).

the pulse (Figures B.14, B.15; $V_{A_1} = 4200$ V, $V_{A_2} = 3800$ V).

The resistors R_1 were selected to adjust the voltage drop time constant at the pulse tail when the switch is turned off. The resistors R_2 were selected to adjust the voltage rise time constant at the pulse front after the switch is turned on, as well as to smooth out the voltage oscillations. Both R_1 and R_2 were type MS power film resistors (15 W) rated for up to 6 kV DC operation, manufactured by Caddock Electronics, Inc.

The TTL pulse width selector circuit (B.2.1) was used to adjust the duration of the high voltage pulse ($C_1 = 0.05$ μF, $R_1 = 10$ kΩ, $R_2 = 156$ Ω, $R_3 = 1$ kΩ). An AT type computer power supply was used to provide +5 V to the TTL circuit and the low voltage side of both of the high voltage switches.

After the pulser has been turned on, the high voltage should be applied to it gradually from 0 V to the desired +HV value. This should be done simultaneously on both channels (A_1 and A_2), to avoid large voltage gradients in TOF MS ion optics. According to the switch manufacturer, instant application of high voltage may damage switch circuits. In addition, the only power supply available was not able to quickly charge a 1 μF capacitor to the necessary few kV.

B.2.4 Frequency Divider

The TTL frequency divider (Figure B.16) is used to divide the frequency of an external source by an integer number N = 1 – 256. The desired divider is selected by setting the jumpers to logical 1 or 0.

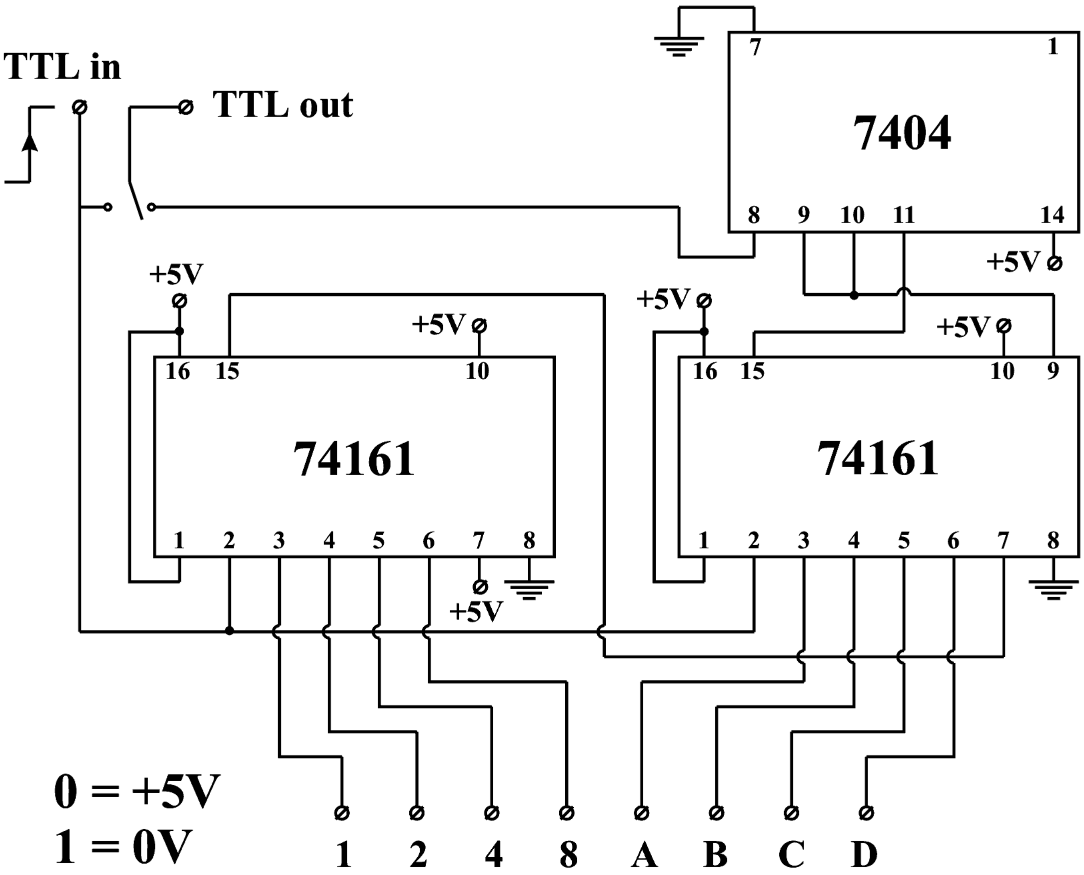

Figure B.16: TTL triggering frequency divider.

Appendix C

Blake Group Spectroscopy Tools Software

C.1 Main Panel

Blake Group Spectroscopy Tools (BGSpecT) is a set of tools for remote control of experiments and data collection. It consists of a set of modules, controlling *instruments* (C.1.1) and *tools* (C.1.2) to work with those instruments (i.e., record spectra or some other signal functions and communicate with instrument devices on low level).

Among the useful features of BGSpecT are that it:

- Simultaneously controls multiple devices of the same kind
- Controls devices via GPIB and RS232 interfaces as well as PC plug-in cards (PCI or ISA)
- Simultaneously controls multiple GPIB boards
- Incorporates smart oscilloscope waveform acquisition
- Enables wavelength source wavelength conversions
- Can Master/Slave lock delay lines from pulse/delay generator
- Has a huge number of supported oscilloscopes
- Easily enables acquisition of spectra

- Can be flexibly configured

- Provides a user friendly interface, with partial Windows XP themes support

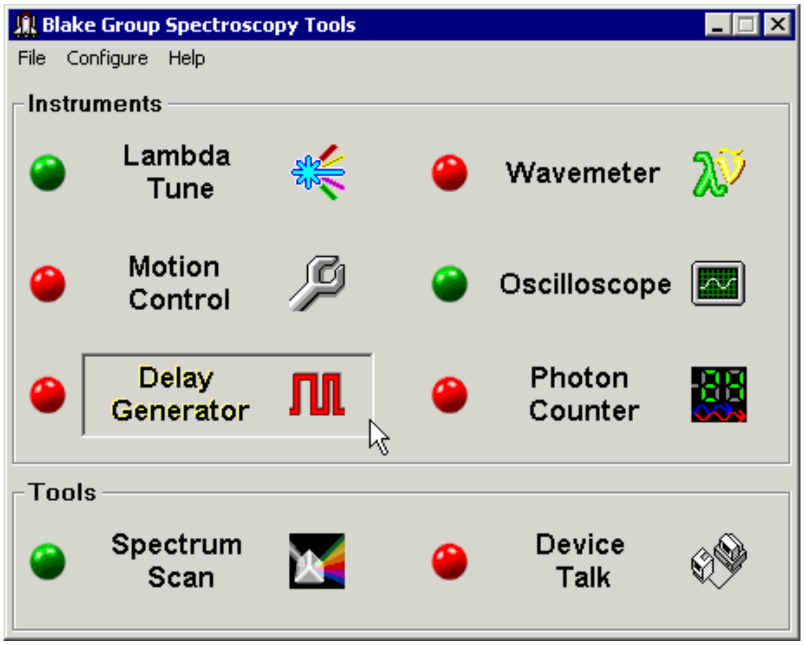

The BGSpecT panel itself is a switch board. It is used to turn On/Off the instrument and tool sub-panels which can only be accessed through the switch board. These sub-panels may be opened by pressing a corresponding button on the BGSpecT panel.

C.1.1 Instruments

Instrument sub-panels communicate with miscellaneous devices and control them. Instrument panels are:

- Lambda Tune (C.2) – controls multiple multi-axis lasers via a Motion Control sub-panel and diode lasers via GPIB and RS232

- Wavemeter (C.3) – controls multiple wavemeters via GPIB and RS232

- Motion Control (C.4) – handles precision motion control micropositioners via PC plug-in cards (ISA)

- Oscilloscope (C.5) – controls multiple oscilloscopes via GPIB, RS232 and PC plug-in cards (PCI or ISA)
- Delay Generator (C.6) – controls multiple pulsed delay generators via GPIB
- Photon Counter (C.7) – controls multiple photon counters via GPIB and RS232

C.1.2 Tools

The tool sub-panels use either Instrument sub-panels to acquire data and perform data analysis, or are used as a general tool for Instrument panel devices. Tool panels are:

- Spectrum Scan (C.8) – records spectra using lambda tune sources, motion control micropositioners and delay generators as sources and oscilloscopes, photon counters and wavemeters as detectors
- Device Talk (C.9) – configures COM port settings for RS232 communication. Can talk to GPIB and RS232 devices using individual device commands

C.1.3 Menus

The program menus are:

- File

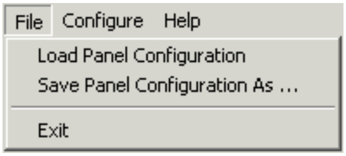

The “Save Window Configuration” menu saves the current On/Off status for sub-panels. The “Load Window Configuration” menu loads the above configuration. When exiting, the program saves the configuration and then loads it automatically the next time it is started.

- Configure

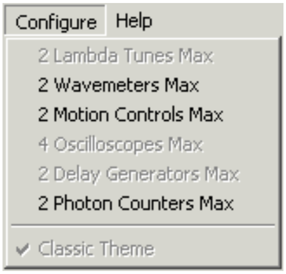

Here, one can change the maximum number of allowed devices in the Instrument panels. Its instrument submenus are disabled if either the corresponding panel or the Spectrum Scan panel is currently open. The valid number of devices is between 1 and 64. Keeping this number small (no larger than needed) helps to speed up multi-device tasks such as reading oscilloscope traces.

The "Classic Theme" menu is enabled only in Windows XP. It switches between the classic look of the program controls (like that in previous Windows versions) and the partial XP themes look (when the menu is not checked).

- Help

This provides help for BGSpecT program. A web browser must be installed to view help files.

C.1.4 System Tray Icon

When the BGSpecT panel is minimized, its icon is placed in a system tray.

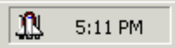

It can be restored by double-clicking the icon in the system tray. Right-clicking on the icon will bring up the following menu that can be used to open/close instrument and tool panels, restore BGSpecT panel to its normal state, or exit the program.

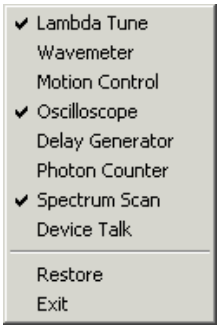

C.1.5 Other

The BGSpecT main directory has 2 sub-directories: *Help* (where all the help files are stored) and *Configs*. The latter is used to store all configuration files that were created automatically. All these files are in ASCII format and all parameters have descriptions. If necessary, they may be modified in any text editor. In general, it is not advised to alter these files.

C.2 Lambda Tune Panel

The Lambda Tune sub-panel is a part of BGSpecT (C.1) that can simultaneously perform remote control of multiple, independent wavelength sources (lasers, monochromators, frequency generators).

The following procedures are available that one can/should perform with the lambda tune sources:

1. Setup communication parameters before establishing remote communication (C.2.1)

2. Setup lambda tune parameters after remote communication has been established (C.2.2)

3. Change the wavelength (C.2.3)

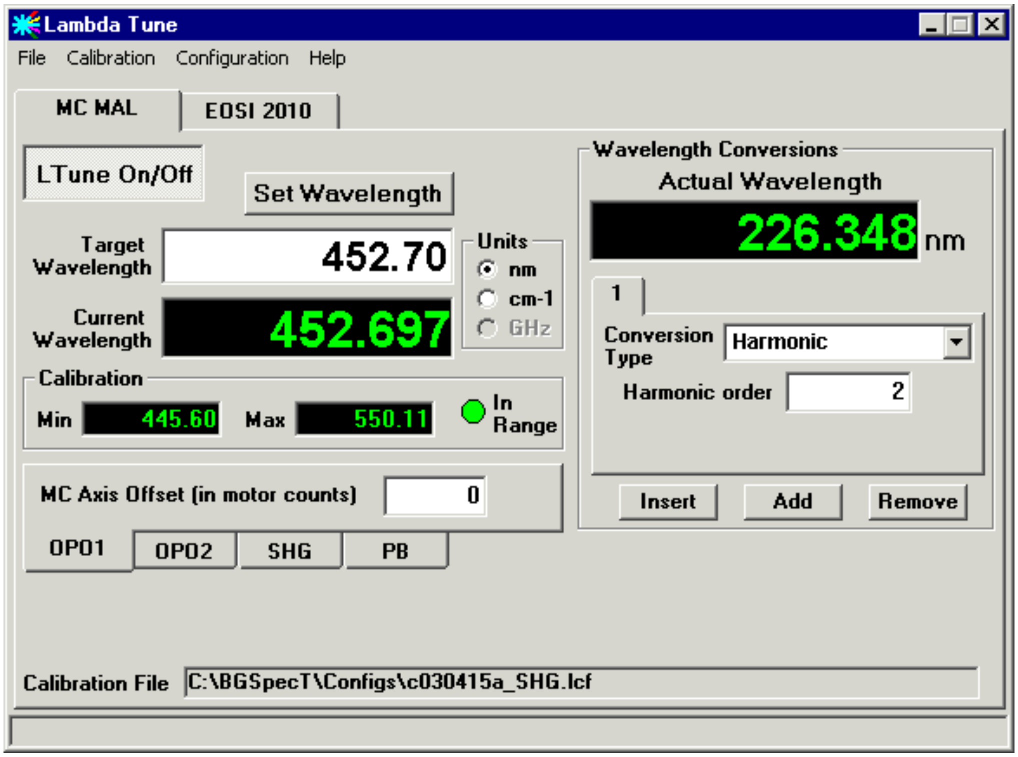

Target Wavelength 452.70

Current Wavelength 452.697

Units: ● nm ○ cm-1 ○ GHz

Calibration Min 445.60 Max 550.11

MC Axis Offset (in motor counts) 0

Actual Wavelength 226.348 nm

1

Conversion Type Harmonic

Harmonic order 2

Calibration File C:\BGSpecT\Configs\c030415a_SHG.lcf

C.2.1 Remote Parameters Setup

To prepare the panel and start communication with a lambda tune device, one first needs to perform some setup through the “Configuration” menu. Please follow the general instructions on how to setup device communications (C.11), substituting the word Device with Lambda Tune where applicable.

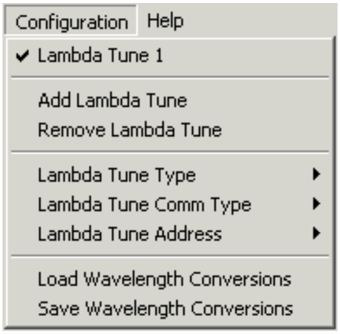

Supported devices are:

- Environmental Optical Sensors Inc. (EOSI, Newport) 2001, 2010 tunable diode lasers

(via GPIB or RS232)

- MultiAxis Laser (OPO, etc.) (via Motion Control panel)

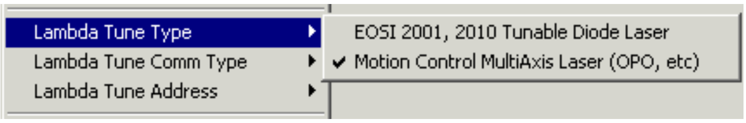

If a few lambda tune sources have been selected, one can switch between them either by clicking the lambda tune tab (the one at the very top) or by choosing the "Configuration ⟶ Lambda Tune *N*" menu.

Once the remote communication with the lambda tune device has been established (by clicking "**LTune On/Off**" button), one can change lambda tune settings and change wavelength.

C.2.2 Lambda Tune Parameters

Once the lambda tune is turned On, the following parameters can be changed:

1. Calibration table – required for proper wavelength determination
2. Wavelength conversions – to show actual wavelength if any manipulations with light were performed (harmonic generation, etc.)
3. Other parameters, some of which are device-specific

C.2.2.1 Calibration File

For the lambda tune to operate properly, it needs a calibration table. If the selected lambda tune has not been turned on before, you will be prompted for a file name. At that point, one can either select an existing calibration or type in a name for a new calibration file.

To perform manipulations with the calibration file, click one of "Calibration" sub-menus.

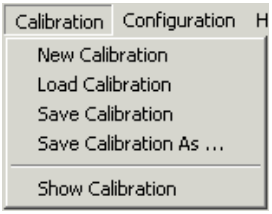

Here, one can create a new calibration, load an existing calibration or save the current calibration. The calibration file name is displayed in the bottom part of the Lambda Tune panel. The "*" (star) symbol after it means that calibration has been changed but not saved.

To access the actual calibration table, one needs to check the "Calibration ⟶ Show Calibration" menu. If this option is chosen, the Lambda Tune Calibration panel window will be open. It can be closed by either clicking the same menu again or selecting the "Window ⟶ Close" menu in the Lambda Tune Calibration panel.

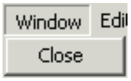

The calibration table will be different for each lambda tune type. The valid calibration range is displayed in the upper left corner of Lambda Tune Calibration panel and under the **Current Wavelength** box on the Lambda Tune panel. Depending on whether the Current Wavelength is within or outside the valid calibration wavelength range, the LED will become green or red, respectively.

The EOSI 2001 and 2010 lasers one can swap diode modules. Each of those modules has a certain tuning range and center wavelength. One can either choose the **Diode Center Wavelength** from the list or type in a custom value if the diode is not in the list. Depending on that value, the diode tuning range will be set automatically.

The MultiAxis laser uses motion axes from the Motion Control panel (C.4) to change the wavelength of a laser or OPO. Hence, one needs to create a table where certain wavelengths correspond to some specific MC axis positions.

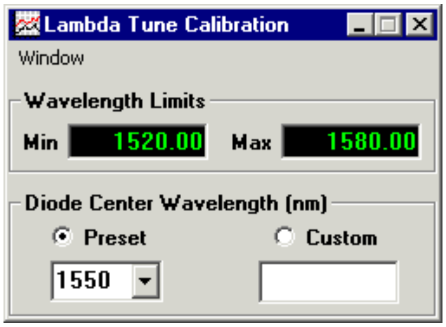

Wavelength Limits

Min 1520.00 Max 1580.00

Diode Center Wavelength (nm)

● Preset ○ Custom

1550

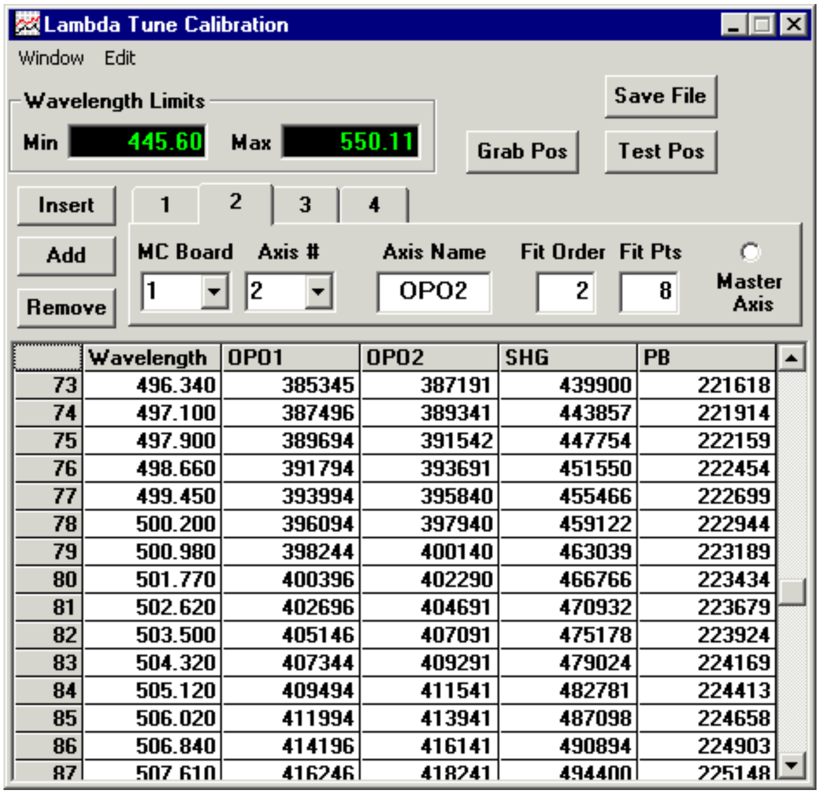

Wavelength Limits

Min 445.60 Max 550.11

MC Board 1 Axis # 2 Axis Name OPO2 Fit Order 2 Fit Pts 8 ○ Master Axis

	Wavelength	OPO1	OPO2	SHG	PB
73	496.340	385345	387191	439900	221618
74	497.100	387496	389341	443857	221914
75	497.900	389694	391542	447754	222159
76	498.660	391794	393691	451550	222454
77	499.450	393994	395840	455466	222699
78	500.200	396094	397940	459122	222944
79	500.980	398244	400140	463039	223189
80	501.770	400396	402290	466766	223434
81	502.620	402696	404691	470932	223679
82	503.500	405146	407091	475178	223924
83	504.320	407344	409291	479024	224169
84	505.120	409494	411541	482781	224413
85	506.020	411994	413941	487098	224658
86	506.840	414196	416141	490894	224903
87	507.610	416246	418241	494400	225148

One can change the number of used axes by clicking the “**Insert**”, “**Add**” or “**Remove**” buttons. The parameters for each axis must then be configured:

1. **MC Board** – the number of a motion control board which the axis is connected to

This is the same as *N* in the Motion Control panel “Configuration ⟶ Motion Control *N*” menu.

2. **Axis #** – the number of the desired axis

3. **Axis Name** – this will be displayed on the Motion Control panel Use distinct names to avoid confusion with the axis assignment

4. **Fit Order** – the order of polynomial used to fit the calibration table for wavelength or axis position interpolation

Such a fit is performed to find new axis positions for a selected wavelength and to find the wavelength for the current axis position.

5. **Fit Pts** - the number of points used in the above fit

6. **Master Axis** - indicates if the axis has been chosen as the master axis

Only the master axis column is used in Wavelength ⟷ Axis position conversions. Positions of all other axes are calculated based on the master axis position. If a position of a non-master axis has been changed (i.e. manually or through the Motion Control panel) without changing master axis position, the calculated current lambda tune wavelength will not change.

The values of the calibration point wavelength and axis positions can be edited directly in table cells. To add a new point, one can simply start editing an empty line in the end of the table or press the "**Grab Pos**" button. The latter will copy the current positions of all axes used in the calibration table. To remove points from the table, select the proper row and click the "Edit ⟶ Delete Point(s)" menu. Multiple row selection is allowed.

Clicking the "**Test Pos**" button will put the axis positions of a selected calibration point to Target absolute positions of those axes in the Motion Control panel. It will also set the destination to "Absolute". However, it will not move the axes. That must be done manually.

“**Save File**” performs the same function as the “Calibration ⟶ Save Calibration” menu in the Lambda Tune panel.

In addition to saving the calibration file manually, a temporary calibration is saved to a file “$__$lcf*N*.$lc” whenever any calibration parameter has been changed. This feature was designed for one step manual Undo and to secure calibration from computer crashes.

C.2.2.2 Wavelength Conversions

If any wavelength conversions are performed with the lambda tune light, the actual wavelength after such conversions can be calculated in the Wavelength Conversions part of the Lambda Tune panel. One can change the number of conversions by clicking “**Insert**”, “**Add**” or “**Remove**” buttons, after which the parameters of each wavelength conversion should be set. These conversions will be applied to the initial lambda tune wavelength in order of their appearance. The calculated **Actual Wavelength** is then displayed.

There are a few wavelength conversions available:

1. **None** – does not do anything; this is the default value, and can also be used to disable some of the conversions
2. **Units** – changes actual wavelength units
3. **Harmonic** – higher order harmonics

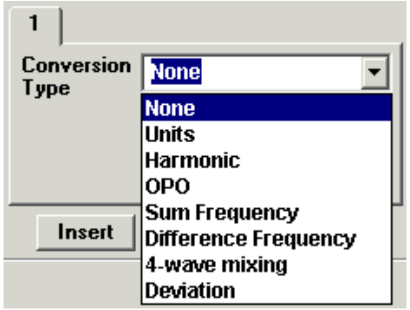

4. **OPO** – complimentary OPO wavelength (signal/idler)

5. **Sum Frequency**

6. **Difference Frequency**

7. **4-wave mixing** – calculates the result of a four-wave mixing of the lambda tune with two other light sources

8. **Deviation** – from a fixed wavelength

Units conversion switches between **nm** (nanometers), **cm^{-1}** (wavenumbers) and **GHz** (gigahertz).

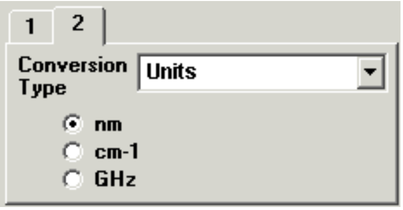

Conversion Type: Units

● nm
○ cm-1
○ GHz

OPO calculates a complimentary signal/idler wavelength if the Current Wavelength is one of them. This conversion requires the wavelength of the pump laser.

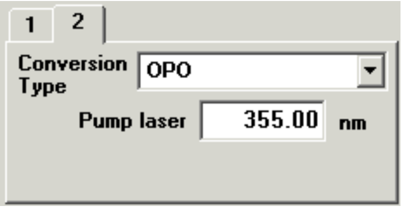

Conversion Type: OPO

Pump laser: 355.00 nm

Sum Frequency conversion calculates the sum wavelength of the current wavelength with another one from a Second source.

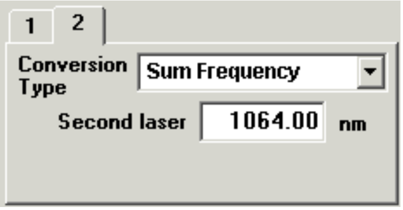

Conversion Type: Sum Frequency

Second laser: 1064.00 nm

Difference Frequency conversion calculates the difference wavelength of the current lambda tune and another Second source. It always returns a positive value, no matter which of the two wavelengths is larger.

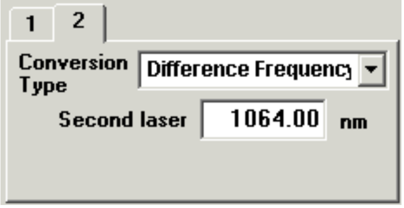

Conversion Type: Difference Frequenc
Second laser: 1064.00 nm

The **Deviation** conversion calculates the deviation wavelength of the current wavelength from a reference wavelength.

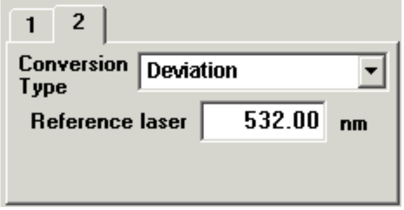

Conversion Type: Deviation
Reference laser: 532.00 nm

It is possible to Save/Load wavelength conversions for a lambda tune set up by clicking the "Configuration ⟶ Save/Load Wavelength Conversions" menu.

C.2.2.3 Other Lambda Tune Parameters

One can change lambda tune **wavelength units** on the right side of Target and Current Wavelength boxes.

There are also some parameters specific to a particular lambda tune type.

For the EOSI 2001 and 2010 lasers, one can change the diode **current** and/or **temperature**, switch between **User** and **Factory** settings, and change the **calibration center wavelength** (the one in the hardware, not in the software calibration table). It is also possible to perform fine wavelength tuning by changing the **Piezo Tune voltage**.

For a MC Multi-Axis laser, it is possible to set a fixed **offset** for any motion control axis. Such an offset might be needed, for example, to compensate for a gradual backlash

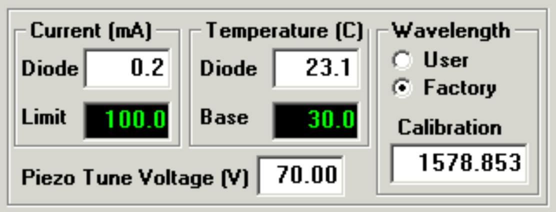

Current (mA)
Diode 0.2
Limit 100.0

Temperature (C)
Diode 23.1
Base 30.0

Wavelength
○ User
● Factory
Calibration 1578.853

Piezo Tune Voltage (V) 70.00

accumulation without re-assigning the axis position value. This helps to avoid laser re-calibration.

C.2.3 Changing Lambda Tune Wavelength

To change the lambda tune wavelength, type the desired value in the **Target Wavelength** box. If the chosen lambda tune target position is outside the valid calibration range, it will be corrected to be within that range. After entering the desired wavelength, simply click the "**Set Wavelength**" button and the wavelength will be changed. If there are a few lambda tune sources in the panel, the above procedure will apply only to the laser whose parameters are displayed on the panel.

C.3 Wavemeter Panel

The Wavemeter sub-panel is part of BGSpecT (C.1) that can simultaneously perform remote control of multiple independent wavemeters.

The following are procedures that one can/should perform with the wavemeters:

1. Setup communication parameters before establishing remote communication (C.3.1)

2. Setup wavemeter parameters after remote communication has been established (C.3.2)

3. Read wavelength (C.3.3)

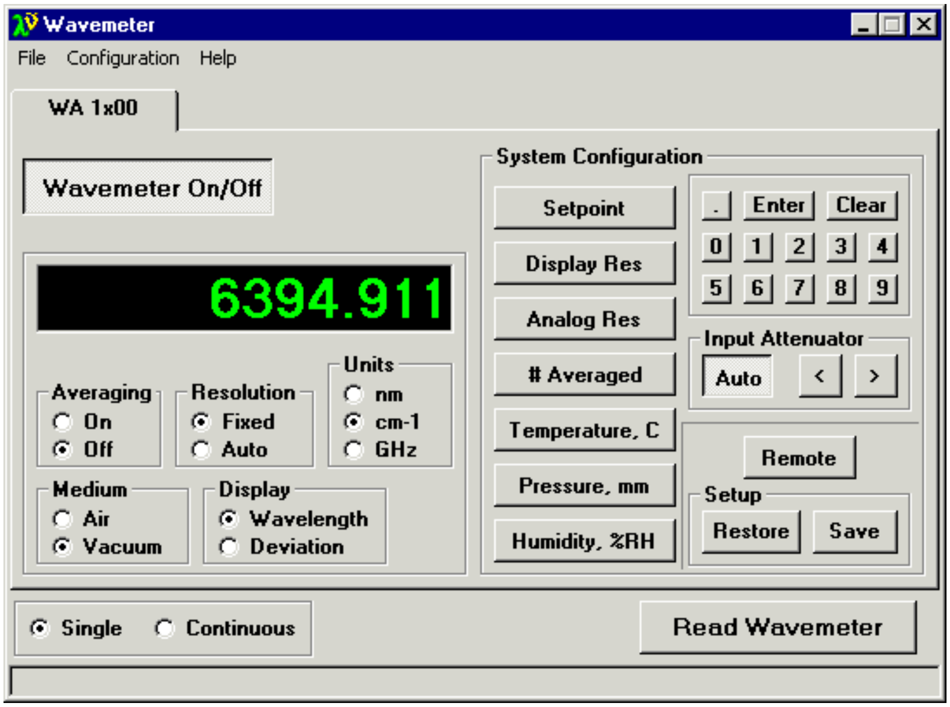

6394.911

Averaging ○ On ● Off

Resolution ● Fixed ○ Auto

Units ○ nm ● cm-1 ○ GHz

Medium ○ Air ● Vacuum

Display ● Wavelength ○ Deviation

● Single ○ Continuous

C.3.1 Remote Parameters Setup

To prepare the panel and start communication with wavemeter(s), one first needs to perform some setup through the “Configuration” menu. Please follow the general instructions on how to setup device communications (C.11), substituting the word Device with Wavemeter where applicable.

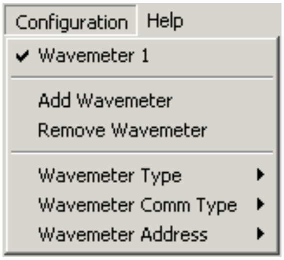

The presently supported wavemeters are:

- Burleigh WA–1000 and WA–1500 (via GPIB and RS232)

If a few wavemeters have been selected, one can switch between them either by clicking the wavemeter tab or by choosing the "Configuration ⟶ Wavemeter *N*" menu.

Once the remote communication with the wavemeter has been established (by clicking "**Wavemeter On/Off**" button), one can change wavemeter settings and read the wavelength.

C.3.2 Wavemeter Parameters

The wavemeter panel for Burleigh WA–1000 and 1500 is designed to mimic the front panel on the hardware wavemeters. Just choose the necessary options.

In addition, one can choose the way in which the wavelength is read from the wavemeter: once or continuously. This is done by selecting "**Single**" or "**Continuous**" mode in the bottom of the panel.

C.3.3 Reading Wavelength

To read the wavemeters, click the "**Read Wavemeter**" button in the bottom of the panel. If a few wavemeters are turned On, wavelengths will be read from all of them. Acquired wavelength and any wavemeter messages are displayed on the panel.

C.4 Motion Control Panel

The Motion Control sub-panel is that part of BGSpecT (C.1) that can simultaneously perform remote control of multiple independent Motion Control boards with up to **8** axes (micro-positioner stepping motors) each.

The following are procedures that one can/should perform with motion control:

1. Setup communication parameters before establishing remote communication (C.4.1)
2. Setup axis parameters after remote communication has been established (C.4.2)

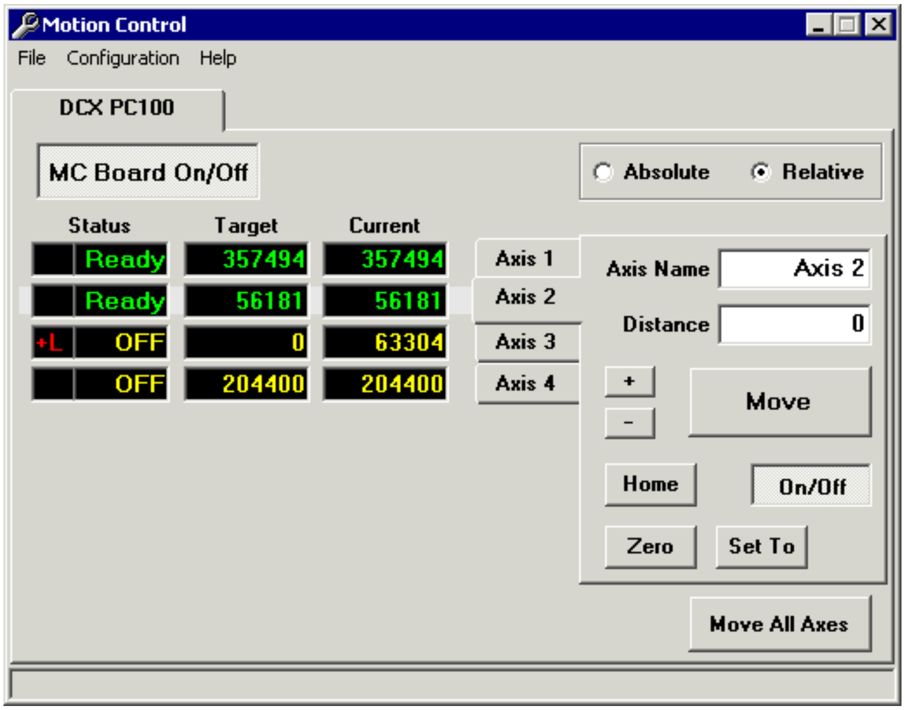

○ Absolute ● Relative

Status		Target	Current
	Ready	357494	357494
	Ready	56181	56181
+L	OFF	0	63304
	OFF	204400	204400

Axis Name: Axis 2

Distance: 0

3. Move axes (C.4.3)

4. Positions file (C.4.4)

C.4.1 Remote Parameters Setup

To prepare the panel and start communication with the Motion Control board(s), one first needs to perform some setup through the “Configuration” menu. Please follow the general instructions on how to setup device communications (C.11), substituting the word Device with Motion Control where applicable.

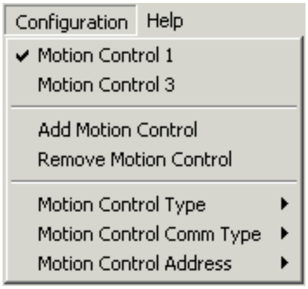

Supported Motion Control boards are:

- Precision MicroControl:

– DC2-PC100, DCX-PC100, DCX-AT100, DCX-AT200, DCX-AT300 series ISA cards

– DCX-PCI100, DCX-PCI300, MFX-PCI1000 series PCI cards

If a few motion control boards have been selected, one can switch between them either by clicking the Motion Control tab (one on the very top) or by choosing the "Configuration ⟶ Motion Control *N*" menu.

Once the remote communication with the motion control board has been established (by clicking "**MC Board On/Off**" button), one can change axes settings and move axes. If the computer has been restarted, the board will not remember its axis positions. You will be prompted to confirm those when turning the board On for the first time.

C.4.2 Motion Axes Parameters

The left half of the panel is for monitoring purposes, and is where the axis position and status are displayed. Note, the **Current** and **Target** positions will be different when the axis is moving.

Switching between different axes is done through the tabs in the middle of the panel. The active axis tab will be right against the corresponding axis status and positions row.

Motion axes can be turned On/Off by clicking the "**On/Off**" button in the bottom of the axis panel.

It is possible to assign a **name** to an axis, which is handy when having to deal with too many of them.

Assigning the value (in motor counts) for the current axis position can be done by clicking the "**Zero**" or "**Set To**" buttons. The former will set the axis position to "0". The latter will set it to the value typed in the **Distance box**. You will be asked to confirm the new axis position assignment.

C.4.3 Moving Axes

The final (**Target**) position of the axis is determined by the number in the **Distance** box. There are two possible destination types: **Absolute** (final motor counts) and **Relative** (the Current axis position is changed by that value). To move one axis, click the“**Move**” button below the Distance box. To move all board axes, click the “**Move All Axes**” button in the lower right corner of the panel. This is equivalent to clicking “Move” buttons for each axis simultaneously. To move an axis to absolute count “0”, click “**Home**” button. “+” and “–” buttons will move an axis to an increase/decrease in its position by the relative value from the Distance box. It is always relative and independent from the Absolute/Relative setting.

While the axis is moving, its position will be tracked and displayed in the **Current** position box.

It is possible to **stop** the axis from moving by clicking a depressed “Move” button. For **emergency stops**, click the depressed “On/Off” buttons.

The current status for all axes is displayed in the **Status** boxes. “OFF” means that the axis is currently turned Off. “Ready” and “Moving” mean that the axis is turned On and is either at rest or moving to a new target position. If there is a red message at the very left, something is not right with the axis operation. “+L” or “–L” means that the stepper motor has reached positive or negative limit, “Err” means all other errors.

C.4.4 Positions File

If the position of any axis has been changed, positions for all axes will be saved in the *Configs* directory in a file with the name:

“MC”+“__t”+BoardType+“__a”+BoardAddress+“.mc1”.

As new backups are made, the extensions for the previous two backups become “.mc2” and “.mc3”. These files are created to remember last axes positions between program startups and computer crashes. The latter two files are saved in case the first one becomes corrupt.

C.5 Oscilloscope Panel

The Oscilloscope sub-panel can simultaneously and remotely control multiple independent oscilloscopes with a total number of channels up to double the number of oscilloscopes. Due to the large number of supported scope models (over 100), this software does not control all possible scope functions, but rather, accesses major common features to acquire waveforms. All waveform manipulations (math, etc) are performed on the PC during post-processing.

The following are procedures that one can/should perform with the scopes:

1. Setup communication parameters before establishing remote communication (C.5.1)
2. Setup scope parameters after remote communication has been established (C.5.3)
3. Acquire and manipulate waveforms (C.5.2)

C.5.1 Remote Parameters Setup

To prepare the panel and start communication with the oscilloscope(s), one first needs to perform some setup through the “Configuration” menu. Please follow the general instructions on how to setup device communications (C.11), substituting the word Device with

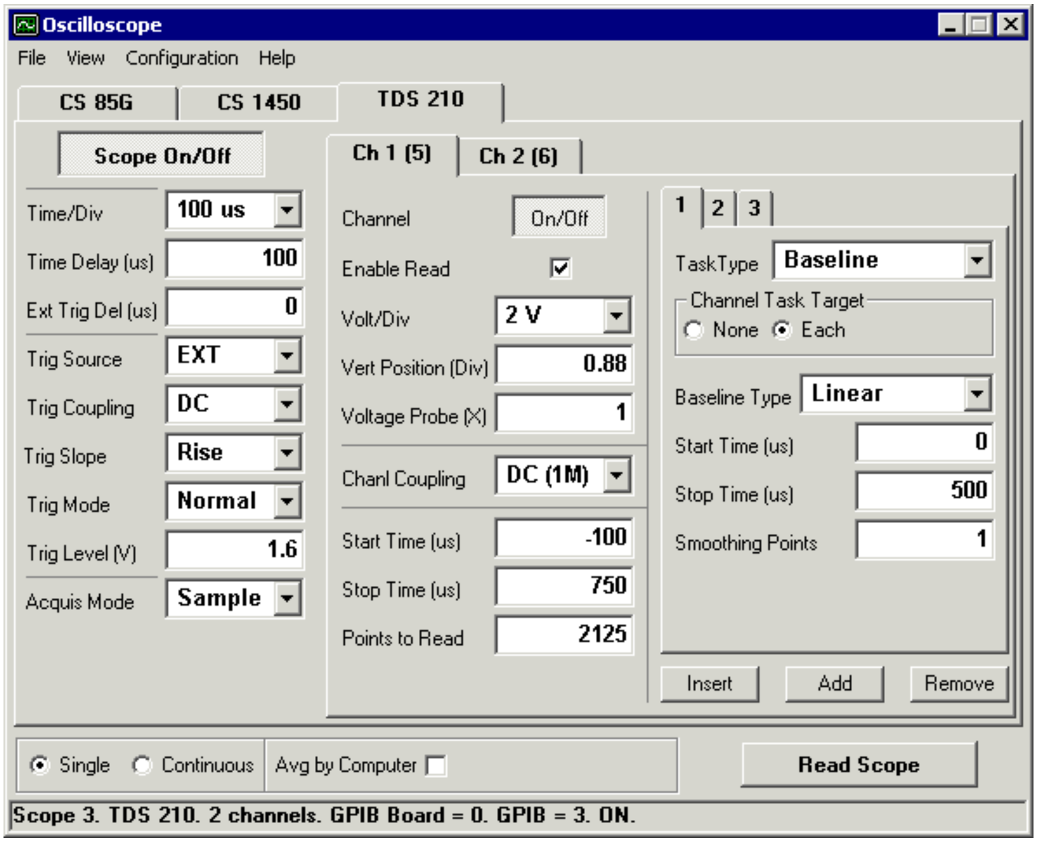

Time/Div: 100 us
Time Delay (us): 100
Ext Trig Del (us): 0
Trig Source: EXT
Trig Coupling: DC
Trig Slope: Rise
Trig Mode: Normal
Trig Level (V): 1.6
Acquis Mode: Sample

Channel: On/Off
Enable Read: ☑
Volt/Div: 2 V
Vert Position (Div): 0.88
Voltage Probe (X): 1
Chanl Coupling: DC (1M)
Start Time (us): -100
Stop Time (us): 750
Points to Read: 2125

TaskType: Baseline
Channel Task Target: ○ None ● Each
Baseline Type: Linear
Start Time (us): 0
Stop Time (us): 500
Smoothing Points: 1

● Single ○ Continuous
Avg by Computer ☐

Scope 3. TDS 210. 2 channels. GPIB Board = 0. GPIB = 3. ON.

Oscilloscope where applicable.

Supported oscilloscopes are:

- Tektronix TDS via GPIB and RS232:

– series 200: 210, 220, 224

– series 300: 310, 320, 340A, 350, 360, 380

– series 1000: 1002, 1012

– series 2000: 2002, 2012, 2014, 2022, 2024

– series 3000: 3012, 3012B, 3014, 3014B, 3032, 3032B, 3034, 3034B, 3052, 3052B, 3054, 3054B

- Tektronix TDS via GPIB:

– series 400: 410, 410A, 420, 420A, 430, 460, 460A

– series 500: 510A, 520A, 520B, 520C, 520D, 524A, 540A, 540B, 540C, 540D, 544A, 580C, 580D

– series 600: 620A, 620B, 620C, 640A, 644A, 644B, 654C, 680B, 680C, 684A, 684B, 684C, 694C

– series 700: 714D, 714L, 724A, 724C, 724D, 744A, 754A, 754C, 754D, 782A, 784A, 784C, 784D, 794D

– series 5000: 5032, 5032B, 5034, 5034B, 5052, 5052B, 5054, 5054B, 5054BE, 5104, 5104B

– series 6000: 6404, 6504, 6604

– series 7000: 7054, 7104, 7154, 7154B, 7254, 7254B, 7304, 7404, 7404B, 7704B

- Tektronix THS via RS232:

– series 700: 710, 710A, 720, 720A, 720P, 730A

- GaGe CompuScope PC plug-in cards (PCI, CompactPCI or ISA):

– 85G, 82G, 8500, 12100, 1250, 1220, 14200, 14100, 1450, 1610, 1602, (6012/PCI) via PCI

– 85GC, 82GC, 14100C, 1610C via CompactPCI

– (8012, 6012, 1012, 512, 2125, 250, 225, LITE via ISA)

- LeCroy 9400A via GPIB and RS232

If a few scopes have been selected, one can switch between them, either by clicking the

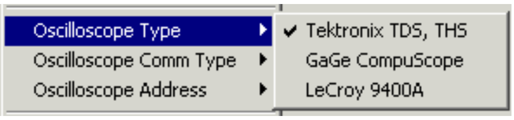

scope tab (the one on the very top) or by choosing the "Configuration ⟶ Scope N" menu.

Once remote communication with the scope has been established (by clicking "**Scope On/Off**" button), one can change scope settings and acquire waveforms.

When turning On remote communication with the scope, the current scope configuration will be retrieved from the scope for GPIB and RS232 scopes. For GaGe CompuScopes, the last used configuration will be restored.

C.5.2 Waveform Acquisition and Manipulation

1. Read
2. View
3. Save

C.5.2.1 Reading Waveforms

To acquire waveforms on the scope and transfer them to the PC, one just needs to click the "Read Scope" button in the lower right corner of the Oscilloscope panel. It becomes active if at least one scope channel is turned On. When multiple scopes are On, their channels are considered by the software as channels of one scope. When acquiring waveforms, all scopes are reset to be triggered at the same time. In case of multiple acquisitions (while "Averaging by Computer" or in "Continuous" mode), scopes are not re-triggered again until all waveforms are transferred to the PC.

Once the waveforms are acquired, they are put through post-processing procedures that are defined for each channel individually under Channel Task tabs.

C.5.2.2 Viewing Waveforms

All new waveforms are displayed in the Oscilloscope Screen panel. One can access it through the "View ⟶ Scope Screen" menu.

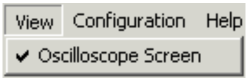

Here, each channel has its own horizontal scale - waveform start/stop times define record limits and the whole record fits into the screen window. One can view time and voltage values for each channel by moving the mouse over the channel traces. These values will be displayed right below the screen part, as well as in a tool tip. There are no time/voltage grids on this panel because each channel may have its own scales.

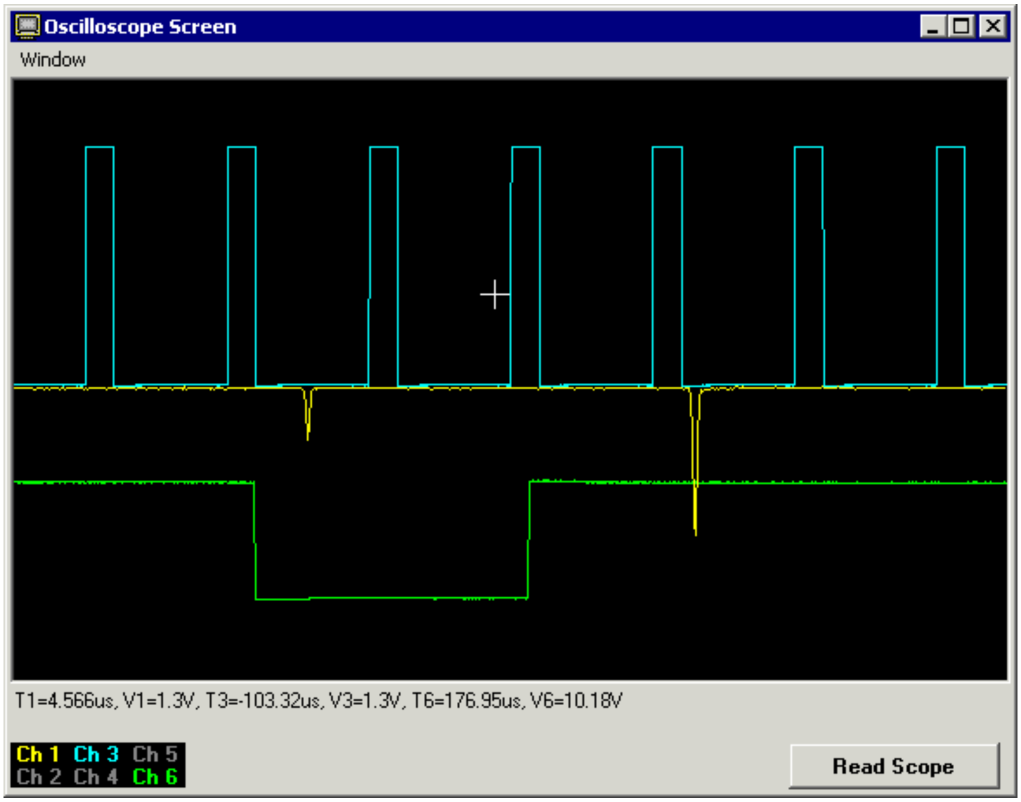

```
T1=4.566us, V1=1.3V, T3=-103.32us, V3=1.3V, T6=176.95us, V6=10.18V
```

Channel numbers on the **labels** are the same as numbers in parenthesis in the channel tabs on the Oscilloscope panel. One can change a default **color** for the channel by double-clicking the channel label in the bottom of the scope screen. A single click on the channel label will bring the trace for that channel on top of others.

If the Oscilloscope Screen panel is closed and reopened, the traces will still be displayed. However, if one clears waveform traces by double clicking on the black area, they will no longer be available. One would have to acquire new traces. The same thing happens if one changes scope or channel critical parameters (time scale, delay time, channel voltage scale, start/stop times, etc.).

The “Read Scope” button on the bottom of the Oscilloscope Screen window performs the same function as the same button in Oscilloscope panel and was put there for user convenience.

Right-clicking the mouse on the screen (black area) will bring up the menu that will allow the user to save channel waveforms into data files (same as described below). Selecting “Clear” from this menu (same as double-clicking on the screen) will remove waveform traces from the screen. Those traces will not be re-displayed until new traces are acquired.

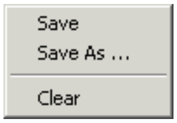

C.5.2.3 Saving Waveforms

If needed, the waveforms can be saved into data files by selecting the “File ⟶ Save” or “File ⟶ Save As” menus in Oscilloscope panel. The “Save As” menu will prompt for file names for each channel. The “Save” menu will save files with automatically generated names into the current scope directory. This directory may be changed through the “File ⟶ Set Directory” menu. If one needs to save waveforms repeatedly, it is advised to use the Autosave option under Channel Tasks.

Depending on whether the box “Time in Time/Div Units” is checked or not, time will be saved either in Time/Div units or in seconds. That value in the checkbox is also used when saving files automatically – via the “File ⟶ Save” menu, Autosave channel task or via the “Other ⟶ Dump Raw Data to File” menu in Spectrum Scan panel (C.8).

Each saved file will have two columns separated by a Tab symbol. The first column is time and the second column is voltage value in volts.

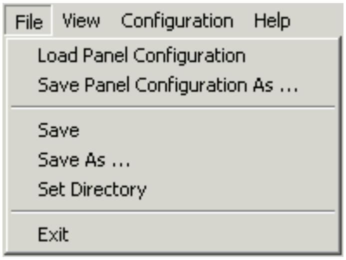

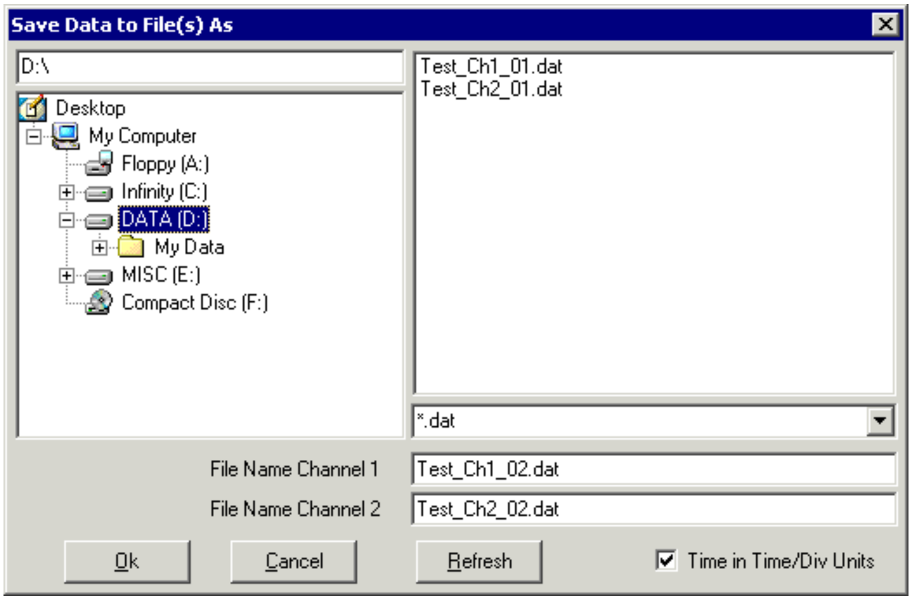

D:\

Test_Ch1_01.dat
Test_Ch2_01.dat

*.dat

File Name Channel 1: Test_Ch1_02.dat

File Name Channel 2: Test_Ch2_02.dat

☑ Time in Time/Div Units

C.5.3 Oscilloscope Parameters Setup

The oscilloscope panel options span over:

1. Panel (all scopes) – software acquisition and averaging modes
2. One scope (all scope channels) – time scale, delay, triggering and scope acquisition

options

3. One scope channel – voltage scale, vertical position, coupling, start/stop times

4. Channel tasks – waveform post processing (baseline, smooth, autosave, voltage dynamic range)

One can also Save and Load such oscilloscope configurations to and from a file.

C.5.3.1 Panel Parameters

Panel-wide parameters are software acquisition and averaging modes. Acquisition mode can be "**Single**" or "**Continuous**" (see the bottom of the Oscilloscope panel). In "Single" mode, the waveforms are acquired only once, which is the same as "Single" triggering mode on stand alone oscilloscopes. In "Continuous" mode, the waveforms are acquired until "Read Scope" button is pressed again, which is similar to "Normal" triggering mode on stand alone oscilloscopes. The reason for having it this way is to make one software oscilloscope out of a few hardware units.

○ Single ● Continuous | Avg by Computer ☑ | Avg Number 25

For averaging, there is a possibility of "**Averaging by Computer**" for acquired waveforms. When this option is enabled, the waveforms are acquired by scopes according to their acquisition mode settings and then are transferred to a PC and averaged by the software. This permits higher levels of synchronization and some post processing before the traces are averaged.

C.5.3.2 Common Scope Parameters

For each scope that is turned ON, one can change a few sets of parameters common to the whole scope:

1. **Time scale** and trigger **delays**
2. **Triggering** options
3. **Acquisition** options

All of these are located on the left side of the Oscilloscope panel.

For stand alone hardware oscilloscopes, one can select **Time/Division**, which is the same as Time/Div or the Horizontal scale on the scope. For GaGe scopes, this will be replaced by the **Sampling Rate** which is inverse of the time interval between two adjacent points in the record. If one of the scopes Time/Div values is not standard (not on the list, but close to another "wrong" value), one should choose that "wrong" setting. The difference adjustment will be done automatically.

Time Delay is the delay time between the trigger position and the first point on the oscilloscope screen, which is not necessarily the first point in the data record. It is positive when the trigger is displayed on the scope screen and negative when the trigger is to the left of the screen. Note that for Tektronix scopes, when such a delay is set to zero the trigger point is on the left of the screen and not in the middle. For oscilloscopes with multiple record lengths, a minimal record length is usually chosen and the delay time is adjusted accordingly. That is why it may be disabled.

External Trigger Delay is used to offset waveforms to "true zero" times in cases when the oscilloscope is being triggered by some delayed signal, but the oscilloscope does not know about the delay.

Currently, the software supports only one **trigger** (no second/delayed trigger) for a scope. All triggering is done only from the "Edge" (e.g. the rise/fall front of the waveform).

In the triggering part of the panel, one can change the **Trigger Source** (one of the channels, External, etc.), **Trigger Coupling** (AC, DC), **Trigger Slope** (Rise, Fall or both), **Trigger Mode** (Single, Normal, Auto, etc.) and **Trigger Level**. For GaGe scopes, the Trigger Mode is replaced by **Channel Mode** (Single, Dual) which shows how many scope channels can be used.

When a scope is acquiring waveforms, the Trigger Mode is set to Single. After all waveforms are transferred to a PC, it is returned to the previous state. For repetitive waveform acquisitions when data acquisition speed is important, it is advised to switch the Trigger Mode to Single.

Acquisition Mode switches between Sample, Average, PeakDetect, Envelope, etc., when applicable. For some of these modes, such as Average or Envelope, one may be able to change the Averaging Number. **Time to Average** is an estimated time that it takes the scope to finish averaging waveforms after it was reset. A computer will wait that long before trying to download the averaged waveform. This is used to minimize communication traffic between the hardware and a PC.

C.5.3.3 Channel Parameters

The user can set up parameters for individual channels. Switching between the channels is done through the channel tab. The **name** of the channel tab is the name of the channel on the scope (Ch 1, Ch A, Aux 1, etc.). The number in parenthesis is the **channel number** in the software, and is the number that goes into the channel label in the Oscilloscope Screen panel. It is also used to identify oscilloscope channels in the Spectrum Scan panel (C.8). The number of channels on the scope is determined by the software automatically. If the software runs out of the maximum allowed number of channels (double the maximum number of devices in the Oscilloscope panel), it may cut off some of the channels that do not fit in.

The “**On/Off**” button turns the channel On and Off, reflecting all changes on the hardware as well (it (dis)appears from the hardware scope screen). For GaGe scopes, this does not change the Channel Mode between Single and Dual. The “**Enable Read**” check does not remove the channel trace from the hardware scope screen. When it is unchecked, the software will not download the waveform to a PC.

One can change a few **voltage** parameters: **Voltage/Division** (vertical scale), **Vertical Position** of the waveform trace and **Voltage Probe** (when applicable). For GaGe scopes, Volt/Div will be replaced by **Voltage Range** – the allowed voltage range for the chosen scale. The full range is 10 divisions for Tektronix scopes and 8 divisions for LeCroy 9400A. The Volt/Div scale may affect the Trigger Level when using this channel as the Trigger Source.

Channel Coupling may be AC, DC, or Ground. The number in parenthesis is input impedance (50 Ohm or 1 MOhm). Channel Coupling may affect allowed Volt/Div scales. If the oscilloscope is triggered from one of its channels, both Volt/Div and channel coupling may affect allowed triggering settings.

The entire waveform does not need to be transferred to a PC. It is possible to choose the time range (**Start** and **Stop** times) that will be downloaded, and only points from this time interval will be plotted in the Oscilloscope Screen panel. Note that the Start/Stop times are in the same units as Time/Div (s, ms, μs, etc.). From the Start/Stop times, the software will calculate the number of **Points to Read** which cannot be changed and is there for information purposes only. Depending on these times, the minimum record length and delay times may be adjusted accordingly. For the LeCroy 9400A, one can **Read 1 Point Out of** N - each Nth point of the record. This approach can be useful when the signal on one channel does not need to have as high a time resolution as another.

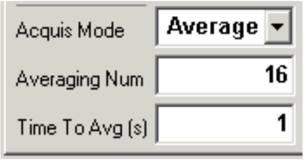

Acquis Mode: Average

Averaging Num: 16

Time To Avg (s): 1

C.5.3.4 Channel Task Parameters

On the right side of the channel panel, one can define **Channel Tasks** - a set of manipulations to be done with the acquired waveform. One can change their number by clicking “**Insert**”, “**Add**” and “**Remove**” buttons. There are a few types of channel tasks:

1. **None** – default value
2. **Dynamic Range**
3. **Baseline**
4. **Autosave**
5. **Smooth**
6. **Scale Up/Down**

All **Start/Stop** times must be within the selected time range for the channel.

Channel tasks can be applied in several ways: None (same as choosing None task), Each (applied to each downloaded waveform), Avg (when Averaging by Computer, applied to the averaged waveform only, not the individual ones), and All (same as Each and Avg together).

All tasks are performed in the order of their appearance and according to their selected time range.

Dynamic Range is the difference between the minimum 5% and maximum 5% points of the waveform in a selected time range. This difference is expressed in % of the whole voltage dynamic range at the selected Volt/Div scale. If the Dynamic Range value does not fit into the **Minimum/Maximum** brackets, all waveforms from this acquisition will be discarded and the acquisition will start again. This task may be very useful when trying to average some fluctuating signal to improve signal contrast and the overall quality of the acquired waveforms. When **Adjust Volt/Div** is checked and the Dynamic Range is below Minimum or above Maximum values, the Volt/Div scale will be increased/decreased before the next acquisition attempt. It is therefore useful for establishing a dynamic voltage scale adjustment during scans.

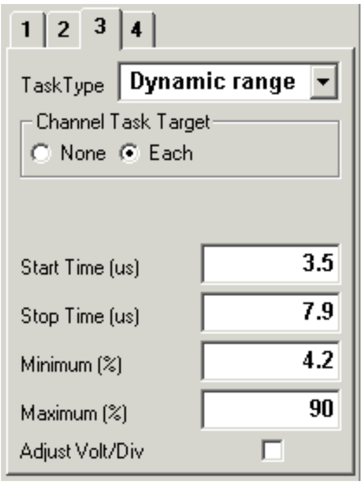

TaskType Dynamic range

Channel Task Target
○ None ● Each

Start Time (us) 3.5
Stop Time (us) 7.9
Minimum (%) 4.2
Maximum (%) 90
Adjust Volt/Div ☐

In the **Baseline** channel task, one can choose among the following baseline subtraction types:

None – default

Linear – subtracts a straight line that goes through Start/Stop points

Vertical – moves the waveform Up/Down to bring the selected Start point to 0 V

Waveform – subtracts a “baseline” waveform that has been obtained by pressing “**Acquire Baseline**” button

In the Linear and Vertical cases, one can choose the **Smoothing Points** number that is used to average this number of points to find better voltage values for baseline Start/Stop points. This may be handy for baselining noisy waveforms.

The **Autosave** channel task will save the selected part of the waveform automatically into a file defined by the **File Mask**. The “*” symbol in it will be substituted by an

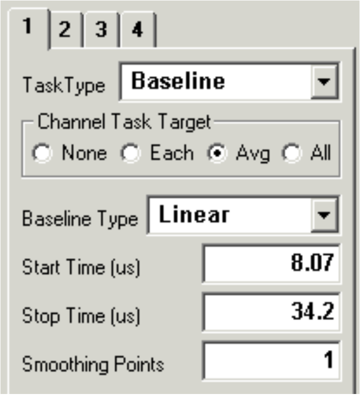

TaskType: Baseline

Channel Task Target: ○ None ○ Each ● Avg ○ All

Baseline Type: Linear

Start Time (us): 8.07

Stop Time (us): 34.2

Smoothing Points: 1

increasing integer number.

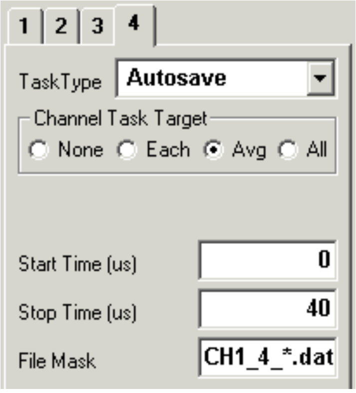

TaskType: Autosave

Channel Task Target: ○ None ○ Each ● Avg ○ All

Start Time (us): 0

Stop Time (us): 40

File Mask: CH1_4_*.dat

The **Smooth** task will average the waveform over a **Smoothing Points** window with a “moving box” method.

The **Scale Up/Down** channel task scales the waveform vertically via multiplying it by the **Scale Factor**. Negative numbers can be used to invert the waveform.

C.5.3.5 Save and Load Configuration

All of the above scope-specific settings may be saved to a file or loaded from a file. To do that, choose the “Configuration ⟶ Save/Load Oscilloscope Config” menu. You will be prompted for a file name.

C.6 Delay Generator Panel

The Delay Generator sub-panel is part of BGSpecT (C.1) that can simultaneously perform remote control of multiple independent delay generators.

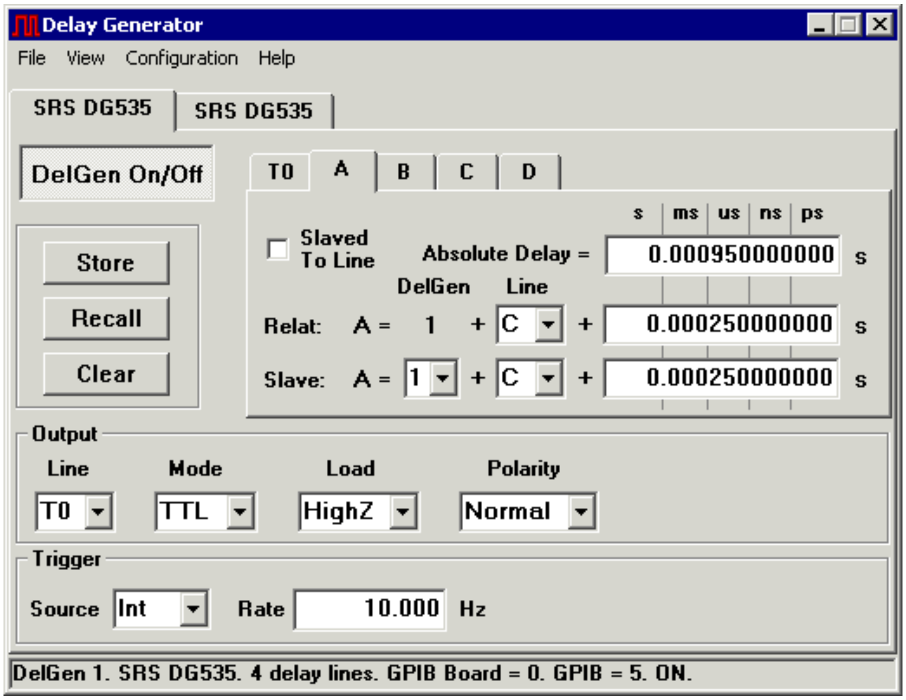

☐ Slaved To Line

Absolute Delay = 0.000950000000 s

DelGen Line

Relat: A = 1 + C + 0.000250000000 s

Slave: A = 1 + C + 0.000250000000 s

Line	Mode	Load	Polarity
T0	TTL	HighZ	Normal

Source Int Rate 10.000 Hz

DelGen 1. SRS DG535. 4 delay lines. GPIB Board = 0. GPIB = 5. ON.

The following are procedures that one can/should perform with the delay generators:

1. Setup communication parameters before establishing remote communication (C.6.1)
2. Setup delay generator parameters after remote communication has been established (C.6.2)
3. Visualize output pulses (C.6.3)

C.6.1 Remote Parameters Setup

To prepare the panel and start communication with delay generator(s), one first needs to perform some setup through the “Configuration” menu. Please follow the general instructions on how to setup device communications (C.11), substituting the word Device with

Delay Generator where applicable.

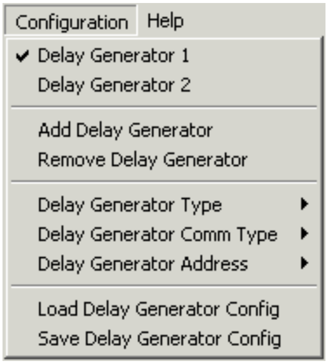

Supported delay generators are:

- Stanford Research Systems (SRS) DG535 (via GPIB)

If a few delay generators have been selected, one can switch between them either by clicking the delay generator tab (that at the very top) or by choosing the "Configuration ⟶ Delay Generator *N*" menu.

Once remote communication with the delay generator has been established (by clicking "**DelGen On/Off**" button), one can change delay generator settings and adjust delays.

Caution! When remote communication is established with the SRS DG535, all device parameters are set to factory default settings. It is advised to store delay generator settings in the device's memory **before** clicking the "DelGen On/Off" button.

C.6.2 Delay Generator Parameters

It is possible to change the following values:

1. Trigger parameters
2. Output line parameters

3. Delay line parameters
4. Save and Load above settings

C.6.2.1 Trigger Parameters

The trigger part of the panel (at the bottom) is responsible for the delay generator triggering mode parameters. Triggering mode is selected from the **Source** list. There are four different modes for the SRS DG535:

1. **Int** – Internal. One can change the **repetition rate**.
2. **Ext** – External (via Ext input). One can set the **threshold** voltage, **slope** and input **impedance**.

Source Ext
Threshold +1.00 V
Slope +
TermZ HighZ

3. **Ss** – Single Shot. Triggering is performed by clicking the "**Single Shot**" button.

Source Ss

4. **Bur** – Burst mode. It is possible to change the burst **rate**, number of burst **pulses** and their **periods**.

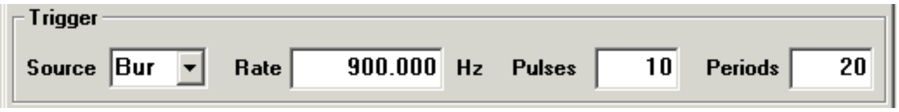

Source Bur
Rate 900.000 Hz
Pulses 10
Periods 20

C.6.2.2 Output Line Parameters

There are 7 output lines that can be configured in the SRS DG535: T0, A, B, ±AB, C, D, ±CD. They are selected from the **Line** list. For each, one can change the **mode**

(TTL, NIM, ECL and VAR), **load** impedance, and **polarity** (except ±AB and ±CD). In the Variable mode, it is possible to change the **amplitude** and **offset** voltages.

Output

Line	Mode	Load	Polarity	Amplitude	Offset
T0	VAR	HighZ	Normal	+1.0 V	0.0 V

C.6.2.3 Delay Line Parameters

For the SRS DG535 delay generator, the number of **delay lines** (A, B, C and D) is different from the number of output lines mentioned above. For each delay line, one can change the **delay time** by changing the number in the **Relative delay** box. The **reference line** for a delay line may be selected from the "**Line**" list. The format of the Relative delay line will then be as follows:

Delay line name = Delay Generator N + Reference line name + Relative delay time (in seconds)

The absolute delay time will be displayed in the **Absolute Delay** box and cannot be changed by typing in that box.

When there are a few delay generators controlled by the software and one of them controls the others through external triggering, it is possible to **synchronize** delay lines from different devices by checking the "**Slaved To Line**" box. Prior to that the following must be done:

1. Click on T0 delay line.

2. From the **Slave DelGel** list, choose the number of the master device that triggers the current device.

3. In the **Slave Line**, choose the delay line on the master device. It must be this line that triggers the current device.

4. Type the delay in the **Slave delay** box. This is the delay generator's lag time between the External and T0 pulses. It is not zero.

5. Click "**Slaved To Line**" box.

6. Perform same operations for the desired line, choosing the desired slave delay time.

Now the Absolute Delay will be shown with respect to the T0 line of the **master** delay generator. Changing the relative delay time for the master delay line will automatically change delay for the slave delay line.

C.6.2.4 Save and Load Settings

All the device-specific settings described above may be **saved** to a file or **loaded** from a file. To do this, choose the "Configuration ⟶ Save/Load Delay Generator Config" menu. You will be prompted for a file name.

For the SRS DG535, it is possible to Store and Recall delay generator settings in devices designated memory locations 1 – 9 by clicking the "**Store**" and "**Recall**" buttons. The "**Clear**" button will set all device parameters to their factory default values.

C.6.3 Visualize Output Delay Pulses

Checking the "View ⟶ Delay View" menu will open the **Delay View** panel.

In this panel, output pulses from all delay generator output lines will be plotted as they would be seen with an oscilloscope. Current time and voltage values can be seen by moving the cursor over the black part of the panel. One can bring a trace for a selected line to the top by clicking its label. Double-clicking a label will allow the user to change the color for

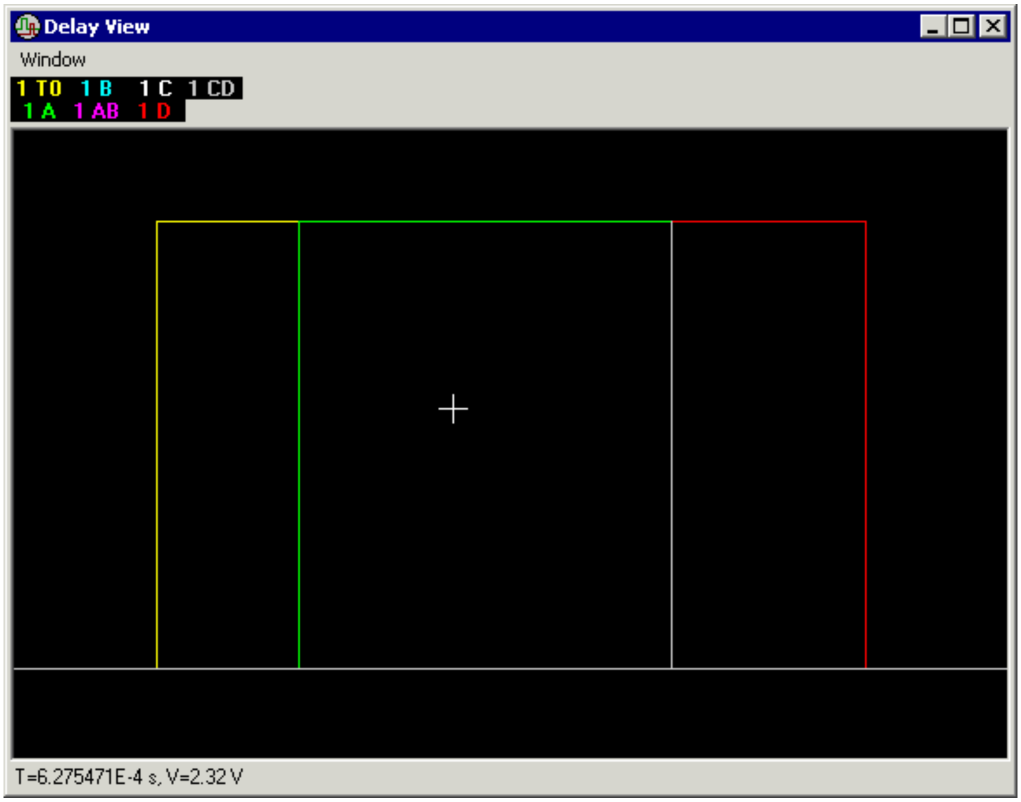

```
T=6.275471E-4 s, V=2.32 V
```

that line. The label name is a combination of the device number in the Delay Generator panel and the output line name.

C.7 Photon Counter Panel

The Photon Counter sub-panel is the part of BGSpecT (C.1) that can simultaneously remotely control multiple independent photon counters.

The following are procedures that one can/should perform with the photon counters:

1. Setup communication parameters before establishing remote communication (C.7.1)
2. Setup photon counter parameters after remote communication has been established (C.7.2)
3. Read counts (C.7.3)

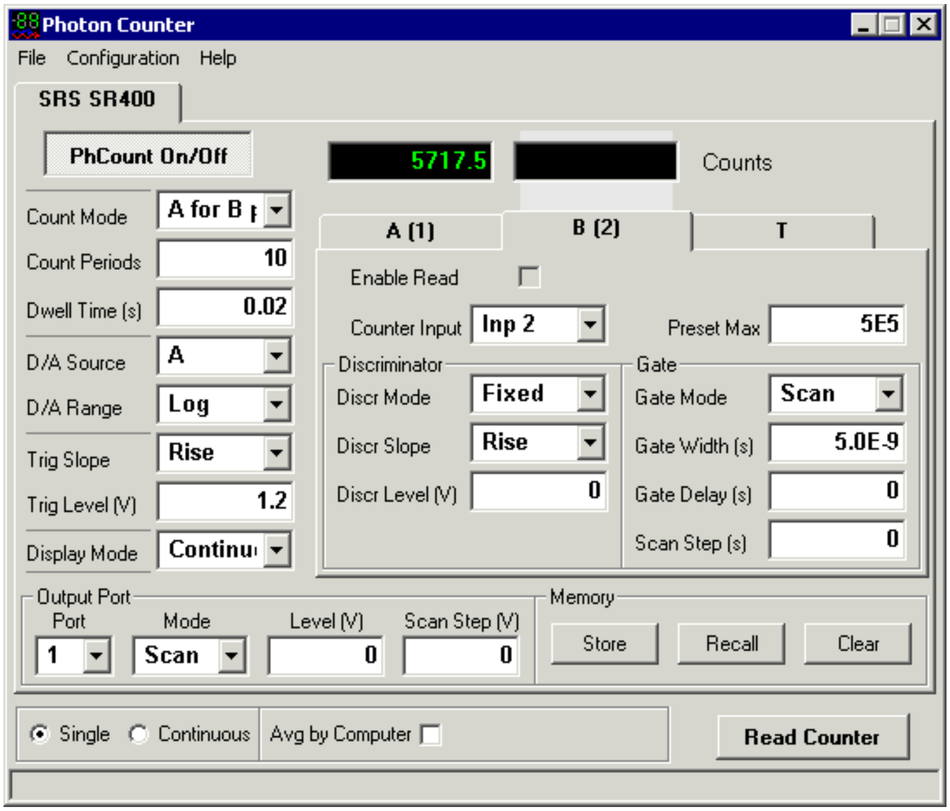

5717.5

Count Mode A for B p
Count Periods 10
Dwell Time (s) 0.02
D/A Source A
D/A Range Log
Trig Slope Rise
Trig Level (V) 1.2
Display Mode Continu

Enable Read ☐
Counter Input Inp 2
Preset Max 5E5

Discr Mode Fixed
Discr Slope Rise
Discr Level (V) 0

Gate Mode Scan
Gate Width (s) 5.0E-9
Gate Delay (s) 0
Scan Step (s) 0

Port	Mode	Level (V)	Scan Step (V)
1	Scan	0	0

● Single ○ Continuous Avg by Computer ☐

C.7.1 Remote Parameters Setup

To prepare the panel and start communication with photon counter(s), one first needs to perform some setup through the "Configuration" menu. Please follow the general instructions on how to setup device communications (C.11), substituting the word Device with Photon Counter where applicable.

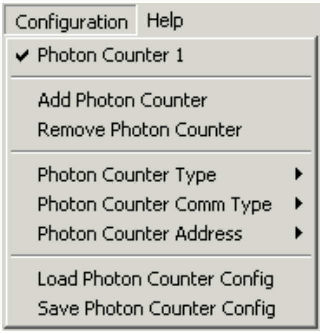

Supported photon counters are:

- Stanford Research Systems (SRS) SR400 (via GPIB and RS232)

If a few photon counters have been selected, one can switch between them either by clicking the photon counter tab or by choosing the "Configuration ⟶ Photon Counter *N*" menu.

Once remote communication with the photon counter has been established (by clicking "**PhCount On/Off**" button), one can change photon counter settings and read counts.

C.7.2 Photon Counter Parameters

Photon Counter panel options span over:

1. Panel (all photon counters) – software acquisition and averaging modes
2. One photon counter (all device counter channels) – counting and display modes, triggering options, output ports
3. One counter channel – counter input, discriminator and gate options

One can also Save and Load a photon counter configuration to and from a file.

C.7.2.1 Panel Parameters

Panel-wide parameters are the software acquisition and averaging modes. Acquisition mode can be "**Single**" or "**Continuous**" (buttons are at the bottom of the Photon Counter panel). In "Single" mode, the counts are acquired only once. In "Continuous" mode, the counts are acquired until the "Read Counter" button is pressed again. This is done so that the software can effectively combine a few hardware photon counters into one software instrument.


● Single ○ Continuous Avg by Computer ☑ Avg Number 50

For averaging, there is the option of "**Averaging by Computer**" for acquired counts. When this option is enabled, the counts are acquired by photon counters according to their settings and are then transferred to a PC and averaged by the software.

C.7.2.2 Common Photon Counter Parameters

Count Mode determines how the counting is performed (A,B, A–B, A+B for T preset, A for B preset). **Count Periods** determines the number of times the counters perform their job. The counts from each of these periods are then averaged into one number. That is why, sometimes, the final number of counts contains extra digits after the decimal point. If, in addition, the Averaging by Computer is performed, the data will be averaged twice. **Dwell Time** is the counter inactive time between two count periods.

D/A Source (A, B, A-B, A+B) and **D/A Range** (Log or Linear) set the front panel D/A output source and the scale range for it.

Trigger Slope (Rise or Fall) and **Trigger Level** determine these parameters for the external trigger input.

Display Mode switches between Continuous and Hold modes.

Output Port parameters determine the properties of Port1 and Port2 outputs on the back panel of the SRS SR400. For each **Port**, one can choose **Mode** (Fixed or Scan) and **Level**. In the Scan mode, **Scan Step** may be changed.

C.7.2.3 Counter Channel Parameters

The user can set up parameters for individual counter channels. Switching between the counters is done through the channel tab. The **name** of the channel tab is the name of the channel on the device (A, B, T). The number in parenthesis is the absolute **channel**

number in the software, and is used to identify counter channels in the Spectrum Scan panel (C.8). The number of channels on the photon counter is determined by the software automatically. If the software runs out of the maximum allowed number of channels (double the maximum number of devices in the Photon Counter panel), it may cut off some of the channels that do not fit.

The "**Enable Read**" check enables/disables downloading counts data from a photon counter to a PC.

Counter Input selects among allowed input channels for each counter (10 MHz, Input 1, Input 2, External Trigger). For a preset counter (usually T, but may be B in A for B preset count mode), one can change the counter preset maximum number (in 10 MHz clock cycles). If this number is reached during the counting, the experiment is ceased.

For each counter **Discriminator**, it is possible to change the **Discriminator Mode** (Fixed or Scan), **Discriminator Slope** (Rise or Fall) and **Discriminator Level**. In the Scan mode, **Scan Step** will also be available.

For counters A and B, one can select **Gate** parameters: **Gate Mode** (CW, Fixed or Scan), **Gate Width** and **Gate Delay**. In Scan mode, **Scan Step** will also be available.

C.7.2.4 Save and Load Settings

All of the above device-specific settings may be **saved** to a file or **loaded** from a file. To do this, choose the "Configuration ⟶ Save/Load Photon Counter Config" menu. You will be prompted for a file name.

For the SRS SR400, it is possible to Store and Recall photon counter settings in devices designated memory locations 1 – 9 by clicking the "**Store**" and "**Recall**" buttons. The "**Clear**" button will set all device parameters to their factory default values.

C.7.3 Reading Counts

To read photon counter counts, click the "**Read Counter**" button in the bottom of the panel. If a few photon counters are turned On, counts will be read from all of them. Acquired counts are displayed at the top of the panel.

C.8 Spectrum Scan Panel

The Spectrum Scan sub-panel is part of BGSpecT (C.1) that uses instrument panels to record spectra. This powerful tool has many fine tuning settings that allow he user to perform more efficient and fast scans. It requires some time to set up, but then the scan can be completely automated and does not require human intervention.

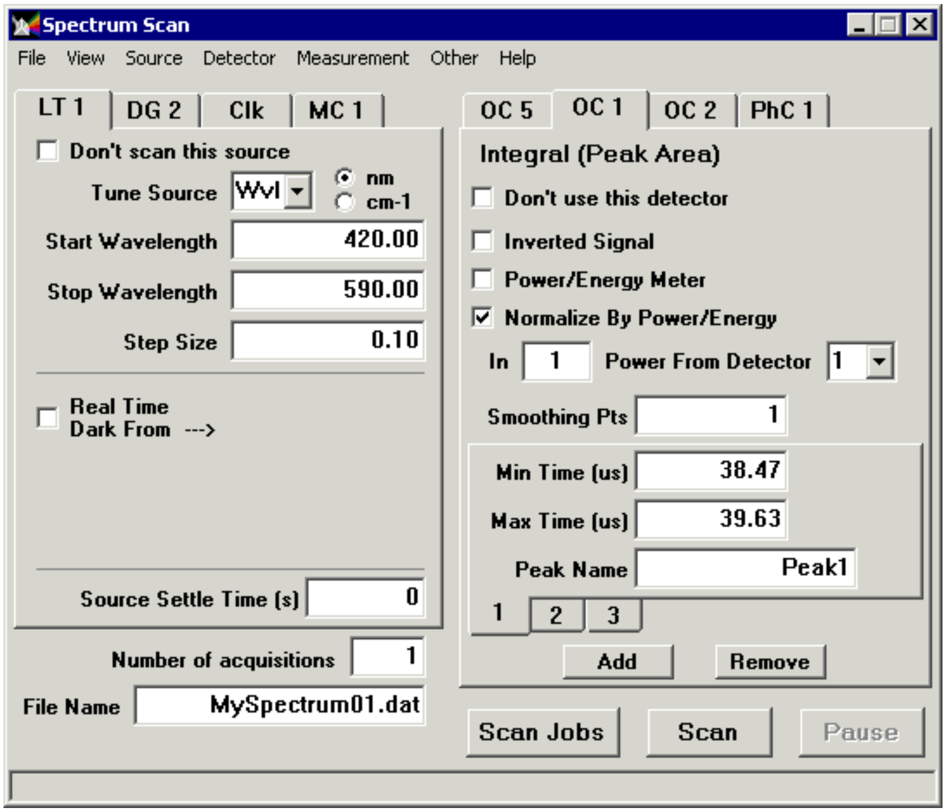

☐ Don't scan this source
Tune Source Wvl ● nm ○ cm-1
Start Wavelength 420.00
Stop Wavelength 590.00
Step Size 0.10
☐ Real Time Dark From --->
Source Settle Time (s) 0
Number of acquisitions 1
File Name MySpectrum01.dat

Integral (Peak Area)
☐ Don't use this detector
☐ Inverted Signal
☐ Power/Energy Meter
☑ Normalize By Power/Energy
In 1 Power From Detector 1
Smoothing Pts 1
Min Time (us) 38.47
Max Time (us) 39.63
Peak Name Peak1

To perform a successful scan, the following needs to be done:

1. Decide on your sources and detectors (C.8.1)
2. Setup sources (C.8.2)
3. Setup detectors (C.8.3)
4. Use Spectrum View (C.8.4)
5. Setup other features (C.8.5)
6. Perform the actual scan (C.8.6)

C.8.1 Sources and Detectors

In Spectrum Scan, the instruments are divided into sources and detectors.

Sources are instruments that are used to change some scan parameters such as wavelength, delay, etc. Hence, devices from Lambda Tune (C.2), Motion Control (C.4) and Delay Generator (C.6) panels may be used as scan sources. In addition, there is a built-in four-channel timer in Spectrum Scan that may be used as a source.

Detectors are instruments that are used to record data (e.g., waveforms, wavelengths). Hence, devices from Oscilloscope (C.5), Wavemeter (C.3) and Photon Counter (C.7) panels may be used as scan detectors.

It is advised to turn on all necessary source and detector devices using their panels before starting the Spectrum Scan panel. Doing so may save some confusion about device availability.

C.8.2 Sources Setup

The sources are located on the left side of the Spectrum Scan panel. The principle of working with sources is similar to that for devices in instrument panels. To access sources, one should first go to the "Source" menu and create a sufficient number by clicking the

“Source ⟶ Add Source” and the “Source ⟶ Remove Source” menus. Switching between different sources can be done either by clicking on the ‘Sources’ tab or by selecting the appropriate “Source ⟶ Source *N*” menu. The maximum allowed number of sources (up to 128) can be changed by clicking “Source ⟶ *N* Sources Max” menu.

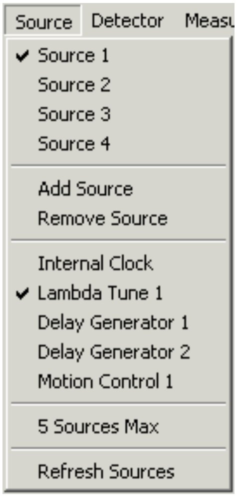

The user should next **assign** some device to each source. The order in which the sources are arranged is very important. When recording a spectrum, the sources are scanned in a nested loop order with the first source on the outermost (that is, the largest) loop and the last source on the inside (the smallest and therefore the most frequently repeated) loop.

Currently available source devices will be displayed under the “Source” menu. They will be in the form of menus with the device name and its number in the instrument panel. Only those devices that have been turned “On” (remote communication successfully established) will be shown. The Internal Clock will always be displayed, since it is built into the Spectrum Scan panel. It is possible to **refresh** the list of currently available source devices by clicking the “Source ⟶ Refresh Sources” menu.

To assign sources, first select the desired source and then choose an appropriate source device. Since many of the source devices have multiple channels, the same device may be assigned to *multiple* sources, but each channel may be assigned to only *one* source. Upon successful assignment, the abbreviated name of the source will be displayed in the source tab.

After the sources have been assigned, each of them should be **configured**. First, a **channel** to scan should be selected for a source. For a lambda tune source, it will be a "Tune source" list; for a delay generator, "Delay Line"; for Motion Control, "MC Axis"; and for Internal Clock, "Clock Channel". Only unassigned channels are displayed in this list.

In the case of the **wavelength**, the user can choose between nanometers and wavenumbers as units.

Now one should choose the desired **Start**, **Stop** and **Step** for the scan. In the case of the wavelength, only values within the lambda tune calibration range will be allowed. The Step Size may be larger than the difference between Stop and Start. In such a cases, only one source position will be used during the scan – Start.

If the menu "Other ⟶ Real Time Dark (Baseline)" is checked, one can collect the **baseline** signal in "real time." In this case, at each source position before recording signal **all** sources, all except Internal Clocks will be moved to their "Dark" positions, that is where the signal consists only of noise, some reference value, or is "off-resonance," etc. "Dark" signal collection happens inside the most enclosed loop, and so acquiring "dark" data doubles the scan time.

To configure **Real Time Dark**, first check the "Real Time Dark from" box. Then select a source and a channel. Only assigned source devices will be available here, but there is no limit on channel numbers. After that, type in the desired value for the "dark" position of that source.

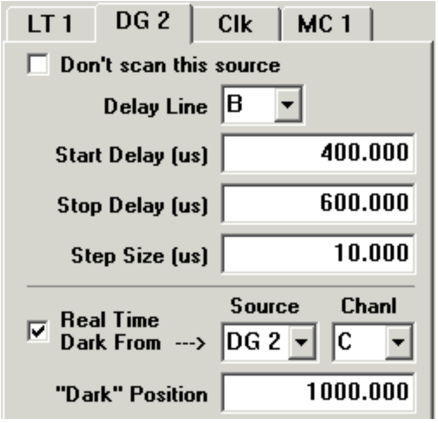

☐ Don't scan this source

Delay Line: B

Start Delay (us): 400.000

Stop Delay (us): 600.000

Step Size (us): 10.000

☑ Real Time Dark From ---> Source: DG 2, Chanl: C

"Dark" Position: 1000.000

If a delay generator was chosen as a scan source, it may be used to trigger the full data acquisition cycle (all necessary devices) from a computer. To do this, one should enable the **Master Trigger** mode by checking the “Other ⟶ Master Trigger” menu. Then, check the “Trig Master” box. Only one delay generator can be used for the Master Trigger, and it must be set to Single Shot triggering mode. The “Trig Rate” is the desired rate of triggering by computer. This is the maximum value. In case the whole data collection is slower than one triggering period, the actual triggering rate will be smaller. This is done to ensure that no data are lost.

Trig Master ☑ Trig Rate (Hz): 10

Source Settle Time is the amount of time between the end of moving the source to a new position and resetting the detectors to start data acquisition. This provides a waiting period for the system under study to adjust to the new conditions. In most cases this time is set to zero.

If for some reason the user does not wish to scan a certain source, it is possible to **disable** it for the scan by checking the “Don’t scan this source” box.

C.8.3 Detectors Setup

The detectors are located on the right side of the Spectrum Scan panel. The principle of working with detectors is similar to that used for sources. To access detectors, one should first go to the "Detector" menu and make enough boxes by clicking the "Detector ⟶ Add Detector" and the "Detector ⟶ Remove Detector" menus. Switching between different detectors can be done either by clicking on the 'Detectors' tab or by selecting the appropriate "Detector ⟶ Detector *N*" menu. The maximum allowed number of detectors (up to 128) can be changed by clicking the "Detector ⟶ *N* Detectors Max" menu.

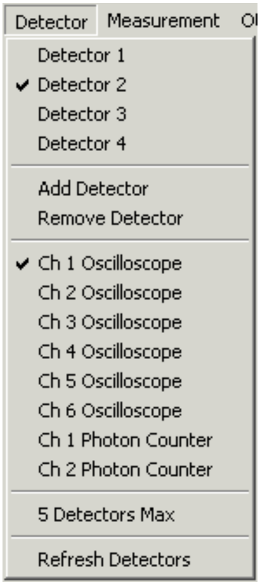

Then, detector should be **assigned** to a device. Currently available detector channels will be displayed under the "Detector" menu. They will be in the form of menus with the device name in the instrument panel and channel number. Only those device channels that have been turned "On" (remote communication successfully established) will be displayed. It is possible to **refresh** the list of currently available detector channels by clicking the "Detector ⟶ Refresh Detectors" menu.

To assign detectors, first select the desired detector and then choose an appropriate device channel. The same device channel may be assigned to multiple detectors in order to be able to perform different post-processing mathematics. Upon successful assignment, the abbreviated name of the detector will be displayed in the detector tab.

After the detectors have been assigned, each of them should be **configured**. First, an available **measurement** type should be selected for a detector. This measurement will be used to find the final number that will be saved in the spectrum file.

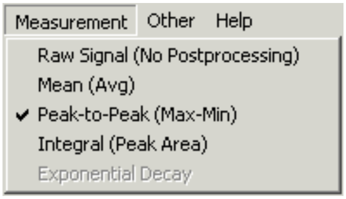

There are a few possible measurement types:

1. **Raw Signal** – no post-processing is done

This is the only type available for the wavemeter and photon counter. For oscilloscopes, no number will be calculated or saved into the spectrum.

2. **Mean** – calculates the average value (mean) for all waveform points

3. **Peak-to-Peak** – finds the difference between the maximum and the minimum in the waveform

4. **Integral** – calculates the area under the curve

5. **Exponential Decay** – calculates the time constant for exponential decay

The user can decide if the original data from detector device should be **inverted** by checking "Inverted Signal" box. The "Power/Energy" meter box can be checked to indicate that the current detector is measuring something like laser **power** or **pulse** energy. This value might be used to normalize data from other detectors, for example.

In Integral measurements, one should make there are an appropriate number of "**peaks**"

– that is, ranges for curve integration. This is done by clicking the “Add” and “Remove” buttons in the bottom of the detector panel. Each of the peaks will then need Min/Max times assigned as well as the peak name.

In the case of an oscilloscope channel as a detector, one should choose the desired **Minimum** and **Maximum** times. They will determine the time interval over which to post-process the measurement. **Smoothing Points** are used in case there is a need to do intermediate data smoothing when performing measurement math.

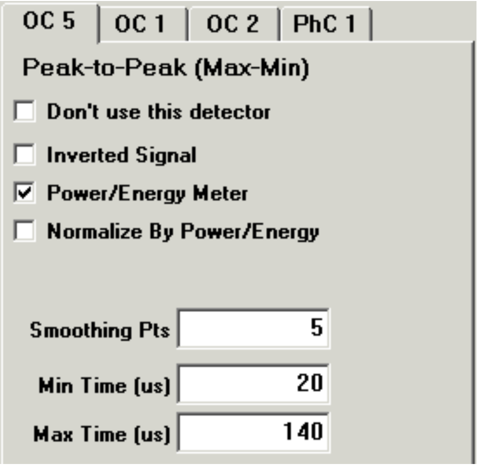

Peak-to-Peak (Max-Min)

☐ Don't use this detector

☐ Inverted Signal

☑ Power/Energy Meter

☐ Normalize By Power/Energy

Smoothing Pts 5

Min Time (us) 20

Max Time (us) 140

If for some reason, the user does not wish to use a certain detector, it is possible to **disable** it for the scan by checking the “Don’t use this detector” box.

C.8.4 Spectrum View

Acquired spectra can be viewed in the Spectrum View panel, accessed via the “View ⟶ Spectrum View” menu.

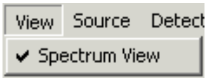

In order to view spectral plots (traces) in Spectrum View, all parameters in that panel must be set before the beginning of the scan.

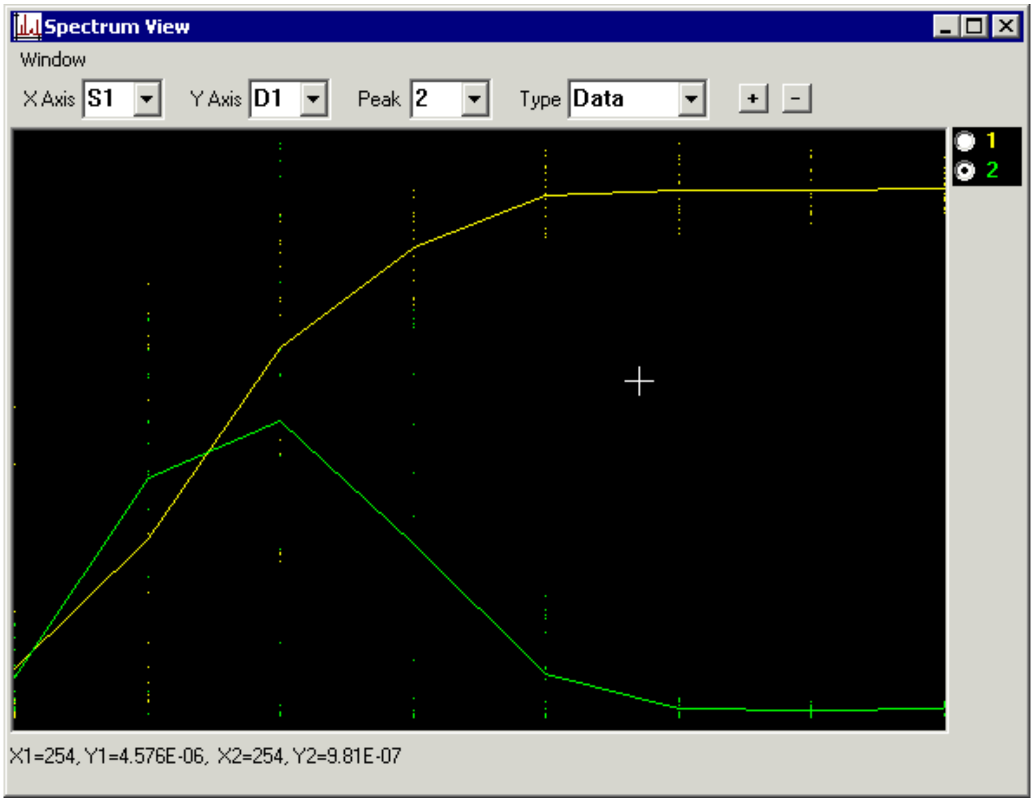

X Axis S1 Y Axis D1 Peak 2 Type Data

X1=254, Y1=4.576E-06, X2=254, Y2=9.81E-07

To **add** and **remove** traces, use the "+" and "–" buttons. Switching between different traces is done by clicking a trace's label on the right side of the panel. Parameters of that trace will be displayed in boxes above the plot area.

For each trace, select references for the X and Y axes of the plot. For the **X** axis, it may be one of the **sources** or detectors (if detector is a wavemeter). For the **Y** axis, only **detectors** are allowed. If the measurement type for a detector is Integral, then the **Peak** box will appear, offering a selection of the peaks whose area is calculated in this detector measurement.

Then choose the plot **type**. It will usually be Data. If Real Time Dark baselining is enabled for some of the sources, Baseline may also be selected to plot the baseline only or Data–Bsl for a difference between normal and dark (baseline) data.

It is possible to change the trace **color** by double-clicking the trace label. Right-click on the label to bring up a menu to choose the trace plotting style: **Line** or **Dots**. If Line is selected, the trace will be plotted as dots connected by lines. If there are a few dots with the same X and different Y, the average Y will be used to plot a line. This usually occurs for multi-dimensional scans (when using a few sources).

The scale on the plot is adjusted to fit the screen for each trace as new points are acquired. To view (X,Y) values, move the mouse over the plot. Current values will be displayed below the plot and in the tool tip.

C.8.5 Other Features

There are a few more things that may be adjusted. For example, the check "Other ⟶ Dump Raw Data to File" menu can be used to **save** all acquired waveforms for oscilloscope channel detectors. The files will be located in the directory with the same name as the spectrum file name and with the extension ".dir." Individual file names will be made from source positions and detector channels. Waveforms acquired for normal source positions will have the extension "*.dat" and those for the "dark" source positions in Real Time Dark mode will have extensions "*.dat.bsl."

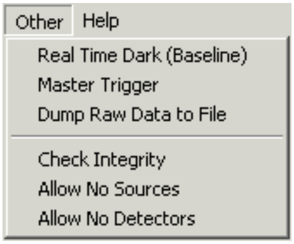

The "Other ⟶ Check Integrity" menu will do a **self-test** to see if all settings are consistent with source and detector device settings. Such a test is always performed in the beginning of each scan. If the test has been passed, the “Scan” button will be enabled, otherwise an error message will be displayed in the bottom of the Spectrum Scan panel. If you are sure that all settings are correct but you still get an error message in the status bar, or “Scan” button is disabled, click that menu to perform the integrity test again.

Usually, if there were no sources or detectors assigned, the integrity test will not allow the scan to be conducted. To override that, the user can check either the “Other ⟶ Allow No Sources” or “Other ⟶ Allow No Detectors” menus.

The “**Number of acquisitions**” button under the source panel determines how many times detector readings are performed at each source position. They are performed one after another at all source positions fixed (inside the most frequent source loop).

The **file name** to store the scan results may be chosen under the number of acquisitions. If a file with that name already exists, it will not be overwritten. Instead, another file with the same name and prefix “*N*__” will be created, where *N* is a positive number (1, 2, ...).

The **directory** for the scan file may be changed by clicking the “File ⟶ Set Spectrum Directory” menu.

One can **Save** and **Load** the above settings into a series of files by clicking the “File ⟶ Save Scan Configuration As” and “File ⟶ Load Scan Configuration” menus. When the scan configuration is being loaded, the software will try to establish remote communication with all necessary devices if it has not been done.

Note that when using the delay generator as a source, its parameters are stored in and recalled from its memory location 9 and is therefore reserved.

If a few scans are to be performed without human intervention, it is possible to place a **few scan jobs** in a queue by clicking the “File ⟶ Add to Job List” menu. The list of such queued jobs may be **purged** by clicking the “File ⟶ Clear Job List” menu. The scan jobs from this list are transferrable between program sessions. The list is **not** purged upon completion of all jobs in it. This should be done manually by clicking the “File ⟶ Clear Job List” menu.

Panel settings can be Saved and Loaded via the “File ⟶ Save Panel Configuration As” and “File ⟶ Load Panel Configuration” menus.

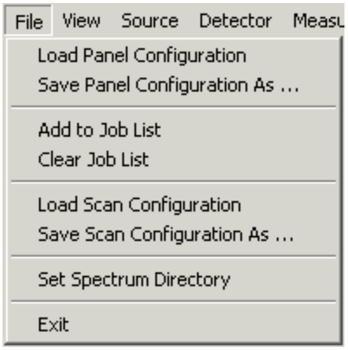

C.8.6 Performing the Scan

If everything was configured properly, the “**Scan**” button will be enabled. Click it to start the **scan**. If the scan needs to be aborted, click the “Scan” button again. This may be done both during the scan and when it was paused.

If there are any scan jobs queued in a **job list**, the “**Scan Jobs**” button will be enabled. By clicking it, one can perform scans from the list. In the case where no prior panel setup is required, scan job configurations will be loaded automatically and scans will be performed in the order of their appearance in the list. Pre-scan panel settings will be discarded if they were not added to the job list.

Clicking the “Scan Jobs” button again will abort all scans in the queue. Clicking the “Scan” button will stop only the current scan job. If there are more scans to be done, the program will proceed with them.

The scan may be **paused** by clicking the “**Pause**” button. This will not allow the user to change scan parameters; however, it would be possible to adjust device parameters at their owner panels. To resume the scan, click the “Pause” button again. Please note that pausing the scan does not halt all operations immediately. Waiting to resume the scan is done after the current detector read cycle is finished.

The scan **results** are saved as lines with numbers separated by the *tab* symbol. The very first line of the file will have source and detector names for easier data identification. At the same time, selected traces are displayed in a Spectrum View (C.8.4) window (if opened).

The acquired data are added to the scan file. If something unexpected happens (computer or equipment crash), the data should not be lost.

During the scan, current job number, source positions and estimated time left will be displayed in the status bar at the bottom of the panel. There, Bsl stands for the “dark” source positions. The percentage of the scan performed will be displayed in a progress bar in the bottom left corner of the panel. When the scan is finished, the total scan time will be displayed.

File Name: MySpectrum01.dat

Job 1 (1). Reading at 452.70nm, 600.00us, 15.0us. Left 00:28:19s

Scan is finished. Total time 00:01:45s

C.9 Device Talk Panel

Device Talk sub-panel is part of BGSpecT (C.1). It serves two purposes:

1. RS232 (COM) port parameter configuration (C.9.1)
2. Talking to GPIB and RS232 devices (C.9.2)

C.9.1 COM Port Settings

Before the connection between a PC and external device can be established via a serial port (COM, RS232), one should set up its parameters to match the hardware device settings. This can be done by selecting appropriate values in the boxes of the "COM Port Settings" tab. These settings may be changed as long as there is no connection with an external device. Once such communication is started, all boxes except the address (COM Port) will not be available for change, but will still show current parameters. All port settings from this tab are saved in configuration files "RS232__port__*N*.cps" in *Configs* directory, where *N* is the port number.

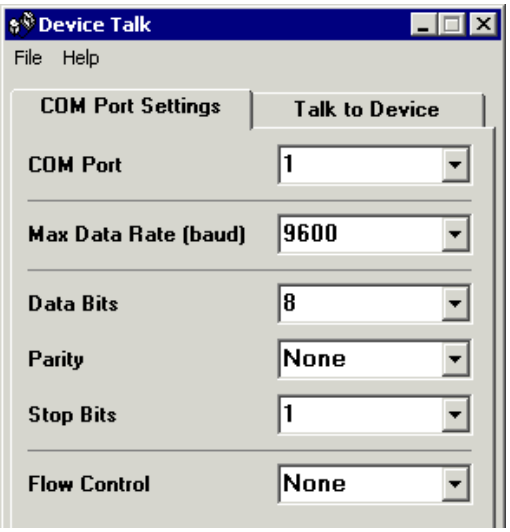

COM Port: 1
Max Data Rate (baud): 9600
Data Bits: 8
Parity: None
Stop Bits: 1
Flow Control: None

C.9.2 Talking to Devices

The "Talk to Device" tab allows the software to establish communication with devices, as well as send commands and receive device responses. It is useful if one needs to send a quick command to a remote device. It is also good for testing purposes.

Both GPIB and RS232 devices are supported in this tab. To be able to talk to a device, one should select its communication **Type** and **Address** (and **GPIB board** for GPIB devices). In the case where these parameters were assigned to some device in one of the BGSpecT sub-panels, such information will be displayed.

One can Start/Stop communication with the device by selecting **Remote Status**. For assigned devices, this will also turn them On/Off in their owner panels. If an assigned device is turned On, its Device ID (as stored in the program) will be displayed. If the devices' remote status was changed via its owner panel, such information may be renewed by clicking the "**Refresh**" button.

It is possible to send a string (command) to a device by clicking the "**Write**" button. The response string from the device may be received by clicking the "**Read**" button. "**Query**" will do both Write and Read. The response from the device is displayed in the window below the buttons.

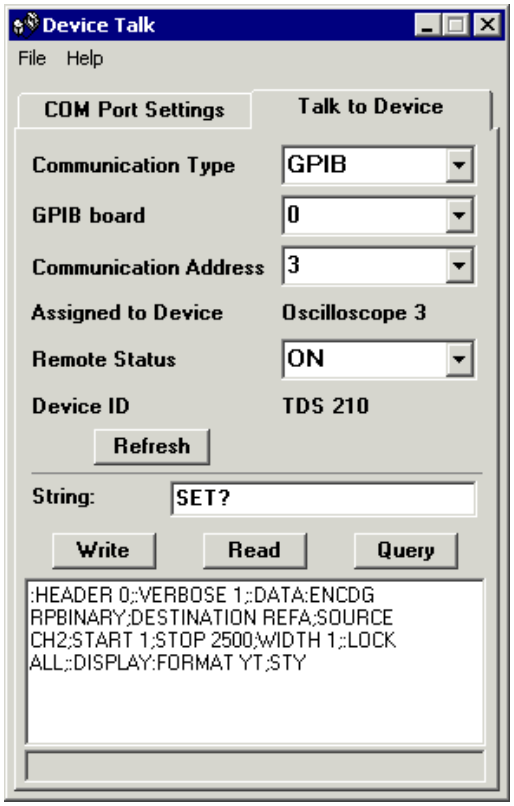

Communication Type: GPIB
GPIB board: 0
Communication Address: 3
Assigned to Device: Oscilloscope 3
Remote Status: ON
Device ID: TDS 210
String: SET?

```
:HEADER 0;:VERBOSE 1;:DATA:ENCDG
RPBINARY;DESTINATION REFA;SOURCE
CH2;START 1;STOP 2500;WIDTH 1;:LOCK
ALL;:DISPLAY:FORMAT YT;STY
```

C.10 Devices

Devices are individual pieces of equipment. They usually have the same names as instruments, although many different devices may be the same kind of instrument. Device types are:

- Lambda Tune
- Wavemeter
- Motion Control
- Oscilloscope
- Delay Generator
- Photon Counter

C.11 Device Setup

After choosing some Instrument sub-panel from BGSpecT, the panel needs to be setup before communication takes place. There are some common guidelines on how to do this, independent of the instrument type.

Each Instrument panel can simultaneously control multiple devices. For example, the Oscilloscope panel can read waveforms from a few independent digital oscilloscopes without having to switch between them, i.e., turning one Off and another one On. Each of the oscilloscopes (or other type of instruments) are referred to as devices (C.10). To setup each device, one needs to follow a few steps by selecting a number of "Configuration" sub-menus:

1. Create device in the panel (C.11.1)
2. Choose device type (C.11.2)
3. Choose device communication type (C.11.3)

4. Choose device communication address (C.11.4)

5. Start communication (C.11.5)

6 (optional). Backup panel configuration (through “File” menu) (C.11.6)

7. Getting help (C.11.7)

C.11.1 Create Device

First, there should be a new device tab created for each device. This is done by clicking “Configuration ⟶ Add Device”. Each time another device is created, in addition to the new tab, a related “Configuration ⟶ Device *N*” menu will appear where *N* is a number. One can create only a certain maximum number of devices that is specified for each instrument panel separately.

Switching between different devices is performed by choosing the respective tab or the “Configuration ⟶ Device *N*” menu.

To remove unnecessary device tabs, one can use the “Configuration ⟶ Remove Device” menu. Each time it is clicked, it will remove the active (selected) device.

C.11.2 Device Type

Each device should be assigned a type, a communication address, and when applicable, a communication type.

Usually, each instrument panel supports a few different device types. The device type may be chosen through selecting one of the “Configuration ⟶ Device Type” sub-menus. This has to be done even if only one device type is supported by the current software version.

C.11.3 Device Communication Type

In most cases, each device has only one communication type. Physical equipment, represented by a device, may be either a PC plug-in card (PCI or ISA) or a stand alone unit with GPIB (IEEE-488.2) or RS232 (COM port on a PC) communication capabilities. Some stand alone units may have both GPIB and RS232 ports. In this case, if supported by the current version of software, the user can change that communication type through the the “Configuration ⟶ Device Comm Type” sub-menus. Otherwise, an appropriate menu will be selected automatically. In addition to this, for communication to take place one may need to carry out some additional steps.

For GPIB devices, a GPIB plug-in card must be installed in the computer along with the GPIB drivers. Both GPIB and RS232 equipment must be connected to a PC by appropriate cables. For RS232 devices, appropriate COM port parameters should be adjusted through the Device Talk (C.9) panel to match the settings on the device itself.

C.11.4 Device Communication Address

Next a communication address should be assigned to the device through one of the “Configuration ⟶ Device Address” sub-menus.

In the case of GPIB devices, it is a GPIB address selected on the physical equipment. It can be a number between 1 and 15. Also, for GPIB devices, one can select what GPIB board the device is connected to by choosing one of the “Configuration ⟶ Device Address ⟶ GPIB *N* Board” sub-menus.

For RS232 devices, it is an address of a COM port on the PC through which communication is supposed to occur. Only addresses of installed COM ports are available.

For PC plug-in cards, the address is a card number or index. Usually, the card manufacturer will supply configuration software for their cards. In such cases, the device address is a card number or index in that configuration software. For example, GaGe CompuScope card numbering starts with 1; if there are 2 cards installed, one of them will have address 1 and another will have address 2. For PMC motion control cards, the numbering starts with 0.

For devices of the same communication type, the same address may be assigned only once. If the address needs to be re-assigned to another device, the user should free that address first by choosing the “Configuration ⟶ Device Address ⟶ Clear” menu.

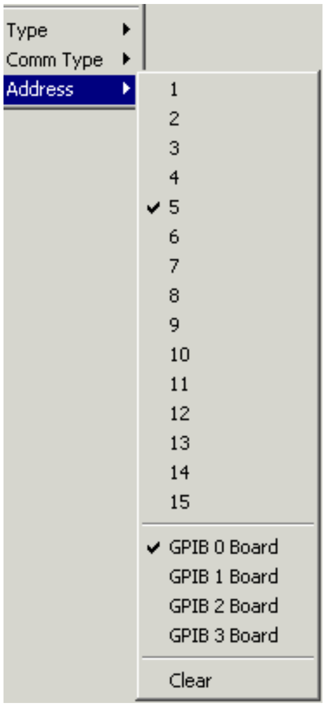

C.11.5 Turning Device On/Off

If all the above has been done correctly, the "Device On/Off" button (in the upper left corner of the panel) will become enabled. To start communication with the physical equipment, simply press this button. In most cases, the software will read device parameters from the equipment, i.e., time and voltage scales from the oscilloscope. In other cases, additional information will need to be supplied, i.e. a calibration file for Lambda Tune. In some stand alone units, when communication is started the panel with knobs on the equipment becomes locked and all control is performed through software only. This is why some functions *must* be set up manually prior to starting communication, in case they are not accessible with software. Remember that the actual equipment should have its power turned on. To gain access to the locked knobs, remote communication must be stopped by pressing the "Device On/Off" button again.

C.11.6 Panel Configuration Backup

Steps 1 through 4 do not have to be repeated every time the instrument panel is started. When closing the panel, information about tabs and devices will be saved in the .ini file. The next time the panel is opened, this information will be retrieved from the file, repeating steps 1-4, but communication will not be started automatically. Step 5 (C.11.5) should be done for each device again.

In addition to the .ini file, one can also save the necessary information to, and load it from, a file through the "File" sub-menus.

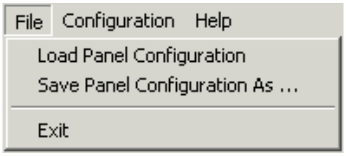

C.11.7 Help

A web browser must be installed to read the Help files. Pressing F1 will bring up help for the active device panel. It can also be selected from the "Help ⟶ Device Help" menu. "Help ⟶ BGSpecT Help" will bring up to the starting help page. "Help ⟶ About ..." menus will give a brief summary for the panel.

C.12 Readme

About Blake Group Spectroscopy Tools, version 3.2:

Blake Group Spectroscopy Tools is a set of tools for the remote control of the experiment and data collection. It consists of the following integrated modules:

Lambda Tune – controls multiple multi-axis lasers via Motion Control sub-panel and diode lasers via GPIB

Wavemeter – controls multiple wavemeters via GPIB and RS232

Motion Control – handles precision motion control micropositioners via PC plug-in cards (PCI or ISA)

Oscilloscope – controls multiple oscilloscopes via GPIB, RS232 and PC plug-in cards (PCI or ISA)

Delay Generator – controls multiple pulse delay generators via GPIB

Photon Counter – controls multiple photon counters via GPIB and RS232

Spectrum Scan – uses the above modules to acquire data (scan spectrum or any other kind of signal dependence)

Device Talk – configures COM ports and talks to individual GPIB and RS232 devices

Useful features:

– Simultaneously controls multiple devices of the same kind

– Controls devices via GPIB and RS232 interfaces as well as PC plug-in cards (PCI or ISA)

– Simultaneously controls multiple GPIB boards

– Smart oscilloscope waveform acquisition

– Wavelength source wavelength conversions

– Master/Slave locking of delay lines from pulse/delay generator

– Huge number of supported oscilloscopes

– Easy spectrum acquisition

– Flexible to configure

– User friendly interface. Partial Windows XP themes support

Installation.

To install the program, copy an executable BGSpecT.exe, along with the *Help* directory into your destination directory. You will also need to put the files from the *sys* directory into your Windows system directory (something like C:\Windows\System or C:\WINNT\system32 – the one that has many DLL files in it). If you are prompted to overwrite your existing files, choose No.

To uninstall this software from your system, just delete the executable and all unnecessary configuration files. No records are made in Windows registry during installation and subsequent use of the program.

Hardware requirements:

Minimum

– CPU - Pentium or better

– RAM - 16 MB

Comfortable

– CPU - Pentium III, Athlon or better, 500 MHz or better

– RAM - 256 MB or larger

All necessary plug-in cards should be installed with the drivers supplied by the manufacturer.

Software requirements:

1. Microsoft Windows 95, 98, ME, NT (3.5+), 2000 or XP
2. Visual Basic 6 runtime files (can be downloaded from the Microsoft website)
3. All necessary drivers for hardware in use, i.e. drivers for GPIB cards (National Instruments only), GaGe CompuScope drivers (version 3.50 and higher), PMC motion control drivers (version 1.3 or higher)

All necessary drivers can be obtained from the hardware manufacturers, and must be installed and properly configured. To communicate with RS232 devices, COM ports should be physically present and enabled (installed) in Windows.

Known incompatibilities and limitations:

1. Hardware drivers. Sometimes plug-in card manufacturers will stop supporting old

hardware in their new driver releases, but the old drivers do not support new hardware. Precision MicroControl driver version 3.0+ supports only new PCI cards; for old ISA cards, use driver versions 2.23 and lower. GaGe CompuScope driver version 3.50 supports only new PCI cards (class CP500); for old ISA and class X012/PCI cards, use driver versions 3.46.02 and lower. However, the older drivers may be incompatible with a currently used SDK based on the 3.50.00 driver.

2. Some legacy devices support only IEEE-488.1 and not the IEEE-488.2 GPIB standard. They may be used with only 1 GPIB board in a system. Among currently supported by this software devices are: LeCroy 9400 oscilloscopes, SRS DG535 delay generators, Burleigh 1000 and 1500 wavemeters, and SRS SR400 photon counters.

3. When turning Off a GPIB device, some devices do not turn off from remote mode because of the above. This happens because these GPIB devices require sending a GPIB command that stops all GPIB communications with all GPIB devices on the bus. Such a command would also disconnect all other GPIB devices in use, and therefore, is sent only when turning Off the last device connected to the board.

4. For Tektronix oscilloscopes, extra options are not supported (such as extra memory, voltage probes, etc.). For GaGe oscilloscopes, some extra options are not supported (such as master/slave, multiple records).

C.13 License Agreement

Blake Group Spectroscopy Tools (BGSpecT) software, California Institute of Technology.

End-User License Agreement.

PLEASE READ THIS DOCUMENT CAREFULLY BEFORE USING THE ENCLOSED

SOFTWARE. THIS AGREEMENT LICENSES THE USE OF THE ENCLOSED SOFTWARE TO YOU AND CONTAINS WARRANTY AND LIABILITY DISCLAIMERS. USING ANY PART OF THE SOFTWARE INDICATES THAT YOU ACCEPT THESE TERMS AND INDICATE YOUR ACCEPTANCE OF THIS LICENSE AGREEMENT AND WARRANTY. IF YOU DO NOT AGREE TO THE TERMS AND CONDITIONS OF THIS AGREEMENT, DO NOT USE THE SOFTWARE.

License:

This Agreement allows you to:

(a) Use the BGSpecT software on a single computer or a single System at a time. The BGSpecT software is licensed only for use on an Approved System.

(b) Make one copy of the BGSpecT software in machine-readable form solely for backup purposes. You must reproduce on any such copy all copyright notices and any other proprietary legends on the original copy of the BGSpecT software.

Restrictions:

You may not make or distribute any copy of BGSpecT software, or electronically transfer the BGSpecT software from one computer to another, or over a network, or from one System to another. You may not decompile, reverse engineer, disassemble, or otherwise reduce the BGSpecT software to a human-perceivable form. You may not modify, rent, lease, lend, resell for profit, distribute or create derivative works based upon the BGSpecT software or any part thereof.

Ownership and Distribution:

The foregoing license grants you limited rights to use the BGSpecT software. Although you own the disk or CD-ROM on which the BGSpecT software is recorded, you do not become the owner of, and California Institute of Technology (and its licensors) retains title to, the BGSpecT software, and all copies thereof, and all associated patent rights, copyrights, trade secret rights and other intellectual property rights therein and thereto. All rights not specifically granted in this Agreement are reserved by California Institute of Technology.

Warranty:

The BGSpecT software and information is provided “as is” without warranty of any kind, either expressed or implied, including but not limited to the implied warranties of merchantability and/or fitness for a particular purpose. The author takes no responsibility for any kind of damage caused by the BGSpecT software. Use this program at your own risk.

Bibliography

[1] P. Jenniskens. "DIB Catalogue." (2001). http://www-space.arc.nasa.gov/~leonid/DIBcatalog.html.

[2] B.J. McCall (2004). http://dib.uiuc.edu/~bjmccall/.

[3] N. Solcà and O. Dopfer. "Protonated benzene: IR spectrum and structure of $C_6H_7^+$." *Angew. Chem. Int. Ed.*, **41**, 3628–3631 (2002).

[4] E. Anders and M. Ebihara. "Solar-system abundances of the elements." *Geochim. Cosmochim. Acta*, **46**, 2363–2380 (1982).

[5] P. Ehrenfreund and S.B. Charnley. "Organic molecules in the interstellar medium, comets, and meteorites: A voyage from dark clouds to the early earth." *Annu. Rev. Astron. Astrophys.*, **38**, 427–483 (2000).

[6] "Identified Interstellar and Circumstellar Molecules." (2004). http://www-691.gsfc.nasa.gov/cosmic.ice.lab/interste.htm.

[7] J. Cernicharo, A.M. Heras, A.G.G.M. Tielens, J.R. Pardo, F. Herpin, M. Guélin and L.B.F.M. Waters. "Infrared Space Observatorys discovery of C_4H_2, C_6H_2, and benzene in CRL 618." *Astrophys. J.*, **546**, L123-L126 (2001).

[8] F.C. Gillett, W.J. Forrest and K.M. Merrill. "8–13-micron spectra of NGC-7027, BD+30°3639, and NGC-6572." *Astrophys. J.*, **183**, 87–93 (1973).

[9] R.W. Russell, B.T. Soifer and S.P. Willner. "4 to 8 micron spectrum of NGC-7027." *Astrophys. J.*, **217**, L149–L153 (1977).

[10] M.M. Phillips, D.K. Aitken and P.F. Roche. "8–13-μm spectrophotometry of galaxies. 1. Galaxies with giant H–II region nuclei." *Mon. Not. R. Astron. Soc.*, **207**, 25–33 (1984).

[11] S.P. Willner, R.C. Puetter, R.W. Russell and B.T. Soifer. "Unidentified infrared spectral features." *Astrophys. Space Sci.*, **65**, 95–101 (1979).

[12] D.K. Aitken. C.G. Wynn-Williams, D.P. Cruikshank, eds., *"Infrared astronomy."* 207, Reidel, Dordrecht (1981).

[13] S.P. Willner. M.F. Kessler, J.P. Phillips, eds., *"Galactic and extragalactic infrared spectroscopy."* 37, Reidel, Dordrecht (1984).

[14] K. Sellgren. "Spatial observations of the Orion nebula in the unidentified 3.28 micron feature." *Astrophys. J.*, **245**, 138–147 (1981).

[15] A. Léger and J.L. Puget. "Identification of the "unidentified" IR emission features of interstellar dust?", *Astron. Astrophys.*, **137**, L5–L8 (1984).

[16] L.J. Allamandola and A.G.G.M. Tielens, and J.R. Barker. "Polycyclic aromatic hydrocarbons and the Unidentified Infrared Emission bands: Auto exhaust along the Milky Way." *Astrophys. J.*, **299**, L93–L97 (1985).

[17] W.W. Duley, D.A. Williams. "The infrared spectrum of interstellar dust: Surface functional groups on carbon." *Mon. Not. R. Astron. Soc.*, **196**, 269–274 (1981).

[18] M. Cohen, A.G.G.M. Tielens and L.J. Allamandola. “A new emission feature in *IRAS* spectra and the polycyclic aromatic hydrocarbon spectrum.” *Astrophys. J.*, **299**, L93–L97 (1985).

[19] L.J. Allamandola, A.G.G.M. Tielens and J.R. Barker. “Interstellar polycyclic aromatic hydrocarbons: The infrared emission bands, the excitation/emission mechanism, and the astrophysical implications.” *Astrophys. J. Suppl. Ser.*, **71**, 733–775 (1989).

[20] L.J. Allamandola, S.A. Sandford, D.M. Hudgins, F.C. Witteborn. “Airborne and laboratory studies of interstellar PAHs.” In *“Airborne astronomy symposium on the galactic ecosystem.”* M.R. Haas, J.A. Davidson, E.F. Erickson, eds., no. 73, 23–32, San Francisco (1995). Astronomical Society of the Pacific.

[21] A.G.G.M. Tielens, E. Peeters. S. Pfalzner, C. Kramer, C. Straubmeier, A. Heithausen, eds., *“The dense interstellar medium in galaxies.”* 497–506, Springer-Verlag, Berlin (2004).

[22] J. Szczepanski and M. Vala. “Laboratory evidence for ionized polycyclic aromatic hydrocarbons in the interstellar medium.” *Nature*, **363**, 699–701 (1993).

[23] D.M. Hudgins, C.W. Bauschlicher, Jr, L.J. Allamandola. “Closed-shell polycyclic aromatic hydrocarbon cations: a new category of interstellar polycyclic aromatic hydrocarbons.” *Spectrochim. Acta A*, **57**, 907–930 (2001).

[24] D.M. Hudgins and L.J. Allamandola. “Interstellar PAH emission in the 11-14 micron region: New insights from laboratory data and a tracer of ionized PAHs.” *Astrophys. J.*, **516**, L41–L44 (1999).

[25] E. Dwek, R.G. Arendt, D.J. Fixsen, T.J. Sodroski, N. Odegard, J.L. Weiland, W.T. Reach, M.G. Hauser, T. Kelsall, S.H. Moseley, R.F. Silverberg, R.A. Shafer, J. Ballester, D. Bazell, and R. Isaacman. "Detection and characterization of cold interstellar dust and polycyclic aromatic hydrocarbon emission, from *COBE* observations." *Astrophys. J.*, **475**, 565–579 (1997).

[26] A.G.G.M. Tielens and T.P. Snow, eds. *"The Diffuse Interstellar Bands."* Kluwer Academic Press, Dordrecht (1994).

[27] M.L. Heger. *Lick Obs. Bull.*, **10**, 146 (1922).

[28] P.W. Merrill. *Publs. Astr. Soc. Pacific*, **46**, 206 (1934).

[29] P.W. Merrill. *Publs. Astr. Soc. Pacific*, **48**, 179 (1936).

[30] G.H. Herbig. "The diffuse interstellar bands. IV. The region 4400–6850 Å." *Astrophys. J.*, **196**, 129–162 (1975).

[31] P. Jenniskens and F.-X. Desert. "A survey of diffuse interstellar bands (3800 – 8680 Å)." *Astron. Astrophys. Suppl. Ser.*, **106**, 39–78 (1994).

[32] J. Krełowski, C. Sneden, D. Hiltgen. "A survey of weak diffuse interstellar bands in selected ranges between 5600 and 7000 Å." *Planet. Space Sci.*, **43**, 1195–1203 (1995).

[33] P. Jenniskens, I. Porceddu, P. Benvenuti, and F.-X. Desert. "Diffuse interstellar bands: Resolved rotational band structure at 5850 Å." *Astron. Astrophys.*, **313**, 649–656 (1996).

[34] L.J. Allamandola. "Laboratory studies of DIB carriers." A.G.G.M. Tielens and T.P. Snow, eds., *"The Diffuse Interstellar Bands."* Kluwer Academic Press, Dordrecht (1994).

[35] S. Leach. “Spectroscopy and photophysics of possible large molecule carriers of the diffuse interstellar bands.” A.G.G.M. Tielens and T.P. Snow, eds., *“The Diffuse Interstellar Bands.”* Kluwer Academic Press, Dordrecht (1994).

[36] A.E. Douglas. “Origin of diffuse interstellar lines.” *Nature*, **269**, 130-132 (1977).

[37] P. Thaddeus. “Carbon chains and the diffuse interstellar bands.” A.G.G.M. Tielens and T.P. Snow, eds., *“The Diffuse Interstellar Bands.”* Kluwer Academic Press, Dordrecht (1994).

[38] M.B. Bell, P.A. Feldman, M.J. Travers, M.C. McCarthy, C.A. Gottlieb and P. Thaddeus. “Detection of $HC_{11}N$ in the cold dust cloud TMC-1.” *Astrophys. J.*, **483**, L61–L64 (1997).

[39] M.B. Bell, P.A. Feldman, J.K.G. Watson, M.C. McCarthy, M.J. Travers, C.A. Gottlieb and P. Thaddeus. “Observations of long C_nH molecules in the dust cloud TMC-1.” *Astrophys. J.*, **518**, 740–747 (1999).

[40] M.C. McCarthy, M.J. Travers, A. Kovács, C.A. Gottlieb and P. Thaddeus. “Eight new carbon chain molecules.” *Astrophys. J. Suppl. Ser.*, **113**, 105–120 (1997).

[41] P. Thaddeus, M.C. McCarthy, M.J. Travers, C.A. Gottlieb and W. Chen. “New carbon chains in the laboratory and in interstellar space.” *Faraday Discuss.*, **109**, 121–135 (1998).

[42] M.C. McCarthy and P. Thaddeus. “Microwave and laser spectroscopy of carbon chains and rings.” *Chem. Soc. Rev.*, **30**, 177–185 (2001).

[43] J.P. Maier. “Electronic spectroscopy of carbon chains.” *Chem. Soc. Rev.*, **26**, 21–28 (1997).

[44] J.P. Maier. “Electronic spectroscopy of carbon chains.” *J. Phys. Chem. A*, **102**, 3462–3469 (1998).

[45] D.A. Kirkwood, M. Tulej, M.V. Pachkov, M. Schnaiter, F. Guthe, M. Grutter, M. Wyss and J.P. Maier, G. Fischer. “Electronic spectra of carbon chain anions: $C_{2n}H^-$ (n=5–12).” *J. Chem. Phys.*, **111**, 9280–9286 (1999).

[46] T. Piño, H.B. Ding, F. Guthe and J.P. Maier. “Electronic spectra of the chains $HC_{2n}H$ (n=8–13) in the gas phase.” *J. Chem. Phys.*, **114**, 2208–2212 (2001).

[47] H. Ding, T.W. Schmidt, T. Piño, A.E. Boguslavskiy, F. Guthe and J.P. Maier. “Gas phase electronic spectra of the linear carbon chains $HC_{2n+1}H$ (n = 3–6, 9).” *J. Chem. Phys.*, **119**, 814–819 (2003).

[48] M. Tulej, D.A. Kirkwood, G. Maccaferri, O. Dopfer and J.P. Maier. “Electronic spectra of linear carbon anions.” *Chem. Phys.*, **228**, 293–299 (1998).

[49] M. Tulej, D.A. Kirkwood, M. Pachkov and J.P. Maier. “Gas-phase electronic transitions of carbon chain anions coinciding with diffuse interstellar bands.” *Astrophys. J.*, **506**, L69–L73 (1998).

[50] G.A. Galazutdinov, J. Krełowski and F.A. Musaev. “On bare carbon chain anions as possible carriers of the diffuse interstellar features.” *Mon. Not. R. Astron. Soc.*, **310**, 1017–1022 (1999).

[51] B.J. McCall, J. Thorburn, L.M. Hobbs, T. Oka and D.G. York. “Rejection of the C_7^- diffuse interstellar band hypothesis.” *Astrophys. J.*, **559**, L49-L53 (2001).

[52] T. Motylewski, H. Linnartz, O. Vaizert and J.P. Maier, G.A. Galazutdinov and F.A. Musaev, J. Krełowski, G.A.H. Walker and D.A. Bohlender. “Gas-phase electronic

spectra of carbon-chain radicals compared with diffuse interstellar band observations." *Astrophys. J.*, **531**, 312–320 (2000).

[53] J.P. Maier, G.A.H. Walker and D.A. Bohlender. "On the possible role of carbon chains as carriers of diffuse interstellar bands." *Astrophys. J.*, **602**, 286–290 (2004).

[54] F. Salama, G.A. Galazutdinov, J. Krełowski, L.J. Allamandola and F.A. Musaev. "Polycyclic aromatic hydrocarbons and the diffuse interstellar bands: A survey." *Astrophys. J.*, **526**, 265–273 (1999).

[55] J. Krełowski, G.A. Galazutdinov, F.A. Musaev and J. Nirski. "Identification of naphthalene cation in space?", *Mon. Not. R. Astron. Soc.*, **328**, 810–814 (2001).

[56] R. Ruiterkamp, T. Halasinski, F. Salama, B.H. Foing, L.J. Allamandola, W. Schmidt and P. Ehrenfreund. "Spectroscopy of large PAHs. Laboratory studies and comparison to the Diffuse Interstellar Bands." *Astron. Astrophys.*, **390**, 1153–1170 (2002).

[57] T.M. Halasinski, D.M. Hudgins, F. Salama, L.J. Allamandola, T. Bally. "Electronic absorption spectra of neutral pentacene ($C_{22}H_{14}$) and its positive and negative ions in Ne, Ar, and Kr matrices." *J. Phys. Chem. A*, **104**, 7484–7491 (2000).

[58] C. Joblin, F. Salama, L. Allamandola. "Absorption and emission spectroscopy of perylene ($C_{20}H_{12}$) isolated in Ne, Ar, and N_2 matrices." *J. Chem. Phys.*, **110**, 7287–7297 (1999).

[59] F. Salama, C. Joblin and L.J. Allamandola. "Electronic absorption spectroscopy of matrix-isolated polycyclic aromatic hydrocarbon cations. II. The phenanthrene cation ($C_{14}H_{10}^+$) and its 1-methyl derivative." *J. Chem. Phys.*, **101**, 10252–10262 (1994).

[60] M. Hartmann, A. Lindinger, J.P. Toennies and A.F. Vilesov. “The phonon wings in the $S_1 \leftarrow S_0$ spectra of tetracene, pentacene, porphin and phthalocyanine in liquid helium droplets.” *Phys. Chem. Chem. Phys.*, **4**, 4839-4844 (2002).

[61] G. Rouillé, S. Krasnokutski, F. Huisken, and T. Henning, O. Sukhorukov and A. Staicu. “Ultraviolet spectroscopy of pyrene in a supersonic jet and in liquid helium droplets.” *J. Chem. Phys.*, **120**, 6028–6034 (2004).

[62] D. Romanini, L. Biennier, F. Salama, A. Kachanov, L.J. Allamandola, F. Stoeckel. “Jet-discharge cavity ring-down spectroscopy of ionized polycyclic aromatic hydrocarbons: Progress in testing the PAH hypothesis for the diffuse interstellar band problem.” *Chem. Phys. Lett.*, **303**, 165–170 (1999).

[63] L. Biennier, F. Salama and L.J. Allamandola, J.J. Scherer. “Pulsed discharge nozzle cavity ringdown spectroscopy of cold polycyclic aromatic hydrocarbon ions.” *J. Chem. Phys.*, **118**, 7863–7872 (2003).

[64] L. Biennier, F. Salama and M. Gupta, A. O’Keefe. “Multiplex integrated cavity output spectroscopy of cold PAH cations.” *Chem. Phys. Lett.*, **387**, 287–294 (2004).

[65] L.A. Chewter, M. Sander, K. Müller–Dethlefs and E.W. Schlag. “High resolution zero kinetic energy photoelectron spectroscopy of benzene and determination of the ionization potential.” *J. Chem. Phys.*, **86**, 7763–7772 (1987).

[66] G.I. Nemeth, H.L. Selzle and E.W. Schlag. “Magnetic ZEKE experiments with mass analysis.” *Chem. Phys. Lett.*, **215**, 151–155 (1993).

[67] J.A. Syage and J.E. Wessel. “Resonance ion dissociation spectroscopy of naphthalene ions prepared in a supersonic expansion.” *J. Chem. Phys.*, **87**, 3313–3320 (1987).

[68] M.C.R. Cockett, H. Ozeki, K. Okuyama and K. Kimura. "Vibronic coupling in the ground cationic state of naphthalene: A laser threshold photoelectron [zero kinetic energy (ZEKE)-photoelectron] spectroscopic study." *J. Chem. Phys.*, **98**, 7763–7772 (1993).

[69] M.C.R. Cockett and K. Kimura. "A study of anthracene-Ar$_n$ ($n = 0-5$) in the ground cationic state by laser threshold photoelectron spectroscopy: Selective ionization of complex isomers formed in the free jet expansion." *J. Chem. Phys.*, **100**, 3429–3441 (1994).

[70] T. Vondrak, S. Sato and K. Kimura. "Zero kinetic energy photoelectron study of the naphthalene–Ar van der Waals complex." *Chem. Phys. Lett.*, **261**, 481–485 (1996).

[71] T. Pino, N. Boudin and P. Bréchignac. "Electronic absorption spectrum of cold naphthalene cation in the gas phase by photodissociation of its van der Waals complexes." *J. Chem. Phys.*, **111**, 7337–7347 (1999).

[72] P. Bréchignac and T. Pino. "Electronic spectra of cold gas phase PAH cations: Towards the identification of the Diffuse Interstellar Bands carriers." *Astron. Astrophys.*, **343**, L49-L52 (1999).

[73] P. Bréchignac, T. Pino, N. Boudin. "Laboratory spectra of cold gas phase polycyclic aromatic hydrocarbon cations, and their possible relation to the diffuse interstellar bands." *Spectrochim. Acta A*, **57**, 745–756 (2001).

[74] N. Boudin , T. Pino and P. Bréchignac. "Visible spectroscopy of polycyclic aromatic hydrocarbons ionic derivatives: Application to astrophysics." *J. Mol. Struct.*, **563**, 209–214 (2001).

[75] T.P. Snow, V. Le Page, Y. Keheyan and V.M. Bierbaum. "The interstellar chemistry of PAH cations." *Nature*, **391**, 259–260 (1998).

[76] E. Herbst and V. Le Page. "Do H atoms stick to PAH cations in the interstellar medium?", *Astron. Astrophys.*, **344**, 310–316 (1999).

[77] T.R. Geballe and T. Oka. "Detection af H_3^+ in interstellar space." *Nature*, **384**, 334–335 (1996).

[78] B.J. McCall, K.H. Hinkle, T.R. Geballe and T. Oka. "H_3^+ in dense and diffuse clouds." *Faraday Discuss.*, **109**, 267–280 (1998).

[79] P.J. Huggins, T.G. Phillips, G. Neugebauer, M.W. Werner, P.G. Wannier and D. Ennis. "Detection of the J = 3–2 lines of HCN, HNC, and HCO^+ in the Orion molecular cloud." *Astrophys. J.*, **227**, 441–445 (1979).

[80] A. Wootten, J.G. Mangum, B.E. Turner, M. Bogey, F. Boulanger, F. Combes, P.J. Encrenaz and M. Gerin. "Detection of interstellar H_3O^+: A confirming line." *Astrophys. J.*, **380**, L79–L83 (1991).

[81] T.G. Phillips, E.F. van Dishoeck and J. Keene. "Interstellar H_3O^+ and its relation to the O_2 and H_2O abundances." *Astrophys. J.*, **399**, 533–550 (1992).

[82] D.B. Milligan, P.F. Wilson, C.G. Freeman, M. Meot-Ner (Mautner) and M.J. McEwan. "Dissociative proton transfer reactions of H_3^+, N_2H^+, and H_3O^+ with acyclic, cyclic, and aromatic hydrocarbons and nitrogen compounds, and astrochemical implications." *J. Phys. Chem. A*, **106**, 9745–9755 (2002).

[83] V. Le Page, T.P. Snow and V.M. Bierbaum. "Hydrogenation and charge states of PAHs in diffuse clouds. I. Development of a model." *Astrophys. J. Suppl. Ser.*, **132**, 233–251 (2001).

[84] V. Le Page, T.P. Snow and V.M. Bierbaum. "Hydrogenation and charge states of PAHs in diffuse clouds. II. Results." *Astrophys. J.*, **584**, 316–330 (2003).

[85] G.A. Olah. "Aromatic substitution. XXVIII. Mechanism of electrophilic aromatic substitutions." *Acc. Chem. Res.*, **4**, 240–248 (1971).

[86] C. Reid. "The aromatic carbonium ions." *J. Am. Chem. Soc.*, **76**, 3264–3268 (1954).

[87] von H. Luther and G. Pockels. "Molekülverbindungen mit ansolvosäuren. 1. Ultraviolettspektren von systemen aromat–aluminiumhalogenid–(halogenwasserstoff)." *Z. Elektrochem.*, **59**, 159–168 (1955).

[88] H.-H. Perkampus and E. Baumgarten. "Proton-addition complexes of aromatic hydrocarbons." *Angew. Chem. Int. Ed.*, **3**, 776–783 (1964).

[89] B.S. Freiser and J.L. Beauchamp. "Photochemistry of organic ions in the gas phase. Comparison of the gas phase photodissociation and solution absorption spectra of benzoyl cation, protonated benzene and protonated mesitylene." *J. Am. Chem. Soc.*, **98**, 3136–3139 (1976).

[90] B.S. Freiser and J.L. Beauchamp. "Acid-base properties of molecules in excited electronic states utilizing ion cyclotron resonance spectroscopy." *J. Am. Chem. Soc.*, **99**, 3214–3225 (1977).

[91] J.L. Beauchamp. Private communication.

[92] H.-J. Köhler and H. Lischka. "Theoretical investigations on carbocations. Structure and stability of $C_3H_5^+$, $C_4H_9^+$ (2–butyl cation), $C_5H_5^+$, $C_6H_7^+$ (protonated benzene) and $C_7H_{11}^+$ (2–norbornyl cation)." *J. Am. Chem. Soc.*, **101**, 3479–3486 (1979).

[93] M. Eckert-Maksić, Z.B. Maksić and M. Klessinger. "Protonation of fused aromatic systems – ab-initio study of some model Wheland intermediates." *Int. J. Quantum Chem.*, **49**, 383–396 (1994).

[94] M.N. Glukhovtsev, A. Pross, A. Nicolaides and L. Radom. "Is the most stable gas-phase isomer of the benzenium cation a face-protonated π-complex?", *J. Chem. Soc. Chem. Commun.*, **1**, 2347–2348 (1995).

[95] R. Sumathy and E.S. Kryachko. "Multiprotonation of benzene: a theoretical study." *J. Phys. Chem. A*, **106**, 510–519 (2002).

[96] N. Solcà and O. Dopfer. "Interaction of the benzenium ion with inert ligands: IR spectra of $C_6H_7^+$–L_n cluster cations (L = Ar, N_2, CH_4, H_2O)." *Chem. Eur. J.*, **9**, 3154–3163 (2003).

[97] W. Jones, P. Boissel, B. Chiavarino, M.E. Crestoni, S. Fornarini, J. Lemaire and P. Maitre. "Infrared fingerprint of protonated benzene in the gas phase." *Angew. Chem. Int. Ed.*, **42**, 2057–2059 (2003).

[98] M.J. Frisch, G.W. Trucks, H.B. Schlegel, G.E. Scuseria, M.A. Robb, J.R. Cheeseman, V.G. Zakrzewski, J.A. Montgomery, Jr, R.E. Stratmann, J.C. Burant, S. Dapprich, J.M. Millam, A.D. Daniels, K.N. Kudin, M.C. Strain, O. Farkas, J. Tomasi, V. Barone, M. Cossi, R. Cammi, B. Mennucci, C. Pomelli, C. Adamo, S. Clifford, J. Ochterski, G.A. Petersson, P.Y. Ayala, Q. Cui, K. Morokuma, D.K. Malick, A.D. Rabuck, K.

Raghavachari, J.B. Foresman, J. Cioslowski, J.V. Ortiz, A.G. Baboul, B.B. Stefanov, G. Liu, A. Liashenko, P. Piskorz, I. Komaromi, R. Gomperts, R.L. Martin, D.J. Fox, T. Keith, M.A. Al-Laham, C. Y. Peng, A. Nanayakkara, M. Challacombe, P.M.W. Gill, B. Johnson, W. Chen, M.W. Wong, J.L. Andres, C. Gonzalez, M. Head-Gordon, E.S. Replogle and J.A. Pople. *"GAUSSIAN 98, Revision A.9."* Gaussian, Inc., Pittsburgh, PA (1998).

[99] P. Hohenberg and W. Kohn. "Inhomogeneous electron gas." *Phys. Rev.*, **136**, B864–B871 (1964).

[100] W. Kohn and L.J. Sham. "Self-consistent equations including exchange and correlation effects." *Phys. Rev.*, **140**, A1133–A1138 (1965).

[101] A.D. Becke. "Density-functional thermochemistry. III. The role of exact exchange." *J. Chem. Phys.*, **98**, 5648–5652 (1993).

[102] C. Lee, W. Yang and R.G. Parr. "Development of the Colle-Salvetti correlation-energy formula into a functional of the electron density." *Phys. Rev. B*, **37**, 785–789 (1988).

[103] A.D. McLean and G.S. Chandler. "Contracted Gaussian basis sets for molecular calculations. I. Second row atoms, Z=11–18." *J. Chem. Phys.*, **72**, 5639–5648 (1980).

[104] R. Krishnan, J.S. Binkley, R. Seeger and J.A. Pople. "Self-consistent molecular orbital methods. XX. A basis set for correlated wave functions." *J. Chem. Phys.*, **72**, 650–654 (1980).

[105] M.J. Frisch, J.A. Pople and J.S. Binkley. "Self-consistent molecular orbital methods. 25. Supplementary functions for Gaussian basis sets." *J. Chem. Phys.*, **80**, 3265–3269 (1984).

[106] T. Clark, J. Chandrasekhar, G.W. Spitznagel and P.v.R. Schleyer. "Efficient diffuse function-augmented basis-sets for anion calculations. 3. The 3–21+G basis set for 1st-row elements, LI–F." *J. Comp. Chem.*, **4**, 294–301 (1983).

[107] *"GaussView, ver. 2.1."* Gaussian, Inc., Pittsburgh, PA (2000).

[108] A.P. Scott and L. Radom. "Harmonic vibrational frequencies: An evaluation of Hartree–Fock, Møller–Plesset, quadratic configuration interaction, density functional theory, and semiempirical scale factors." *J. Phys. Chem.*, **100**, 16502–16513 (1996).

[109] J.M.L. Martin, J. El-Yazal and J.-P. François. "Structure and vibrational spectrum of some polycyclic aromatic compounds studied by density functional theory. 1. Naphthalene, azulene, phenanthrene and anthracene." *J. Phys. Chem.*, **100**, 15358–15367 (1996).

[110] M.W. Wong. "Vibrational frequency prediction using density functional theory." *Chem. Phys. Lett.*, **256**, 391–399 (1996).

[111] A. Miani, E. Cané , P. Palmieri and A. Trombetti, N.C. Handy. "Experimental and theoretical anharmonicity for benzene using density functional theory." *J. Chem. Phys.*, **112**, 248–259 (2000).

[112] E. Cané, A. Miani, P. Palmieri, R. Tarroni and A. Trombetti. "The gas-phase infrared spectra of anthracene-h_{10} and anthracene-d_{10}." *J. Chem. Phys.*, **106**, 9004–9012 (1997).

[113] "NIST Chemistry WebBook." (2003). http://webbook.nist.gov/chemistry/.

[114] E.P. Hunter, S.G. Lias. "Evaluated gas phase basicities and proton affinities of molecules: An update." *J. Phys. Chem. Ref. Data*, **27**, 413–656 (1998).

[115] J.W. Hager, S.C. Wallace. “Two-laser photoionization supersonic jet mass spectrometry of aromatic molecules.” *Anal. Chem.*, **60**, 5–10 (1988).

[116] C.W. Bauschlicher, Jr and S.R. Langhoff. “Bond dissociation energies for substituted polycyclic aromatic hydrocarbons and their cations.” *Mol. Phys.*, **96**, 471–476 (1999).

[117] C.W. Bauschlicher, Jr. “The reaction of polycyclic aromatic hydrocarbon cations with hydrogen atoms: the astrophysical implications.” *Astrophys. J.*, **509**, L125–L127 (1998).

[118] R.J. McMahon, M.C. McCarthy, C.A. Gottlieb, J.B. Dudek, J.F. Stanton and P. Thaddeus. “The radio spectrum of the phenyl radical.” *Astrophys. J.*, **590**, L61–L64 (2003).

[119] D.J. DeFrees, A.D. McLean and E. Herbst. “Theoretical investigation of the interstellar CH_3NC/CH_3CN ratio.” *Astrophys. J.*, **293**, 236–242 (1985).

[120] C. Joblin, C. Masselon, P. Boissel, P. de Parseval, S. Martinovic and J.F. Muller. “Simulation of interstellar aromatic hydrocarbons using ion cyclotron resonance. Preliminary results.” *Rapid Comm. Mass Spectrom.*, **11**, 1619–1623 (1997).

[121] M. Hirama, T. Ishida, J.-I. Aihara. “Possible molecular hydrogen formation mediated by the radical cations of anthracene and pyrene.” *J. Comp. Chem.*, **24**, 1378–1382 (2003).

[122] J.B. Foresman, M. Head-Gordon, J.A. Pople and M.J. Frisch. “Toward a systematic molecular orbital theory for excited states.” *J. Phys. Chem.*, **96**, 135–149 (1992).

[123] J.M.O. Matos, B. Roos and P.-Å. Malmqvist. "A CASSCF–CCI study of the valence and lower excited states of the benzene molecule." *J. Chem. Phys.*, **86**, 1458–1466 (1987).

[124] J.V. Goodpaster, J.F. Harrison and V.L. McGuffin. "*Ab Initio* Study of Polycyclic Aromatic Hydrocarbons in Their Ground and Excited States." *J. Phys. Chem. A*, **102**, 3372–3381 (1998).

[125] R. González-Luque, L. Serrano-Andrés, M. Merchán, M.P. Fülscher. "Theoretical characterization of the absorption spectra of phenanthrene and its radical cation." *Theor. Chem. Acc.*, **110**, 224–232 (2003).

[126] J.L. Weisman, T.J. Lee and M. Head-Gordon. "Electronic spectra and ionization potentials of a stable class of closed shell polycyclic aromatic hydrocarbon cations." *Spectrochim. Acta A*, **57**, 931–945 (2001).

[127] T. Hashimoto, H. Nakano and K. Hirao. "Theoretical study of the valence $\pi \rightarrow \pi^*$ excited states of polyacenes: Benzene and naphthalene." *J. Chem. Phys.*, **104**, 6244–6258 (1996).

[128] J.B. Foresman and Æ. Frisch. *"Exploring Chemistry with Electronic Structure Methods."* second ed., Gaussian, Inc., Pittsburgh, PA (1996).

[129] G. Müller, J.Y. Fan, J.L. Lyman, W.E. Schmid and K.L. Kompa. "Two-laser resonance-enhanced photoionization spectrum of benzene." *J. Chem. Phys.*, **90**, 3490–3497 (1989).

[130] T. Troxler, R. Knochenmuss and S. Leutwyler. "Isomer-specific spectra and ionization potentials of van der Waals clusters." *Chem. Phys. Lett*, **159**, 554–558 (1989).

[131] J.W. Hager and S.C. Wallace. "Two-laser photoionization supersonic jet mass spectrometry of aromatic molecules." *Anal. Chem.*, **60**, 5–10 (1988).

[132] E.A. Mangle and M.R. Topp. "Excited-state dynamics of jet-cooled pyrene and some molecular complexes." *J. Phys. Chem.*, **90**, 802–807 (1986).

[133] *"ChemOffice 2000: ChemDraw, Chem3D, ChemFinder."* CambridgeSoft Corp., Cambridge, MA (2000).

[134] D.C. Harris and M.D. Bertolucci. *"Symmetry and Spectroscopy. An introduction to vibrational and electronic spectroscopy."* Dover Publications, Inc., New York (1989).

[135] Y. Ohshima and Y. Endo. "Structure of C_3S studied by pulsed-discharge-nozzle Fourier-transform microwave spectroscopy." *J. Mol. Spectr.*, **153**, 627–634 (1992).

[136] M. Tulej, D.A. Kirkwood, G. Maccaferri, O. Dopfer and J.P. Maier. "Electronic spectra of linear carbon anions." *Chem. Phys.*, **228**, 293–299 (1998).

[137] S. Davis, D.T. Anderson, G. Duxbury and D.J. Nesbitt. "Jet-cooled molecular radicals in slit supersonic discharges: Sub-Doppler infrared studies of methyl radical." *J. Chem. Phys.*, **107**, 5661–5675 (1997).

[138] D. Rolland, A.A Specht, M.W. Blades, J.W. Hepburn. "Resonance enhanced multiphoton dissociation of polycyclic aromatic hydrocarbons cations in an RF ion trap." *Chem. Phys. Lett.*, **373**, 292–298 (2003).

[139] W.H. Robertson, J.A. Kelley and M.A. Johnson. "A pulsed supersonic entrainment reactor for the rational preparation of cold ionic complexes." *Rev. Sci. Instr.*, **71**, 4431–4434 (2000).

[140] W.C. Wiley, I.H. McLaren. "Time-of-flight mass spectrometer with improved resolution." *Rev. Sci. Instr.*, **26**, 1150–1157 (1955).

[141] V.I. Karataev, B.A. Mamyrin and D.V. Shmikk. "New method for focusing ion bunches in time-of-flight mass spectrometers." *Sov. Phys. – Tech. Phys. USSR*, **16**, 1177 (1972).

[142] B.A. Mamyrin, V.I. Karataev, D.V. Shmikk and V.A. Zagulin. "Mass-reflectron: A new nonmagnetic time-of-flight high-resolution mass-spectrometer." *Sov. Phys. – JETP*, **64**, 82–89 (1973).

[143] D.A. Rodham. "Spectroscopic studies of the gas phase complexes benzene–ammonia, sodium–water, and sodium–ammonia." Ph.D. thesis, *California Institute of Technology* (1997).

[144] S. Wu. "Development of broadly tunable parametric light sources and their application to alkali metal – small molecule cluster spectroscopy." Ph.D. thesis, *California Institute of Technology* (1999).

[145] H. Zhang. "Spectroscopic studies of N_2O and HNO_4: A window into the global biogeochemistry of nitrogen." Ph.D. thesis, *California Institute of Technology* (2001).

[146] S. Wu, G.A. Blake, Z.Y. Sun and J.W. Ling. "Simple, high-performance type II β–BaB_2O_4 optical parametric oscillator." *Appl. Optics*, **36**, 5898–5901 (1997).

[147] G. Anstett, G. Göritz, R. Urschel, R. Wallenstein, A. Borsutzky. "Reduction of the spectral width and beam divergence of a BBO–OPO by using collinear type–II phase matching and back reflection of the pump beam." *Appl. Phys. B*, **72**, 583–589 (2001).

[148] D.J. Armstrong and A.V. Smith. "Demonstration of improved beam quality in an image-rotating optical parametric oscillator." *Optics Lett.*, **27**, 40–42 (2002).

[149] B.S. Freiser and J.L. Beauchamp. "Laser photodissociation of benzene radical cations. Evidence for a two photon process involving a long lived intermediate." *Chem. Phys. Lett.*, **35**, 35–40 (1975).

[150] O. Dopfer, R.V. Olkhov and J.P. Maier. "Infrared photodissociation spectra of the CH stretch vibrations of $C_6H_6^+$–Ar, $C_6H_6^+$–N_2, and $C_6H_6^+$–$(CH_4)_{1-4}$." *J. Chem. Phys.*, **111**, 10754–10757 (1999).

[151] R.G. Satink, H. Piest, G. von Helden and G. Meijer. "The infrared spectrum of the benzene-Ar cation." *J. Chem. Phys.*, **111**, 10750–10753 (1999).

[152] J.M. Bakker, R.G. Satink, G. von Helden and G. Meijer. "Infrared photodissociation spectroscopy of benzene–Ne,Ar complex cations." *Phys. Chem. Chem. Phys.*, **4**, 24–33 (2002).

[153] H. Piest, G. von Helden and G. Meijer. "Infrared spectroscopy of jet-cooled cationic polyaromatic hydrocarbons: Naphthalene." *Astrophys. J.*, **520**, L75–L78 (1999).

[154] J.A. Piest, J. Oomens, J. Bakker, G. von Helden and G. Meijer. "Vibrational spectroscopy of gas-phase neutral and cationic phenanthrene in their electronic groundstates." *Spectrochim. Acta A*, **57**, 717–735 (2001).

[155] S. Suzuki, P.G. Green, R.E. Bumgarner, S. Dasgupta, W.A. Goddard, G.A. Blake. "Benzene forms hydrogen-bonds with water." *Science*, **257**, 942–944 (1992).

[156] E.S. Kryachko and M.T. Nguyen. "Low energy barrier proton transfer in protonated benzene–water complex." *J. Phys. Chem. A*, **105**, 153–155 (2001).

[157] P.M. Palmer, M.R. Topp. "Electronic spectroscopy of jet-cooled anthracene$(H_2O)_n$ clusters ($n = 1 - 16$): comparisons of inhomogeneous structure." *Chem. Phys.*, **239**, 65–81 (1998).

[158] P.M. Palmer, M.R. Topp. "Spectroscopic properties of jet-cooled methanol clusters ($n = 1 - 6$) attached to anthracene." *Chem. Phys. Lett.*, **292**, 307–316 (1998).